Cavity-free nano-magnomechanics with a thin-film magnon waveguide supported by cantilever and bridge geometries

Harvey Brown

Doctor of Philosophy

THE UNIVERSITY OF YORK

School of Physics, Engineering and Technology

March 2024

THE UNIVERSITY OF YORK

Abstract

While photons have been widely explored for the development of platforms that couple quantum objects together, there are fundamental constraints that limit their applications. Typically, these photons populate cavities whereby supported resonant frequencies are dependent on the geometry of the device, and there is little scope offered to change this in-situ. Magnons, on the other hand, can couple to a variety of subsystems such as photons and phonons and support a broad frequency range dependent on an applied biasing field. The interaction between magnons and phonons, parametric in nature, has been explored experimentally prior using a sphere of yttrium-iron-garnet and a copper cavity, although the device implementation is bulky and incompatible with on-chip realisations. To this end, this thesis examines the possibility of a 'cavity-free' realisation of parametric magnon-phonon coupling, in which the device need not be situated within a physical cavity, rather driven by a superconducting wave-guide. For this, magnons supported in thin films of yttrium-iron-garnet are coupled to the phonon modes of the bulk substrates on which it is grown to mediate coupling. This offers both a nano-scale implementation compatible with chip designs as well as the promise of a versatile device in which substrates of a smaller mechanical damping could easily be integrated.

The theory of coupling between phonons and magnons is derived assuming that the bulk substrate can be treated as an Euler-Bernoulli beam and that the thin magnetic film does not impact the elastic dynamics. Analysis finds that a single magnon-phonon coupling rate some three to four orders of magnitude larger than that previously reported using the YIG sphere and copper cavity device setup, and that cooperativities on the order of 100s to 1000s should be attainable using this newly proposed device. This thesis also considers a number of bench-marking phenomena to establish where the device sits in the larger landscape of coupled systems. For a pre-cooled device at currently attainable cryogenic temperatures, accessing the mechanical ground state should be feasible. The emergence of magnomechanically induced transparency windows is also considered, and the strength of the magnon-phonon interaction leads to behaviour of the mechanical sidebands previously unseen. Lastly, the magnon spring effect is found to permit significant spring-hardening of the phonons almost 3 orders of magnitude larger than previously reported even in the resolved-sideband regime.

Declaration

I declare that this thesis is a presentation of original work of which I am the sole author. This work has not previously been presented for an award at this, or any other, University. All sources are acknowledged as References

Acknowledgements

I firstly extend my gratitude to those that have been involved with the supervision of this project; Dr. Stuart Cavill, Dr. Aires Ferreira, and Dr. Ignacio Wilson-Rae. Their contributions to the support and guidance of this research over the past four years has proved invaluable, as well as their feedback on the writing of this thesis.

I wish to thank Dr. Daniel Cheshire and Jack Pearce of the Condensed Matter Group at York, for not only their insights into physics but also for providing the encouragement to persevere. I couldn't have asked for a better office environment.

The list of those that have provided nonacademic support is long, but there are a number of people deserving of recognition. I owe a heartfelt thank you to Ellen and Olivia, for filling my days with laughter. There's no doubt that without their influence my days of research and writing would have been a lot more dreary. I also thank Liv from ASC Performance who has provided constant encouragement in training sessions, both physically and mentally, between my rants on research and chin-ups.

Mostly, I want to thank my family. Without the love and support of my parents, Angela and Tim, and my sister, Emilie, this journey would not have been possible. Collectively, they have fostered my scientific curiosity since the beginning of my education and provided an environment for me to flourish that I find myself lucky to have received - I could not have undertaken this thesis without them. I am forever indebted to the unquestioning love of my dogs, Evie and Brie, who have provided it unconditionally in the way that only a pet can throughout the best and worst times of this journey. Sadly, Brie did not get to celebrate the culmination of this work with me, but her influence can be seen by the very fact that this thesis has been written; I dedicate it to the pair of them and my family.

For Evie and Brie, Angela and Tim, and Emilie.
Thank you for your unfaltering love.

Contents

List of Figures

List of Tables

List of Symbols

c	Speed of light in vaccuum
g_{e}	Electron g-factor
μ_{B}	Bohr magneton
k_{B}	Boltmann constant
a_0	Unit cell length
$\mathbf{M}$	Magnetisation vector
M_{s}	Saturation magnetisation
$\mathbf{m}$	Reduced magnetisation magnetisation, $\mathbf{m} = \mathbf{M}/M_{\mathrm{s}}$
α	Gilbert damping
$\mathcal{J}$	Exchange energy
α_{ex}	Cubic crystal exchange constant
$\hat{N}$	Diagonalised demagnetisation tensor
$\mathbf{H}_{\mathrm{d}}$	Demagnetisation field, $\mathbf{H}_{\mathrm{d}} = 4\pi\hat{N} \cdot \mathbf{M}$
$\mathbf{H}_{\mathrm{e}}$	Zeeman (external or applied) field
$\mathbf{H}_{\mathrm{ex}}$	Exchange field
u_{ik}	Strain tensor
u_i	Flexural deflection profile
σ_{ik}	Stress tensor
c_{ii}	Elastic modulii
E	Young's modulus
ν	Poisson's ratio
I	Second moment of area, $I = \int_A y^2 \, \mathrm{d}A$
$L_{\mathrm{m,R}}$	Length of rectangular magnetic film, mechanical resonator
$w_{\mathrm{m,R}}$	Width of rectangular magnetic film, mechanical resonator
$t_{\mathrm{m,R}}$	Thickness of rectangular magnetic film, mechanical resonator
U_{me}	Magnetoelastic energy density
$B_{1,2}$	First, second magnetoelastic constant
ω_{m}	Magnon mode angular frequency
Δ_{m}	Magnon mode spacing
ω_{cav}	Cavity (transmission line) angular frequency
ω_{R}	Mechanical mode angular frequency

κ_{ex}	Cavity (transmission line) decay rate into magnon modes
κ_{m}	Magnon mode line-width
Γ_{R}	Mechanical mode damping
P_{in}	Input power into cavity (transmission line) modes
n_{mag}	Number of magnomechanically relevant magnons
$\bar{n}_{th}$	Average number of thermal phonons, $\bar{n}_{th} = (\exp(\hbar\omega_R/k_{BT}) - 1)^{-1}$
g_0	Single magnon-phonon coupling strength
g	Multimagnon-phonon coupling strength, $g = g_0\sqrt{n_{mag}}$
$\mathcal{C}$	Magnon-phonon cooperativity
$\mathcal{C}_q$	'Quantum' magnon-phonon cooperativity, $\mathcal{C}_q = \mathcal{C}/\bar{n}_{th}$

Chapter 1

Introduction

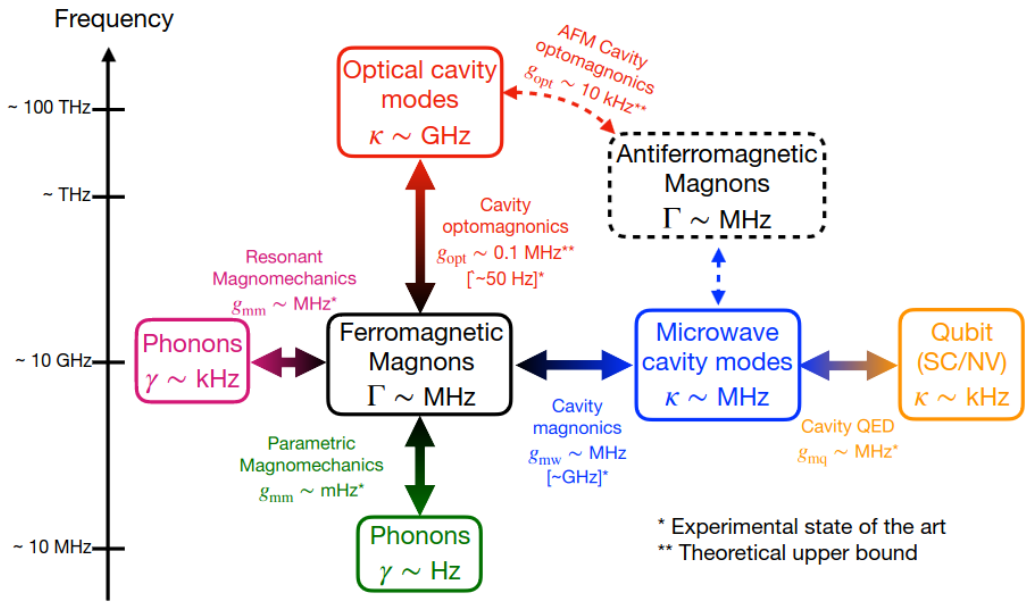

FIGURE 1.1: Characteristic frequencies and decay rates for various degrees of freedom able to be coupled to spin-waves. γ, κ, and Γ are the decay rates of the phonons, photons, and magnons, respectively [1].

Mechanical oscillators have been widely explored as a mediator between different systems, in which a number of possible forces are exploited to couple the mechanical vibrations (phonons) to optical photons. Specifically, optomechanics is the research field which explores these couplings and the effects that they can produce [2]. Contributions to the field have been made in considering the radiation force [3, 4, 5], the electrostatic force [6, 7], and the piezoelectric force [8, 9]. Within these systems, however, there is often an intrinsic lack of tunability of the photons, where supported photon frequencies are dictated by the geometry of the device with little scope to modify this in situ.

Magnons, on the other hand, offer a promising candidate to replace photons in devices that interact with mechanical oscillators. To this end, it is essential to have magnons with as long a lifetime as is practical, and as many of them as is possible. The ferrimagnet yttrium-iron-garnet, referred to as YIG in literature, is a promising material. YIG has many magnetic properties which make it appealing for such uses [10, 11], including it's low magnetic damping, the ability to grow high-quality single crystal samples [12, 13], high spin-density [14], and highly pronounced non-linear dynamics [15].

In superseding photons with magnons, a number of benefits may be noted. Firstly, magnons are able to couple to a wide variety of degrees of freedom through a number of interactions as shown in Fig. 1.1, taken from Saitoh, Kikkawa and Hioki's contribution to the *Roadmap on Spin-Wave Computing* [1]. As examples, magnons may be coupled to microwave photons via the Zeeman interaction [16], or coupled to optical photons via the Faraday effect [17, 18]. Experimental works have shown the strong coupling of magnons and cavity microwave photons [19, 20], leading to significant progress in quantum information [21, 22, 23], as well as strongly coupling magnons to optical photons [17]. Additionally, magnons are able to support a rich frequency landscape and a high degree of tunability, with frequencies being dictated simply by the strength, and direction with respect to the magnetisation, of the biasing magnetic field [24]. Often, this is a parameter that is trivial to control in experiments. In principle, these considerations alleviate the restrictions put forth by photons while still retaining comparable coupling schemes, and offer a new regime of hybrid systems to consider and explore.

Magnons may also be coupled to mechanics through the magnetoelastic interaction [25, 26]. In this, the strain of the lattice couples to magnetic moment sites through their displacement as the material undergoes deformation. Most of the work involving this interaction has been done in the resonant scheme, in which magnons and phonons are of the same frequency. The first work to demonstrate coherent magnomechanical coupling in which there were parametric excitations (that is, magnon frequencies on the order of GHz and phonons on the order of MHz) came in 2016 from Zhang *et al.* [27], where coherent coupling was observed in a magnon-photon-phonon system driven by a magnetic cavity. Since then, a number of theoretical proposals relying on this form of interaction and experimental set-up have followed, most notably in quantum information processing [28, 29], entanglement of states [30, 31] and state squeezing [32].

There are, however, still notional improvements to be made with regards to the implementation as proposed by Zhang et. al. Their demonstration of magnomechanical coupling utilised a YIG magnetic sphere of diameter 250 μm, as well as placing the YIG sphere inside an RF cavity of dimensions $4.4 \times 2.1 \times 0.72\,\mathrm{cm}^3$, giving the device a large footprint and preventing implementations for on-chip schemes. Further, the usage of YIG as both the magnetic and elastic medium presents a case for potential improvements given YIG's relatively poor mechanical Q-factor [33] by optomechanical viewpoints [34, 35, 36]. Clearly, this leads to a need to explore alternative schemes in which a magnomechanically coupled device can be both made smaller and in such a way that the elastic dynamics may be improved, or at the very least incorporate the scope for this. To this end, this thesis is focused on the implementation of a physically cavity-free nano-scale magnomechanical device, in which a YIG thin film grown on a gadolinium-gallium-garnet substrate is coupled to a superconducting wave-guide.

Chapter 2 of this thesis introduces the theory of magnetism and of spin-wave excitations as viewed from the Landau-Lifshitz-Gilbert equation. Chapter 3 then introduces the important aspects of elasticity, stress, and strain, beginning with general equations and then applying them to the geometry of cantilevers and bridges. Chapter 4 introduces the mathematics of optomechanics pertinent to deriving a new theory of magnomechancis, including the theory of cavities and the quantum equations of motion. Chapter 5 then introduces this theory of thin-film magnomechanics, deriving the single and multimagnon-phonon coupling strength, g_0 and g respectively, under the assumption of a flat magnetisation mode profile. It then moves to include higher order corrections to the theory as a result of a physically accurate

mode profile. Chapter 6 reviews some potential applications for this new theory and feasible attainment of ground-state cooling. Chapter 7 introduces the replacement of the GGG substrate with a high-Q silicon nitride film to explore potential improvements to the magnomechanical parameters. In Appendix A, the modes of a transmission line are quantised from the Lagrangian of the system, and the creation and annihilation operators for the voltage modes are derived. Appendix B presents a brief review of the magnetic susceptibility tensor of ferromagnetics for the specific case of an infinite thin film with anisotropy and magnetisation parallel to the surface of the film. Appendix C presents a review of the magnetostatic modes of a thin film using the susceptibility prior derived and obtains an expression for the characteristic equation of the wave-vectors of the modes, and lastly Appendix D presents the proof of the orthogonality of the Euler-Bernoulli eigenmodes required to ignore normalisation constants in the quantum theory.

Chapter 2

Magnetism

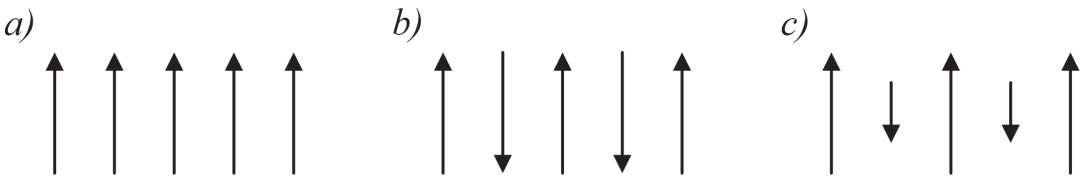

FIGURE 2.1: Pictorial representations of the magnetic moments in (a) ferromagnetism, (b) antiferromagnetism, and (c) ferrimagnetism.

Many crystals have an ordered magnetic structure, arising from its electron configuration. In such crystals and in the absence of an external magnetic field, the average magnetic moment of (at least) an atom in each unit cell is non-zero. These magnetic moments originate from the unpaired electron's orbital and spin angular momenta.

For some materials, in the absence of an external field the resultant magnetic moments are orientated randomly due to thermal fluctuations and the material has a net zero total magnetic moment. In being subjected to an external magnetic field, the moments can be made to align with the direction of the field, but fundamentally the material does not possess a net magnetic moment without this persuasion. Materials whose unpaired electrons behave as such are said to be paramagnetic.

In some materials, there is correlation between the directions of the electron's spins of each atom, which is due to the principle of indistinguishability of identical particles. From this comes the Pauli Exclusion Principle, which is stated as the wavefunction of a fermion system must be antisymmetric with respect to the interchange of the coordinate and spin variables. This gives rise to a preferential alignment of spins, and the dependence of the energy of a system on the magnitude of the resultant spins is known as the exchange interaction. Ultimately, this is then what results in the phenomena known as ferromagnetism.

The simplest form of magnetically ordered crystals are ferromagnets, such as Fe, Ni, and Co [37, 38, 39, 40]. In these, the average magnetic moments are aligned through the exchange interaction provided that temperatures of the system remain below the Curie temperature, above which thermal disorder dominates and causes ferromagnetic ordering to be lost. This gives rise to a spontaneous magnetisation, even in the absence of external magnetic fields.

Conceptually the 'opposite' of the ferromagnet are the antiferromagnets (which includes carbonates, anhydrous sulphates, oxides, and flourides of Mn, Ni, Co, and Fe [41, 42, 43]). In these, the magnetic moments compensate each other within the unit cell in the absence of a magnetic field. They are described using sub-lattices, each having a non-zero magnetic moment. In analogy to the Curie temperature of

ferromagnets, antiferromagnetic ordering only occurs if the temperature remains below the Néel temperature.

There are magnetically ordered crystals which consist of a number of sublattices in which the magnetic moments are not compensated, known as ferrimagnets [44] (named as such after ferrites [45, 46], in which ferrimagnetism is often displayed). Ferrimagnets are like antiferromagnets in that there are sub-lattices of opposing magnetic moments but these are not equal, and so ferrimagnets show a spontaneous magnetisation. With regards to temperatures, ferrimagnets are only ferrimagnetic below the Curie temperature, the same as ferromagnets.

This list is not exhaustive, rather it forms a simplistic overview of magnetism, and Fig. 2.1 shows these forms of magnetism pictorially. More exotic forms of magnetism can exist which are technologically relevant, including quantum spin liquids [47], metamagnetism [48], superparamagnetism [49], and helimagnetism [50]. This thesis restricts itself to the consideration of ferro- and ferrimagnetism.

2.1 Coulomb exchange

To illustrate the exchange interaction, consider here a simple system of a hydrogen molecule. The hydrogen molecule consists of two electrons interacting electrostatically both with each other, as well as with the two protons. When two nuclei are at fixed differences away from each other, the Hamiltonian for the system of electrons must be

$$\mathcal{H} = \frac{\mathbf{p}_1^2 + \mathbf{p}_2^2}{2m_\mathrm{e}} + e^2\left(\frac{1}{r_{\alpha\beta}} + \frac{1}{r_{12}} - \frac{1}{r_{\alpha 1}} - \frac{1}{r_{\alpha 2}} - \frac{1}{r_{\beta 1}} - \frac{1}{r_{\beta 2}}\right) \tag{2.1}$$

where $\mathbf{p}_1$ and $\mathbf{p}_2$ are the electron momentum operators, m_e and e are the electron mass and charge respectively, and $r = r_{\alpha\beta}$ is the distance between the particles α and β where 1 and 2 refer to the electrons and α and β are used to denote the different nuclei. In this Hamiltonian, terms involving the momentum operators represent the kinetic energy of the electrons, $r_{\alpha 1}$ and $r_{\beta 2}$ the potential energy of attraction between electrons and their associated protons, r_{12} the potential energy of proton-proton repulsion, $r_{\alpha\beta}$ the potential energy of electron-electron repulsion, and $r_{\alpha 2}$ and $r_{\beta 1}$ the potential energy electron-proton attraction between the counter-host proton.

The wave-function ψ describing the system may be written as a product of spatial and spin wave-functions

$$\psi(\mathbf{r}_1\sigma_1, \mathbf{r}_2\sigma_2) = \phi(\mathbf{r}_1, \mathbf{r}_2)\chi(\sigma_1, \sigma_2) \tag{2.2}$$

where σ_1 and σ_2 are projections of the electron spins on a given axis (typically considered as the z-axis of the system), and ϕ and χ are the spatial and spin parts of the wave-function, respectively.

To satisfy the exclusion principle, ψ must be antisymmetric with respect to the simultaneous interchange of the coordinates and of the spin variables of the electrons. In practice, this means that an antisymmetric spatial function is associated with a symmetric spin function, and vice versa. The function χ will be symmetric if the resultant spin S of the two electrons is equal to 1, and antisymmetric is the resultant spin is equal to 0. The spatial function will be antisymmetric for $S = 1$ and symmetric for $S = 0$, which are denoted ϕ_a and ϕ_s.

Assuming that the interaction is weak such that the system is in its ground state, a wave-function compatible with the fermionic nature of electrons can be found from

perturbation theory and approximated by

$$\begin{aligned}\phi_{\mathrm{s}}(\mathbf{r}_1,\mathbf{r}_2) &= \frac{1}{\sqrt{2(1+\gamma^2)}}\left(\phi(\mathbf{r}_{\alpha 1})\phi(\mathbf{r}_{\beta 2})+\phi(\mathbf{r}_{\alpha 2})\phi(\mathbf{r}_{\beta 1})\right), \quad S=0\\ \phi_{\mathrm{a}}(\mathbf{r}_1,\mathbf{r}_2) &= \frac{1}{\sqrt{2(1-\gamma^2)}}\left(\phi(\mathbf{r}_{\alpha 1})\phi(\mathbf{r}_{\beta 2})-\phi(\mathbf{r}_{\alpha 2})\phi(\mathbf{r}_{\beta 1})\right), \quad S=1\end{aligned} \tag{2.3}$$

In this, it is defined $\phi(\mathbf{r}_{\alpha \mathrm{i}})$ is the normalised wave function of the hydrogen atom consisting of the i-th electron and the α-th nucleus, and

$$\gamma = \int \phi(\mathbf{r}_{\alpha 1})\phi(\mathbf{r}_{\beta 1})\,\mathrm{d}\mathbf{r}_1. \tag{2.4}$$

The energies of the molecules in states corresponding to $S=1$ and $S=0$ are then found as

$$\begin{aligned}E_{\uparrow\uparrow}(r) &= \int \phi_{\mathrm{a}}(\mathbf{r}_1,\mathbf{r}_2)\mathcal{H}\phi_{\mathrm{a}}(\mathbf{r}_1,\mathbf{r}_2)\,\mathrm{d}\mathbf{r}_1\mathrm{d}\mathbf{r}_2,\\ E_{\uparrow\downarrow}(r) &= \int \phi_{\mathrm{s}}(\mathbf{r}_1,\mathbf{r}_2)\mathcal{H}\phi_{\mathrm{s}}(\mathbf{r}_1,\mathbf{r}_2)\,\mathrm{d}\mathbf{r}_1\mathrm{d}\mathbf{r}_2,\end{aligned} \tag{2.5}$$

where $\uparrow\uparrow$ and $\uparrow\downarrow$ correspond to $S=1$ and $S=0$, respectively. Substituting for ϕ_{a} and ϕ_{s}, the energies of each of these states then can be expressed as

$$E_{\uparrow\uparrow}(r) = \frac{A(r)-B(r)}{\sqrt{1-\gamma^2}}, \qquad E_{\uparrow\downarrow}(r) = \frac{A(r)+B(r)}{\sqrt{1+\gamma^2}}. \tag{2.6}$$

where it is defined

$$A(r) = \int U^* \phi^2(\mathbf{r}_{\alpha 1})\phi^2(\mathbf{r}_{\beta 2})\,\mathrm{d}\mathbf{r}_1\mathrm{d}\mathbf{r}_2, \tag{2.7}$$

$$B(r) = \int U^* \phi(\mathbf{r}_{\alpha 1})\phi(\mathbf{r}_{\beta 1})\phi(\mathbf{r}_{\alpha 2})\phi(\mathbf{r}_{\beta 2})\,\mathrm{d}\mathbf{r}_1\mathrm{d}\mathbf{r}_2, \tag{2.8}$$

$$U = e^2\left(\frac{1}{r}+\frac{1}{r_{12}}+\frac{1}{r_{\alpha 2}}+\frac{1}{r_{\beta 1}}\right). \tag{2.9}$$

In the expressions for E the terms independent of r have been omitted as representing the energy of two atoms of hydrogen at an infinite distance from each other.

The term $A(r)$ represents the electrostatic interaction energy of the two atoms on the assumption that each electron is rigidly fixed to one of the other nuclei. The term $B(r)$ represents the exchange energy, in which the consideration is that in one state electron 1 'belongs' to nuclei α and electron 2 'belongs' to nuclei β, and in the other state it is vice versa.

An important aspect of the exchange energy is that is falls of dramatically (in fact, exponentially) with increasing distance between nuclei due to containing an overlap of $\phi(\mathbf{r}_{\alpha i})$ and $\phi(\mathbf{r}_{\beta i})$, and this overlap falls off rapidly with increasing r. This consideration shows clearly that there is a purely quantum-mechanical interaction of electron exchange which leads to an effective interaction between atoms that is highly sensitive to the spins when only the Coulomb interaction and particle indistinguishability are considered

For a negative exchange energy (i.e. $B(r) < 0$), then the state with $S=0$ has a lower energy than that of the $S=1$ state and is established as a preferable state. In ferromagnets, however, the exchange energy is positive ($B(r) > 0$) and the state with $S=1$ has lower energy than that of the $S=0$ state such that the spins of all atoms of a ferromagnet in the ground state are preferentially parallel.

It is often convenient to introduce the operator relating the electron spin operators $\mathbf{s}_1$ and $\mathbf{s}_2$ via the Hamiltonian

$$\mathcal{H} = -\mathcal{J}\mathbf{s}_1 \cdot \mathbf{s}_2 + E(r) \tag{2.10}$$

where $\mathcal{J}$ and E are both functions of r and are chosen such that the eigenvalues of the operator $\mathcal{H}$ are equal to $E_{\uparrow\uparrow}(r)$ and $E_{\uparrow\downarrow}(r)$. Noting that $\mathbf{s}_1 \cdot \mathbf{s}_2 = \frac{1}{2}(\mathbf{s}_1 + \mathbf{s}_2)^2 - \frac{1}{2}(\mathbf{s}_1^2 + \mathbf{s}_2^2)$ which may then be further expressed as $\frac{1}{2}S(S+1) - \frac{3}{4}$ has eigenvalues of $-\frac{3}{4}$ for $S = 0$ and $\frac{1}{4}$ for $S = 1$, these functions are set to

$$\mathcal{J} = E_{\uparrow\downarrow}(r) - E_{\uparrow\uparrow}(r), \tag{2.11}$$

$$E(r) = \tfrac{3}{4}E_{\uparrow\uparrow}(r) + \tfrac{1}{4}E_{\uparrow\downarrow}(r), \tag{2.12}$$

correspond to the exchange energy and the mean energy. This Hamiltonian is the exchange Hamiltonian for electrons and is denoted

$$\mathcal{H}_\mathrm{e} = -\mathcal{J}\mathbf{s}_1 \cdot \mathbf{s}_2. \tag{2.13}$$

There is a maximum temperature in ferromagnets known as the Curie temperature, often denoted T_C, above which ferromagnets will no longer exhibit ferromagnetic behaviour and transition to paramagnetic behaviour. There are a number of factors which contribute to the Curie temperature, but the most fundamental of them is that the thermal energy cannot exceed the exchange energy, else the parallel alignment of spins becomes no longer preferential. The problem was first considered by Weiss [51], in which he introduced a constant (known as the Weiss constant, n_W), which described the constant of proportionality between the internal 'molecular field', and the magnetisation of the ferromagnet. The Curie temperature is then expressed as [52]

$$T_\mathrm{C} = n_\mathrm{W}C = n_\mathrm{W}\frac{\mu_0 n g_\mathrm{e}^2 \mu_\mathrm{B}^2 J(J+1)}{3k_\mathrm{B}} \tag{2.14}$$

where n is the number of magnetic atoms per unit volume, J is the total angular momentum, g_J is the Landé g-factor, μ_B is the Bohr magneton, μ_0 is the permeability of free space, k_B is the Boltzmann constant, and C is known as the Curie constant and is a property of the material.

2.2 Exchange energy of a ferromagnet

In order to find the Hamiltonian for a ferromagnet, there are a number of assumptions made to simplify the mathematical form. First, any relativistic interactions are neglected, and the initial Hamiltonian is assumed to contain only the Coulomb interaction energy between electrons and between electrons and nuclei, and the kinetic energy of any particles. It is then assumed that the crystal is formed similar to the hydrogen molecule, in that it consists of individual atoms, each of which contains a single electron in it's ground state, and that all atoms in the ferromagnet have spins $s = 1/2$. With these considerations, the prior Hamiltonian in Eq. 2.13 may be used to find an approximate energy of the ferromagnetic crystal. It is also assumed that the correct representation of a ferromagnet near it's ground state is obtained as a sum of the exchange Hamiltonian for all pairs of atoms, expressed as

$$\mathcal{H}_\mathrm{e} = -\frac{1}{2}\sum_{l \neq m} \mathcal{J}(\mathbf{R}_{lm})\mathbf{s}_l \cdot \mathbf{s}_\mathrm{m} \tag{2.15}$$

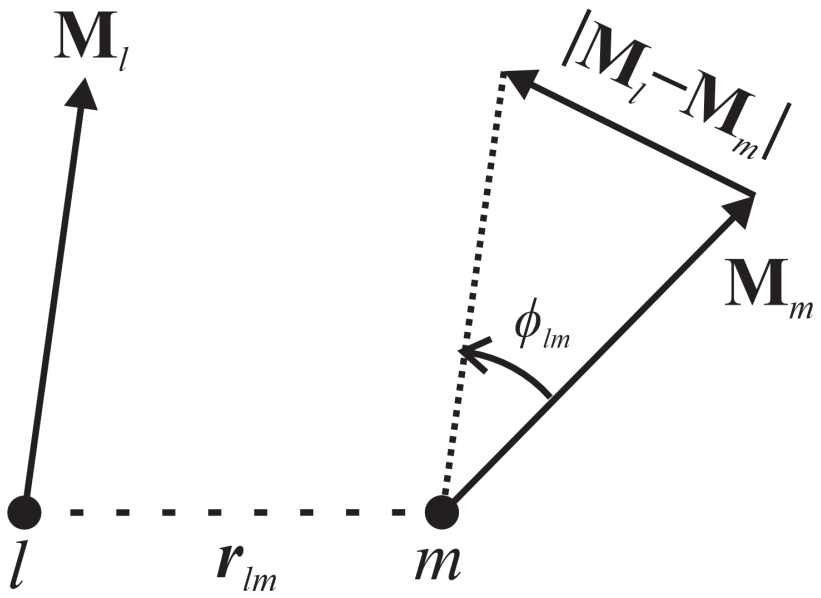

FIGURE 2.2: Two magnetic moments in consideration in the ferromagnetic lattice.

where l and m denote the l-th and m-th lattice sites, and $\mathcal{J}(\mathbf{R}_{lm})$ is a function of the radius vector $\mathbf{R}_{lm}$ between the two sites, only of appreciable size for adjacent lattice sites. For a ferromagnet, this function is taken to be positive (i.e $\mathcal{J}(\mathbf{R}_{lm}) > 0$). Finally, it is then extrapolated that this Hamiltonian is not only valid for $s = 1/2$, but for arbitrary atomic spins.

As the exchange integral falls off rapidly with atom separation, the sum across all pairs can be reduced to that of nearest neighbours only. Each lattice site is assumed to be a centre of symmetry, such that the exchange integral between pairs of nearest neighbours is symmetric, and hence is reduced to a constant $\mathcal{J}(\mathbf{R}_{lm}) \equiv \mathcal{J}$. Taking a semiclassical consideration of the Hamiltonian, as the structure is considered near it's ground-state, the angle of alignment between nearest neighbour spins must be small ($\phi_{lm} << 1$ for all l and m). With these in mind, a simple swap of the dot product in the Hamiltonian to the form in which the angle of alignment is considered can be employed;

$$\mathcal{H}_{\mathrm{e}} = -\frac{1}{2}\mathcal{J}s^2 \sum_{l \neq m} \cos(\phi_{lm}). \tag{2.16}$$

Then, with the small angle expansion for $\cos(\phi)$ the Hamiltonian can be written as

$$\mathcal{H}_{\mathrm{e}} \approx \mathcal{H}_0 - \frac{1}{2}\frac{\mathcal{J}s^2}{2} \sum_{l \neq m} \phi_{lm}^2. \tag{2.17}$$

Here, the term $\mathcal{H}_0$ refers to the energy of the fully aligned state and can be neglected as an arbitrary constant. For small deflections in the angle of alignment between moments (the reader is referred to Fig. 2.2), one can apply the small angle approximation for the arc of a circle. Considering now the spins as magnetic moments (and in ignoring relativistic effects the interchange of the two presents no issues), it is found

$$\phi_{lm} \approx \frac{\mathbf{M}_l - \mathbf{M}_m}{\mathbf{M}_l} = |\mathbf{M}_l - \mathbf{M}_m|\,. \tag{2.18}$$

As the exchange integral has been assumed to fall off rapidly with distance between

sites, an expansion of a vector in powers of $x_i - x_i'$, where summation is implied over the coordinates $i = x, y, z$. To first order in the term $|\mathbf{M}_l - \mathbf{M}_m|$ [53], one finds

$$|\mathbf{M}_l - \mathbf{M}_m| \approx |(\mathbf{R}_{lm}.\nabla)\mathbf{M}|\,. \tag{2.19}$$

The Hamiltonian found in Eq. 2.15 may then be expressed as

$$\mathcal{H}_\mathrm{e} = \frac{1}{2}\frac{\mathcal{J}s^2}{2}\sum_{l\neq m}\left[(\mathbf{R}_{lm}.\nabla)\mathbf{M}\right]^2, \tag{2.20}$$

where the static energy term associated with the fully aligned state $\mathcal{H}_0$ has now been neglected. Finally, replacing summation with integration over the ferromagnetic body and assuming cubic symmetry, one finds for the exchange energy

$$E_\mathrm{e} = \int_V w_\mathrm{e}\,\mathrm{d}V \tag{2.21}$$

where the energy density is

$$w_\mathrm{e} = \frac{1}{2}\alpha_\mathrm{ex}\left(\frac{\partial\mathbf{M}}{\partial x_l}\right)^2 \tag{2.22}$$

with α_ex defined as $\alpha_\mathrm{ex} = \frac{\mathcal{J}s^2 z}{2a}$ for z nearest neighbours in a unit cell of side length a.

An alternative but equivalent treatment follows from the consideration of the magnetic moment density operator [54]. In this procedure, for a generic structure in which each lattice site is a centre of symmetry the energy density, the energy is expressed as

$$w_\mathrm{e} = \frac{1}{2}\alpha_{lm}\frac{\partial\mathbf{M}}{\partial x_l}\frac{\partial\mathbf{M}}{\partial x_m}, \tag{2.23}$$

where summation notation is implied over repeat indices. Under cubic symmetry, there exists the reduction $\alpha_{lm} = \alpha_\mathrm{ex}\delta_{lm}$ and the expression derived in Eq. 2.22 above is recovered.

In general, contributions to the effective field which acts upon the magnetisation can be found as the function derivative of the associated energy density with respect to the magnetisation [54]. The exchange energy density then yields the exchange field as

$$\mathbf{H}_\mathrm{ex} = \alpha_\mathrm{ex}\nabla^2\mathbf{M}. \tag{2.24}$$

2.3 Demagnetisation

When a ferromagnetic body of finite size is magnetised by an external magnetic field, free poles are formed on the ends. These free poles act to produce an associated magnetic field opposing the magnetisation, known as the demagnetising field and often denoted $\mathbf{H}_\mathrm{d}$. The strength of the demagnetising field is proportional to the free pole density, and in turn the magnetisation.

In considering a uniformly magnetised ferromagnet [54, 55], the demagnetising field inside the ferromagnet may be expressed as

$$\mathbf{H}_\mathrm{d} = -4\pi\hat{N}(\mathbf{r})\cdot\mathbf{M} \tag{2.25}$$

where $\hat{N}(\mathbf{r})$, known as the demagnetisation tensor, is given by

$$N_{ik}(\mathbf{r}) = -\frac{1}{4\pi}\frac{\partial^2}{\partial x_i \partial x_k}\int_V \frac{\mathrm{d}\mathbf{r}'}{|\mathbf{r}-\mathbf{r}'|}. \tag{2.26}$$

In general, the demagnetisation field is not uniform. However, for a ferromagnet of the form of an arbitrary ellipsoidal shape and of constant magnetisation, the field inside the ellipsoid will be uniform. Assuming that a coordinate system is aligned with the major axes, denoted a, b, c, of an ellipsoid the demagnetisation tensor is diagonalised and has only diagonal elements.

For a sphere, these semi-axis are equal and the demagnetisation tensor components then take the convenient analytic form

$$N_1 = 1/3, \qquad N_2 = 1/3, \qquad N_3 = 1/3. \tag{2.27}$$

For a prolate ellipsoid of revolution, in which the rationalised coordinates satisfy $(x^2/a^2) + (y^2+z^2)/b^2 = 1$ and $a > b$, then the demagnetisation tensor coefficients take the analytic form

$$N_1 = \frac{1-e^2}{2e^3}\left(\ln\frac{1+e}{1-e} - 2e\right), \quad N_2 = N_3 = \frac{1}{2}(1-N_1), \quad e = \sqrt{1-\frac{b^2}{a^2}}. \tag{2.28}$$

Lastly, for an oblate ellipsoid, in which rationalised coordinates satisfy $(x^2+y^2)/a^2 + z^2/c^2 = 1$ and $a > c$, then the demagnetisation tensor coefficients take the analytic form

$$N_1 = N_2 = \frac{1}{2}(1-N_3), \quad N_3 = \frac{1-e^2}{e^3}\left(e - \arctan e\right), \quad e = \sqrt{\frac{a^2}{c^2} - 1}. \tag{2.29}$$

These geometries form the only exact analytic reductions for the demagnetisation tensor, although some geometries may be approximated as limits of these geometries. The cylinder is well-approximated as a limit of the prolate ellipsoid for which $a >> b$, finding for the demagnetisation tensor coefficients

$$N_1 = 0, \qquad N_2 = 1/2, \qquad N_3 = 1/2, \tag{2.30}$$

within the bulk of the cylinder. Likewise, the thin plate is well-approximated as a limit of the oblate ellipsoid for which $a, b >> c$, finding for the demagnetisation tensor coefficients

$$N_1 = 0, \qquad N_2 = 0, \qquad N_3 = 1, \tag{2.31}$$

well within the bulk of the plate.

When the external field is uniform and the body has the form of an ellipsoid, then the field and the magnetisation inside the body will also be uniform. The relationship between the magnetic field inside the body $\mathbf{H}_\mathrm{i}$ and the magnetisation $\mathbf{M}$ and external field $\mathbf{H}_\mathrm{e}$ is then of form

$$\mathbf{H}_\mathrm{i} = \mathbf{H}_\mathrm{d} + \mathbf{H}_\mathrm{e} = \mathbf{H}_\mathrm{e} - 4\pi\hat{N}\cdot\mathbf{M}. \tag{2.32}$$

One can find the approximate error associated with the assumption of limiting geometry by using an approximation that the demagnetisation tensor scales linearly with distance from the source [56, 57]. For a film magnetised uniformly along the z-axis, N_z is proportional to $1/L_\mathrm{m}$ such that $N_z = N_0/L_\mathrm{m}$ for some proportionality constant N_0. Assuming for the other components also this same relation, the system

of components can be expressed as

$$N_x = \frac{N_0}{t_\mathrm{m}}, \qquad N_y = \frac{N_0}{w_\mathrm{m}}, \qquad N_z = \frac{N_0}{L_\mathrm{m}}. \tag{2.33}$$

With $N_x + N_y + N_z = 1$ and performing the algebra, the proportionality constant is expressed as

$$N_0 = \frac{L_\mathrm{m} w_\mathrm{m} t_\mathrm{m}}{t_\mathrm{m}\left(L_\mathrm{m} + w_\mathrm{m}\right) + L_\mathrm{m} w_\mathrm{m}}. \tag{2.34}$$

The 'approximate' behaviour of the demagnetisation tensor components in their application to a (nearly) valid assumption of a thin plate may be deduced as

$$\begin{aligned} N_x &= \frac{L_\mathrm{m} w_\mathrm{m}}{t_\mathrm{m}\left(L_\mathrm{m} + w_\mathrm{m}\right) + L_\mathrm{m} w_\mathrm{m}}, \\ N_y &= \frac{L_\mathrm{m} t_\mathrm{m}}{t_\mathrm{m}\left(L_\mathrm{m} + w_\mathrm{m}\right) + L_\mathrm{m} w_\mathrm{m}}, \\ N_z &= \frac{w_\mathrm{m} t_\mathrm{m}}{t_\mathrm{m}\left(L_\mathrm{m} + w_\mathrm{m}\right) + L_\mathrm{m} w_\mathrm{m}}. \end{aligned} \tag{2.35}$$

It can readily be shown that in the limit $L_\mathrm{m}, w_\mathrm{m} >> t_\mathrm{m}$ the demagnetisation coefficients in Eq. 2.31 are recovered.

2.4 Anisotropy

Most ferromagnets are characterised by a *magnetocrystalline anisotropy*, where the preferred directions for the magnetisation coincide with the crystallographic axes, and hence the anisotropy energy depends on the angles of the magnetisation with these directions. In addition to this, there is also *magnetoelastic anisotropy*, in which preferred directions are established with regards to the directions of external mechanical stresses. There is also *shape anisotropy*, in which there is a dependence on the orientation of the magnetisation with respect to some ellipsoidal axes due to the demagnetisation tensor, as seen in Sec. 2.3. There are further forms of anisotropy (for example, thermal anisotropy from temperature gradients), but these are of little concern to our purposes and play (very) minor roles in the descriptions to follow.

Magnetocrystalline anisotropy

Magnetocrystalline anisotropy is relativistic in nature, resulting from purely magnetic dipole interactions between the magnetic moments of atoms and the interaction between the magnetic moments and the electric field of the crystal (known as spin-orbit coupling). The symmetry of the anisotropy is dependent on the crystal symmetry. For a cubic crystal, the magnetocrystalline anisotropy energy density can be expressed in terms of the directional cosines $\alpha_1, \alpha_2, \alpha_3$ of the magnetisation vector relative to cube edges. Given the cubic symmetry, the expression must be an even power of each α_i and invariant under changes of α_i among themselves [58]. The lowest order of these requirements is the expression of second degree: $\alpha_1^2 + \alpha_2^2 + \alpha_3^2$, which is trivially 1 by definition. The next form is of fourth degree, having form $\alpha_1^2\alpha_2^2 + \alpha_1^2\alpha_3^2 + \alpha_1^2\alpha_3^2$. The next term is of sixth degree, having form $\alpha_1^2\alpha_2^2\alpha_3^2$, and the pattern follows forward. The magnetocrystalline antistropy energy density, U_K, is

then of the form

$$U_{\mathrm{K}} = K_0 + K_1(\alpha_1^2\alpha_2^2 + \alpha_1^2\alpha_3^2 + \alpha_2^2\alpha_3^2) + K_2\alpha_1^2\alpha_2^2\alpha_3^2 + ... \tag{2.36}$$

Very generally, the fourth degree is as high as required for simplistic considerations. As such, for cubic crystals the anisotropy energy density can be simplified to

$$U_K = K_1(\alpha_1^2\alpha_2^2 + \alpha_1^2\alpha_3^2 + \alpha_2^2\alpha_3^2) \tag{2.37}$$

where the constant term is neglected as an off-set.

In determining the preferential directions, the sign of the prefactor K_1 is the deciding factor. For a value $K_1 > 0$, the easy axes are aligned with the cube edges and the hard axes are along the cube diagonals. For the reverse case of $K_1 < 0$, the easy axes are aligned with the cube diagonals and the hard axes are along the cube edges.

Shape anisotropy

It was seen in Sec. 2.3 that the demagnetisation tensor is a convenient representation of the magnetostatic field under the assumption of ellipsoidal geometry where the internal magnetisation may be regarded as uniform. There is still, however, an anisotropy that is dependent on the geometry of the material and originates from this demagnetisation interaction. The internal fields may be split into two components [59]

$$\begin{aligned} \mathbf{H}_{\mathrm{i}}(\mathbf{r}) &= \mathbf{H}_{\mathrm{e}}(\mathbf{r}) + \mathbf{H}_{\mathrm{d}}(\mathbf{r}) \\ \mathbf{B}_{\mathrm{i}}(\mathbf{r}) &= \mathbf{B}_{\mathrm{e}}(\mathbf{r}) + \mathbf{B}_{\mathrm{d}}(\mathbf{r}) \end{aligned} \tag{2.38}$$

for an applied field $\mathbf{H}_{\mathrm{e}}$ and demagnetisation field $\mathbf{H}_{\mathrm{d}}$. The two demagnetising fields are related by the integral [59]

$$\int_{\text{all space}} \mathbf{B}_{\mathrm{d}} \cdot \mathbf{H}_{\mathrm{d}} \, \mathrm{d}\tau = 0 \tag{2.39}$$

where $\mathrm{d}\tau$ is used to signify the integration is taken over all space. If an applied field is not present, the energy of the demagnetisation field is the integral over all space of the energy density $\mathbf{H}_{\mathrm{d}}/8\pi$, finding

$$\begin{aligned} E_{\mathrm{d}} = \frac{1}{8\pi}\int_{\text{all space}} \mathbf{H}_{\mathrm{d}}^2 \, \mathrm{d}\tau &= \frac{1}{8\pi}\int_{\text{all space}} (\mathbf{B}_{\mathrm{d}} - 4\pi\mathbf{M}) \cdot \mathbf{H}_{\mathrm{d}} \, \mathrm{d}\tau \\ &= -\frac{1}{2}\int_{\text{all space}} \mathbf{M} \cdot \mathbf{H}_{\mathrm{d}} \, \mathrm{d}\tau \\ &= -\frac{1}{2}\int_{V} \mathbf{M} \cdot \mathbf{H}_{\mathrm{d}} \, \mathrm{d}V \end{aligned} \tag{2.40}$$

where one uses the result $\int_{\text{all space}} \mathbf{B}_{\mathrm{d}} \cdot \mathbf{H}_{\mathrm{d}} \, \mathrm{d}\tau = 0$, and to restrict the last line to the volume of the ferromagnetic body it is noted that there is no magnetisation outside of the ferromagnetic body.

Magnetoelastic anisotropy

Coupling between magnetic and elastic systems exists as the intermolecular interactions depend on the distances between atoms (or ions). As such, when a system

undergoes deformation these distances marginally change and these forces are compensated accordingly. With this in mind, one can write a phenomenological expression from the considerations of symmetry, in particular limited to the case where the crystal is cubic.

To then find the dependence of the magnetocrystalline anisotropy energy on mechanical strains, an expansion of Eq. 2.36 may be performed under the assumption that the strains are small finding

$$U \approx (U_{\mathrm{K}})_0 + \sum_{i,j} \left(\frac{\partial U_{\mathrm{K}}}{\partial u_{ij}} \right)_0 u_{ij} + ..., \tag{2.41}$$

which implicitly assumes that the directional cosines and the crystal lattice share the same basis and the notation $(...)_0$ denotes evaluation at the point in which there is no strain. The partial differentials are then found as

$$\begin{aligned} \partial U_{\mathrm{K}}/\partial u_{xx} &= B_1 \alpha_1^2, & \partial U_{\mathrm{K}}/\partial u_{xy} &= B_2 \alpha_1 \alpha_2, \\ \partial U_{\mathrm{K}}/\partial u_{yy} &= B_1 \alpha_2^2, & \partial U_{\mathrm{K}}/\partial u_{yz} &= B_2 \alpha_2 \alpha_3, \\ \partial U_{\mathrm{K}}/\partial u_{zz} &= B_1 \alpha_3^2, & \partial U_{\mathrm{K}}/\partial u_{xz} &= B_2 \alpha_1 \alpha_3. \end{aligned} \tag{2.42}$$

where B_1 and B_2 are constants known as the magnetoelastic coupling constants. One then finds

$$\begin{aligned} U = K_1(\alpha_1^2\alpha_2^2 + \alpha_2^2\alpha_3^2 + \alpha_1^2\alpha_3^2) \\ + B_1(\alpha_1^2 u_{xx} + \alpha_2^2 u_{yy} + \alpha_3^2 u_{zz}) + 2B_2(\alpha_1\alpha_2 u_{xy} + \alpha_1\alpha_3 u_{xz} + \alpha_2\alpha_3 u_{yz}) \end{aligned} \tag{2.43}$$

where the factor of two arises from symmetry. The magnetoelastic energy density is identified as

$$\begin{aligned} U_{\mathrm{me}} = B_1(m_x^2 u_{xx} + m_y^2 u_{yy} + m_z^2 u_{zz}) \\ + 2B_2(m_x m_y u_{xy} + m_x m_z u_{xz} + m_y m_z u_{yz}). \end{aligned} \tag{2.44}$$

where one makes use of the definition of the direction cosines and the expression is given in terms of the normalised magnetisation $m_i = M_i/M$s

2.5 Magnetisation dynamics

The classical dynamics of magnetisation are governed by the precession of magnetic moments. Magnetic moments preferentially want to align with an effective field, $\mathbf{H}_{\mathrm{eff}}$, determined by the contributions to the magnetic free energy as

$$\mathbf{H}_{\mathrm{eff}} = \mathbf{H}_{\mathrm{a}} + \mathbf{H}_{\mathrm{d}} + \mathbf{H}_{\mathrm{ext}} + \mathbf{H}_{\mathrm{exc}} \tag{2.45}$$

where $\mathbf{H}_{\mathrm{a}}$ is the total anisotropy field contribution, $\mathbf{H}_{\mathrm{d}}$ is the demagnetisation field contribution, $\mathbf{H}_{\mathrm{ext}}$ is the external applied field contribution (often called the Zeeman field or the bias field), and $\mathbf{H}_{\mathrm{exc}}$ is the exchange field contribution. Other contributions to the effective field exist, but the contributions above are the dominant ones.

Landau and Lifshitz proposed an equation for describing these dynamics [60], referred to as the LL equation, or the LLG equation when the influence of damping is included [61]. In essence, this equation represents a torque exerted on the magnetic moments by a field $\mathbf{H}_{\mathrm{eff}}$, which in turn induces precessional motion about the effective field. Gilbert added a damping term to this, which acts to provide a

life-time of the oscillations. In full, the equation reads as

$$\frac{\partial \mathbf{M}}{\partial t} = -\gamma_g \mathbf{M} \times \mathbf{H}_{\text{eff}} + \frac{\alpha}{M_s}\left(\mathbf{M} \times \frac{\partial \mathbf{M}}{\partial t}\right) \tag{2.46}$$

where γ_g is the electron gyromagnetic ratio and α is a dimensionless factor known as the Gilbert damping parameter. For materials in which $\alpha = 0$, then precessional motion is maintained indefinitely.

Solutions to the LLG offer resonant precessional modes for of the magnetisation of a material at frequencies $\omega_m(\mathbf{k})$, where $\mathbf{k}$ is the wave-vector of the mode; this phenomena is known as ferromagnetic resonance (FMR). The classical description of this resonance was put forth by Kittel [62, 63], stemming from observations of Griffiths [64] in which resonance of values higher than the Larmor frequency was observed. Kittel solved the LL equation for analytic geometries under the assumption of an applied radio-frequency field for the lowest order wave-vector (a stationary mode) and in which there was no damping. In this, the macrospin approach was adopted, $\sum_i \mathbf{m}_i = \mathbf{M}$, for which all magnetic moments are assumed to precess in phase. Precessional motion frequencies were then identified by $\omega_m = \gamma_g \mathbf{H}_{\text{eff}}$, where $\mathbf{H}_{\text{eff}}$ is $(\mathbf{H}\left[\mathbf{H} + 4\pi\mathbf{M}\right])^{1/2}$ for a film geometry, $\mathbf{H} + 2\pi\mathbf{M}$ for a long cylinder of circular cross-section, and $\mathbf{H}$ for a sphere.

An alternative treatment of FMR involves a quantum description, in which there is a separation of the electron energies due to the Zeeman interaction. If the RF photons have an energy that matches the splitting within the broadening of the mode frequency, then there is excitation from the low energy state to the high energy state and resonance occurs. This resonance occurs for a time proportional to the Gilbert damping, and after this time the RF photon is remitted, allowing the spins to relax back into their ground state [65].

The Kittel mode of a thin film

The geometry of interest for the magnetic structure considered within this thesis is proposed here, consisting of an infinite thin film of which the lowest-order ferromagnetic resonant frequency (the Kittel mode) is of interest. A magnetic structure of dimensions $L_m, w_m >> t_m$ as the length, width and thickness, is assumed, and the surface and thickness of the structure is taken to be parallel to the $y-z$ plane and x axis, respectively. The structure is subjected to a bias field $\mathbf{H}_e = H_e\hat{z}$ along it's length, sufficiently large to saturate the magnet fully along the z-axis. Associated with this magnetisation is a demagnetisation field $\mathbf{H}_m$ and an exchange field H_{exc} as derived in Eq. 2.24. This coordinate system, structure, and it's magnetisation scheme is depicted in Fig 2.3. Contributions to the magnetocrystalline anistropy are known to be weak in YIG and is neglected from the Kittel mode description - should this be required, then assuming an easy axis alignment coinciding with the applied field and an appropriate redefinition of the Zeeman field can be used to recover the correct expression. The influence of damping is also not considered, although this does not present a modification to the resonant frequency, only it's line-width. With these fields, the effective field may be expressed as

$$\mathbf{H}_{\text{eff}} = \mathbf{H}_e + \alpha_{ex}\nabla^2\mathbf{M} - 4\pi\hat{N}\cdot\mathbf{M}. \tag{2.47}$$

When the ferromagnetic body is at saturation, the magnetisation of the precessional mode may be thought of as a static saturation component augmented with

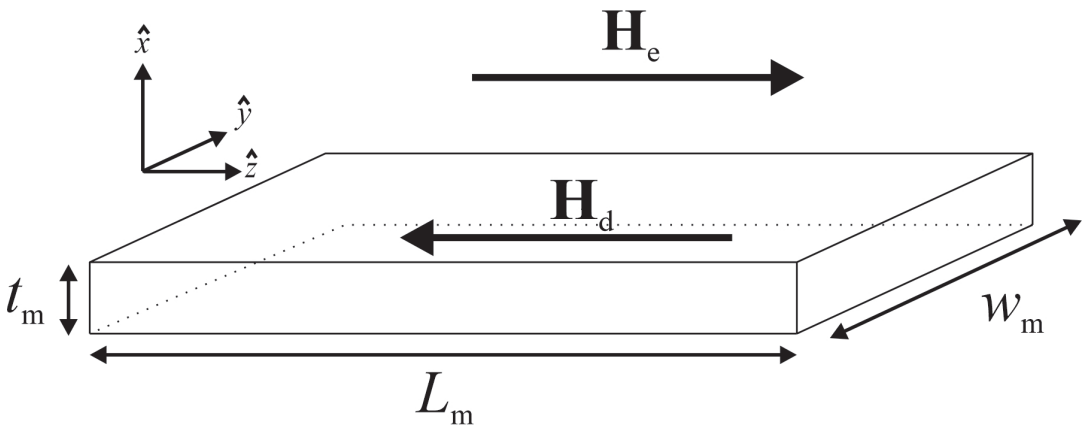

FIGURE 2.3: Orientation of the magnetic thin film. Here, $\mathbf{H}_e$ and $\mathbf{H}_m$ are the applied bias field and the associated demagnetisation field, respectively.

some small fluctuations about it. As the magnitude of the magnetisation vector is preserved (ie. $|\mathbf{m}| = 1$), then for a structure saturated along it's length in the $\hat{z}$ direction, one can adopt this description to find

$$|\mathbf{m}|^2 \approx (\hat{z} + \delta\mathbf{m}) \cdot (\hat{z} + \delta\mathbf{m}) = 1. \tag{2.48}$$

Note that such a description implicitly assumes $|\delta\mathbf{M}| << M_s$ to consider a static saturation magnetisation which is true for small driving magnetic fields. This can further be approximated for small fluctuations as

$$\delta m_z = \sqrt{1 - (\delta m_x^2 + \delta m_y^2)} - 1. \tag{2.49}$$

Expanded to first order in the small fluctuations then finds, an expression can be deduced for the z-component of the fluctuations

$$\delta m_z \approx -\frac{1}{2}\left(\delta m_x^2 + \delta m_y^2\right). \tag{2.50}$$

Contributions to the fluctuations of the magnetisation from δm_z are then second order, and it can be assumed that oscillations of the magnetisation for the lowest order mode occur in the plane perpendicular to the applied field. The magnetisation of the mode, dependent on position $\mathbf{r}$ and time t, may be written

$$\mathbf{m}(\mathbf{r}, t) = \hat{z} + \delta\mathbf{m}(\mathbf{r}, t). \tag{2.51}$$

The linearised LL equation (which is to say that terms only first order in time are retained) can then be expressed in this reduced magnetisation as

$$\frac{\partial\delta\mathbf{m}}{\partial t} = -\gamma_g\left(\hat{z} \times \left(\alpha_{ex} M_s \nabla^2 \delta\mathbf{m} - 4\pi M_s \hat{N} \cdot \delta\mathbf{m}\right) + \delta\mathbf{m} \times \left(\mathbf{H}_e - 4\pi\hat{N} \cdot \hat{z}\right)\right). \tag{2.52}$$

So far, the above expression is completely general for any geometry where magnetocrystalline anisotropy may be neglected with a saturating field along the length of a magnetised structure. The assumption made for the Kittel mode is that oscillations of the magnetisation are homogeneous, such that the magnitude of fluctuations are not dependent on position within the film. This reduces $\delta\mathbf{m}(\mathbf{r}, t) = \delta\mathbf{m}(t)$. To lowest

order in the small fluctuations, this spatially homogeneous Kittel mode is expressed

$$\mathbf{m}(t) = \hat{z} + \left(\delta m_x(t), \delta m_y(t), 0\right). \tag{2.53}$$

In order to solve the linearised Landau-Lifshitz equation, eigenmode solutions are sought in which time dependence is taken as harmonic $\propto \exp\left(-i\omega_{\mathrm{m}}t\right)$, forming the Kittel mode description as

$$\delta\mathbf{m}(t) = \left(\delta m_x, \delta m_y, 0\right) e^{-i\omega_{\mathrm{m}}t}. \tag{2.54}$$

Upon direct substitution into Eq. 2.52, the equation

$$i\omega_{\mathrm{m}}\delta\mathbf{m} = \gamma_g \left(\hat{z} \times -4\pi M_{\mathrm{s}}\delta m_x\hat{x} + \delta\mathbf{m} \times H_{\mathrm{e}}\hat{z}\right) \tag{2.55}$$

is yielded, where the exchange field does not contribute to the Kittel mode dynamics due to the spatial homogeneity of the mode. This may then be expressed as two equations in the components δm_x and δm_y:

$$\begin{aligned} i\omega_{\mathrm{m}}\delta m_x &= \gamma_{\mathrm{g}} H_{\mathrm{e}}\delta m_y, \\ i\omega_{\mathrm{m}}\delta m_y &= -\gamma_{\mathrm{g}}\left(4\pi\delta m_x + H_{\mathrm{e}}\delta m_x\right). \end{aligned} \tag{2.56}$$

Solving these equations for ω_{m}, one finds the expression for the Kittel mode angular frequency [24]

$$\omega_{\mathrm{m}} = \gamma_{\mathrm{g}}\sqrt{H_{\mathrm{e}}\left(H_{\mathrm{e}} + 4\pi M_{\mathrm{s}}\right)}. \tag{2.57}$$

Equally, the polarisation of the Kittel mode is found by substitution of this frequency into the component expressions, yielding

$$\left(\delta m_x, \delta m_y\right) \propto \left(1, i\sqrt{1 + \frac{4\pi M_{\mathrm{s}}}{H_{\mathrm{e}}}}\right) \tag{2.58}$$

which represents oscillations of δm_x and δm_y $\pi/2$ out of phase with each other, and with δm_y having a larger magnitude. This produces an elliptical polarisation as one would expect for an infinite thin flm; as δm_x increases, there is an associated demagnetisation field that acts to squash this component that δm_y does not experience due to geometry.

Resonance is characterised by a line-width of the mode, often referred to as the decay rate. While oscillations have a preferential resonant frequency to be driven at, energy losses of the mode due to damping lead to a Lorentzian profile for which line-widths are larger when energy losses are larger. In the analogy of an oscillating mass on a spring, the line-width is determined by a viscous damping factor related to the density of the medium through which these oscillations occur. The larger this damping factor, the wider the line-width and energy losses in undergoing oscillations leading to short lifetimes of modes [66]. Mathematically, one expresses this as

$$Q = \frac{\omega}{\Delta\omega} \tag{2.59}$$

In the case of magnetic media, the line-width of the ferromagnetic resonant mode is related to the Gilbert damping which can be considered as an effective $Q-$factor. As such, the decay rate of the magnon mode may be approximated using

$$\kappa_{\mathrm{m}} \approx \alpha\omega_{\mathrm{m}}. \tag{2.60}$$

For the low damping material YIG and considering typical ferromagnetic resonance frequencies (on the order of a few to tens of GHz), rudimentary estimates suggest decay rates on the order of $10^5 - 10^7$ Hz.

Chapter 3

Elasticity

The study of acoustic waves and vibrations has been of interest for hundreds of years, beginning first with their applications to music. Pythagoras, a notable lyre player, studied the relation between length of strings of a lyre and their pitch under constant tension in the 6th Century BCE. In the late 1500s, Galileo's father, Vincenzo Galilei, described what lute players at the time already knew; that the pitch of a stretched string is not only dependent on it's length, but also on the mass density of the string. Marin Marsenne was then the first to publish this information as a formula in *Harmonie Universelle* [1], but couldn't explain the origin of overtunes as mathematicians at the time lacked the knowledge that a string can support shorter waves than the one that is the full length of the string. Another notable achievement came from Robert Hooke in 1678, when he formulated the proportionality between stress and strain in elastic bodies, a law which is now known as Hooke's law. In 1744 and 1751, Leonard Euler and Daniel Bernoulli, respectively, developed equations for the vibrations of beams, a theory known as Euler-Bernoulli beam theory, and presented a major contribution not only to the theory of elasticity, but also to architecture, and forms the basis of elasticity that is required for this thesis - that is, elasticity applied to a specific geometry of a beam. These equations break down at high frequency, where predicted eigenmodes are seen to be unbounded and deviate from what observed frequencies of beams [67]. Other contributions for beam geometry came in the late 1800s from Rayleigh [68] in investigating the propagation of elastic waves along an elastic surface, whereby he considered the addition of rotary-inertia effects. This theory predicted that the frequency of eigenmodes should be bounded, but still over-predicted the observed frequencies. The last major contribution came in the 1900s from Timoshenko [69, 70], whereby his beam theory included the additional of shear deformations. This theory offers the most accurate frequencies a general mathematical model has obtained to date as compared to the exact solutions [71], and only falls short of applying finite element analysis to the general structure itself [72].

While the Rayleigh theory and Timoshenko theory offer increasingly more accurate results as compared to the Euler-Bernoulli beam theory [73], the Euler-Bernoulli theory is perfectly valid under certain approximations. The dispersion relation for cylindrical bars from general elasticity was given by Bancroft [74], and Hudson [75] carried out the necessary computations to show how the phase velocity of flexural waves depends on the ratio between their wavelength and the radius of the cylinder. For Euler-Bernoulli beam theory, the phase velocity of a circular rod of diameter a may be expressed as

$$\bar{c} = \pi \bar{k} \tag{3.1}$$

[1] Mersenne, Marin (1636) *Harmonie Universelle*

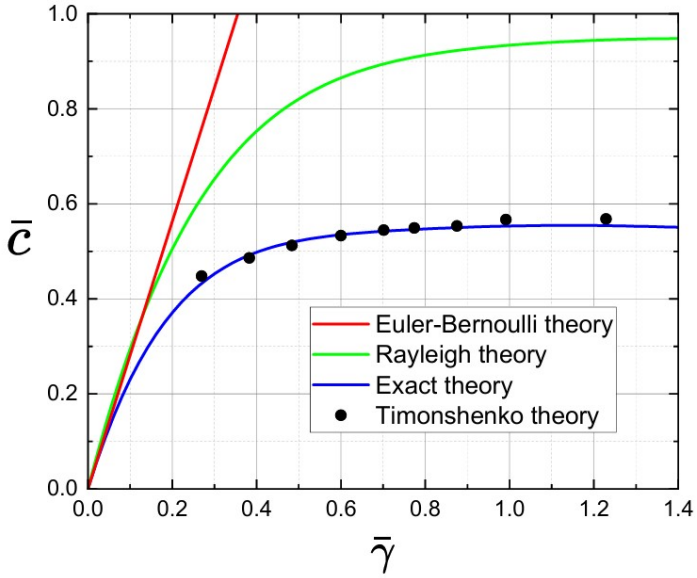

FIGURE 3.1: Dispersion relations from the Euler-Bernoulli, Rayleigh, Timonshenko beam theories alongside the solutions obtained by the theory of linear elasticity [67].

where it is defined $\bar{c} = {}^{c}/_{(E/\rho)^{\frac{1}{2}}}$ and $\bar{k} = {}^{ak}/_{2\pi}$, with E as the Young's modulus and ρ the density. While this gives a dispersion that is unbounded (and hence cannot be physical), it still proves an accurate theory provided that $\bar{k} \leq 0.1$, or equivalently $ka << 1$ for some characteristic length a in the cross-section which will vary depending on the geometry of said cross-section. It is shown in Fig. 3.1 the dispersion relations as compared to the calculations of Bancroft and Hudson pertaining to a circular rod of diameter a which demonstrates the good agreement for small wavevector dimension products.

Considered in this Chapter are the concepts of stress and strain, and their applications to the bending of beams; that is, structures in which the widths and thicknesses of the cross-section are much less than the length of the structure. Elasticity is also framed within the context of crystal structures, for which, like magnetism, variations in elastic parameters exist dependent on the angles made with the crystal structure. Lastly, the Euler-Bernoulli beam equation is derived, and its eigenmodes are solved for specific boundary conditions represented the cases of cantilevers and bridges.

3.1 Strain, stress, and Hooke's law

Materials exist in which, when an applied force acts on the solid body, deformation occurs to some extent. The extent to which deformation occurs depends not only on the elastic character of the body, but also on the magnitude of the force applied. With this deformation comes an associated change in the shape of the body, as well as the volume of it. The position of a point inside the body in a Cartesian coordinate system is described by a radius vector from an origin, consisting of three components

$$\mathbf{r} = (x_1, x_2, x_3). \tag{3.2}$$

When a solid body undergoes a deformation every point, in general, is subsequently displaced by an amount. Considered is a particular point, for which it is denoted the radius vector prior to deformation as $\mathbf{r}$, with the radius vector after deformation denoted as $\mathbf{r}'$ with associated coordinates x_i'. Then, the displacement of this particular point is defined by the vector $\mathbf{r}' - \mathbf{r}$, denoted by $\mathbf{u}$, where

$$u_i = x_i' - x_i. \tag{3.3}$$

The vector $\mathbf{u}$ is called the displacement vector. The coordinates x_i' are a function of the coordinates x_i, and so the vector $\mathbf{u}$ is also a function of the coordinates x_i. If $\mathbf{u}$ is given as a function of x_i then the deformation is entirely determined.

When a solid body undergoes deformation, the distances between points prior to and post deformation evidently change. Considering two points close together such that the total derivative is the best approximation, then the radius vector joining them before deformation is $\mathrm{d}x_i$ and likewise after deformation is $\mathrm{d}x_i' = \mathrm{d}x + \mathrm{d}u_i$. The distance between two points in consideration is then, prior to deformation,

$$\mathrm{d}l = \sqrt{\mathrm{d}x_1^2 + \mathrm{d}x_2^2 + \mathrm{d}x_3^2} \tag{3.4}$$

and, after deformation,

$$\mathrm{d}l' = \sqrt{\mathrm{d}x_1'^2 + \mathrm{d}x_2'^2 + \mathrm{d}x_3'^2}. \tag{3.5}$$

Implying summation over like indices, it is defined $\mathrm{d}l^2 = \mathrm{d}x_i^2$, $\mathrm{d}l'^2 = \mathrm{d}x_i'^2 = (\mathrm{d}x_i + \mathrm{d}u_i)^2$. On substituting for the total derivative $\mathrm{d}u_i = (\partial u_i/\partial x_k)\mathrm{d}x_k$, the displacement after deformation is given by

$$\mathrm{d}l'^2 = (\mathrm{d}x_i + \mathrm{d}u_i)^2 = \mathrm{d}l^2 + 2\frac{\partial u_i}{\partial x_k}\mathrm{d}x_i\mathrm{d}x_k + \frac{\partial u_i}{\partial x_k}\frac{\partial u_i}{\partial x_l}\mathrm{d}x_k\mathrm{d}x_l \tag{3.6}$$

As summation in the second term is over i and k, it can be interchanged $(\partial u_i/\partial u_k)\mathrm{d}x_i\mathrm{d}x_k = (\partial u_k/\partial u_i)\mathrm{d}x_i\mathrm{d}x_k$ without loss of generality. Likewise, in the third term interchange of i and l is performed, such that

$$\mathrm{d}l'^2 = \mathrm{d}l^2 + 2u_{ik}\mathrm{d}x_i\mathrm{d}x_k \tag{3.7}$$

where the tensor u_{ik} is defined as

$$u_{ik} = \frac{1}{2}\left(\frac{\partial u_i}{\partial x_k} + \frac{\partial u_k}{\partial u_i} + \frac{\partial u_l}{\partial x_i}\frac{\partial u_l}{\partial x_k}\right). \tag{3.8}$$

These expressions give the change in length of an element of length when a solid body is deformed.

The tensor u_{ik} is known as the strain tensor, and is symmetrical

$$u_{ik} = u_{ki} \tag{3.9}$$

from its definition by writing

$$2\left(\frac{\partial u_i}{\partial x_k}\right)\mathrm{d}x_i\mathrm{d}x_k = \left(\frac{\partial u_i}{\partial x_k} + \frac{\partial u_k}{\partial x_i}\right)\mathrm{d}x_i\mathrm{d}x_k. \tag{3.10}$$

As with any symmetrical tensor, it can be diagonalised. The resulting axes are then the principle axes of the tensor, often taken to coincide with the principle axes of

geometry (for example, the axes of a cuboid).

For almost all cases, it can be seen that strains are small. Changes in distances within a body are generally always small compared to the distance itself, and relative extensions are small compared to unity. If a body undergoes small deflections, then the components of the strain tensor are small by extension. There are, however, cases that exist in which the displacement vector may be large relative to the distance even for small strains. One such example is that of a thin rod, in which the deflection of the free can be large even though the extension and compression within piece-wise elements of the rod is small. Another example of note where this idea also occurs is in thin plates where the same idea applies. As for the vast majority of cases the displacement vector is small for small deformations, the last term in Eq. 3.8 may be neglected as being second order in the small parameter u_i, giving the expression

$$u_{ik} = \frac{1}{2}\left(\frac{\partial u_i}{\partial x_k} + \frac{\partial u_k}{\partial x_i}\right). \tag{3.11}$$

which is often what is given as the strain tensor rather than it's full expression.

When deformation is absent from a solid body, the arrangement of molecules within the body corresponds to that which is in a thermal equilibrium state. Considering an element of that body, then the net sum of the forces acting on that element must be zero. In undergoing deformation, the equilibrium state is disturbed, and forces arise which act to restore the body back to it's equilibrium state. These are known as *internal stresses*, and are the result of interaction forces between molecules. The effect of these forces is considered to only extend as far as the distance which separates molecules. In the theory of elasticity, however, the distances considered are much greater than that of molecular ones. These molecular forces are therefore 'near-action' forces which act only on neighbouring points. Hence, it follows that the forces exerted on elements of a body from neighbouring elements act only on the surface of said element.

Considered here is the force acting on an element of the body. The total force is the sum of all the forces acting on the volume element, and can be written as the volume integral

$$\mathbf{F}_{\text{tot}} = \int \mathbf{F}\,\mathrm{d}V \tag{3.12}$$

where $\mathbf{F}$ is the force per unit volume. The forces from portions of the volume element which act on each other must cancel, and so the total force can be regarded as the sum of the forces exerted on the volume element from surrounding volume elements. It has been noted, however, that these forces act on the surface of the element, and so the integral can be represented as an integral over the surface. Each component of $\int F_i\,\mathrm{d}V$ of the internal stresses may then be transformed into surface integrals. To do so, it must be the case that F_i is the divergence of a tensor of rank two in the form of

$$F_i = \frac{\partial \sigma_{ik}}{\partial x_k}. \tag{3.13}$$

The force on any volume can then be written as an integral over a closed surface

$$\int F_i\,\mathrm{d}V = \int \frac{\partial \sigma_{ik}}{\partial x_k}\,\mathrm{d}V = \oint \sigma_{ik}\mathrm{d}n_k \tag{3.14}$$

where $\mathrm{d}n_i$ are the components of the surface element vector directed along the outward normal.

In analogy with the strain tensor, σ_{ik} is known as the stress tensor. As shown

from Eq. 3.14, $\sigma_{ik}\mathrm{n}_k$ is the i-th component of the force on the surface element d$\mathbf{n}$. The component σ_{ik} of the stress tensor is the i-th component of the force on the unit area perpendicular to the x_k-axis. To illustrate this, the force on the unit area perpendicular to the x-axis normal to the area is σ_{xx}, and the tangential forces are σ_{yx} and σ_{zx}

The moment of the force $\mathbf{F}$ can be written in component form as $F_i x_k - F_k x_i$ where x_i are the coordinates of the point of application of the force. The moment of forces on the whole volume is then

$$\mathcal{M}_{ik} = \int (F_i x_k - F_k x_i)\ \mathrm{d}V \tag{3.15}$$

where $(F_i x_k - F_k x_i)\mathrm{d}V$ defines the moment of forces on a volume element. Substituting for Eq. 3.13 and utilising the product rule, it is found

$$\mathcal{M}_{ik} = \int \left(\frac{\partial \sigma_{il}}{\partial x_l} x_k - \frac{\partial \sigma_{kl}}{\partial x_l} x_i\right) \mathrm{d}V = \int \frac{\partial\left(\sigma_{il} x_k - \sigma_{kl} x_l\right)}{\partial x_l} - \int \left(\sigma_{il}\frac{\partial x_k}{\partial x_l} - \sigma_{kl}\frac{\partial x_i}{\partial x_l}\right) \tag{3.16}$$

For the second term $\partial x_k/\partial x_l = \delta_{kl}$. The first term may also be turned into an integral over a surface, such that

$$\mathcal{M}_{ik} = \oint \left(\sigma_{il} x_k - \sigma_{kl} x_i\right)\ \mathrm{d}n_l + \int \left(\sigma_{ki} - \sigma_{ik}\right)\ \mathrm{d}V \tag{3.17}$$

For M_{ik} to be a surface integral only as required by it's definition, then the second integral must vanish which requires that

$$\sigma_{ik} = \sigma_{ki}. \tag{3.18}$$

Hence, the stress tensor is also symmetrical. For arbitrary deformation, it is not the case that the non-diagonal terms are zero. Not only is there normal forces, but there is also shearing (tangential) forces which move elements relative to each other.

Let $\mathbf{P}$ be the external force on unit area of the surface of body, such that $\mathbf{P}\mathrm{d}n$ acts on the surface element dn. For equilibrium to hold, this must be balanced by the internal stresses $\sigma_{ik}\mathrm{d}n_k$ acting on that element. Thus $P_i\mathrm{d}n - \sigma_{ik}\mathrm{d}n_k = 0$. With $\mathrm{d}n_k = n_k\mathrm{d}n$ for $\mathbf{n}$ is a unit vector outward normal to the surface, it is found

$$\sigma_{ik} n_k = P_i \tag{3.19}$$

which must be satisfied at every point on the surface of a body in equilibrium.

In considering the symmetry of the free energy density as a function of the strain tensor [76], the lowest order form is must posses is given by the expression

$$F = F_0 + \frac{1}{2}\lambda u_{ii}^2 + \mu u_{ik}^2 \tag{3.20}$$

where the quantities λ and μ are called Lamé coefficients, and are given with units of Pascals.

The change in volume of a solid body from a deformation is given by the sum of the diagonal components of the strain tensor, u_{ii}. If this sum is zero, then the volume of the body is unchanged and only it's shape is altered. This type of deformation is called a *pure shear* deformation. On the other hand, there exists deformations which cause changes in volume of a body, but leave it's shape unchanged. Such a deformation is represented by $u_{ik} = \text{constant} \times \delta_{ik}$, and is called *hydrostatic compression*. Any

deformation may be represented by a sum of pure shear and hydrostatic compression, such that the components of the strain tensor may be expressed as

$$u_{ik} = \left(u_{ik} - \tfrac{1}{3}\delta_{ik}u_{ll}\right) + \tfrac{1}{3}\delta_{ik}u_{ll}. \tag{3.21}$$

In this, the first term is a pure shear term as the sum of it's diagonal components is zero. The second term is then a hydrostatic compression term.

It is convenient to replace Eq. 3.20 using this representation of pure shear and hydrostatic compression. Substituting for Eq. 3.21 into Eq. 3.20, one may obtain

$$F = \mu\left(u_{ik} - \tfrac{1}{3}\delta_{ik}u_{ll}\right)^2 + \tfrac{1}{2}Ku_{ll}^2 \tag{3.22}$$

where the constant term F_0 from the free energy density is neglected. The quantities K and μ are known as the *bulk modulus* (or modulus of compression) and the *shear modulus* (or modulus of rigidity), respectively. The Lamé coefficients are recovered from K by

$$K = \lambda + \frac{2}{3}\mu. \tag{3.23}$$

The total derivative of the free energy density with respect to the strain tensor components is expressed as

$$\mathrm{d}F = Ku_{ll}\mathrm{d}u_{ll} + 2\mu\left(u_{ik} - \tfrac{1}{3}u_{ll}\delta_{ik}\right)\mathrm{d}(u_{ik} - \tfrac{1}{3}u_{ll}\delta_{ik}). \tag{3.24}$$

In the second term of this, multiplication of the first parenthesis by δ_{ik} gives zero (note that it reduces to $u_{ll} - u_{ll}$), and so the expression may be simplified to

$$\mathrm{d}F = \left[Ku_{ll}\delta_{ik} + 2\mu\left(u_{ik} - \tfrac{1}{3}u_{ll}\delta_{ik}\right)\right]\mathrm{d}u_{ik} \tag{3.25}$$

where it is written $\mathrm{d}u_{ll} = \delta_{ik}\mathrm{d}u_{ik}$.

In considering the thermodynamics of an elastic body at equilibrium [76], the stress tensor can be related to the free energy density via the relation

$$\sigma_{ik} = \left(\frac{\partial F}{\partial u_{ik}}\right)_T. \tag{3.26}$$

Hence, an expression for the stress tensor in terms of the strain tensor for an isotropic body is found as

$$\sigma_{ik} = Ku_{ll}\delta_{ik} + 2\mu\left(u_{ik} - \tfrac{1}{3}\delta_{ik}u_{ll}\right). \tag{3.27}$$

In particular, this shows that if a deformation is purely shear or hydrostatic compression then the relation between the stress and strain tensors is determined entirely by the modulus of rigidity or the modulus of compression respectively.

The opposite of this function is also worth finding, and can be done so by expressing u_{ik} in terms of σ_{ik}. The sum σ_{ii} of the diagonal terms is found from Eq. 3.27, yielding

$$u_{ii} = \frac{\sigma_{ii}}{3K} \tag{3.28}$$

which in substituting into Eq. 3.27 finds

$$u_{ik} = \frac{\delta_{ik}\sigma_{ll}}{9K} + \frac{\left(\sigma_{ik} - \tfrac{1}{3}\delta_{ik}\sigma_{ll}\right)}{2\mu}. \tag{3.29}$$

It is seen from Eq. 3.29 that the strain tensor is a linear function of the stress tensor,

which is to say that deformation is proportional to the applied forces. This is known as *Hooke's law*.

3.2 Homogenous deformations

To illustrate the use of Hooke's law, consider here an example of the simple extension of a thin rod. The axis of the rod is assumed to be along the z-axis and a force per unit area $\mathbf{p}$ is be applied to the ends of the rod in both directions, where this force acts uniformly over the end surfaces. As this constitutes a homogenous deformation, the simplification that the strain tensor is constant through the body of the rod can be made. In turn, this requires the stress tensor must also be constant, which may also be determined from the condition in Eq. 3.19. There are no external forces in consideration on the side surfaces of the rod, and so for these orientations it is trivially $\sigma_{ik}\mathbf{n}_k = 0$. As the unit vector on the sides of the rod is perpendicular to the z-axis in which the force per unit area acts, it then follows that all components of σ_{ik} other than σ_{zz} are zero, and on the end surfaces $\sigma_{zz} = p$.

From Eq. 3.29, all components of u_{ik} with $i \neq k$ are zero. What components remain are then expressed as

$$u_{xx} = u_{yy} = -\frac{1}{3}\left(\frac{1}{2\mu} - \frac{1}{3K}\right)p, \quad u_{zz} = \frac{1}{3}\left(\frac{1}{3K} + \frac{1}{\mu}\right)p. \tag{3.30}$$

The component u_{zz} gives the relative lengthening of the rod in undergoing a homogeneous deformation from a force per unit area $\mathbf{p}$. The coefficient of p is called the *coefficient of extension*, and it's reciprocal is the *modulus of extensions*, or *Young's modulus*, E, defined as

$$u_{zz} = \frac{p}{E} \quad \text{where} \quad E = \frac{9K\mu}{3K + \mu} \tag{3.31}$$

The transverse components u_{xx} and u_{yy} give the relative compression of the rod in the transverse directions. The ratio of transverse compression to longitudinal extension is called *Poisson's ratio*, defined as

$$u_{xx} = -\nu u_{zz} \quad \text{where} \quad \nu = \frac{1}{2}\frac{3K - 2\mu}{3K + \mu} \tag{3.32}$$

and takes values between 0 and $1/2$. A larger Poisson's ratio means that there is a higher degree of relative deformation in the transverse directions. A material possessing a Poisson ratio of 0 would be one that would collapse under transverse deformation. It is often customary in elasticity to use E and ν as the base coefficients, rather than K and μ, and so Hooke's law is redefined in terms of these parameters as

$$u_{ik} = \frac{1}{E}\left[(1+\nu)\sigma_{ik} - \nu\delta_{ik}\sigma_{ll}\right]. \tag{3.33}$$

3.3 Bending of rods

When a rod undergoes bending, there are sections of the rod's body that are compressed, and there are sections that are stretched. Lines on the compressed side a stretched, and those on the stretched side are compressed. At the interface of these two phenomena is a neutral surface which undergoes neither.

Consider a small element of length of the rod, whereby bending may be small. A coordinate system is defined such that the origin is on the neutral surface, and the z-axis is parallel to the length. Bending then occurs in the zy plane.

The external forces on the sides of a thin bent rod may assumed to be small compared with the internal stresses, and so can be taken as zero in determining the boundary conditions (a criterion referred to as traction-free boundaries). Expressed in terms of the stress tensor, it is found $\sigma_{ik}n_k = 0$, or $\sigma_{xx}n_x + \sigma_{xy}n_y = 0$ as $n_z = 0$, and similarly for $i = y, z$. Take a point on the circumference of the cross-section for which the normal, $\mathbf{n}$, is parallel to the x-axis, which by symmetry must have another such point on the opposite side. At both of these points, $n_y = 0$ and hence $\sigma_{xx} = 0$. As the rod is thin, one is free to assume σ_{xx} must be small everywhere if it vanishes at the sides. From this, one finds $\sigma_{xx} = 0$ throughout the whole cross-section, with the same argument holding for all components of the stress tensor except σ_{zz} which is seen to be nonzero. A deformation in which there is only a nonzero component in σ_{zz} is seen as simple extension, although the amount of extension varies point to point in the cross-section giving rise to the bending profile.

The relative extension at points within the rod can be determined as such; consider an element of length $\mathrm{d}z$ parallel to the rod, and in undergoing bending length is denoted $\mathrm{d}z'$, where both of these points considered points are close to the origin. When undergoing bending, the only points to remain unchanged are those that lay on the neutral axis betwixt the regions of stresses and strains. The radius of curvature of the neutral surface in undergoing bending is denoted as R. With these considerations, the length elements $\mathrm{d}z$ and $\mathrm{d}z'$ may be regarded as arcs of circles, having radii of R and $R + x$ respectively, where x is the coordinate of where the length element $\mathrm{d}z'$ lays. Then

$$\mathrm{d}z' = \frac{R+x}{R}\mathrm{d}z = \left(1 + \frac{x}{R}\right)\mathrm{d}z \tag{3.34}$$

from which the relative extension is found as

$$\frac{\mathrm{d}z' - \mathrm{d}z}{\mathrm{d}z} = \frac{x}{R}. \tag{3.35}$$

This must be equal to the component u_{zz} of the strain tensor by definition. The component of the stress tensor can then be found by using Hooke's law of simple extension, $\sigma_{zz} = Eu_{zz}$, giving

$$\sigma_{zz} = \frac{Ex}{R}. \tag{3.36}$$

It can further be shown that this condition sets the centre of mass to coincide with the neutral axis by considering the plane at which the stress vanishes.

The free energy per unit volume of a deformed rod the rod is given by [76]

$$\frac{1}{2}\sigma_{ik}u_{ik} = \frac{1}{2}\sigma_{zz}u_{zz} = \frac{1}{2}\frac{Ex^2}{R^2}. \tag{3.37}$$

Integrating over the cross section, it is then found

$$\frac{1}{2}\frac{E}{R^2}\int_A y^2 \mathrm{d}n \tag{3.38}$$

which is the free energy per unit length of the a bent rod. Since the rod is thin, R may be regarded as the radius of curvature of the rod itself, taken as a line. In this expression, it is often convenient to introduce the second moment of area, defined

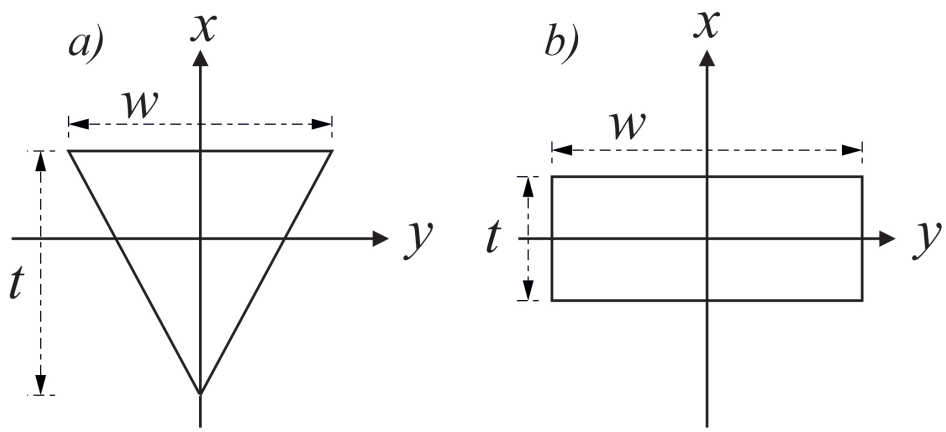

FIGURE 3.2: Orientation of the (a) isosceles and (b) rectangular cross-sections.

as

$$I_y = \int_{\mathrm{A}} x^2 \mathrm{d}n \tag{3.39}$$

in analogy to the moment of inertia, but with the surface element dn instead of the mass element. The free energy per unit length of the rod can then be written

$$\frac{1}{2}\frac{EI_y}{R^2}. \tag{3.40}$$

Of particular interest to the purpose of this thesis are rods of cross-sections of rectangles and isosceles triangles, which offer a flat surface to deposit material on top of. The two geometries are depicted in Fig. 3.2, where their centroids coincide with the neutral surface. For these, the principle axes about which the second area moment of inertia is taken are expressed as

$$I_{x,\mathrm{rec}} = \frac{wt^3}{12} \qquad I_{y,\mathrm{rec}} = \frac{w^3 t}{12}, \tag{3.41}$$

$$I_{x,\mathrm{iso}} = \frac{wt^3}{36} \qquad I_{y,\mathrm{iso}} = \frac{w^3 t}{36}. \tag{3.42}$$

The bending moment, which is the moment of the internal stress forces on a given cross-section, may also be determined. A force $\sigma_{zz}\mathrm{d}n = (xE/R)\,\mathrm{d}n$ acts along the z-direction of the surface element dn of the cross-section. The moment about the y-axis is then $x\sigma_{zz}\mathrm{d}n$, such that the total moment of the forces about this axis is

$$\mathcal{M}_y = \frac{E}{R}\int_A x^2 \mathrm{d}n = \frac{EI_y}{R}, \tag{3.43}$$

where the symbol $\mathcal{M}$ has been used to avoid confusion with the magnetisation. It is then seen that the curvature of the rod is proportional to the bending moment. Similarly, the moment of forces about the x-axis is

$$\mathcal{M}_x = \frac{E}{R}\int_A y^2 \mathrm{d}n = \frac{EI_x}{R} \tag{3.44}$$

The quantity EI_y (and similarly EI_x for the other principle axis) is known as the *flexural rigidity*, and is considered as the amount of moment required to produce bending. A larger flexural rigidity denotes a 'stiffer' axis than that of a smaller one.

The slope of the beam in general is approximated by the angle made with the

neutral surface to the z-axis. For small angles, and assuming deflections in the xz-plane only, this may be approximated with

$$\theta(z) \approx \frac{\mathrm{d}\phi}{\mathrm{d}z} \tag{3.45}$$

where ϕ is the deflection of the neutral surface of the beam. For an infinitesimal element $\mathrm{d}z$, one can then use the relation $\mathrm{d}z = R\mathrm{d}\theta$ to find for the radius of curvature

$$\frac{1}{R} = \frac{\mathrm{d}\theta}{\mathrm{d}z} = \frac{\mathrm{d}^2\phi}{\mathrm{d}z^2}. \tag{3.46}$$

The z-directed strain is then $u_{zz} = x/R$ and, in using the formula for simple extension $\sigma_{zz} = Eu_{zz}$, the components of Hooke's law from Eq. 3.33 find

$$\begin{aligned} u_{xx} = u_{yy} &= -\nu x \frac{\mathrm{d}^2 y}{\mathrm{d}z^2} \\ u_{zz} &= x \frac{\mathrm{d}^2 y}{\mathrm{d}z^2} \end{aligned} \tag{3.47}$$

With the consideration that deflection only occurs in the xz -plane, one can also re-express the moment about the x-axis as

$$\mathcal{M}_x = EI_x \frac{\mathrm{d}^2\phi}{\mathrm{d}z^2} \tag{3.48}$$

Further, from this consideration of pure bending in the xz plane only, the shearing force, V_x, is then defined as

$$V_x = -\frac{\mathrm{d}\mathcal{M}_x}{\mathrm{d}z}. \tag{3.49}$$

3.4 The elastic properties of crystals

The general form of the free energy density of a deformed crystal is given as a tensor form [76]

$$F = \frac{1}{2}\lambda_{iklm} u_{ik} u_{lm} \tag{3.50}$$

where λ_{iklm} is a fourth-rank tensor, denoted the elastic modulus tensor. As the strain tensor is symmetric, the product $u_{ik}u_{lm}$ is unchanged in swapping the pairings i, k or l, m, or i, l and k, m. The tensor is therefore defined to have the same properties

$$\lambda_{iklm} = \lambda_{kilm} = \lambda_{ikml} = \lambda_{lmik}. \tag{3.51}$$

In the absence of these symmetries, the number of components would be $3^4 = 81$, but taking into account 6 equivalent pairs of i, j and l, m, the total number of independent components is the same as the number of components in a 6×6 symmetric matrix. This is 6 for the diagonal entries, and 15 for the off-diagonal entries, finding 21 independent components in total. The stress tensor, in accordance with Eq. 3.26, is then found as

$$\sigma_{ik} = \frac{\partial F}{\partial u_{ik}} = \lambda_{iklm} u_{lm} \tag{3.52}$$

where terms of $\mathrm{d}u_{ik}$ appear twice due to the symmetry for $i \neq k$, and hence the factor of 2 is lost.

For crystals, which implicitely have symmetries, then relations exist between the components of λ_{iklm} to reduce the number of independent components further. Of particular note for our interests is cubic systems.

In a cube, there are three mutually orthogonal axes having reflection symmetry, about which it is assumed the system axes are set. As there is four-fold rotational symmetry, the different components of the tensor is limited to at most λ_{xxxx}, λ_{zzzz}, λ_{xxzz}, λ_{xxyy}, λ_{xyxy}, λ_{xzxz}. Considering rotations of $\frac{1}{2}\pi$ about the x and y axes finds that successive pairs of components are equal, and so only 3 different components remain. Adopting the Voigt notation to coincide with literature, in which the indexes become $xx = 1$, $yy = 2$, and $xy = 4$, and $\lambda = c$, the elastic free energy density of the crystal may be expressed as

$$U_\mathrm{e} = \frac{1}{2}c_{11}(u_{xx}^2 + u_{yy}^2 + u_{zz}^2) + c_{12}(u_{xx}u_{yy} + u_{xx}u_{zz} + u_{yy}u_{zz}) + 2c_{44}(u_{xy}^2 + u_{xz}^2 + u_{yz}^2). \tag{3.53}$$

To find the Young's modulus of a cubic crystal as a function of the axes directions, the axes of coordinate are taken along the three orthogonal axes of tetragonal symmetry. Let the axis of a rod cut from a cubic crystal be along the unit vector direction $\mathbf{n}$. Assuming traction free boundaries, the stress tensor must satisfy

i. when σ_{ik} is multiplied by n_i the extending force is then parallel to the $\mathbf{n}$.

ii. when σ_{ik} is multiplied by a vector perpendicular to $\mathbf{n}$ the resulting extending force must be 0.

As such, the tensor must be of the form $\sigma_{ik} = pn_in_k$, where p is the extension force per unit area at the ends of the rod. The free energy density of the cubic crystal has been found in Eq. 3.53, and so now Eq. 3.52 is applied directly directly. For the non diagonal components, it is trivial to see

$$\sigma_{xy} = \frac{\partial F}{\partial u_{xy}} = 2c_{44}u_{xy} \tag{3.54}$$

where the components of u_{ik} with $i \neq k$ give twice the value of the corresponding σ_{ik} as the strain tensor appears twice in $\mathrm{d}F = \sigma_{ik}\mathrm{d}u_{ik}$ due to its symmetry. From this, by comparison, one may identify

$$u_{xy} = p\frac{n_xn_y}{2c_{44}}. \tag{3.55}$$

To determine the diagonal components;

$$\sigma_{xx} = \frac{\partial F}{\partial u_{xx}} = c_{11}u_{xx} + c_{12}(u_{yy} + u_{zz}) = pn_x^2 \tag{3.56}$$

$$\sigma_{yy} = \frac{\partial F}{\partial u_{yy}} = c_{11}u_{yy} + c_{12}(u_{xx} + u_{zz}) = pn_y^2 \tag{3.57}$$

$$\sigma_{zz} = \frac{\partial F}{\partial u_{zz}} = c_{11}u_{zz} + c_{12}(u_{xx} + u_{yy}) = pn_z^2 \tag{3.58}$$

Rearranging Eq. 3.56 for $c_{11}u_{xx}$, and substituting in Eq. 3.57 and Eq. 3.58 finds

$$c_{11}u_{xx} = pn_x^2 - \frac{c_{12}}{c_{11}}\left(pn_y^2 + pn_z^2 - c_{12}(u_{yy} + u_{zz}) - 2c_{12}u_{xx}\right). \tag{3.59}$$

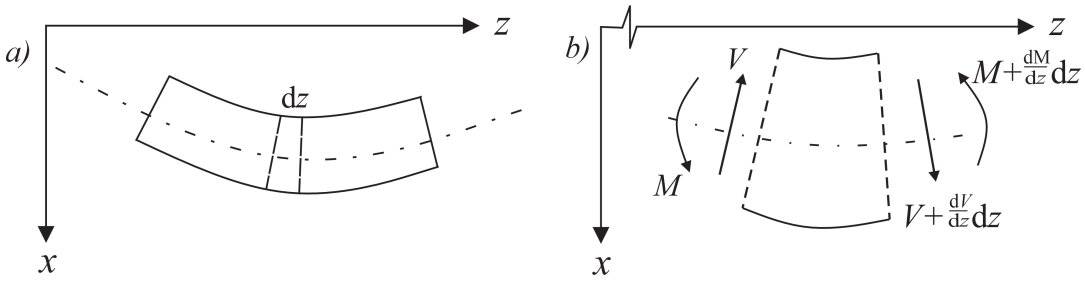

FIGURE 3.3: (a) A thin rod undergoing transverse motion, and (b) a zoom-in of an element of the rod.

Finally, substituting for $c_{12}(u_{yy}+u_{zz})$ from Eq. 3.56 and noting the relation $n_x^2+n_y^2+n_z^2=1$ one arrives at

$$u_{xx}=p\frac{(c_{11}+2c_{12})n_x^2-c_{12}}{(c_{11}-c_{12})(c_{11}+2c_{12})} \tag{3.60}$$

where similar expressions exists for the other components.

The relative longitudinal extension of a rod is found as

$$u=\frac{\mathrm{d}l'-\mathrm{d}l}{\mathrm{d}l} \tag{3.61}$$

where $\mathrm{d}l'$ is given by Eq. 3.7 and $\mathrm{d}x_i/\mathrm{d}l=n_i$. For small deformations, and hence $\mathrm{d}l$ small, the displacement is found as $u=u_{ik}n_in_k$. It has been shown in Eq. 3.31 that, upon extending to the three-dimensional case, the Young's modulus is determined by $p=Eu$. Hence, Young's modulus as a function of crystal direction is given by the expression

$$\frac{1}{E}=\frac{c_{11}+c_{12}}{(c_{11}-c_{12})(c_{11}+2c_{12})}+\left(\frac{1}{c_{44}}-\frac{2}{c_{11}-c_{12}}\right)\left(n_x^2n_y^2+n_x^2n_z^2+n_y^2n_z^2\right) \tag{3.62}$$

which has extremum values in the directions of the edges of the cube, and of the spatial diagonals of the cube. With regards to the value in the first set of brackets of the second term, the elastic anisotropy parameter is introduced

$$A=\frac{2c_{44}}{c_{11}-c_{12}}. \tag{3.63}$$

This quantifies the extent to which elastic anisotropy is present in the crystal. When this parameter is equal to 1, then the crystal is elastically isotropic and the second term in Eq. 3.62 vanishes.

3.5 The Euler-Bernoulli equation

Consider the thin rod as depicted in Fig. 3.3(a), as well as the differential element, $\mathrm{d}z$, as shown in Fig. 3.3(b). The subscript x from the moments and shearing forces is dropped and it is assumed that this becomes obvious by considering motion only in the xz plane. In considering this element, there are the bending moment, M, the shear force, V, and the variations of the two acting.

To find the equation of motion for the differential element in the vertical direction, Newton's second law is used

$$-V + \left(V + \frac{\partial V}{\partial z}\mathrm{dz}\right) = \rho A \mathrm{dz}\frac{d^2y}{dt^2} \tag{3.64}$$

where A is the cross section of the beam and ρ is it's mass density per unit volume. This reduces further to

$$\frac{\partial V}{\partial z} = \rho A \frac{\partial^2 y}{\partial t^2}. \tag{3.65}$$

Substituting the equation relating the shearing force to the bending moment, Eq. 3.49, into this then yields

$$-\frac{\partial^2 \mathcal{M}}{\partial z^2} = \rho A \frac{\partial^2 y}{\partial t^2} \tag{3.66}$$

and finally, substituting the expression for the bending moment in Eq. 3.48 gives

$$\frac{\partial^2}{\partial z^2}\left(EI_x \frac{\partial^2 y}{\partial z^2}\right) + \rho A \frac{\partial^2 y}{\partial t^2} = 0. \tag{3.67}$$

This is then the governing equation for the transverse motion of a thin rod. In the case that the material is homogeneous such that E is independent of position and that the cross-section is constant such that I is constant, then Eq. 3.67 reduces to simpler form

$$\frac{\partial^4 y}{dz^4} + \frac{1}{a^2}\frac{\partial^2 y}{\partial t^2} = 0 \tag{3.68}$$

where it is defined

$$a^2 = \frac{EI_x}{\rho A}. \tag{3.69}$$

Note that this is not a wave equation, nor does a have equivalent dimensions to velocity.

There are a number of restrictions placed on this theory for which their relevance is stated.

i. The restriction of homogeneity of the beam as well as the cross section being constant in reducing Eq. 3.67 to Eq. 3.68 is not a fundamental step, and is assumed to simplify the mathematics required. It is perfectly valid to analyse beams without these properties through Eq 3.67, with the addition of some mathematical complexities to solve.

ii. Should the assumption of small deflections made to arrive at Eq. 3.46 not be the case, then the full expression for the curvature would be required rather than the simplification to the second-derivative of deflection.

iii. It has been assumed that the deflections occur in the xz plane only, which requires that the cross-section be symmetric with respect to this plane. Should this not be the case, then coupled torsional-flexural modes would need to be considered.

iv. Rotational-inertia effects have been neglected. The translational and kinetic energies are expressed as

$$\mathrm{d}T_\mathrm{t} = \frac{1}{2}\mathrm{d}m\left(\frac{\partial \phi}{\partial t}\right)^2 \quad \text{and} \quad \mathrm{d}T_\mathrm{r} = \frac{1}{2R}\mathrm{d}m\left(\frac{\partial \Omega}{\partial t}\right)^2 \tag{3.70}$$

where dm is the mass of the element dz, R is it's radius of gyration, and $\partial\Omega/\partial t$ is the rotational velocity. The rotational energy is small and negligible compared to the translational energy as so it may be assumed that the rotational velocity is small.

v. The assumption of the Euler-Bernoulli criterion, in that plane sections remain as such, is only valid for pure bending. When shearing forces are present, the assumption of this hypothesis essentially requires there is an in infinite shear rigidty, which is to say that shearing deformations are neglected.

3.6 Solutions to the Euler-Bernoulli equation

To find solutions to Eq. 3.68, a separable solution is assumed of the form

$$y(z,t) = \phi(z)T(t). \tag{3.71}$$

By substitution into Eq. 3.68 and noting that each must be equal to some shared constant, it is found

$$a^2\frac{\phi''''(z)}{\phi(z)} = -\frac{\ddot{T}(t)}{T(t)} = \omega_{\mathrm{R}}^2. \tag{3.72}$$

It is readily apparent from Eq. 3.72 that simple harmonic motion exists for $T(t)$ and yields a general solution of

$$T(t) = A\cos(\omega t) + B\sin(\omega t) \tag{3.73}$$

subject to the boundary conditions of the system, from which the constants A and B may be determined.

To find a solution for the spatial dependence, it is standard to assume a trial solution of

$$\phi(z) = C_1\sin(k_n z) + C_2\cos(k_n z) + C_3\sinh(k_n z) + C_4\cosh(k_n z) \tag{3.74}$$

where k_n, called the frequency parameter, is defined by

$$k_n^4 = \frac{\omega_{\mathrm{R}}^2}{a^2}. \tag{3.75}$$

However, it is more convenient for this specific case to order the trial solution as

$$\begin{aligned}\phi(z) = D_1\left(\cos(k_n z) + \cosh(k_n z)\right) + D_2\left(\cos(k_n z) - \cosh(k_n z)\right)\\ D_3\left(\sin(k_n z) + \sinh(k_n z)\right) + D_4\left(\sin(k_n z) - \sinh(k_n z)\right).\end{aligned} \tag{3.76}$$

There are 3 primary classes of boundary conditions to consider that present supports (or lack thereof) at the extremes of the beam. These are commonly referred to as *pinned*, *clamped*, and *free* boundaries.

- In *pinned* boundary conditions, rotations are possible but the displacement and bending moment are zero, leading to

$$\phi(z_{\text{pinned}}, t) = 0 \quad \text{and} \quad \frac{\partial^2\phi(z_{\text{pinned}}, t)}{\partial z^2} = 0 \tag{3.77}$$

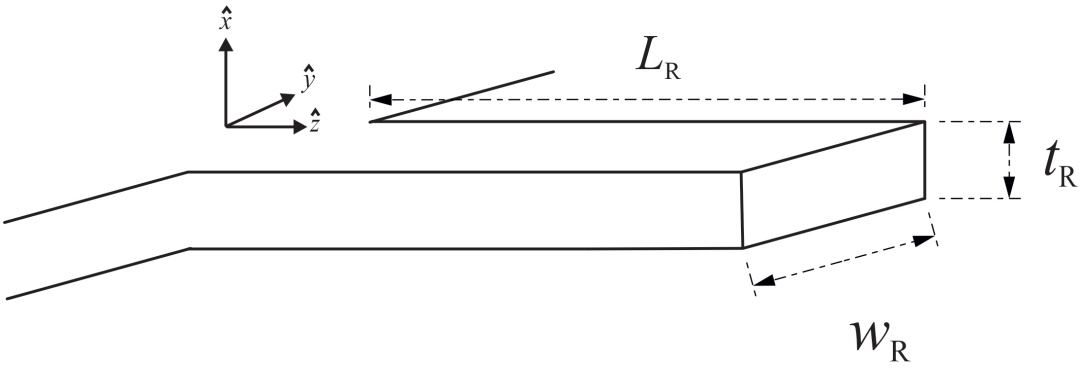

FIGURE 3.4: A cantilevered Euler-Bernoulli beam.

- In *clamped* boundary conditions, the support is rigid and does not permit displacement or rotation, leading to

$$\phi(z_{\text{clamped}}, t) = 0 \quad \text{and} \quad \frac{\partial \phi(z_{\text{clamped}}, t)}{\partial z} = 0 \tag{3.78}$$

- In *free* boundary conditions, there is no support and displacement is possible, but there are no stresses or moments, leading to

$$\frac{\partial^2 \phi(z_{\text{free}}, t)}{\partial z^2} = 0 \quad \text{and} \quad \frac{\partial^3 \phi(z_{\text{free}}, t)}{\partial z^3} = 0 \tag{3.79}$$

Cantilever beam

Assumed is that a cantilevered beam of length a L_R coincides with the z axis, and is to the right of the neutral axis, as shown in Fig. 3.4. Also assumed is that the cross-section, generic in nature but symmetric with respect to the plane of flexure, is sufficiently small compared to the beam's length and hence the beam obeys Eq. 3.68. Such a beam will have a deflection profile, denoted $\phi_n(z)$, where n denotes the mode number.

For this beam geometry, the ends of the beam impose a clamped boundary at the beam support, with boundary condition given by Eq. 3.78, and a free boundary, with boundary condition given by Eq. 3.79, at the left end and right end, respectively. Applying first the clamped boundary, one finds

$$\begin{aligned} \phi_n(0) &= 2D_1 = 0 \\ &\Rightarrow D_1 = 0 \end{aligned} \tag{3.80}$$

$$\begin{aligned} \phi_n'(0) &= 2D_3 = 0 \\ &\Rightarrow D_3 = 0 \end{aligned} \tag{3.81}$$

Applying now the free boundary, one finds

$$\begin{aligned} \phi_n''(L) &= 0 \\ &= k_n^2 D_2 \left(-\cos(k_n L) - \cosh(k_n L)\right) + k_n^2 D_4 \left(-\sin(k_n L) - \sinh(k_n L)\right) \end{aligned} \tag{3.82}$$

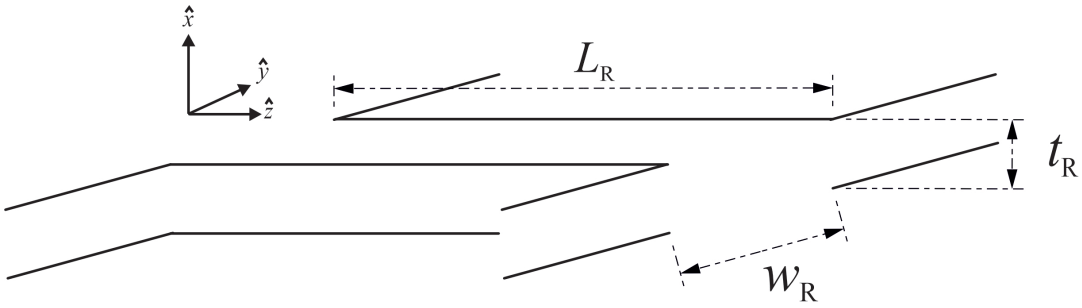

FIGURE 3.5: A bridged Euler-Bernoulli beam.

$$\begin{aligned}\phi_n'''(L) &= 0 \\ &= k_n^3 D_2 \left(\sin(k_n L) - \sinh(k_n L)\right) + k_n^3 D_4 \left(-\cos(k_n L) - \cosh(k_n L)\right)\end{aligned} \tag{3.83}$$

Representing Eq. 3.82 and Eq. 3.83 as a matrix

$$\begin{pmatrix} -\cos(k_n L) - \cosh(k_n L) & -\sin(k_n L) - \sinh(k_n L) \\ \sin(k_n L) - \sinh(k_n L) & -\cos(k_n L) - \cosh(k_n L) \end{pmatrix} \begin{pmatrix} D_2 \\ D_4 \end{pmatrix} = \begin{pmatrix} 0 \\ 0 \end{pmatrix} \tag{3.84}$$

for which solutions can only exist when the determinant is equal to 0, it is then possible to show

$$\cos^2(k_n L) + \sin^2(k_n L) + \cosh^2(k_n L) - \sinh^2(k_n L) + 2\cos(k_n L)\cosh(k_n L) = 0. \tag{3.85}$$

This equation may further be reduced to find the characteristic equation

$$\cos(k_n L)\cosh(k_n L) + 1 = 0, \tag{3.86}$$

which gives permissible values of $k_n L$ for the cantilever. Rearranging Eq. 3.82 for D_4,

$$D_4 = D_2 \left[\frac{-\cos(k_n L) - \cosh(k_n L)}{\sin(k_n L) + \sinh(k_n L)}\right] \tag{3.87}$$

which upon substitution into Eq. 3.76 alongside with Eq. 3.80 and Eq. 3.81, the full general solution is given by the function

$$\phi_n(z) = D_2 \left[\cosh(k_n z) - \cos(k_n z) + \frac{\cos(k_n L) + \cosh(k_n L)}{\sin(k_n L) + \sinh(k_n L)} \left(\sin(k_n z) - \sinh(k_n z)\right)\right] \tag{3.88}$$

where -1 has been factored into D_2 as an arbitrary phase. This is the static deflection profile of a cantilever beam.

Bridged beam

Assumed is bridged beam of length a L_R which coincides with the z axis, and is to the right of the neutral axis, as shown in Fig. 3.5. As was the case prior, the cross-section, generic but symmetric, is taken to be sufficiently small compared to the beam's length and hence the beam obeys Eq. 3.68. Again, such a beam will have a deflection profile, denoted $\phi_n(z)$, where n again denotes the mode number.

For this beam geometry, the ends of the beam impose a double clamped boundary by the supports, with the boundary conditions given again by Eq. 3.78. Applying

first the clamped boundary at the left end, one finds

$$\phi_n(0) = \phi_n(L) = \phi_n'(0) = \phi_n'(L) = 0. \tag{3.89}$$

As is the case in the cantilever beam, the boundary conditions require that

$$D_1 = D_3 = 0. \tag{3.90}$$

Applying now the clamped boundary at the right end,

$$\begin{aligned}\phi_n(L) &= 0 \\ &= D_2\left(\cos(k_nL) - \cosh(k_nL)\right) + D_4\left(\sin(k_nL) - \sinh(k_nL)\right),\end{aligned} \tag{3.91}$$

$$\begin{aligned}\phi_n'(L) &= 0 \\ &= kD_2\left(-\sin(k_nL) - \sinh(k_nL)\right) + kD_4\left(\cos(k_nL) - \cosh(k_nL)\right).\end{aligned} \tag{3.92}$$

Representing Eq. 3.91 and Eq. 3.92 as the matrix

$$\begin{pmatrix} \cos(k_nL) - \cosh(k_nL) & \sin(k_nL) - \sinh(k_nL) \\ -\sin(k_nL) - \sinh(k_nL) & \cos(k_nL) - \cosh(k_nL) \end{pmatrix} \begin{pmatrix} D_2 \\ D_4 \end{pmatrix} = \begin{pmatrix} 0 \\ 0 \end{pmatrix} \tag{3.93}$$

and solving again for the determinant equal to 0, the expression

$$\cos^2(k_nL) + \sin^2(k_nL) + \cosh^2(k_nL) - \sinh^2(k_nL) - 2\cos(k_nL)\cosh(k_nL) = 0. \tag{3.94}$$

is yielded. Again, this may further be reduced to the characteristic equation which gives permissible values of k_nL for the bridge

$$\cos(k_nL)\cosh(k_nL) - 1 = 0. \tag{3.95}$$

Rearranging Eq. 3.92 for D_4

$$D_4 = D_2\left[\frac{\sin(k_nL) + \sinh(k_nL)}{\cos(k_nL) - \cosh(k_nL)}\right] \tag{3.96}$$

which upon substitution into Eq. 3.76 alongside Eq. 3.90, the full general solution is given by the function

$$\phi_n(z) = D_2\left[\cos(k_nz) - \cosh(k_nz) + \frac{\sin(k_nL) + \sinh(k_nL)}{\cos(k_nL) - \cosh(k_nL)}\left(\sin(k_nz) - \sinh(k_nz)\right)\right] \tag{3.97}$$

3.7 Frequency parameter and mode shapes

The characteristic equations for permissible frequency parameters of the cantilever and bridge, given in Eq. 3.86 and Eq. 3.95, are transcendental equations that may be solved numerically to yield their values of k_nL. Shown in Table 3.1 are the first few roots of these characteristic equations. These have the property that as the mode number increases the spacing between successive the modes approaches that of π for both cases. Also shown in Fig. 3.6 are the first three deflection modes for the cantilever and bridge assuming that the profiles are length normalised and $D = 1$. The bridge, being doubly clamped, has a deflection and curvature profile that alternates

Function	k_1L	k_2L	k_3L	k_4L	k_5L
$\cos(k_nL)\cosh(k_nL)+1=0$	0.597π	1.494π	2.500π	3.500π	4.500π
$\cos(k_nL)\cosh(k_nL)-1=0$	1.506π	2.500π	3.500π	4.500π	5.500π

TABLE 3.1: Roots of Eq. 3.86 and Eq. 3.95 in terms of the frequency parameter k_nL

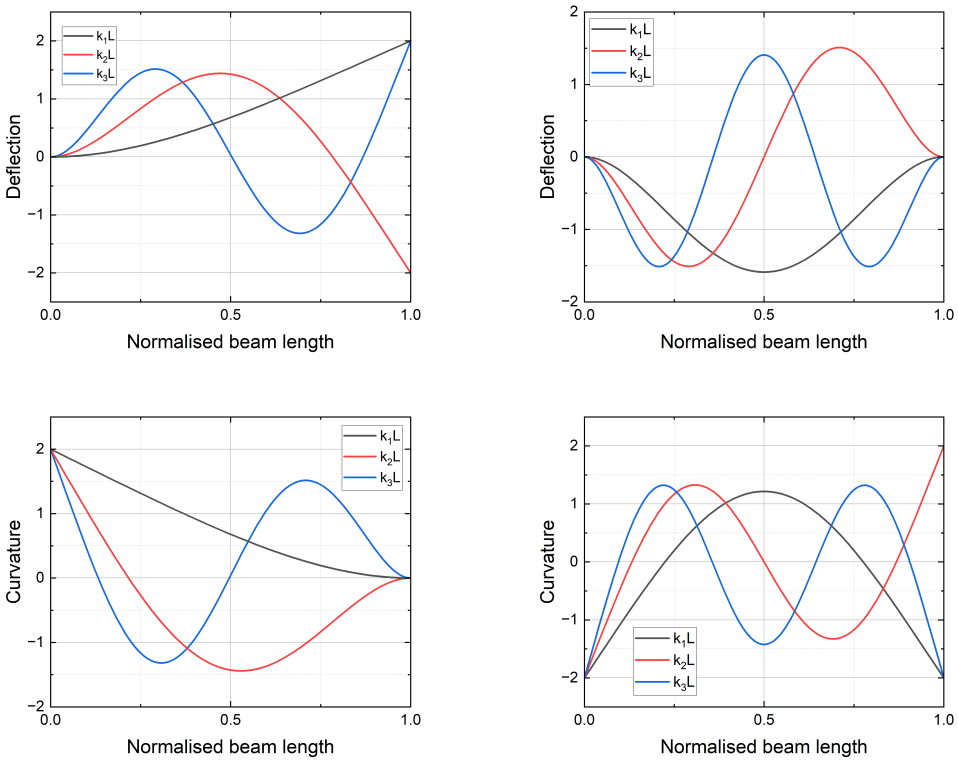

FIGURE 3.6: Deflection profiles for the cantilever and bridge beams [top], and their curvatures [bottom], as obtained from Euler-Bernoulli beam theory.

between an even and off function. Lastly, shown in Fig. 3.7 is a comparison of the frequency of beams of different cross-sections (square, annulus, circular, and isosceles) for modes $n = [1, 8]$. For illustrative purposes, the dimensions have been taken as a width $w = 400\,\text{nm}$ to set a scaling factor, and then taken $t = w$ for the square and isosceles, and $L = 100w$. For the circle and annulus, the radii have been taken as $r_2 = r = w/2$ and $r_1 = r_2/2$. The inset shows the frequencies of these structures for the fundamental mode.

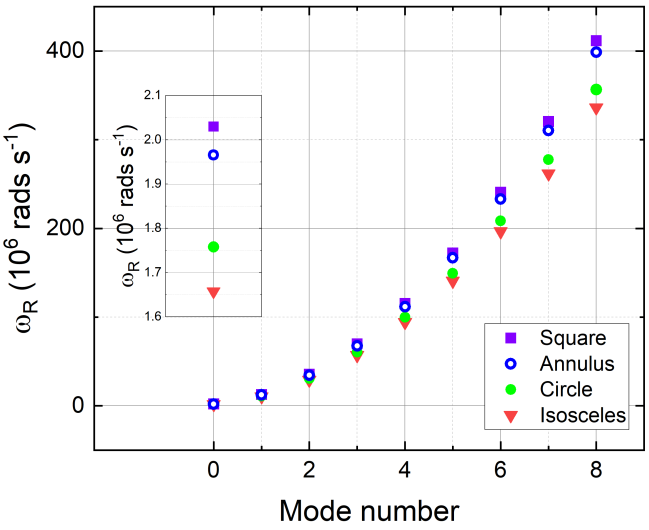

FIGURE 3.7: First 8 flexural mode frequencies of square, annulus, circular, and isosceles cross-sections for a cantilever. The inset shows the frequencies of these structures for the fundamental flexural mode.

Chapter 4

Optomechanics

Fundamentally, light carries momentum through which it is able to exert a force. Often, this force is referred to as the radiation-pressure force. Postulation of this force dates back to the 1600s, and Maxwell predicted that electromagnetic radiation can exert forces through the electromagnetic stress-tensor in the late 1800s. Experimental proof of such forces didn't come until the early 1900s [77, 78], and given that the force a beam of light exerts is small (in fact, inversely proportional to the speed of light), it proved difficult at the time to separate this force from the dominating thermal effects. Einstein's analysis[1] of the statistics on the fluctuations of the radiation force proved fundamental to this end in resolving radiation-pressure from this thermal background. Optomechanics is the research field which is concerned with the interaction of light with mechanical degrees of freedom through the radiation-pressure force, and is the easiest formalism to frame the context of magnomechanics within.

In the years since these discoveries, there has been a great deal of interest into the applications of optomechanics, driven by a number of reasons. Firstly, there is immense interest in sensitive detection of forces, displacements, and masses. In part, this has been driven by the need for this detection in macroscopic mirrors (for example, with use in LIGO for the detection of gravitational waves) [79], but there also exists this need towards the micro- and nano-mechanical scales [80] for various sensing purposes. Further, there is also great interest in the practical applications of the manipulation of mechanical oscillators in the quantum regime. In particular, optomechanical systems have a wide variety of uses, with effects such as optical spring effect (also known as the light induced spring constant), [81, 82] and the associated bistablilty [83, 84], which in turn have led to exploitations allowing the cooling of mechanical resonators down to their ground state [5, 85, 86, 87, 88]. Other applications include uses in the transfer of states [89, 90] (of particular importance to quantum information and quantum computing in mediating transfer between of qubits to longer-lived mechanical excitations), squeezing of states [91, 92, 93], phonon lasing [94, 95], as well as the controlling of the optical response of media via the optomechanical interaction [96, 97, 98] in analogy to the electromagnetically induced transparency [99], which can have applications in the amplification and filtering of states [100]. There are also applications of optomechanics in testing the fundamental limits of quantum mechanics [101, 102].

While the mathematics used in optomechanics is often stated under the assumption of a radiation-pressure force, and most of the experimenal successes have used this form, the derivations are (for the most part) completely general to modes driven through a field [103, 104, 105]. For example, from the optomechanical perspective, the Hamiltonian often begins with that of two single modes, a cavity mode and a

[1] An English translation of the proceedings given by Einstein can be found at http://physics.ucsc.edu/~ccrummer/radal.pdf

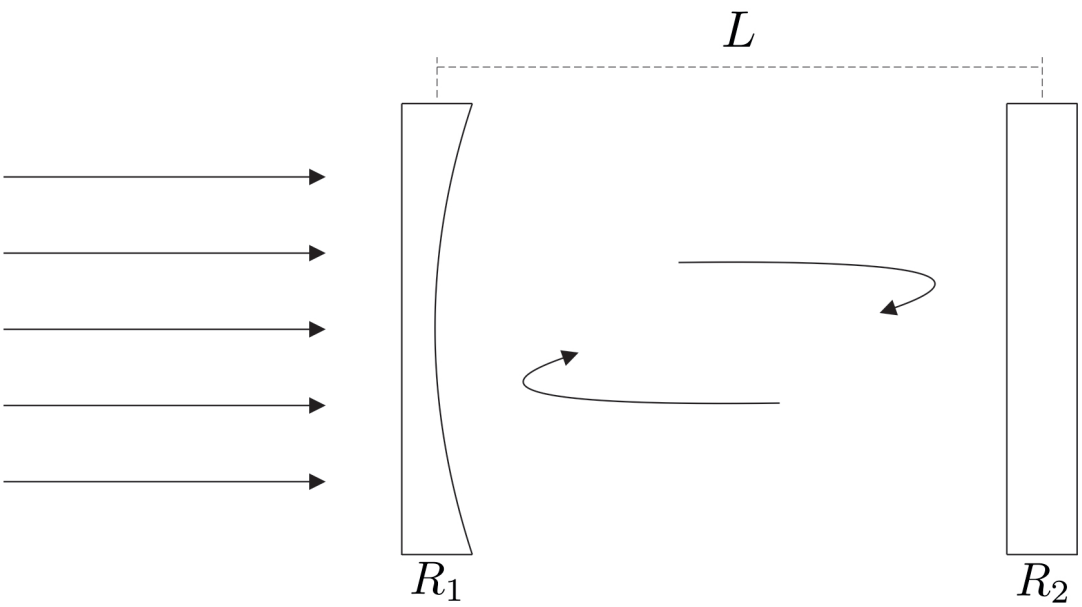

FIGURE 4.1: A basic Fabry-Perot inferetometer, consisting of two mirrors of reflectivity R_1 and R_2 separated by a distance L being illuminated by light

phonon mode, and a laser drive Hamiltonian. There is, however, nothing distinguishing about this. It is equally general to assume the two single modes are, in the case of this thesis, a magnon mode and a phonon mode, and the laser drive Hamiltonian can be considered as that of a microwave field drive. This only amounts to a redefinition of the creation and annihilation operators, but the form of the Hamiltonian remains the same. As the vast majority of review papers and proposals are based on the perspective of optomechanics, it is natural to follow this interpretation of the maths.

4.1 Classical Descriptions of a Cavity

While the form of the experimental set-up may be different (notably, the geometry and the force through which the systems are coupled), all systems of coupled oscillators can be unified under a mathematical description. To this end, illustrated here is this concept by considering the description of a classical cavity. This cavity takes the form of a Fabry-Perot inferetometer, which is depicted in Fig. 4.1. A Fabry-Perot inferetometer is formed by two highly reflective plane-parallel mirrors, separated by a distance L. If one of the mirrors is illuminated with monochromatic laser light, the cavity becomes populated with photons. For such a cavity, the wavelengths that are supported by the mirrors are given by

$$\lambda_{\text{cav}} = \frac{2L}{m}, \tag{4.1}$$

where m is the mode number. Note that the polarisation of the photons has been ignored, which only acts to introduce a multiplicative constant and has no bearing on the nature of the physics. With these mirrors, there are a series of supported angular frequencies at resonance given by

$$\omega_{\text{cav}} = \frac{\pi m c}{L}, \tag{4.2}$$

where c is the speed of light through the medium between the two mirrors (in most cases this is either vacuum or air). The separation between these angular frequencies is trivially

$$\Delta_{\text{cav}} = \frac{\pi c}{L}. \tag{4.3}$$

While the mirrors are of high-reflectivity, this reflectivity is not infinite. Consequently, photons may be 'lost' from the cavity through the mirrors. In addition to this, photons in the cavity are absorbed by the mirrors, as well as having the potential to scatter out of the cavity. These effects result in the loss of photons, defined as a photon intensity decay rate, κ.

Given that a portion of this decay rate is intrinsic to the cavity, cavities are often characterised by a quality factor, denoted by Q. First, consider the photon lifetime, denoted τ, which is conceptually thought of as the 'average' time in which a photon 'exists' within the cavity, and is given as the reciprocal of the decay rate. Then, the cavity Q-factor may be expressed as

$$Q_{\text{cav}} = \omega_{\text{cav}}\tau = \frac{\omega_{\text{cav}}}{\kappa} \tag{4.4}$$

A larger Q implies that photons have a longer lifetime, and it is preferential to have as large a Q as is possible. Another useful parameter in characterising cavities is the optical finesse, given by

$$\mathcal{F} = \frac{\Delta_{\text{cav}}}{\kappa} \tag{4.5}$$

which quantifies an average number of 'round trips' before the photon leaves the cavity. A high finesse cavity has a long photon lifetime within the cavity.

As part of the cavity decay rate is intrinsic to the cavity itself, it is instructive to separate it into two components. These components are κ_{ex}, a contribution which includes the input and output coupling into the cavity via lasing, and κ_0, a contribution which includes the internal intrinsic losses of the system. In the case of a cavity with high Q, the relation between these is

$$\kappa = \kappa_{\text{ex}} + \kappa_0. \tag{4.6}$$

For the Fabry-Perot cavity of this discussion, κ_{ex} would be attributed to the loss-rate at the input mirror, and κ_0 is attributed to internal losses (absorption, scattering, and transmission at the second mirror).

4.2 The Interaction of Light with Matter

Optomechanics performed using a Fabry-Perot cavity may be interpreted using radiation pressure. Considered still is the case of a Fabry-Perot resonator, but one of the mirrors is suspended such that it is free to oscillate. Following from quantum theory, it is known that light carries momentum, p, determined by

$$\mathbf{p} = \hbar\mathbf{k} \tag{4.7}$$

where $\hbar$ is the reduced Planck's constant, and k is the wavevector of the photons. As the light circulates in the cavity, a momentum transfer occurs at each reflection from the end mirrors, imparting a momentum

$$\Delta p = 2\hbar k \tag{4.8}$$

to the mirror. In everyday life, this effect is minuscule and is virtually undetectable. However, when the mirror masses are very small (and hence the momentum transfer becomes appreciable), and when the number of photons impinging on the mirror is large, the effect can become influential.

It is important to note that this effect does not simply accumulate and consistently move the suspended mirror away and elongate the cavity ad infinitum. The effect that the movement of the suspended mirror has on the photons within the cavity must be taken into account. As the mirror is displaced, the cavity length changes and with this is a change in the resonant angular frequency of the cavity. Due to this, the detuning

$$\Delta = \omega_{\mathrm{L}} - \omega_{\mathrm{cav}} \tag{4.9}$$

of the driving laser with the cavity frequency is changed, which determines the population of the cavity. At smaller detunings, more light is able to enter the cavity as it is closer to the resonant angular frequency of the cavity. However, as this detuning grows, the radiation pressure falls as light is unable to enter, and the mirror begins to return to the original position, again, changing the resonant cavity angular frequency. Thus, it is seen that the radiation pressure is dependant on the mirror displacement.

4.3 Hamiltonian formulation of coupling

The Hamiltonian of a system of electromagnetic radiation interacting with a vibrational mode of an oscillator [106, 107] can be each be represented as simple harmonic oscillators at their respective frequencies, written as

$$\mathcal{H} = \hbar\omega_{\mathrm{cav}}\hat{a}^{\dagger}\hat{a} + \hbar\omega_{\mathrm{R}}\hat{b}^{\dagger}\hat{b} \tag{4.10}$$

where $\hat{a}^{\dagger}$ $(\hat{a})$ and $\hat{b}^{\dagger}$ $(\hat{b})$ are the creation (annihilation) operators for the photon and phonon modes, respectively. Introducing the fact now that the end mirror of the cavity is suspended and hence free to move, the cavity frequency may be expanded as a function of displacement to find the approximation

$$\omega_{\mathrm{cav}}(x) \approx \omega_{\mathrm{cav}} + x\frac{\partial\omega_{\mathrm{cav}}}{\partial x} + \ldots \tag{4.11}$$

where for most optomechanical systems it is sufficient to retain only linear terms in the displacement. Substitution of this into the harmonic oscillator Hamiltonian of the cavity finds

$$\hbar\omega_{\mathrm{cav}}(x)\hat{a}^{\dagger}\hat{a} \approx \hbar\left(\omega_{\mathrm{cav}} + \hat{x}\frac{\partial\omega_{\mathrm{cav}}}{\partial x}\right)\hat{a}^{\dagger}\hat{a} \tag{4.12}$$

where the displacement has been promoted to the quantum version

$$\hat{x} = x_{\mathrm{ZPF}}\left(\hat{b} + \hat{b}^{\dagger}\right). \tag{4.13}$$

with $x_{\mathrm{ZPF}} = \sqrt{\hbar/2m_{\mathrm{eff}}\omega_{\mathrm{R}}}$ as the zero-point fluctuation of the oscillator of effective mass m_{eff}. Introduced now is the single photon-phonon coupling rate,

$$g_0 = \frac{\partial\omega_{\mathrm{cav}}}{\partial x}x_{\mathrm{ZPF}} \tag{4.14}$$

such that the optomechanical Hamiltonian can be written

$$\mathcal{H}_{\mathrm{OM}} = \hbar\omega_{\mathrm{cav}}\hat{a}^\dagger\hat{a} + \hbar\omega_R\hat{b}^\dagger\hat{b} - \hbar g_0\hat{a}^\dagger\hat{a}\left(\hat{b}+\hat{b}^\dagger\right) = \mathcal{H}_0 + \mathcal{H}_{\mathrm{int}} \tag{4.15}$$

where g_0 quantifies the strength of the interaction between a single phonon with a single photon. In this description, it has been assumed the Hamiltonian is simply modelled as two harmonic oscillators. This, however, does not encapsulate all aspects of the physics, and the full Hamiltonian will also include the frictional effects in moving the mirror, thermal creation of phonons, photon decay, and driving forces. These effects are most easily described using input-output formalism.

It is convenient when discussing the optical modes to transform to a rotating frame at the laser frequency, ω_{L}. To do so, a transformation $\hat{U} = \exp\left(i\omega_{\mathrm{L}}\hat{a}^\dagger\hat{a}t\right)$is applied, such that

$$\hat{U}\left(\hat{a}^\dagger\exp\left(-i\omega_{\mathrm{L}}t\right) + \hat{a}\exp\left(i\omega_{\mathrm{L}}t\right)\right)\hat{U}^\dagger = \hat{a}^\dagger + \hat{a}. \tag{4.16}$$

This then generates a new Hamiltonian [108]

$$\mathcal{H} = \hat{U}\mathcal{H}_{\mathrm{old}}\hat{U}^\dagger - i\hbar\hat{U}\frac{\partial\hat{U}^\dagger}{\partial t}, \tag{4.17}$$

where $\mathcal{H}_{\mathrm{old}}$ is the Hamiltonian in the non-rotating frame. It may then be shown

$$\hat{U}\mathcal{H}_{\mathrm{old}}\hat{U} = \hbar\omega_{\mathrm{cav}} + \hbar\omega_{\mathrm{R}}(\hat{b}^\dagger\hat{b}) - \hbar g_0\hat{a}^\dagger\hat{a}\left(\hat{b}+\hat{b}^\dagger\right), \qquad -i\hbar\frac{\partial\hat{U}}{\partial t} = -\hbar\omega_{\mathrm{L}}\hat{a}^\dagger\hat{a}, \tag{4.18}$$

from which, it is found

$$\mathcal{H} = -\hbar\Delta\hat{a}^\dagger\hat{a} + \hbar\omega_{\mathrm{R}}\hat{b}^\dagger\hat{b} - \hbar g_0\hat{a}^\dagger\hat{a}\left(\hat{b}+\hat{b}^\dagger\right) \tag{4.19}$$

where the detuning is defined as $\Delta = \omega_{\mathrm{L}} - \omega_{\mathrm{cav}}$.

4.4 Input-Output Theory

The internal dynamics of a cavity coupled to electromagnetic radiation in a quantum mechanical description can be achieved in using master equations [109]. However, if the fields being emitted or reflected are of interest, then it is necessary to use a formalism known as input-output theory [110, 111], stemming from the Heisenberg equation of motion [108]. Input-output theory describes the time-evolution of a quantum operator and considers the quantum fluctuations introduced from a coupling port into the cavity. The quantum fluctuations constantly replenish the photon amplitude, which is known to decay at the rate $\kappa/2$. The resulting Heisenberg-Langevin equation for the cavity amplitude being driven by a laser is found as

$$\frac{\mathrm{d}\hat{a}}{\mathrm{d}t} = -\frac{i}{\hbar}\left[\hat{a},\mathcal{H}\right] - \frac{\kappa}{2}\hat{a} - \sqrt{\kappa}\hat{a}_{\mathrm{in}} \tag{4.20}$$

where $\mathcal{H}$ is the Hamiltonian of the system, the second term represents a linear damping of the cavity due to photon leakage, and the third term describes the driving of the cavity due to noise from the bath, (where it is normalised $\hat{a}_{\mathrm{in}}^\dagger\hat{a}_{\mathrm{in}}$ is the photon number flux such that $\hat{a}_{\mathrm{in}}$ is in units of $\frac{1}{\sqrt{\mathrm{time}}}$). In the case where there is no coupling

in the system, it is found that [2]

$$\dot{\hat{a}} = -\frac{\kappa}{2}\hat{a} + i\Delta\hat{a} + \sqrt{\kappa_{ex}}\hat{a}_{in} + \sqrt{\kappa_0}\hat{f}_{in} \tag{4.21}$$

where $\hat{f}_{in}$ denotes the mechanical dissipation associated with the decay rate κ_0. The field that is reflected by the cavity is found as

$$\hat{a}_{out} = \hat{a}_{in} - \sqrt{\kappa_{ex}}\hat{a}. \tag{4.22}$$

Focusing not on the operators, but instead their classical average quantities, then Eq. 4.21 and Eq. 4.22 can be solved, where $\langle f_{in} \rangle = 0$, to find

$$\langle \hat{a} \rangle = \frac{\sqrt{\kappa_{ex}}\,\langle \hat{a}_{in} \rangle}{\frac{\kappa}{2} - i\Delta}. \tag{4.23}$$

The steady-state photon population is then

$$\bar{n}_{cav} = |\langle \hat{a} \rangle|^2 = \frac{\kappa_{ex}}{\Delta^2 + (\frac{\kappa}{2})^2}\frac{P}{\hbar\omega_L} \tag{4.24}$$

where the parameter, P, is the input power launched into the cavity by the laser, with

$$P = \hbar\omega_L \bar{n}_{cav} = \hbar\omega_L\,|\langle \hat{a}_{in} \rangle|^2 \tag{4.25}$$

4.5 Operator equations of motion

Mechanical motion induces a shift to the optical mode resonance frequency, altering the intensity of the light in the cavity, and hence inducing a radiation pressure force on the motion. As the decay rate of the cavity introduce a delay between the motion and changes in the force, this is known as *dynamical back-action*.

To analyse dynamical back-action, again the formalism of input-output theory is adopted. Both the cavity field amplitude, $\hat{a}$, and the mechanical field amplitude, $\hat{b}$, are driven by the thermal noise entering the system. Their time evolution can be described by quantum Heisenberg-Langevin equations of the form

$$\frac{d\hat{a}}{dt} = -\frac{\kappa}{2}\hat{a} + i\left(\Delta + G\hat{x}\right)\hat{a} + \sqrt{\kappa_{ex}}\hat{a}_{in} + \sqrt{\kappa_0}\hat{f}_{in}, \tag{4.26}$$

$$\frac{d\hat{b}}{dt} = \left(-i\omega_R - \frac{\Gamma_R}{2}\right)\hat{b} + ig_0\hat{a}^\dagger\hat{a} + \sqrt{\Gamma_R}\hat{b}_{in} \tag{4.27}$$

where it is defined κ_{ex} as the coupling into the cavity, κ_0 as the overall decay rate of the cavity, and Γ_R as the mechanical damping.

The classical averaged versions of these equations may also be given by assuming $\alpha(t) = \langle \hat{a}(t) \rangle$ and $x(t) = \langle \hat{x}(t) \rangle$, from which the amplitudes of the light and oscillator can be written, as

$$\frac{d\alpha}{dt} = -\frac{\kappa}{2}\alpha + i\left(\Delta + Gx\right)\alpha + \sqrt{\kappa_{ex}}\alpha_{in} \tag{4.28}$$

$$m_{eff}\frac{d^2x}{dt^2} = -m_{eff}\omega_R^2 x - m_{eff}\Gamma_R\frac{dx}{dt} + \hbar G\,|\alpha|^2 \tag{4.29}$$

where fluctuations have been neglected as a result of the averaging. Note that, to obtain Eq. 4.29, one is writing the equation of motion for the displacement of a damped simple harmonic oscillator with an additional coupling term into the system $\hbar G\bar{n}_{\mathrm{cav}}$.

The equations of motion, Eq. 4.26 and Eq. 4.27, are non-linear as they contain products of the mechanical oscillator amplitude and the cavity field, or the radiation pressure force (proportional to the photon number) that is quadratic in the photon operators. As such, there is no exact solution to these, either analytically or numerically. These can, however, be linearised about a fluctuation by again using $\hat{a} = \alpha + \delta\hat{a}$. Keeping only terms that are linear, the fluctuations may be expressed as

$$\frac{d\delta\hat{a}}{dt} = \left(i\Delta - \frac{\kappa}{2}\right)\delta\hat{a} + ig\left(\hat{b} + \hat{b}^{\dagger}\right) + \sqrt{\kappa_{\mathrm{ex}}}\delta\hat{a}_{\mathrm{in}} + \sqrt{\kappa_0}\hat{f}_{\mathrm{in}}, \tag{4.30}$$

$$\frac{d\hat{b}}{dt} = \left(-i\omega_{\mathrm{R}} - \frac{\Gamma_{\mathrm{R}}}{2}\right)\hat{b} + ig\left(\delta\hat{a} + \delta\hat{a}^{\dagger}\right) + \sqrt{\Gamma_{\mathrm{R}}}\hat{b}_{\mathrm{in}}. \tag{4.31}$$

The coupling between the optical and vibrational degrees of freedom are now linear, with the strength determined by the field-enhanced coupling rate $g = g_0\sqrt{\bar{n}_{\mathrm{cav}}}$. These equations are often the starting point for describing coupled quantum systematic phenomena, including cooling, normal-mode splitting, and amplification. For the classical regime of the equations, 4.28 and 4.29, the linearisation process can be applied. In this, notation is simplified with $a = \langle\hat{a}\rangle$ and $x = \langle\hat{x}\rangle$ and find for the linearisation process

$$\frac{\mathrm{d}\delta a}{\mathrm{d}t} = \left(i\Delta - \frac{\kappa}{2}\right)\delta a + iGax, \tag{4.32}$$

$$m_{\mathrm{eff}}\frac{\mathrm{d}^2x}{\mathrm{d}t^2} = -m_{\mathrm{eff}}\omega_{\mathrm{R}}^2x - m_{\mathrm{eff}}\Gamma_{\mathrm{R}}\frac{\mathrm{d}x}{\mathrm{d}t} + \hbar G\left(a^*\delta a + a\delta a^*\right). \tag{4.33}$$

There is also an associated form of these equations expressed in frequency space, whereby $\hat{b}\left[\omega\right]$ and $\delta\hat{a}\left[\omega\right]$ represent the Fourier transforms of the operators $\hat{b}$ and $\delta\hat{a}$ respectively. In this formalism, differentiation produces a prefactor of $-i\omega$ and the substitution for the Fourier components produces the equations finding

$$-i\omega\delta a\left[\omega\right] = \left(i\Delta - \frac{\kappa}{2}\right)\delta a\left[\omega\right] + iGax\left[\omega\right], \tag{4.34}$$

$$-m_{\mathrm{eff}}\omega^2x\left[\omega\right] = -m_{\mathrm{eff}}\omega_{\mathrm{R}}^2x\left[\omega\right] - i\omega m_{\mathrm{eff}}\Gamma_{\mathrm{R}}x\left[\omega\right] + \hbar G\left(a^*\delta a\left[\omega\right] + a(\delta a^*)\left[x\right]\right). \tag{4.35}$$

where $(\delta a^*) = \delta a\left[-\omega\right]^*$.

4.6 Strong coupling and normal mode splitting

When the cavity-enhanced coupling rate approaches the decay rate of the system, $g \sim \kappa$, it will be observed that new features appear as a consequence of the Hamiltonian. This regime is referred to as the strong coupling regime. In this, the driven optical mode (in analogy to magnon mode) and the mechanical mode hybridise to form two new modes, whereby the splitting between the two modes is given by $2g$.

The transition to the strong coupling regime is fully described by the equations of motion. If the redefinitions $\Delta \equiv \Delta + i\kappa/2$ and $\omega_{\mathrm{R}} \equiv \omega_{\mathrm{R}} - i\Gamma_{\mathrm{R}}$ are made, then the eigenvalues of the matrix describing the relation between the time-derivatives of the averages (ie. $\langle\delta\dot{\hat{a}}\rangle$ such that the noise fluctuations can be neglected) and the averages

themselves are found as

$$\omega_{\pm} = \frac{-\Delta + i\left(\kappa + \Gamma_R\right) + \omega_R}{2} \pm \sqrt{g^2 + \frac{1}{4}\left(\Delta + i\left(\kappa - \Gamma_R\right) - \omega_R\right)^2}. \tag{4.36}$$

Using the further redefinition $\delta = -\Delta - \omega_R$, it is finally found

$$\omega_{\pm} = \omega_R + \frac{\delta}{2} - \frac{i\left(\kappa + \Gamma_R\right)}{2} \pm \sqrt{g^2 + \left(\frac{\delta + i\left(\Gamma_R - \kappa\right)}{2}\right)^2} \tag{4.37}$$

At resonance $\Delta = -\omega_R$ and hence $\delta = 0$. Making the assumption $\kappa >> \Gamma_R$, which for most realisations of interest will be true, then this reduces the form of the eigenvalues to

$$\omega_{\pm} = \omega_R - i\frac{\kappa}{2} \pm \sqrt{g^2 - \left(\frac{\kappa}{2}\right)^2}. \tag{4.38}$$

At the threshold $g = \kappa/2$, the roots change from purely imaginary to real valued, corresponding to the transition into the strong coupling regime.

4.7 Dynamical backaction

In the event that the light force reacts immediately to the mechanical motion, then the equilibrium position is shifted and a new 'effective' spring constant is produced[81]. At large enough intensities, it can be the case that the potential added by the light force means that it may develop into a double potential well, leading to what is referred to as static bistability [112]. This typically occurs at detunings corresponding to cooling, which provides a limit to the achievable temperatures in the regime $\kappa >> \omega_R$.

Considering dynamical effects, for which $\kappa << \omega_R$ and referred to the 'resolved sideband' regime, then Eq. 4.34 and Eq. 4.35 are used as the starting points. To begin with, consider the response of an oscillator in the absence of any coupling into the system. In such a circumstance, the mechanical oscillator has a mechanical susceptibility expressed as [66]

$$\mathcal{X}^{-1}\left(\omega\right) = m_{\text{eff}}\left(\left(\omega_R^2 - \omega^2\right) - i\Gamma_R\omega\right) \tag{4.39}$$

which produces the familiar Lorentzian response of mechanical oscillators driven at a variable frequency, ω. In the event that there were to exist coupling into the system, then there is a related shift to the susceptibility which encompasses the effect of the coupling on the oscillations. This can be expressed

$$\mathcal{X}_{\text{eff}}^{-1}\left(\omega\right) = \mathcal{X} + \Sigma\left(\omega\right). \tag{4.40}$$

By solving Eq. 4.34 and Eq. 4.35, it will be shown that the susceptibility then has a modification [113] as

$$\Sigma\left(\omega\right) = 2m_{\text{eff}}\omega_R^2 g^2\left(\frac{1}{\left(\Delta + \omega\right) + i\kappa/2} + \frac{1}{\left(\Delta - \omega\right) - i\kappa/2}\right) \tag{4.41}$$

which encompasses the coupling, where $g = g0\sqrt{\bar{n}_{\text{cav}}}$. It is often defined [2] that

$$\Sigma\left(\omega\right) \equiv m_{\text{eff}}\omega\left(2\delta\omega_R\left(\omega\right) - i\Gamma_c\right) \tag{4.42}$$

where Γ_c is the additional coupling-provided damping. With this redefinition, it is then found

$$\delta\omega_R(\omega) = \frac{\mathrm{Re}\Sigma(\omega)}{2\omega m_{\mathrm{eff}}} = g^2\frac{\omega_R}{\omega}\left(\frac{\Delta+\omega}{(\Delta+\omega)^2+(\kappa/2)^2} + \frac{\Delta-\omega}{(\Delta-\omega)^2+(\kappa/2)^2}\right) \tag{4.43}$$

$$\Gamma_c = \frac{\mathrm{Im}\Sigma(\omega)}{m_{\mathrm{eff}}} = g^2\frac{\omega_R}{\omega}\left(\frac{\kappa}{(\Delta+\omega)^2+(\kappa/2)^2} - \frac{\kappa}{(\Delta-\omega)^2+(\kappa/2)^2}\right) \tag{4.44}$$

which are also valid for the strong coupling regime. The term $\delta\omega_R$ leads to an effect known as the optical spring effect, in which the mechanical oscillator is either spring softened or hardened depending on the detuning of the laser. A complete discussion of the optical spring effect and its uses is lengthy and does not represent the sole interest of this thesis; the interested reader to literature [114, 115].

Assuming that $\omega = \omega_R$, then the coupling damping rate is expressed

$$\Gamma_c = g^2\left(\frac{\kappa}{(\Delta+\omega_R)^2+(\kappa/2)^2} - \frac{\kappa}{(\Delta-\omega_R)^2+(\kappa/2)^2}\right) \tag{4.45}$$

from which the full effective damping of the oscillator is found as the sum of the mechanical damping, Γ_m, and the coupling-provided damping. As the optical damping rate can be negative or positive depending on the detuning, the damping of the oscillator can either be decreased, leading to cooling, or increased, leading to heating. Considering this equation only in the resolved sideband regime, then a further simplification can be made. The function has maxima and minima at the sidebands (i.e. $\Delta = \pm\omega_R$), from which the maximum cooling rate can be approximated as

$$\Gamma_c = \frac{4g^2}{\kappa}. \tag{4.46}$$

Chapter 5

Thin-film magnon-phonon coupling

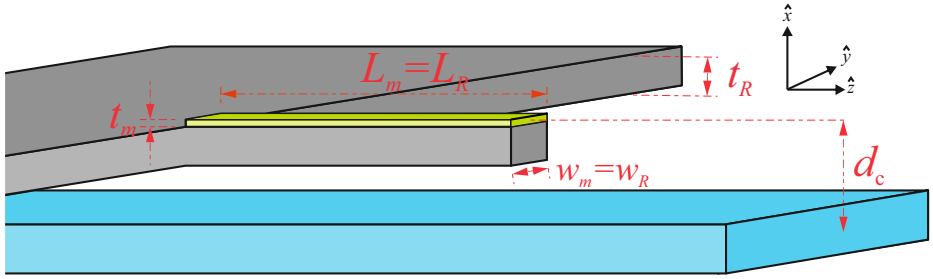

FIGURE 5.1: A basic pictorial representation of the device proposed. The device consists of a YIG thin film, shown in yellow, deposited on-top of a functionalised GGG substrate, shown in grey, whereby the substrate has been manufactured as a cantilever cleaved from and still attached to the bulk GGG, forming a chip. This YIG on this chip is then a distance d_c above a superconducting transmission line, shown in blue.

While the current experimental proposal for magnomechanics presents coherent coupling in a hybrid magnon-photon-phonon system, the achieved magnon-phonon cooperativity is only of order unity, and the device has a large footprint due to the use of a cavity preventing on-chip designs. To this end, it is proposed within this thesis an alternative approach to the device design inspired by a number of recent technological advances.

The strong coupling between magnetic and photonic systems was hypothesised and explored by Soykal *et al.* [116, 117], in which they theoretically investigated the interaction of a nanomagnet with a single photonic mode inside a cavity. In these works, they predicted the feasibility of a strong interaction between light and matter, made possible by a high spin density. A significant experimental work came from Zhang *et al.* [19], in which they demonstrated such a light-matter hybrid system, and showed the strong interaction between a magnetic and photonic system by placing a mm-sized YIG sphere at the maximal point in a photonic cavity's field. The primary findings in this work was to demonstrate ultrastrong coupling, and find a cooperativity between their systems of $\mathcal{C} = 12600$. Other notable works came from Li *et al.* [118], in which they further reduced the size of the magnet, taking the number of spins from 10^{17}, as demonstrated by Zhang, to 10^{13}. To do this, they utilised a permalloy stripe of dimensions 500 μm by 8 μm by 50 nm above a niobium superconducting co-planar waveguide, electrically isolated by a MgO layer. With this, it was seen that strong coupling could be attained, and that cooperativities of 160 were achieved. In a similar work, Hou *et al.* [119] also used a superconducting CPW and

a permalloy stripe of dimensions 900 μm by 14 μm by 30 nm, and achieved a cooperativity of 68. While these cooperativies obtained are some two orders of magnitude lower than those attained by Zhang, they represented significant progress to utilising on-chip devices with dimensions being brought to the micro-scale. While strong magnon-cavity photon realisations form a cornerstone of the field [19] utilising YIG spheres and copper cavities, the recent advances using superconducting co-planar wave-guides allow for strong magnon-photon coupling with overall footprints of devices on the order of hundreds of nanometers [120] and circumvents the need for a physical cavity. The required pre-cooling of these waveguides to exhibit their superconducting nature could be employed as a benefit in using the device for ground state cooling. Similar developments have been made in the field of nanofabrication, where the deposition of YIG films that are on the order of tens of to hundreds of nanometers in width [121, 122] are shown to have similarly low damping to that of bulk YIG, as well as recent works showing the possibility of milling YIG films into micron-sized YIG cantilevers [123, 124] and bridges [125] and retaining sufficiently low Gilbert damping. These developments ground this proposal in reality.

Consider a GGG substrate which has been functionalised into geometry that presents a beam free to resonate. This beam may either be in the configuration of a bridge, in which both ends of the beam remain connected to the bulk of substrate, or that of a cantilever in which only one end of the beam is connected to the bulk of the substrate. This beam has dimensions $L_R > w_R \gtrsim t_R$ for the length, width and thickness of the beam respectively, and the cross-sectional area these dimensions form is assumed to be either rectangular or isosceles which should be geometries easy to fabricate given available processes. Deposited onto the top-most surface of the beam is a YIG film which has dimensions $L_m \gtrsim w_m >> t_m$, as the length, width, and thickness of the film respectively. Clearly, with the geometry of the beam it is required $L_m \leq L_R$. An additional constraint is made on the width of the magnetic film (although one that is not necessarily fundamental to the device) and restrict considerations to a geometry which imposes $w_m = w_R$ as the smaller of the two lateral dimensions of the resonator. The case $L_m = L_R$ is then the case in which the the surface of the beam is entirely covered the the YIG thin film. In the case that $L_m < L_R$, the central position of the magnetic thin film can be varied, provided that the full extent of the thin film remains on the beam and has a strain profile as the beam-film complex undergoes flexural motion. The nanostructure is a central distance d_c (that is, from the centre of the transmission line to the centre of the magnetic structure) above a superconducting transmission line used to excite the Kittel mode of the magnetic structure. This transmission line is assumed to be sufficiently long compared to the length of the nanostructure such that any edge effects to the magnetic field can be neglected. A biasing field of H_e is applied along the length of the film, assumed to be sufficiently strong so as to saturate the magnetic structure along it's length. This device is shown in Fig. 5.1, where the specific case of the cantilever is depicted.

Thin film YIG has an exceptionally low coercivity, with values reported < 1 Oe [126], meaning that small biasing fields can be used to produce a saturated magnetisation state, a requirement necessary for compatibility with superconducting wave-guides to avoid the breakdown field. It is also achievable to attain a saturation magnetisation of $4\pi M_s \approx 1750$ Oe with these thin film configurations [127], comparable to that of bulk YIG. Thin film YIG grown on GGG substrates are also known to exhibit low magnetic damping, with reported values of $\alpha \sim 10^{-4} - 10^{-5}$ at room temperature in literature for films of thicknesses of tens of, to hundreds of, nanometers [12, 128, 129], with thicker films generally showing a lower damping

[130]. In this work, it is preferential to have films in the sub-100 nm thickness region in functionalising thin films [131]; while this is not something that is explicitly considered within this thesis, it is evidently a novelty of the device that the current magnomechanical device set-up cannot present. As YIG is a popular material used for spintronic purposes [132], the device presented within has the scope to be easily incorporated in current spintronic designs. With this in mind, the thin film of YIG is taken to be composed of 25 atomic layers (where one atomic layer has lattice constant $a_0 = 12.376$Å), corresponding to a nominal thickness of ~ 31 nm, and estimate the damping of this film as $\alpha = 10^{-4}$ in line with current literature. Note, however, that films grown to 3.7 nm have exhibited damping at this same order of magnitude [133]. in recent years. YIG is well-suited over other magnetic materials for magnomechanical applications due to its high spin density (required for appreciable magnon-photon coupling), its insulating properties (providing a playground for purely magnetoelastic coupling), its low damping (making realising strong coupling easier over other materials), and progress with manufacturing enabling ultra-thin films (required to ignore the effect of an elastic interface).

The elastic properties of GGG have been determined by Graham and Chang [134], in which they found for the elastic moduli $c_{11} = 2.857 \times 10^{12}\,\mathrm{dyne/cm^2}$, $c_{12} = 1.148 \times 10^{12}\,\mathrm{dyne/cm^2}$, and $c_{44} = 0.902 \times 10^{12}\,\mathrm{dyne/cm^2}$. Calculating the elastic anisotropy parameter given in Eq. 3.63, a value of $A_{\mathrm{GGG}} = 1.056$ is found for the crystal. As such, the crystallographic orientation of the GGG crystal structure with respect to the orientation of the beam axes is of little consequence, and the crystal can be considered elastically isotropic. With this, the Young's modulus of the structure is estimated as $E_{\mathrm{GGG}} \approx 2.2 \times 10^{12}\,\mathrm{dyne/cm^2}$. The Poisson ratio of the material can also be determined from these constants, and with these a value of $\nu_{\mathrm{GGG}} = c_{12}/(c_{11} + c_{12}) = 0.287$ is found. Similarly, the elastic properties of YIG have been determined by Clark and Strakna [135] (with more recent ab initio studies in good agreement [136]). It was found for the elastic modulii $c_{11} = 2.69 \times 10^{12}\,\mathrm{dyne/cm^2}$, $c_{12} = 1.08 \times 10^{12}\,\mathrm{dyne/cm^2}$, and $c_{44} = 0.764 \times 10^{12}\,\mathrm{dyne/cm^2}$. Calculating again the elastic anisotropy parameter, one finds a value $A_{\mathrm{YIG}} = 0.95$, which again can be roughly interpreted as elastic isotropy. Then, the Young's modulus is $E_{\mathrm{YIG}} \approx 2.10 \times 10^{12}\,\mathrm{dyne/cm^2}$ and a Poisson ratio of $\nu_{\mathrm{YIG}} = 0.286$.

There are numerous works that measure the strength of the magnetoelastic interaction in YIG through a variety of techniques [137, 138, 139], from which it is possible to determine the magnetoelastic constants. To date, the most often used measurements of the magnetoelastic constants are determined as $B_1 = 3.48 \times 10^6\,\mathrm{erg/cc}$ and $B_2 = 6.96 \times 10^6\,\mathrm{erg/cc}$ at room temperature [139, 140], which puts the strength of this interaction weaker than those of other garnet structures [141].

While direct measurements of the Q-factor of beam-like devices fabricated from GGG do not appear in literature, studies have been performed on the attenuation of sound waves in bulk GGG [142, 143, 144]. Specifically, taking the attenuation coefficient of $0.9\,\mathrm{m^{-1}}$ for a 0.418 GHz acoustic wave at a longitudinal speed of $6400\,\mathrm{ms^{-1}}$ [142], one can infer a Q-factor for the bulk crystal as $Q_{\mathrm{bulkGGG}} \approx 10^5$. In functionalising the bulk crystal to a nano-sized device, an impact is expected to the detriment of the Q-factor whereby clamping losses and surface losses become appreciable methods of energy loss within the structure [145]. With this in mind, a value $Q_{\mathrm{GGG}} \approx 10^4$ is taken as a conservative estimate for the Q-factor of a functionalised GGG substrate. Note that the Q-factor of YIG beams fabricated in literature corresponds to roughly $Q_{\mathrm{YIG}} \approx 10^3$ [124], roughly an order of magnitude less than that postulated of the GGG beam.

To preserve the Q-factor of the GGG beam in depositing another elastic layer on

the surface, the geometry of the device must be considered as having the thickness of the magnetic structure much less than that of the elastic resonator ($t_m << t_R$) as the lowest order consideration such that the effect of the elastic interaction between the two layers and the additional mass can be considered negligible. In essence, this is taking the limit that there is no material on the surface which evidently should tend to that of the bare cantilever. However, it has been noted that the coating of mechanical resonators even with a thin layer still impacts the Q-factor [146]. In the study, a coating of gold was deposited onto the top of a silicon dioxide cantilever, of thickness ratio $t_{Au}/t_{SiO_2} \approx 0.1$. This in turn produced a reduction of around 20% in the Q-factor in vacuum conditions (from 500 to 400), and an improvement of around 50% in the Q-factor (from 10 to 25) at atmospheric conditions. It is important to note that the Poisson ratios of SiO_2 and gold are $\nu_{SiO_2} \approx 0.20$ [147] and $\nu_{Au} \approx 0.42$ [148], respectively. These values present a large mismatch in elastic characters of both layers. The elastic characteristics between GGG and YIG, however, are far more similar than those of SiO_2 and gold, and so it would be reasonable to expect these deviations to be less significant. With this, it seems intuitive to take the proposed value of the Q-factor for GGG beam as simply an order of magnitude rather than definitive.

The original research within this Chapter is contained within the following Sections. Sections 5.1.1 and 5.1.2, wherein a simplified Hamiltonian for the spin-waves is obtained alongside the implications in their quantisation. Sec. 5.2 then contains details on the single magnon-phonon coupling rates attainable for cantilever and bridge geometries. Sec. 5.3 then contains research on the influence of the Kittel mode profile, and applies Guslienko's theory of dipolar pinning [149] to determine the relevence of higher order effects. Sec. 5.4 evaluates the coupling of transmission line photons into into the magnon modes in order to determine the number of magnomechanically relevent magnons. Sec. 5.5 is somewhat hybrid, in that it begins with a recap of the types of magnon modes following from literature. It then applies this beginning with an expansion of the characteristic wave-vector in an approach unseen in literature and uses it to estimate the frequency-separation of the next nearest magnon mode and whether a single-mode model is applicable. Lastly, Sec. 5.6 performs optimisation of the theory to determine the largest magnomechanical parameters attainable.

5.1 Quantisation of magnons

To adopt a quantum approach to magnons and write their Hamiltonian as a simple harmonic oscillator, the first required step is to obtain creation and annihilation operators for the Kittel mode. Many of those who have done this step do so using the Fourier transform of the operators [150], wherein to use this Fourier basis they have presupposed that the system is translationally variant. Much of this thesis aims to address the influence of the demagnetisation field whereby a translational invariance cannot be presupposed. Therefore, one is required to make use of a Bogoliubov transformation and proceed with an analysis of the coherent mode to determine the appropriate prefactors in the quantisation.

In disturbing the equilibrium state of a given magnetic moment in a ferromagnet, the moment will process and a spin wave will propagate throughout the crystal. The energy of this spin-wave must be equal to the excitation energy of the crystal that was required to cause the change in orientation of the atomic spin. This energy of an elementary excitation of the spin-wave may be obtained from multiplying it's

frequency, $\omega_{\mathrm{m}}(\mathbf{k})$ by $\hbar$, where the energy

$$\mathcal{E}_{\mathrm{m}}(\mathbf{k}) = \hbar\omega_m(\mathbf{k}) \tag{5.1}$$

can be regarded as the energy of a particle, and the quantity $\mathbf{p} = \hbar\mathbf{k}$ can be regarded as it's momentum. This 'particle' is what is referred to as a magnon. If the excitation energy E_{m} of the ferromagnet is small, then it may be regarded as a sum of energies of each of the individual spin-waves propagating, which is to say it is the sum of the magnon energies

$$E_{\mathrm{m}}\{n\} = \sum_{\mathbf{k}} \hbar\omega_{\mathrm{m}}(\mathbf{k})n(\mathbf{k}).s \tag{5.2}$$

where $n(\mathbf{k})$ is the number of magnons of wave-vector $\mathbf{k}$, and summation is taken over all $\mathbf{k}$.

As is standard in quantum physics, creation and annihilation operators can be introduced to manipulate these 'particles'. Introduced here are the creation operator for a magnon, $c_j^\dagger(\mathbf{k})$, and the annihilation operator for a magnon, $c_j(\mathbf{k})$. These operators create and destroy a magnon of type j and with wave-vector $\mathbf{k}$ and satisfy the standard commutation relations

$$\left[c_j(\mathbf{k}), c_{j'}^\dagger(\mathbf{k}')\right] = \delta_{jj'}\delta(\mathbf{k}-\mathbf{k}'), \qquad \left[c_j(\mathbf{k}), c_{j'}(\mathbf{k}')\right] = 0. \tag{5.3}$$

The Hamiltonian for a magnetically ordered crystal can now be expressed in terms of these magnon creation and annihilation operators. Assuming that the magnons do not interact with each other, then this Hamiltonian has the form

$$\mathcal{H}_{\mathrm{m}} = \sum_{\mathbf{k},j} \hbar\omega_{\mathrm{m},j}(\mathbf{k})c_j^\dagger(\mathbf{k})c_j(\mathbf{k}), \tag{5.4}$$

where the sum is taken over all values of the wave-vector $\mathbf{k}$ and type indices j. The eigenvalues of the operator are then the spin wave energies

$$E_{\mathrm{m}} = \sum_{\mathbf{k},j} \hbar\omega_{\mathrm{m},j}(\mathbf{k})n_j(\mathbf{k}). \tag{5.5}$$

Prior in Sec. 2.2, the Hamiltonian of a ferromagnet was expressed in terms of the atomic-spin operators. Consider now the extension that it is required to express the Hamiltonian in terms of the creation and annihilation operators of magnons. To do so, the work of Holstein and Primakoff [151] is followed, in which they introduced operators $a_l^\dagger$ and a_l that satisfy the commutation relations

$$\left[a_l, a_{l'}^\dagger\right] = \delta_{ll'}. \tag{5.6}$$

and defined a set of operators as

$$\begin{aligned} s_l^+ &= s_l^x + is_l^y = \sqrt{2s}a_l^\dagger\sqrt{1-\frac{a_l^\dagger a_l}{2s}} \\ s_l^- &= s_l^x - is_l^y = \sqrt{2s}\sqrt{1-\frac{a_l^\dagger a_l}{2s}}a_l \\ s_l^z &= -s + a_l^\dagger a_l. \end{aligned} \tag{5.7}$$

These operators, s_l^+ and s_l^-, are the spin raising and lowering operators, and the

operators $a_l^\dagger$ and a_l are bosonic operators. If the number of spins that are excited is small compared to the total number of spins, (i.e. if $a_l^\dagger a_l << s$), then it is possible to approximate

$$\left(1 - \frac{a^\dagger a}{2s}\right) \approx 1. \tag{5.8}$$

Hence, the operators reduce to

$$\begin{aligned} s_l^+ &= s_l^x + i s_l^y \approx \sqrt{2s} a_l^\dagger \\ s_l^- &= s_l^x - i s_l^y \approx \sqrt{2s} a_l \\ s_l^z &= -s + a_l^\dagger a_l, \end{aligned} \tag{5.9}$$

and a single boson excitation flips a spin.

Returning now to Eq. 2.15, and performing substitution for $\mathbf{s}$ from Eq. 5.9, one finds the expression

$$\begin{aligned} \mathcal{H} &= -\frac{1}{2}\mathcal{J} \sum_{l \neq m} \left[\frac{1}{2}\left(s_l^- s_m^+ + s_l^+ s_m^-\right) + s_l^z s_m^z\right] \\ &= -\frac{1}{2}\mathcal{J} \sum_{l \neq m} \left[s a_l a_m^\dagger + s a_l^\dagger a_m - s a_l^\dagger a_l - s a_m^\dagger a_m + a_l^\dagger a_l a_m^\dagger a_m + 2s^2\right]. \end{aligned} \tag{5.10}$$

This Hamiltonian includes terms which implicitly couple spin-sites (terms acting on site l mixed with terms acting on site m), and so any excitation as a result of these operators must be one that is collective. Another consequence of note of this Hamiltonian is that this is not diagonal one. It is therefore necessary to perform a transformation which will result in a diagonalised Hamiltonian to arrive at operators that quantise the spin-waves. This unitary transformation is the Bogolyubov transformation, and can be written in the form [152]

$$\begin{aligned} a(\mathbf{k}) &= u_{\mathbf{k}} c(\mathbf{k}) + v_{\mathbf{k}} c^\dagger(-\mathbf{k}), \\ a^\dagger(\mathbf{k}) &= u_{\mathbf{k}}^* c^\dagger(\mathbf{k}) + v_{\mathbf{k}}^* c(-\mathbf{k}), \end{aligned} \tag{5.11}$$

where $u_{\mathbf{k}}$ and $v_{\mathbf{k}}$ are functions of the wavevector $\mathbf{k}$.

The operators in Eq. 5.9 may be expressed in terms of the reduced magnetisation. Considering the spin magnetic moments for electrons, and taking the magnetic body at saturation, these operators can be written in terms of the fluctuation of the magnetisation as each electron is excited from it's ground state and flipping the orientation of the moment. By inspection of the relation $\mathbf{M} = g_e \mu_B \mathbf{S}$, one may write ladder operators for the fluctuations of the magnetisation from Eqs. 5.9, and find

$$\begin{aligned} \delta m^+ &= \sqrt{\frac{2 g_e \mu_B}{M_s}} a^\dagger, \\ \delta m^- &= \sqrt{\frac{2 g_e \mu_B}{M_s}} a, \\ \delta m_z &= -\frac{g_e \mu_B}{M_s} a^\dagger a, \end{aligned} \tag{5.12}$$

where the subscript l is dropped for breivity. The raising and lowering operators for the x and y components of the fluctuation of the magnetisation are then written as

$$\begin{aligned}\delta m_x &= \frac{1}{2}\left(\delta m^+ + \delta m^-\right) = \sqrt{\frac{g_e \mu_B}{2M_s}}\left(a + a^\dagger\right), \\ \delta m_y &= \frac{1}{2i}\left(\delta m^+ - \delta m^-\right) = i\sqrt{\frac{g_e \mu_B}{2M_s}}\left(a - a^\dagger\right).\end{aligned} \tag{5.13}$$

5.1.1 The Kittel mode Hamiltonian

Beginning here is the presentation of the work performed in order to derive a theory of thin-film magnomechanics. To apply the Bogolyubov transformation for the specific case of the Kittel mode of YIG in such a way that the coefficients of the transformation in Eq. 5.11 are completely determined, it will be necessary to have an approximation for the spin-wave Hamiltonian of the Kittel mode. This Hamiltonian can be obtained by considering the Hamiltonian of a ferromagnet under the assumption of a negligible anisotropy and by ignoring the effect of exchange.

Consider the classical Hamiltonian for a thin plate ferromagnetic body at saturation, with equivalent geometry to the device proposal. To recapitulate, this forms a magnetic structure $L_m > w_m >> t_m$, (and associated volume V_m), laying in the $y-z$ plane, exposed to a saturating bias field $H_e\hat{z}$ which induces an associated demagnetisation field $\mathbf{H}_d$. Within these approximations, the classical Hamiltonian for this can be expressed as the energy associated with bias field and the internal demagnetisation field. This Hamiltonian is found as [59]

$$\mathcal{H}_m = -\int_{V_m} \mathbf{M}\cdot\mathbf{H}_e \, dV - \frac{1}{2}\int_{V_m} \mathbf{M}\cdot\mathbf{H}_d \, dV \tag{5.14}$$

where the first term represents the Zeeman field energy and the second term represents the demagnetisation field energy.

The Kittel mode description adopted in this case amounts to what has been seen in Sec. 2.5. A saturation magnetisation is assumed along the z-axis, with dominant fluctuations of the magnetisation δm_x and δm_y in the x- and y- directions. At this stage, the fluctuations of δm_z are also included along the saturation direction, known to be second order in the fluctuations δm_x and δm_y. Evaluate of the Hamiltonian is then performed under this description of the magnetisation. Note that this Kittel mode description assumes that the fluctuations of the magnetisation do not vary spatially with position inside the magnetic structure which is not something that is implicitly justified for a finite structure. Regardless, this description then expresses the magnetisation as

$$\mathbf{m} = \frac{\mathbf{M}}{M_s} = (0,0,1) + \left(\delta m_x, \delta m_y, \delta m_z\right). \tag{5.15}$$

For the Zeeman field contribution to the Hamiltonian, it is simple to find

$$-M_s\int_{V_m} \mathbf{m}\cdot\mathbf{H}_e \, dV = -M_s H_e V_m\left(1+\delta m_z\right) = -M_s H_e V_m\left(1 - \frac{1}{2}\left(\delta m_x^2 + \delta m_y^2\right)\right). \tag{5.16}$$

The demagnetisation energy contribution is somewhat more laborious. Given that

the ferromagnetic body can be roughly approximated as a prolate ellipsoid, the demagnetisation tensor noted in Sec. 2.3 may be used to express

$$
\begin{aligned}
-\frac{M_\mathrm{s}}{2}\int_{V_\mathrm{m}} \mathbf{m}\cdot\mathbf{H}_\mathrm{d}\,\mathrm{d}V &= \frac{4\pi M_\mathrm{s}^2}{2}\int_{V_m} \mathbf{m}\cdot\left(\hat{N}\cdot\mathbf{m}\right)\,\mathrm{d}V \\
&= \frac{4\pi M_\mathrm{s}^2 V_\mathrm{m}}{2}\left(N_x\delta m_x^2 + N_y\delta m_y^2 + N_z\left(1+\delta m_z\right)^2\right). \qquad (5.17)
\end{aligned}
$$

With the coefficients found in Eq. 2.35, the terms in the demagnetisation evaluate to

$$
\begin{aligned}
2\pi M_\mathrm{s}^2 V_\mathrm{m} N_x \delta m_x^2 &= 2\pi M_\mathrm{s}^2 V_\mathrm{m}\delta m_x^2 \frac{L_\mathrm{m} w_\mathrm{m}}{t_\mathrm{m}\left(L_\mathrm{m}+w_\mathrm{m}\right)+L_\mathrm{m}w_\mathrm{m}} \\
&\approx 2\pi M_\mathrm{s}^2 V_\mathrm{m}\delta m_x^2, \\
2\pi M_\mathrm{s}^2 V_\mathrm{m} N_y \delta m_y^2 &= 2\pi M_\mathrm{s}^2 V_\mathrm{m}\delta m_x^2 \frac{L_\mathrm{m} t_\mathrm{m}}{t_\mathrm{m}\left(L_\mathrm{m}+w_\mathrm{m}\right)+L_\mathrm{m}w_\mathrm{m}} \\
&\approx 2\pi M_\mathrm{s}^2 L_\mathrm{m} t_\mathrm{m}^2 \delta m_y^2, \\
2\pi M_\mathrm{s}^2 V_\mathrm{m} N_z &= 2\pi M_\mathrm{s}^2 V_\mathrm{m} \frac{w_\mathrm{m} t_\mathrm{m}}{t_\mathrm{m}\left(L_\mathrm{m}+w_\mathrm{m}\right)+L_\mathrm{m}w_\mathrm{m}} \\
&\approx 2\pi M_\mathrm{s}^2 w_\mathrm{m} t_\mathrm{m}^2, \\
4\pi M_\mathrm{s}^2 V_\mathrm{m} N_z \delta m_z &= -2\pi M_\mathrm{s}^2 V_\mathrm{m}\left(\delta m_x^2+\delta m_y^2\right)\frac{w_\mathrm{m} t_\mathrm{m}}{t_\mathrm{m}\left(L_\mathrm{m}+w_\mathrm{m}\right)+L_\mathrm{m}w_\mathrm{m}} \\
&\approx -2\pi M_\mathrm{s}^2 w_\mathrm{m} t_\mathrm{m}^2\left(\delta m_x^2+\delta m_y^2\right), \\
2\pi M_\mathrm{s}^2 V_\mathrm{m} N_z \delta m_z^2 &= 2\pi M_\mathrm{s}^2 V_\mathrm{m}\delta m_z^2 \frac{w_\mathrm{m} t_\mathrm{m}}{t_\mathrm{m}\left(L_\mathrm{m}+w_\mathrm{m}\right)+L_\mathrm{m}w_\mathrm{m}} \\
&\approx 2\pi M_\mathrm{s}^2 w_\mathrm{m} t_\mathrm{m}^2 \delta m_z^2.
\end{aligned} \qquad (5.18)
$$

where the geometry $t_\mathrm{m} << L_\mathrm{m}, w_\mathrm{m}$ of the structure has been used to reduce terms in fractions. The full Hamiltonian of a ferromagnetic body exposed to a biasing magnetic field at saturation supporting a spatially homogeneous Kittel mode is then expressed as

$$
\begin{aligned}
\mathcal{H}_\mathrm{m} = &-M_\mathrm{s}H_\mathrm{e}V_\mathrm{m} + 2\pi M_\mathrm{s}^2 w_\mathrm{m} t_\mathrm{m}^2 \\
&+\frac{1}{2}M_\mathrm{s}H_\mathrm{e}V_\mathrm{m}\left(\delta m_x^2+\delta m_y^2\right) + 2\pi M_\mathrm{s}^2 V_\mathrm{m}\delta m_x^2 \\
&+2\pi M_\mathrm{s}^2 L_\mathrm{m} t_\mathrm{m}^2 \delta m_y^2 - 2\pi M_\mathrm{s}^2 w_\mathrm{m} t_\mathrm{m}^2\left(\delta m_x^2+\delta m_y^2-\delta m_z^2\right).
\end{aligned} \qquad (5.19)
$$

In discussing Eq. 5.19, terms that are static in the magnetisation do not contribute to the dynamics of spin-waves - as such, the first line may be neglected. Neglected also are the terms of order t_m^2 since the geometry imposes $t_\mathrm{m} << w_\mathrm{m}, L_\mathrm{m}$. The Hamiltonian of the spatially homogeneous Kittel mode is then

$$
\mathcal{H}_\mathrm{SW} \approx \frac{1}{2}M_\mathrm{s}H_\mathrm{e}V_\mathrm{m}\left(\delta m_x^2+\delta m_y^2\right) + 2\pi M_\mathrm{s}^2 V_\mathrm{m}\delta m_x^2. \qquad (5.20)
$$

5.1.2 Quantisation of the Kittel mode

With the Hamiltonian in Eq. 5.20, the Bogolyubov transformation may be applied to find magnon creation and annihilation operators specific to the Kittel mode. To do so, given that the $c-$numbers are not defined, it is necessary to use a state for which

the evolution is known and apply the Kittel mode Hamiltonian. One such state is the coherent state [108], for which the quantum state has dynamics that follow the evolution of the evolution of the classical state with finite amplitude α_l (for the l-th mode of the LLG equation), such that

$$c_l \left|\alpha_l\right\rangle = \alpha_l e^{-i\omega_\mathrm{m} t} \left|\alpha_l\right\rangle, \qquad c_n \left|\alpha_l\right\rangle = 0 \quad n \neq l \tag{5.21}$$

with

$$\mathcal{H}_\mathrm{SW}\left(\left\langle \delta m_x(t)\right\rangle_l, \left\langle \delta m_y(t)\right\rangle_l\right) = \hbar\omega_l \left|\alpha_l\right|^2 \tag{5.22}$$

where $\left\langle \delta m_{x,y}(t)\right\rangle_l \equiv \langle \alpha_l | \delta m_{x,y}(t) | \alpha_l \rangle$ follows the classical evolution of the state. For the Kittel mode specifically, it may be written

$$\begin{aligned} \langle \alpha_l | c_0^2 | \alpha_l \rangle &= \left(\alpha_l e^{-i\omega_\mathrm{m} t}\right)^2 \\ \langle \alpha_l | c_0^{\dagger 2} | \alpha_l \rangle &= \left(\alpha_l^* e^{i\omega_\mathrm{m} t}\right)^2 \\ \langle \alpha_l | c_0 c_0^\dagger | \alpha_l \rangle &= \langle \alpha_l | c_0^\dagger c_0 + 1 | \alpha_l \rangle = \alpha_l^* \alpha_l + 1 \end{aligned} \tag{5.23}$$

where the specificity of the creation and annihilation operators to the Kittel mode is denoted with a subscript 0. If the transformation in Eq. 5.11 is applied to the operators found in Eq. 5.13, one finds

$$\delta m_{x,0} = \sqrt{\frac{g_\mathrm{e}\mu_\mathrm{B}}{2M_\mathrm{s}}}\left((u_0 + v_0)c_0 + (u_0^* + v_0^*)c_0^\dagger\right), \tag{5.24}$$

$$\delta m_{y,0} = \sqrt{\frac{g_\mathrm{e}\mu_\mathrm{B}}{2M_\mathrm{s}}}\left(-i(u_0 - v_0)c_0 + i(u_0^* - v_0^*)c_0^\dagger\right). \tag{5.25}$$

The classical polarisation of this mode representing it's temporal evolution has already been found in Eq. 2.58, in which it was seen that the x and y fluctuations of the magnetisation oscillate $\pi/2$ out of phase and of different relative amplitudes. One may then write

$$\left\langle \delta m_y^{(+)}(t)\right\rangle_0 = i\sqrt{1 + \frac{4\pi M_\mathrm{s}}{H_\mathrm{e}}}\left\langle \delta m_x^{(+)}(t)\right\rangle_0, \tag{5.26}$$

for the creation terms, and the annihilation terms are instead proportional to $\exp\left(-i\omega_\mathrm{m} t\right)$, seen by complex conjugation. This equation represents the relation between the evolution of the expectation value of the two. With this expression, a relation between v_0 and u_0 can be written such that

$$v_0 - u_0 = \sqrt{1 + \frac{4\pi M_\mathrm{s}}{H_\mathrm{e}}}(u_0 + v_0) = \sqrt{1 + \frac{4\pi M_\mathrm{s}}{H_\mathrm{e}}}A_0 \tag{5.27}$$

where $A_0 = u_0 + v_0$ and is chosen to be real. Substituting 5.27 into Eq. 5.24 one finds

$$\begin{aligned} \delta m_{x,0}^2 &= \frac{g_\mathrm{e}\mu_\mathrm{B}}{2M_\mathrm{s}}\left(A_0 c_0 + A_0^* c_0^\dagger\right)^2, \\ &= \frac{g_\mathrm{e}\mu_\mathrm{B}}{2M_\mathrm{s}}\left(A_0^2 c_0 c_0 + A_0^* A_0\left(2c_0^\dagger c_0 + 1\right) + A_0^{*2} c_0^\dagger c_0^\dagger\right). \end{aligned} \tag{5.28}$$

Using now the relations listed in Eq. 5.23, it can be deduced that

$$\begin{aligned}\langle \delta m_{x,0}(t)^2 \rangle &= \frac{g_e \mu_B}{2M_s} \left(\left(A_0 \alpha_l e^{-i\omega_m t} \right)^2 + A_0^* A_0 \left(2\alpha_l \alpha_l^* + 1 \right) + \left(A_0^* \alpha_l^* e^{i\omega_m t} \right)^2 \right) \\ &= \frac{g_e \mu_B}{2M_s} \left(\left(A_0 \alpha_l e^{-i\omega_m t} + A_0^* \alpha_l^* e^{i\omega_m t} \right)^2 + A_0 A_0^* \right) \\ &= \frac{2 g_e \mu_B}{M_s} A_0^2 \alpha_l^2 \cos^2(\omega_m t) + \frac{g_e \mu_B}{2M_s} A_0^2 \end{aligned} \tag{5.29}$$

where the last term in Eq. 5.29 may be neglected as a static offset. Likewise for $\delta m_{y,0}(t)$, substituting Eq. 5.27 into Eq. 5.25 finds

$$\begin{aligned}\delta m_{y,0}^2 &= -\frac{g_e \mu_B}{2M_s} \left(A_0 \eta c_0 - A_0^* \eta c_0^\dagger \right)^2 \\ &= -\frac{g_e \mu_B \eta^2}{2M_s} \left(A_0^2 c_0 c_0 - A_0^* A_0 \left(c_0 c_0^\dagger + c_0^\dagger c_0 \right) + A_0^{*2} c_0^\dagger c_0^\dagger \right) \end{aligned} \tag{5.30}$$

where it is defined $\eta = \sqrt{1 + 4\pi M_s / H_e}$ for convenience of presentation. Again using the relations in Eq. 5.23, a similar expression is arrived at

$$\begin{aligned}\langle \delta m_{y,0}(t)^2 \rangle &= -\frac{g_e \mu_B \eta^2}{2M_s} \left(\left(A_0 \alpha_l e^{-i\omega_m t} \right)^2 - A_0 A_0^* \left(2\alpha_l \alpha_l^* + 1 \right) + A_0 A_0^* \left(A_0^* \alpha_l^* e^{i\omega_m t} \right)^2 \right), \\ &= -\frac{g_e \mu_B \eta^2}{2M_s} \left(\left(A_0 \alpha_l e^{-i\omega_m t} - A_0^* \alpha_l^* e^{i\omega_m t} \right)^2 - A_0 A_0^* \right), \\ &= \frac{2 g_e \mu_B \eta^2}{M_s} A_0^2 \alpha_l^2 \sin^2(\omega_m t) + \frac{g_e \mu_B \eta^2}{2M_s} A_0^2 \end{aligned} \tag{5.31}$$

where again the last term in Eq. 5.31 is neglected as an offset.

The Hamiltonian of the Kittel mode that was derived in Sec. 5.1.1 may now be used to determine the form of the spin-wave operators. The spin-wave Hamiltonian, evaluated at the expectations of $\langle \delta m_{x,0}(t)^2 \rangle$ and $\langle \delta m_{y,0}(t)^2 \rangle$ must have the relation given in Eq. 5.22 as this is the property of the coherent state. Hence, it is found

$$2 g_e \mu_B V_m A_0^2 \left(\left(\frac{H_e}{2} + 2\pi M_s \right) \cos^2(\omega_m t) + \left(1 + \frac{4\pi M_s}{H_e} \right) \frac{H_e}{2} \sin^2(\omega_m t) \right) = \hbar \omega_m. \tag{5.32}$$

Substitution for the Kittel mode frequency from Eq. 2.57 and taking $t = 0$ finally finds

$$2 g_e \mu_B V_m A_0^2 \left(2\pi M_s + \frac{H_e}{2} \right) = g_e \mu_B H_e \left(1 + \frac{4\pi M_s}{H_e} \right)^{\frac{1}{2}} \tag{5.33}$$

from which it can be infered

$$A_0 = \sqrt{\frac{1}{V_m}} \left(1 + \frac{4\pi M_s}{H_e} \right)^{-\frac{1}{4}}. \tag{5.34}$$

Hence, the fluctuations of the spatially homogeneous Kittel mode are quantised as

$$\begin{aligned}\delta m_{x,0}^{+} &= \sqrt{\frac{\hbar\gamma_{\mathrm{g}}}{2M_{\mathrm{s}}V_{\mathrm{m}}}}\left(1+\frac{4\pi M_{\mathrm{s}}}{H_{\mathrm{e}}}\right)^{-\frac{1}{4}} c_0^{\dagger} \\ \delta m_{y,0}^{+} &= i\sqrt{\frac{\hbar\gamma_{\mathrm{g}}}{2M_{\mathrm{s}}V_{\mathrm{m}}}}\left(1+\frac{4\pi M_{\mathrm{s}}}{H_{\mathrm{e}}}\right)^{\frac{1}{4}} c_0\end{aligned} \tag{5.35}$$

where it is defined $\gamma_{\mathrm{g}} = g_{\mathrm{e}}\mu_{\mathrm{B}}/\hbar$.

5.2 Single magnon-phonon coupling

By expanding the magnetocrystalline anisotropy density as a function of small strains, it has been seen in Sec. 2.4 that the magnetoelastic energy density of a magnetic substrate undergoing strain can be expressed as

$$U_{\mathrm{me}} = B_1\left(m_x^2 u_{xx} + m_y^2 u_{yy} + m_z^2 u_{zz}\right) + B_2\left(m_x m_y u_{xy} + m_x m_z u_{xz} + m_y m_z u_{yz}\right),$$

where B_i is the i-th magnetoelastic constant, m_i is the i-th component of the reduced magnetisation $m_i = M_i/M_{\mathrm{s}}$, and u_{ii} are the components of the Cartesian strain tensor.

Considered here is the application of magnetoelastic energy density to the case of YIG deposited onto an elastic beam such that the single coupling between magnons and phonons can be elucidated. It has been seen in Eq. 3.47 that for a simple Euler-Bernoulli beam there are no shearing strains and so $u_{ik} = 0$ for $i \neq k$ As such, the second term may be neglected in Eq. 2.4. Under the description of the simple spatially homogeneous Kittel mode magnetisation, the magnetoelastic energy density may be split into a static term, denoted $U_{\mathrm{me},0}$, and a fluctuating term, denoted δU_{me}. Substituting the Kittel mode description into the magnetoelatic energy density and retaining terms up to second order in the spin-wave operators, it is found

$$\delta U_{\mathrm{me}} = U_{\mathrm{me}} - U_{\mathrm{me},0} = B_1\left(\delta m_x^2 u_{xx} + \delta m_y^2 u_{yy} + 2\delta m_z^2 u_{zz}\right) \tag{5.36}$$

When considering the coupling between magnons and phonons, only the dynamical term is of consequence and the static magnetoelastic energy density term does not affect the dynamics of the coupling; it may be neglected.

The displacement operator of a single mechanical mode, labelled n, can be expressed as [153, 154]

$$\hat{u}_n = \sqrt{\frac{\hbar}{2\rho\omega_{\mathrm{R}}}}\mathbf{u}_n\left(b_n + b_n^{\dagger}\right) \tag{5.37}$$

where $\mathbf{u}_n = \mathcal{N}\phi_n$ is the n-th mode profile of phonon frequency ω_{R}, ρ is the density of the material, and

$$\mathcal{N}2\int_V \phi^2 = 1. \tag{5.38}$$

Correct to first order of the deflection profile, it is sufficient to say that the displacement profile of a Euler-Bernouilli beam is simply given by the deflection profile [154], given in Eq. 3.88 and Eq. 3.97 for a cantilever and bridge, respectively. The

normalisation for both structures can then be found as

$$\mathcal{N} = \sqrt{\frac{1}{\int_{A_\mathrm{R}} \mathrm{d}A \int_{L_\mathrm{R}} \phi_n^2 \mathrm{d}z}} = \sqrt{\frac{1}{A_\mathrm{R} L_\mathrm{R}}}, \tag{5.39}$$

where A_R is the cross-sectional area of the mechanical resonator, taken to be constant, and L_R is the resonator length. Note that $D = 1$ has been taken, given that the states form an orthogonal set (c.f. Sec. D) and the displacement operator accounts for the zero-point motion. With the quantisation of the displacement profile, the strains from Eq. 3.47 can be expressed as

$$\begin{aligned} u_{xx} = u_{yy} &= -\nu x \sqrt{\frac{\hbar}{2\rho\omega_\mathrm{R}}} \sqrt{\frac{1}{A_\mathrm{R} L_\mathrm{R}}} \frac{\mathrm{d}^2\phi_n}{\mathrm{d}z^2} \left(\hat{b}_n + \hat{b}_n^\dagger\right) \\ u_{zz} &= x \sqrt{\frac{\hbar}{2\rho\omega_\mathrm{R}}} \sqrt{\frac{1}{A_\mathrm{R} L_\mathrm{R}}} \frac{\mathrm{d}^2\phi_n}{\mathrm{d}z^2} \left(\hat{b}_n + \hat{b}_n^\dagger\right) \end{aligned} \tag{5.40}$$

In Sec. 5.1.2 the operators for the fluctuations of the magnetisation of the spatially homogeneous Kittel were quantised as

$$\begin{aligned} \delta\hat{m}_x &= \sqrt{\frac{\hbar\gamma_\mathrm{g}}{2M_\mathrm{s}V_\mathrm{m}}} \left(1 + \frac{4\pi M_\mathrm{s}}{H_\mathrm{e}}\right)^{-\frac{1}{4}} (c_0 + c_0^\dagger) \\ \delta\hat{m}_y &= i\sqrt{\frac{\hbar\gamma_\mathrm{g}}{2M_\mathrm{s}V_\mathrm{m}}} \left(1 + \frac{4\pi M_\mathrm{s}}{H_\mathrm{e}}\right)^{\frac{1}{4}} (c_0 - c_0^\dagger) \\ \delta\hat{m}_z &\approx -\frac{1}{2}\left(\delta\hat{m}_x^2 + \delta\hat{m}_y^2\right) \end{aligned} \tag{5.41}$$

In constructing terms for Eq. 5.36, those proportional to c_0^2 and $c_0^{\dagger 2}$ may be neglected under the rotating wave approximation as being higher order in the magnon frequency and hence not coupling. For terms linear in $c_0^\dagger c_0$, it is found

$$\begin{aligned} \delta m_x^2 u_{xx} &= -\frac{\hbar\gamma_\mathrm{g}}{M_\mathrm{s}V_\mathrm{m}} \left(1 + \frac{4\pi M_\mathrm{s}}{H_\mathrm{e}}\right)^{-\frac{1}{2}} \nu x \sqrt{\frac{\hbar}{2\rho\omega_\mathrm{R}}} \sqrt{\frac{1}{A_\mathrm{R} L_\mathrm{R}}} \frac{\mathrm{d}^2\phi_n(z)}{\mathrm{d}z^2} c_0^\dagger c_0 \left(b_n + b_n^\dagger\right), \\ \delta m_y^2 u_{yy} &= -\frac{\hbar\gamma_\mathrm{g}}{M_\mathrm{s}V_\mathrm{m}} \left(1 + \frac{4\pi M_\mathrm{s}}{H_\mathrm{e}}\right)^{\frac{1}{2}} \nu x \sqrt{\frac{\hbar}{2\rho\omega_\mathrm{R}}} \sqrt{\frac{1}{A_\mathrm{R} L_\mathrm{R}}} \frac{\mathrm{d}^2\phi_n(z)}{\mathrm{d}z^2} c_0^\dagger c_0 \left(b_n + b_n^\dagger\right), \\ \delta m_z^2 u_{zz} &= -\frac{1}{2\nu}(\delta m_x^2 u_{xx} + \delta m_y^2 u_{yy}). \end{aligned} \tag{5.42}$$

With these terms, the magnetoelastic energy density can be constructed in terms of the magnon and phonon creation and annihilation operators to extract the single magnon-phonon coupling strength. For the coupled fluctuations of this density, one finds

$$\begin{aligned} \delta U_\mathrm{me} = -\frac{B_1 (\nu + 1) \hbar\gamma_\mathrm{g}}{M_\mathrm{s}V_\mathrm{m}} \sqrt{\frac{\hbar}{2\rho\omega_\mathrm{R}}} \sqrt{\frac{1}{A_\mathrm{R} L_\mathrm{R}}} \left(\left(1 + \frac{4\pi M_\mathrm{s}}{H_\mathrm{e}}\right)^{\frac{1}{2}} + \left(1 + \frac{4\pi M_\mathrm{s}}{H_\mathrm{e}}\right)^{-\frac{1}{2}}\right) \\ x \frac{\mathrm{d}^2\phi_n(z)}{\mathrm{d}z^2} c_0^\dagger c_0 \left(b_n + b_n^\dagger\right). \end{aligned} \tag{5.43}$$

Since for the consideration of the thin film nanostructure proposed the device

has $t_m << t_R$, the strain through the thickness of the film can be taken to be uniform and therefore be evaluated at the interface such that $x \rightarrow t_R/2$. Integrating the magnetoelastic energy density over the bounds of the magnetic structure, it is found

$$\int_{V_m} \delta U_{me} = - \frac{B_1 (\nu + 1) \hbar \gamma_g}{M_s} \sqrt{\frac{\hbar}{2\rho\omega_R}} \sqrt{\frac{1}{A_R L_R}} \frac{t_R}{2} \left(\left(1 + \frac{4\pi M_s}{H_e}\right)^{\frac{1}{2}} + \left(1 + \frac{4\pi M_s}{H_e}\right)^{-\frac{1}{2}} \right) \times \frac{1}{V_m} \int_{V_m} \frac{d^2\phi_n(z)}{dz^2} c_0^\dagger c_0 \left(b_n + b_n^\dagger\right) \quad (5.44)$$

and hence

$$\mathcal{H}_{me} = - \frac{B_1 (\nu + 1) \hbar \gamma_g}{M_s} \sqrt{\frac{\hbar}{2\rho\omega_R}} \sqrt{\frac{1}{A_R L_R}} \frac{t_R k^2}{2} \left(\left(1 + \frac{4\pi M_s}{H_e}\right)^{\frac{1}{2}} + \left(1 + \frac{4\pi M_s}{H_e}\right)^{-\frac{1}{2}} \right) \times \left\langle \tilde{\phi}_n(z)'' \right\rangle_{S_m} c_0^\dagger c_0 \left(b + b^\dagger\right) \quad (5.45)$$

where $\tilde{\phi}_n(z)''$ is expressed in units of k^2, and $< ... >_{S_m}$ denotes the spatial average of the function within angular brackets over the surface of the magnetic structure. By comparison to the interaction Hamiltonian seen in Eq. 4.15, the single magnon-phonon coupling strength, g_0, can be identified as

$$g_0 = \frac{B_1 (\nu + 1) \gamma_g}{2\sqrt{2} M_s} \sqrt{\frac{\hbar}{L_R}} \left(\frac{1}{EI\rho A_R}\right)^{\frac{1}{4}} t_R k \left(\left(1 + \frac{4\pi M_s}{H_e}\right)^{\frac{1}{2}} + \left(1 + \frac{4\pi M_s}{H_e}\right)^{-\frac{1}{2}} \right) \times \left\langle \tilde{\phi}_n(z)'' \right\rangle_{S_m} \quad (5.46)$$

where the definition of ω_R is assumed from Eq. 3.75 and Eq. 3.69, and the negative sign is dismissed as an irrelevent phase-factor, to yield an expression as a function of the fundamental parameters to the device configuration. This formula is valid for any shape of magnetic texture in which the Kittel mode of the film couples to the elastic mode of an Euler-Bernoulli beam, provided that it is thin with respect to the resonator thickness and that the approximations in considering the effective magnetic field hold (that the demagnetisation tensor coefficients obey Eq. 2.35, and that the magnteocrystalline anisotropy can be neglected). In principle, this limits the geometry to oblate ellipsoidal shapes, or limits thereof (i.e. plates or disks). Another fundamental constraint on the application of this theory with regards to the elastic equations follows from Eq. 3.1, in which the Euler-Bernoulli beam theory is only known to hold for small products of the wave-vector and transverse dimensions. These inequalities are stated as

$$k w_R << 1 \quad \text{and} \quad k t_R << 1. \quad (5.47)$$

Clearly, if $w_R > t_R$ then one needs only evaluate the largest of the inequalities to ensure that the elastic description is valid.

Eq. 5.46 offers a rich parameter space to optimise to, and under the approximations made is independent of the resonator thickness (note that A_R and I introduce

Parameter	Value	Reference
$4\pi M_s$	1750 Oe	[127]
B_1	3.48×10^6 dyne/cm^2	[140]
ν_{GGG}	0.287	[134]
E_{GGG}	2.2×10^{12} dyne/cm^2	[134]
ρ_{GGG}	7.085 g/cm^3	[134]
t_m	$25a_0$	

TABLE 5.1: Choice parameters for use in g_0^{rec} and their sources where applicable.

a factor of $1/t_R^4$). If the simplification that the magnetic material is rectangular in geometry, then one may separate the spatial average into two independent integrals. In doing so, the spatial average then has no variation across the width of the magnetic structure, as the deflection profile is a function of the variable z only. The form of g_0 is then simplified further to

$$g_0^{rec} = \frac{B_1(\nu+1)\gamma_g}{2\sqrt{2}M_s}\sqrt{\frac{\hbar}{L_R}}\left(\frac{1}{EI\rho A_R}\right)^{\frac{1}{4}} t_R k\left(\left(1+\frac{4\pi M_s}{H_e}\right)^{\frac{1}{2}}+\left(1+\frac{4\pi M_s}{H_e}\right)^{-\frac{1}{2}}\right) \times \left\langle \tilde{\phi}_n(z)'' \right\rangle_{L_m}. \quad (5.48)$$

where $< ... >_{L_m}$ is now used to denote the length average of the function within angular brackets over the length of the magnetic structure.

With regards to the shape of the cross-section of the resonator, it was stated in the proposal of the device that given the design constraints the GGG beam is assumed to have either a rectangular or isosceles cross-section. Due to both the lower mode frequencies, as well as the smaller cross-sectional area for equivalent widths and thicknesses, the isosceles cross-section offers a numerical pre-factor that boost the value of g_0 over the what would be attained for comparable dimensions of the device in assuming a rectangular elastic resonator cross-section. Mathematically, this is expressed as

$$\frac{A_{iso}}{A_{sq}} = \frac{1}{2} \qquad \text{and} \qquad \frac{I_{iso}}{I_{sq}} = \frac{1}{3}, \quad (5.49)$$

which leads to an multiplicative increase to the value of g_0 of $6^{1/4} \approx 1.5$ for the isosceles elastic resonator cross-section compared to that the rectangular one.

The following sections look to characterise g_0^{rec} for both a cantilever and a bridge elastic resonator onto which a thin film of YIG is applied. As the curvature $\phi_n''(z)$ of the resonator varies as a function of position along the resonator, it would seem instructive to also vary the effective central position of the magnetic material for the scheme $L_M < L_R$. To this end, it is shown g_0^{rec} as a function of width, w_m, and length, L_m, for an exemplar somewhat arbitrary range than presents a nanoscale configuration that also satisfies the mode validity criterion in Eq. 5.47. As g_0^{rec} is independent of the resonator thickness, no variation is performed for this parameter. With the width of the magnetic structure as the smaller of the two lateral dimensions of the device, the length of magnetic structure is investigated for schemes $L_m \leq L_R$. Presented in Table 5.1 is a recap of the parameters chosen for the YIG/GGG complex which were noted in the introduction to this chapter.

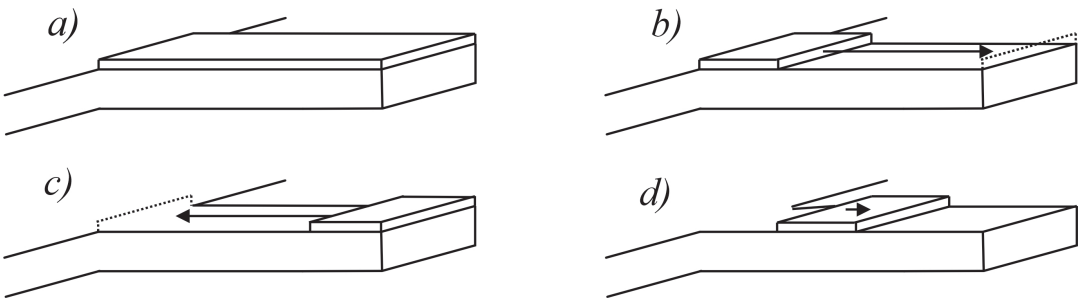

FIGURE 5.2: Placement and movement of the magnetic section deposited on top of the cantilever corresponding to the itemised list.

5.2.1 Cantilever

For the cantilever/YIG elastic resonator, there are a number of regimes to consider in optimising g_0^{rec}. The most intuitive of these is to simply cover the entirety of the topmost surface of the cantilever with YIG. However the curvature of the resonator, which varies as a function of position, could also presents schemes that may obtain preferential values. These regimes are depicted in Fig. 5.2, and are described as

(a) A cantilever resonator in which the surface is completely covered in magnetic material.

(b) A cantilever resonator in which the central placement of the magnetic structure begins at the fixed end of the cantilever, and is varied to the midpoint of the cantilever as a parameter to optimise.

(c) A cantilever resonator in which the the central placement of the magnetic structure begins at the free end of the cantilever, and is varied to the midpoint of the cantilever as a parameter to optimise.

(d) A cantilever resonator in which the central placement of the magnetic material varies along the cantilever's length, for varying lengths of magnetic material.

Explored within this section is the influence of the position of the YIG magnetic material.

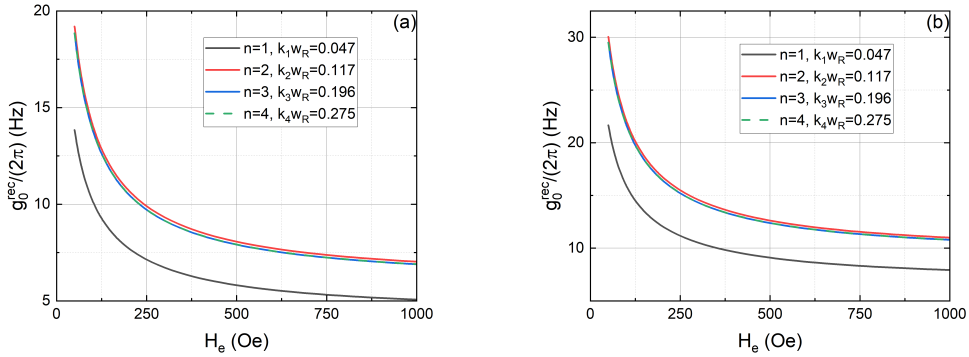

FIGURE 5.3: g_0^{rec} for a cantilever resonator assuming the surface is covered with thin film YIG. (a) corresponds to a square cross-section, and (b) corresponds to an isosceles cross-section

Shown in Fig. 5.3 is the behaviour of g_0^{rec} for the case of the cantilever resonator of (a) square cross-section and (b) isosceles cross -section with thin film YIG fully covering the surface of the resonator. As example dimensions, considered are an elastic resonator length $L_{\text{R}} = L_{\text{m}} = 20\,\mu\text{m}$ and cross-sectional dimensions $w_{\text{R}} = t_{\text{R}} = 500\,\text{nm}$. In this figure, plotted are g_0^{rec} for the first 4 flexural modes of the cantilever for both the rectangular and isosceles cross-sections as a function of applied magnetic field. In considering g_0^{rec} for the fundamental mode ($n = 1$) and the second mode ($n = 1$), there is an increase of some 50% to the value. However, higher modes than $n = 2$ appear to converge to the same values of g_0^{rec} as that of $n = 1$, and appreciable increases to g_0^{rec} are only seen between the fundamental and second mode. Listed also in the figure is the mode validity parameter from Eq. 5.47, which requires that the cantilever resonator be made longer, thinner, or a combination of both, in order to be satisfied to a reasonable degree. With the mode validities in mind, the following discussion is limited to the fundamental mode only - g_0^{rec} scales as $L_{\text{R}}^{1/2}$, and so moving to the longer cantilever resonators in order to access higher order modes is detrimental to g_0^{rec}. It is also seen that smaller applied fields offer higher values for g_0^{rec}, but fields strong enough to saturate the magnetic moments in thin film YIG are still required. With this in mind, and in accordance with the plots, a tentative $H_{\text{e}} = 350\,\text{Oe}$ is taken as the nominal field moving forward. While the coercivity of YIG is known to be 2 to 3 order of magnitude smaller than this, it is assumed that the 350 Oe field is sufficiently strong to account for any kinds of deviations from the saturated state that arise close edges of the structure that arise as a result of the demagnetisation field. In principle, one needs only have a field large enough to make the volume of structure in which these deviations exist sufficiently small.

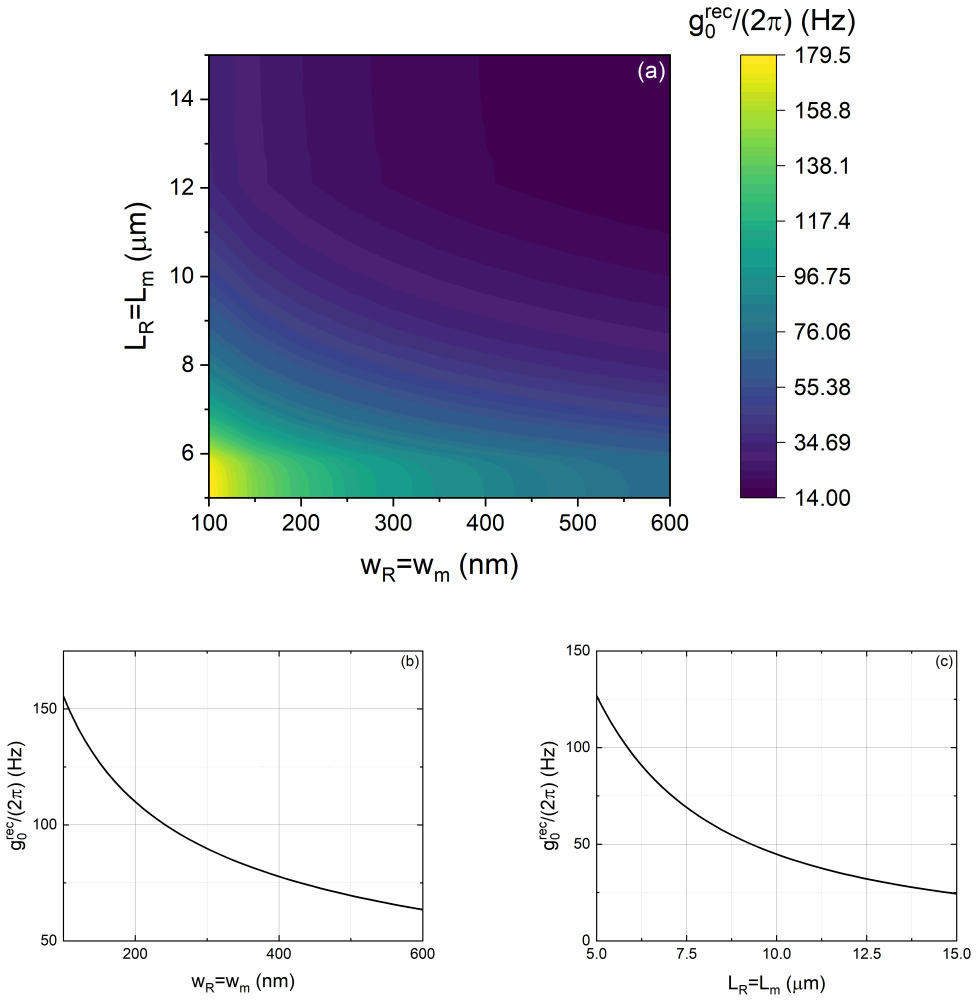

FIGURE 5.4: (a) g_0^{rec} of a cantilever resonator with a surface covered with thin film YIG as a function of L_{R} and w_{R}. Line scans are taken through (a) at (b) $L_{\mathrm{R}} = 5.5\,\mu$m and (c) $w_{\mathrm{R}} = 0.2\,\mu$m.

Shown in Fig. 5.4 is the dependence of g_0^{rec} on the cantilever resonator dimensions. It is assumed that the resonator surface is entirely covered with thin film YIG, corresponding to case (a) mentioned prior. Chosen for the resonator dimensions is to plot the function in the range of lengths $L_{\mathrm{m}} = L_{\mathrm{R}} = [5:15]\ \mu$m and cross-sectional dimensions $w_{\mathrm{R}} = w_{\mathrm{m}} = t_{\mathrm{R}} = [100:600]$ nm to give a scope of attainable values. These ranges have been chosen such that that any combination of length and width can be interpreted to satisfy the mode validity criterion in Eq. 5.47, with the largest product corresponding to a value $k_1 w_{\mathrm{R}} \approx 0.225$ for minimal L_{R} and maximal w_{R}. An applied field of $H_{\mathrm{e}} = 350\,$Oe is assumed, and the cross-sectional area is taken to be isosceles since this geometry gives larger values of g_0^{rec} as compared to square cross-sections. Shown also in 5.4 are line-scans, taken at values $L_{\mathrm{R}} = 5.5\,\mu$m and $w_{\mathrm{R}} = 200\,$nm. These plots depict the expected $L_{\mathrm{R}}^{-1/2}$ and w_{R}^{-1} dependence. The value of g_0^{rec} is maximised for $S_{\mathrm{R}} = L_{\mathrm{R}} w_{\mathrm{R}} \to 0$ but this clearly offers little use physically, further displays the ineffability of using higher order modes - the shrinking of dimensions is preferable for maximising g_0^{rec} whereas accessing higher order modes requires making longer and thinner structures.

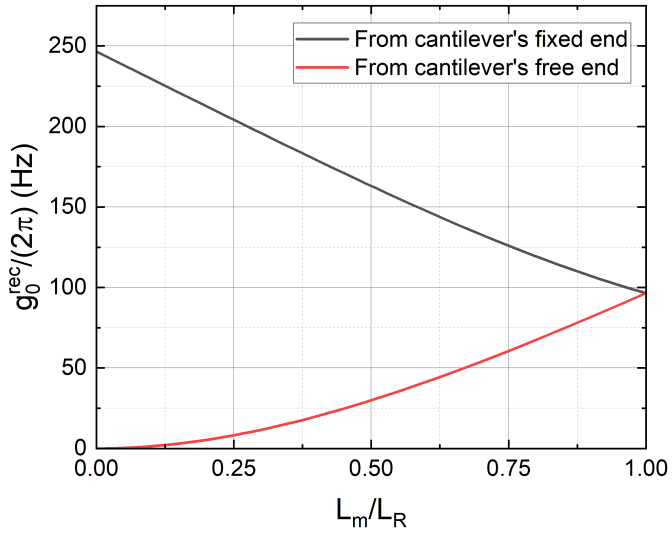

FIGURE 5.5: g_0^{rec} for a cantilever resonator expressed in terms of the ratio of coverage of thin film YIG to resonator length, L_m/L_R. The black curve corresponds to case (ii) and the red curve corresponds to case (iii) in Fig. 5.2

Fig. 5.5 shows the behaviour for g_0^{rec} as a function of the ratio of thin film YIG structure length to cantilever resonator length (i.e. as a function of L_m/L_R) for the fundamental resonator mode. In this figure, two cases are presented. In the first case (the black line), the origin of coordinates is taken to begin at the fixed end of the cantilever. In the second, the origin of coordinates is taken to begin at the free end of the cantilever (the red line). These correspond to cases (b) and (c) mentioned prior. Nominal dimensions of $L_\text{R} = 6\,\mu\text{m}$ and $w_\text{R} = 200\,\text{nm}$ have been taken, an applied field of $H_\text{e} = 350\,\text{Oe}$ has been assumed, and the cross-section is taken to be isosceles. Note that there is an indeterminacy as the ratio $L_\text{m}/L_\text{R} \to 0$ in which g_0^{rec} tends to infinity which has not been captured in the figure. This is an extension of the behaviour seen in Fig. 5.4, in which g_0^{rec} was maximised for $S_\text{R} \to 0$. At ratios of 1, the two approaches coverage converge to the same value, regardless of which end of the cantilever the ratio is taken from which is to be expected of a fully covered cantilever. Curvature of the cantilever plays a larger role in the approach from the free end, as the curvature from the fixed end is roughly linear for the first half (c.f. Fig. 3.6). In partial coverage of the cantilever, larger values of g_0^{rec} are attainable in covering from the fixed end of the cantilever rather than the free end, corresponding to where the strain is largest.

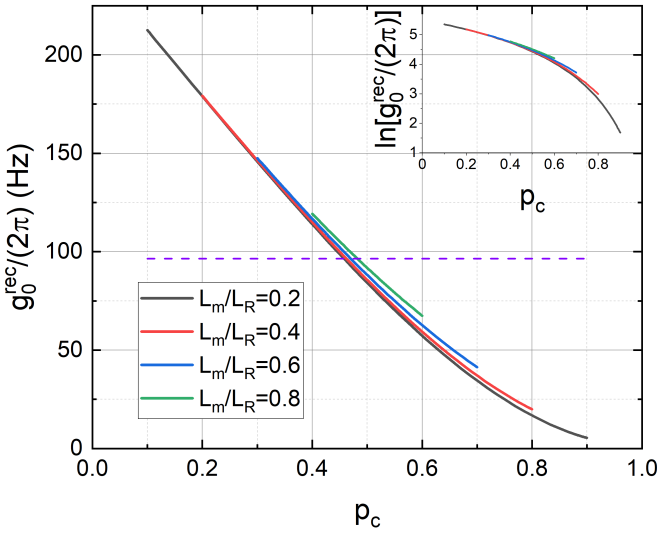

FIGURE 5.6: g_0^{rec} for a cantilever resonator in moving magnetic structure sections along the resonator's length. The dotted line indicates the value of g_0^{rec} for full coverage with magnetic structure.

Lastly, Fig. 5.6 shows how g_0^{rec} varies in moving segments of thin film YIG of lengths $0.2L_{\text{R}}$, $0.4L_{\text{R}}$, $0.6L_{\text{R}}$, and $0.8L_{\text{R}}$ along the length of the cantilever for it's fundamental mode, corresponding to case (d). To express this, a central magnetic length is introduced, defined as

$$L_{\text{c}} = \frac{1}{2}\frac{L_{\text{m}}}{L_{\text{R}}}. \tag{5.50}$$

The central magnetic position, p_{c}, is then varied in the interval $p_{\text{c}} = [L_{\text{c}} : 1 - L_{\text{c}}]$, where $p_{\text{c}} = L_{\text{c}}$ is taken to start from the cantilever's fixed end, and g_0^{rec} is expressed as a function of p_{c}. Nominal dimensions of $L_{\text{R}} = 6\,\mu$m and $w_{\text{R}} = 200\,$nm are again assumed, alongside an applied field of $H_{\text{e}} = 350\,$Oe, and isosceles cross-section. As was seen in Fig. 5.5, owing to the linearity of the curvature of the cantilever, the different lengths follow largely the same trajectory for the first half of the cantilever. Depicted in the figure as the dotted line is the value of g_0^{rec} in assuming full coverage of the resonator with magnetic structure as a benchmark comparison. Again, placement towards the fixed end of the cantilever offers preferential values than placement towards the free end.

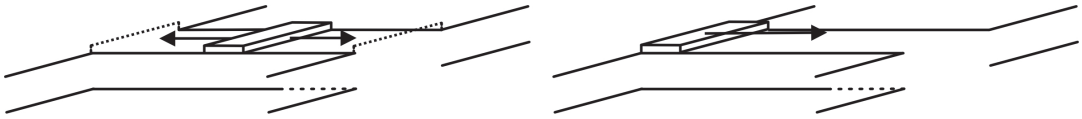

FIGURE 5.7: Placement and movement of the magnetic section depositied on top of the bridge corresponding to the itemised list.

5.2.2 Bridge

The bridge resonator is able to offer larger values of g_0^{rec} for directly equivalent dimensions, but g_0^{rec} becomes 0 for certain placements of magnetic material owing to the symmetry of the bridge's curvature. In assuming the geometry of a bridge, the parameter $k_n L$ is larger than that of the cantilever, which means that directly comparable dimensions are not always attainable given that the mode validity criterion in Eq. 5.47 is harder to meet. With the dimensions considered for the cantilever ($L_{\text{R}} = 6\,\mu\text{m}$ and $w_{\text{R}} = 200\,\text{nm}$), these may still be used for the bridge but note is made of the higher $k_1 w_{\text{R}} \approx 0.16$, compared to a value of 0.063 for the cantilever. These dimensions then give a direct baseline to compare the two approaches. To this end, considered also is the same value of applied field, $H_{\text{e}} = 350\,\text{Oe}$, and the cross-section is also assumed to be isosceles. The curvature of the bridge is an odd function, and so the length average that arises in the derivation of g_0^{rec} prevents covering the entire bridge surface with thin film YIG, lest g_0^{rec} be rendered useless. As with the cantilever, the $L^{-1/2}$ and w^{-1} scaling still holds from it's formula and so showing g_0^{rec} as a function of length and width is neglected. Hence, considered are only two cases;

(a) A bridge resonator in which the central placement of the magnetic structure is held at the centre of the resonator and the length of the magnetic structure is varied towards L_{R}.

(b) A bridge resonator in which the central placement of the magnetic structure begins at a fixed end of the bridge, and is varied towards the midpoint of the bridge as a parameter to optimise.

These cases are depicted in Fig. 5.7. Note that the symmetry of the the bridge's deflection profile presents a redundancy in case (b), in that whichever free end is chosen is equivalent.

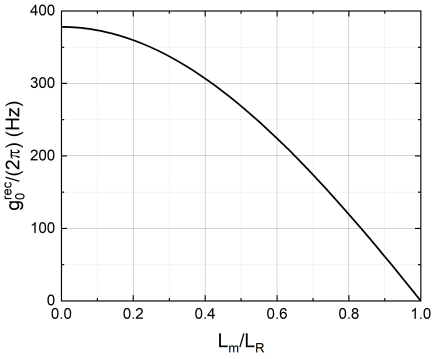

FIGURE 5.8: g_0^{rec} for a bridge resonator as a function of the ratio of magnetic structure length to resonator length, with the magnetic structure placed at the central position $p_c = L_R/2$.

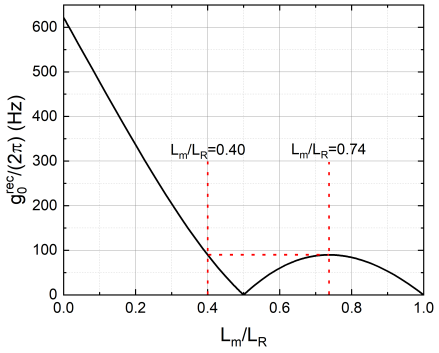

FIGURE 5.9: g_0^{rec} for a bridge resonator as a function of the ratio of magnetic length to resonator length, with the magnetic structure beginning from a fixed end of the bridge.

Fig. 5.8 shows how g_0^{rec} varies for the bridge resonator as a function of the ratio L_m/L_R where the thin film YIG's central position is at the bridge's midpoint, corresponding to case (i). Again, the value of g_0^{rec} is maximised as $S_R \to 0$ which offers little use physically. Further, it is seen that g_0^{rec} is 0 for a ratio $L_m/L_R = 1$, corresponding to a bridge resonator in which the surface is fully covered with thin film YIG. From a manufacturing perspective, fully covering the surface would be convenient but the symmetry of the curvature prevents this.

Fig. 5.9 shows how g_0^{rec} varies for the bridge resonator as a function of the ratio L_m/L_R, where now the central position of the magnetic structure is assumed to begin at a fixed end of the bridge, corresponding to case (ii). Due to the symmetry of the deflection profile (a consequence of the clamped-clamped boundary conditions), which fixed end of the bridge the central position is assumed to begin from is of no distinction, and either approach provide equivalent values of g_0^{rec} up to a phase factor. Note that the symmetry of the bridge's curvature not only precludes full coverage with magnetic material, but also coverage of the first half (or, equally, the second half). For obtaining larger values of g_0^{rec} within this scheme, it is preferable to have lengths of magnetic material $L_m < 0.4L_R$. At ratios $L_m/L_R = 0.4$ and $L_m/L_R = 0.74$ the same value of g_0^{rec} is obtained.

5.3 The effect of the magnetisation mode profile

While the notion of a 'flat' magnetisation profile for the Kittel mode simplifies the derivations, it is physically inaccurate. In considering a film at saturation supporting a spin wave, Maxwell's equations impose that tangential components of the magnetic field and the normal components of the magnetic field be continuous across the surfaces of the film [54]. For this to be true, the fluctuations of the magnetisation must vanish at the bounding surfaces of the magnetic structure. These boundary conditions alone, however, leave the amplitude of the magnetisation fluctuations undefined [149]. A basic consideration of this behaviour is to model the mode profile as having sinusoidal dependence through the transverse dimensions of the film [155]. For the geometry assumed for the device proposed within this thesis, this

spatial dependence gives the fluctuations of δm_x and δm_y the result that they vanish at the transverse boundaries of the film. For high aspect ratio structures, work suggests that this consideration is also insufficient [156], and that quantisation of the wave-vector in the smaller of the transverse dimension results in an 'effective' magnetic width $w_{\text{eff}} > w_{\text{m}}$ such that individual components of the fluctuation no longer vanish at the boundary of this smaller transverse dimension. Considered here both of these cases, and their impact on g_0^{rec} is assessed.

5.3.1 Simple trigonometric dependence

As the most basic model of the two cases, that in which simple cosine dependencies of periods $2L_{\text{m}}$ and $2w_{\text{m}}$ is considered first, such that both δm_x and δm_y vanish at the transverse boundaries of the magnetic structure. For this, the fluctuations of the magnetisation of the Kittel mode may be expressed as

$$(\delta m_x, \delta m_y) \rightarrow (\delta m_x, \delta m_y) \cos\left(\frac{\pi y}{w_{\text{m}}}\right) \cos\left(\frac{\pi z}{L_{\text{m}}}\right). \tag{5.51}$$

where δm_z will also have a spatial dependence entering through Eq. 2.50. The Kittel mode which was previously considered to be homogeneous will then have spatial dependence included as

$$\mathbf{m} = \frac{\mathbf{M}}{M_{\text{s}}} = (0,0,1) + (\delta m_x \hat{x} + \delta m_y \hat{y}) \cos\left(\frac{\pi y}{w_{\text{m}}}\right) \cos\left(\frac{\pi z}{L_{\text{m}}}\right) + \delta m_z \hat{z}. \tag{5.52}$$

One can now proceed in the same fashion as in Eq. 5.15 in finding the Hamiltonian for the Kittel mode. For the Zeeman energy, it is found

$$\begin{aligned} &-M_{\text{s}} \int_{V_{\text{m}}} \mathbf{m} \cdot \mathbf{H}_{\text{e}} \, \mathrm{d}V \\ &\quad = -M_{\text{s}} H_{\text{e}} V_{\text{m}} + \frac{1}{2} M_{\text{s}} H_{\text{e}} \left(\delta m_x^2 + \delta m_y^2\right) \int_{V_{\text{m}}} \cos^2\left(\frac{\pi y}{w_{\text{m}}}\right) \cos^2\left(\frac{\pi z}{L_{\text{m}}}\right) \mathrm{d}V \end{aligned} \tag{5.53}$$

As the integral above enters the proceeding work a number of times, it is stated that

$$\int_{V_{\text{m}}} \cos^2\left(\frac{\pi y}{w_{\text{m}}}\right) \cos^2\left(\frac{\pi z}{L_{\text{m}}}\right) \mathrm{d}V = V_{\text{m}} \int_{-\frac{1}{2}}^{\frac{1}{2}} \mathrm{d}x \int_{-\frac{1}{2}}^{\frac{1}{2}} \cos^2(\pi y) \, \mathrm{d}y \int_{-\frac{1}{2}}^{\frac{1}{2}} \cos^2(\pi z) \, \mathrm{d}z = \frac{V_{\text{m}}}{4} \tag{5.54}$$

where integration by substitution is used for the middle step. Hence the Zeeman energy term evaluates to

$$-M_{\text{s}} \int_{V_{\text{m}}} \mathbf{m} \cdot \mathbf{H}_{\text{e}} \, \mathrm{d}V = -M_{\text{s}} H_{\text{e}} V_{\text{m}} + \frac{1}{8} M_{\text{s}} H_{\text{e}} V_{\text{m}} \left(\delta m_x^2 + \delta m_y^2\right) \tag{5.55}$$

For the demagnetisation energy term, one finds

$$\begin{aligned}
&-\frac{4\pi M_\mathrm{s}^2}{2}\int_{V_\mathrm{m}} \mathbf{m}\cdot\left(\hat{N}\cdot\mathbf{m}\right)\,\mathrm{d}V \\
&= 2\pi M_\mathrm{s}^2\int_{V_\mathrm{m}}\left(\cos^2\left(\frac{\pi y}{w_\mathrm{m}}\right)\cos^2\left(\frac{\pi z}{L_\mathrm{m}}\right)\left(N_x\delta m_x^2+N_y\delta m_y^2\right)+N_z\left(1+\delta m_z\right)^2\right)\mathrm{d}V \\
&= \frac{1}{4}\left(2\pi M_\mathrm{s}^2 V_\mathrm{m}\left(N_x\delta m_x^2+N_y\delta m_y^2\right)\right)+2\pi M_\mathrm{s}^2 V_\mathrm{m}N_z-\frac{1}{4}\left(2\pi M_\mathrm{s}^2 V_\mathrm{m}N_z\left(\delta m_x^2+\delta m_z^2\right)\right) \\
&\quad+\frac{9}{64}\left(2\pi M_\mathrm{s}^2 V_\mathrm{m}N_z\delta m_z^2\right)
\end{aligned} \tag{5.56}$$

which can be seen to be fractions of the terms already derived Eq. 5.18. Hence

$$\begin{aligned}
\mathcal{H}_\mathrm{m} =& -M_\mathrm{s}H_\mathrm{e}V_\mathrm{m}+2\pi M_\mathrm{s}^2 w_\mathrm{m}t_\mathrm{m}^2 \\
&+\frac{1}{4}\left(\frac{1}{2}M_\mathrm{s}H_\mathrm{e}V_\mathrm{m}\left(\delta m_x^2+\delta m_y^2\right)+2\pi M_\mathrm{s}^2 V_\mathrm{m}\delta m_x^2\right) \\
&+\frac{1}{4}\left(2\pi M_\mathrm{s}^2 L_\mathrm{m}t_\mathrm{m}^2\delta m_y^2-2\pi M_\mathrm{s}^2 w_\mathrm{m}t_\mathrm{m}^2\left(\delta m_x^2+\delta m_y^2-\frac{9}{16}\delta m_z^2\right)\right).
\end{aligned} \tag{5.57}$$

The Hamiltonian for the Kittel mode under the assumption of a mode profile is then found with the same considerations prior (i.e. neglect terms which do not fluctuate and terms proportional to t_m^2) to find

$$\mathcal{H}_\mathrm{SW}\approx\frac{1}{4}\left(\frac{1}{2}M_\mathrm{s}H_\mathrm{e}V_\mathrm{m}\left(\delta m_x^2+\delta m_y^2\right)+2\pi M_\mathrm{s}^2 V_\mathrm{m}\delta m_x^2\right). \tag{5.58}$$

which is $1/4$ of the Hamiltonian for the Kittel mode under the assumption of a flat mode profile.

As before, substitution of Eq. 5.29 and 5.31 into Eq. 5.22 is performed to find the quantisation of the mode profiled Kittel mode fluctuations. With the simplification that the profiled Hamiltonian is $1/4$ of the flat Hamiltonian and taking $t=0$, it is found

$$\frac{g_\mathrm{e}\mu_\mathrm{B}}{2}V_\mathrm{m}A_0^2\left(2\pi M_\mathrm{s}+\frac{H_\mathrm{e}}{2}\right)=g_\mathrm{e}\mu_\mathrm{B}H_\mathrm{e}\left(1+\frac{4\pi M_\mathrm{s}}{H_\mathrm{e}}\right)^{\frac{1}{2}}, \tag{5.59}$$

from which A_0 is found as

$$A_0=2\sqrt{\frac{1}{V_\mathrm{m}}}\left(1+\frac{4\pi M_\mathrm{s}}{H_\mathrm{e}}\right)^{-\frac{1}{4}}. \tag{5.60}$$

The Kittel mode fluctuations are then

$$\begin{aligned}
\delta m_{x,0}^{+} &= \sqrt{\frac{2\hbar\gamma_\mathrm{g}}{M_\mathrm{s}V_\mathrm{m}}}\left(1+\frac{4\pi M_\mathrm{s}}{H_\mathrm{e}}\right)^{-\frac{1}{4}}c_0^\dagger\cos\left(\frac{\pi y}{w_\mathrm{m}}\right)\cos\left(\frac{\pi z}{L_\mathrm{m}}\right) \\
\delta m_{y,0}^{+} &= i\sqrt{\frac{2\hbar\gamma_\mathrm{g}}{M_\mathrm{s}V_\mathrm{m}}}\left(1+\frac{4\pi M_\mathrm{s}}{H_\mathrm{e}}\right)^{\frac{1}{4}}c_0\cos\left(\frac{\pi y}{w_\mathrm{m}}\right)\cos\left(\frac{\pi z}{L_\mathrm{m}}\right)
\end{aligned} \tag{5.61}$$

where it is again used $\gamma_\mathrm{g}=g_\mathrm{e}\mu_\mathrm{B}/\hbar$. Note that these have a pre-factor of 2 relative to those derived under the assumption of a flat mode profile.

5.3.2 Single magnon-phonon coupling strength

The creation and annihilation operators for the fluctuations of the magnetisation of the Kittel mode under the assumption of a spatial cosine dependence then follows the exact same procedure as in Sec. 5.2. These operators are then quantised as

$$\begin{aligned}\delta m_x &= \sqrt{\frac{2\hbar\gamma_g}{M_s V_m}}\left(1+\frac{4\pi M_s}{H_e}\right)^{-\frac{1}{4}}(c_0+c_0^\dagger)\cos\left(\frac{\pi y}{w_m}\right)\cos\left(\frac{\pi z}{L_m}\right),\\ \delta m_y &= i\sqrt{\frac{2\hbar\gamma_g}{M_s V_m}}\left(1+\frac{4\pi M_s}{H_e}\right)^{\frac{1}{4}}(c_0-c_0^\dagger)\cos\left(\frac{\pi y}{w_m}\right)\cos\left(\frac{\pi z}{L_m}\right),\\ \delta m_z &\approx -\frac{1}{2}(\delta m_x^2+\delta m_y^2).\end{aligned} \tag{5.62}$$

In constructing terms fluctuations of the magnetoelastic energy density (Eq. 5.36), terms proportional to c_0^2 and $c_0^{\dagger 2}$ may again be neglected under the rotating wave approximation. With this, one finds to second order in the spin-wave operators

$$\begin{aligned}\delta m_x^2 u_{xx} = &-\frac{4\hbar\gamma_g}{M_s V_m}\left(1+\frac{4\pi M_s}{H_e}\right)^{-\frac{1}{2}} \nu x\sqrt{\frac{\hbar}{2\rho\omega_R}}\sqrt{\frac{1}{A_R L_R}}\\ &\times\frac{d^2\phi_n(z)}{dz^2}c_0^\dagger c_0\left(b+b^\dagger\right)\cos^2\left(\frac{\pi y}{w_m}\right)\cos^2\left(\frac{\pi z}{L_m}\right),\end{aligned}$$

$$\begin{aligned}\delta m_y^2 u_{yy} = &-\frac{4\hbar\gamma_g}{M_s V_m}\left(1+\frac{4\pi M_s}{H_e}\right)^{\frac{1}{2}} \nu x\sqrt{\frac{\hbar}{2\rho\omega_R}}\sqrt{\frac{1}{A_R L_R}}\\ &\times\frac{d^2\phi_n(z)}{dz^2}c_0^\dagger c_0\left(b+b^\dagger\right)\cos^2\left(\frac{\pi y}{w_m}\right)\cos^2\left(\frac{\pi z}{L_m}\right),\end{aligned}$$

$$\delta m_z^2 u_{zz} = -\frac{1}{2\nu}(\delta m_x^2 u_{xx}+\delta m_y^2 u_{yy}). \tag{5.63}$$

and hence the fluctuations of the magnetoelastic energy density is expressed as

$$\begin{aligned}\delta U_{me} = &-\frac{4B_1(\nu+1)\hbar\gamma_g}{M_s V_m}\sqrt{\frac{\hbar}{2\rho\omega_R}}\sqrt{\frac{1}{A_R L_R}}\left(\left(1+\frac{4\pi M_s}{H_e}\right)^{\frac{1}{2}}+\left(1+\frac{4\pi M_s}{H_e}\right)^{-\frac{1}{2}}\right)\\ &\times x\cos^2\left(\frac{\pi y}{w_m}\right)\cos^2\left(\frac{\pi z}{L_m}\right)\frac{d^2\phi_n(z)}{dz^2}c_0^\dagger c_0\left(b+b^\dagger\right).\end{aligned} \tag{5.64}$$

Again, using the geometry of the structure proposed ($t_m << t_R$), the strain may be considered to be uniform over the thin film and hence be evaluated at the interface such that $x \to t_R/2$. Integrating over the structure, it is found

$$\begin{aligned}&\int_{V_m}\delta U_{me} =\\ &-\frac{4B_1(\nu+1)\hbar\gamma_g}{M_s}\sqrt{\frac{\hbar}{2\rho\omega_R}}\sqrt{\frac{1}{A_R L_R}}\frac{t_R}{2}\left(\left(1+\frac{4\pi M_s}{H_e}\right)^{\frac{1}{2}}+\left(1+\frac{4\pi M_s}{H_e}\right)^{-\frac{1}{2}}\right)\\ &\times\frac{1}{V_m}\int_{V_m}\cos^2\left(\frac{\pi y}{w_m}\right)\cos^2\left(\frac{\pi z}{L_m}\right)\frac{d^2\phi_n(z)}{dz^2}c_0^\dagger c_0\left(b+b^\dagger\right).\end{aligned} \tag{5.65}$$

Rescaling the magnetic origin such that it coincides with the elastic origin of the beam, the expression becomes

$$\int_{V_m} \delta U_{me} = -\frac{4B_1\,(\nu+1)\,\hbar\gamma_g}{M_s}\sqrt{\frac{\hbar}{2\rho\omega_R}}\sqrt{\frac{1}{A_R L_R}}\frac{t_R k^2}{2}\left(\left(1+\frac{4\pi M_s}{H_e}\right)^{\frac{1}{2}}+\left(1+\frac{4\pi M_s}{H_e}\right)^{-\frac{1}{2}}\right) \times\left\langle \sin^2\left(\frac{\pi y}{w_m}\right)\sin^2\left(\frac{\pi z}{L_m}\right)\tilde{\phi}_n(z)''\right\rangle_{S_m} c_0^\dagger c_0\left(b+b^\dagger\right) \quad (5.66)$$

where $\tilde{\phi}_n(z)''$ is again $\phi_n(z)''$ expressed in units of k^2, and $< ... >_{S_m}$ denotes the spatial average of the enclosed function over the magnetic surface. By comparison with the interaction Hamiltonian, the single magnon-phonon coupling strength can be identified as

$$g_0 = \frac{4B_1(\nu+1)\gamma_g}{2\sqrt{2}M_s}\sqrt{\frac{\hbar}{L_R}}\left(\frac{1}{EI\rho A_R}\right)^{\frac{1}{4}} t_R k\left(\left(1+\frac{4\pi M_s}{H_e}\right)^{\frac{1}{2}}+\left(1+\frac{4\pi M_s}{H_e}\right)^{-\frac{1}{2}}\right) \times\left\langle \sin^2\left(\frac{\pi y}{w_m}\right)\sin^2\left(\frac{\pi z}{L_m}\right)\tilde{\phi}_n(z)''\right\rangle_{S_m} \quad (5.67)$$

Eq. 5.67 offers some differences to that in Eq. 5.46, most notably that there is a prefactor of 4 which provides a simple numerical boost to the values of g_0. However, due to the profiling of the curvature which enters in the spatial average, it is not that trivial to assume that Eq. 5.10 provides a betterment in all scenarios.

The simplification that the magnetic surface is assumed to be rectangular is again made, such that the spatial average may be separated into y and z components. Under this assumption, the expression becomes

$$g_0^{rec} = \frac{B_1(\nu+1)\gamma_g}{\sqrt{2}M_s}\sqrt{\frac{\hbar}{L_R}}\left(\frac{1}{EI\rho A_R}\right)^{\frac{1}{4}} t_R k\left(\left(1+\frac{4\pi M_s}{H_e}\right)^{\frac{1}{2}}+\left(1+\frac{4\pi M_s}{H_e}\right)^{-\frac{1}{2}}\right) \times\left\langle \sin^2\left(\frac{\pi z}{L_m}\right)\tilde{\phi}_n(z)''\right\rangle_{L_m} \quad (5.68)$$

where $< ... >_{L_m}$ denotes the length average of the enclosed function over the magnetic length. In comparing g_0^{rec} of flat magnetisation profile to that of a trigonometric profile, the ratio of the two is expressed as

$$\frac{g_0^{rec}(\text{trigonometric profile})}{g_0^{rec}(\text{flat profile})} = 2\times\frac{\langle\phi_n(z)''\rangle_{L_m}}{\left\langle \sin^2\left(\frac{\pi z}{L_m}\right)\phi_n(z)''\right\rangle_{L_m}}. \quad (5.69)$$

In order to gain an effective boost to g_0^{rec} in adopting a more physical description of the mode profile, it is required that the ratio of the length averages of the trigonometric profile and the flat profile be greater than $1/2$.

5.3.3 Cantilever

In including a more accurate description of the Kittel mode profile, the argument included in the spatial (or length) average is no longer simply that of the curvature.

In essence, this curvature is windowed by the same function that describes the spatial dependence of the magnetisation in that the two are multiplied. Not only is there a difference in the pre-factor of g_0^{rec}, but there will also exist a difference to the spatial averages themselves. Repeated here are the same plots as in Sec. 5.2.1 but instead using Eq. 5.67 to characterise the behaviour of g_0^{rec} and determine the impact of the magnetisation profile. To this end, comparable dimensions as were used for the previous figures are assumed. To recapitulate these, considered are $L_{\mathrm{R}} = 6\,\mu\mathrm{m}$ and $w_{\mathrm{R}} = 200\,\mathrm{nm}$), and applied field of $H_{\mathrm{e}} = 350\,\mathrm{Oe}$, and the cross-section of the resonator is assumed to be isosceles in shape.

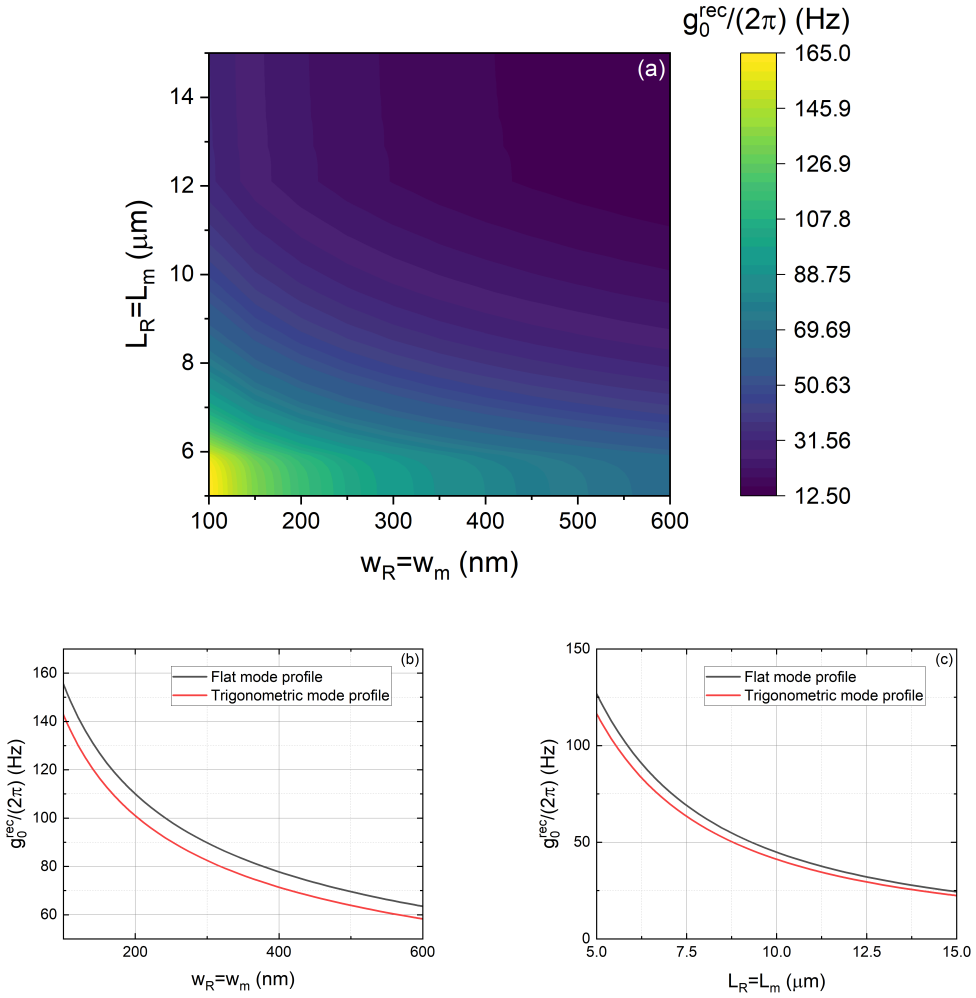

FIGURE 5.10: (a) Trigonometric mode profile g_0^{rec} of a fully covered cantilever resonator as a function of L_{R} and w_{R}. Line scans are taken through (a) at (b) $L_{\mathrm{R}} = 5.5\,\mu$m and (c) $w_{\mathrm{R}} = 0.2\,\mu$m and include comparison to the flat mode profile.

First, shown in Fig 5.10 is the analogous plot to Fig. 5.4. This is the dependence of g_0^{rec} for the fundamental flexural mode in varying the width and length of the cantilever resonator, assuming that the surface is fully covered with thin film YIG. Dimensions and applied field are chosen exactly the same of those in Fig. 5.4 ($L_{\mathrm{m}} = L_{\mathrm{R}} = [5:15]\ \mu$m, isosceles cross-sectional dimensions $w_{\mathrm{R}} = t_{\mathrm{R}} = [100:600]$ nm, applied field $H_{\mathrm{e}} = 350\,$Oe), and line-scans are taken through the same region. Relative to the flat mode profile, there is a net loss to the parameter g_0^{rec}. Inclusion of a physically representative mode profile is detrimental for maximisation, but unavoidable in considering a realistic Kittel mode for a thin film. With regards to the scaling of g_0^{rec} with length, the $L_{\mathrm{R}}^{-1/2}$ behaviour is no longer exactly preserved for the trigonometric mode profile given that the length of the magnetic material enters into the spatial average through the spatial dependence of the magnetisation. In moving to lengths longer than considered, it would appear that the inclusion of the mode profile would become beneficial. While the inclusion of a realistic mode profile is detrimental, the percentage decrease is less than 10% for this geometry.

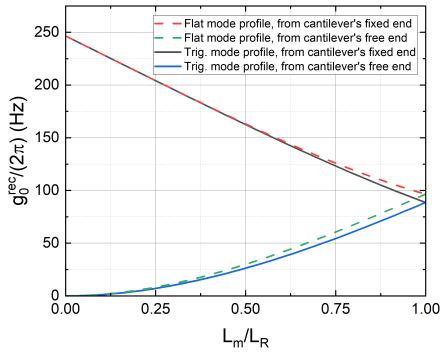

FIGURE 5.11: Trigonometric mode profile g_0^{rec} for a cantilever resonator assuming for a ratio of coverage of magnetic structure, $L_{\mathrm{m}/L_{\mathrm{R}}}$, with origins taken at the cantilever's fixed or free end.

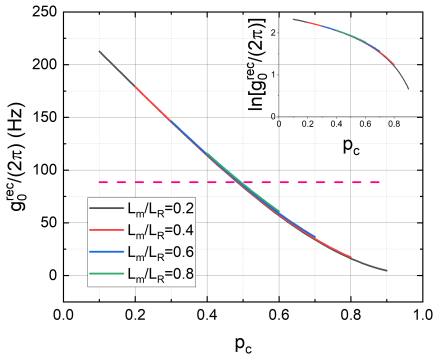

FIGURE 5.12: Trigonometric mode profile g_0^{rec} for a cantilever resonator in moving magnetic structure sections along the resonator's length. The dotted line indicates the value of g_0^{rec} for full coverage with magnetic structure.

Fig. 5.11 shows the analogous plot to Fig. 5.5. This is dependence of g_0^{rec} as a function of the ratio $L_{\mathrm{m}}/L_{\mathrm{r}}$ for the fundamental mode. The same two cases are presented as was done prior, with the ratio of resonator to magnetic structure lengths having origins taken at the the cantilever's fixed or free end for either case. The inclusion of a physically realistic trigonometric mode profile offers little affect to the theory derived, and only produces a marginal loss to the value of g_0^{rec}. This loss appears dependent on the length ratio, with the largest loss seen for a coverage ratio of $L_{\mathrm{m}}/L_{\mathrm{r}} = 1$ and the impact of the inclusion of the profile being minimised as the ratio $L_{\mathrm{m}}/L_{\mathrm{R}}$ becomes smaller.

Lastly, Fig. 5.12 shows the analogous plot to Fig. 5.6. This is how g_0^{rec} varies as sections of magnetic structure of lengths of $0.2L_{\mathrm{R}}$, $0.4L_{\mathrm{R}}$, $0.6L_{\mathrm{R}}$ and $0.8L_{\mathrm{R}}$ are moved along the length of the resonator. The same presentation of the data is used as in Fig. 5.6, in which the central magnetic position of the magnetic material with respect to the length of the resonator, p_{c}, is introduced to describe it's placement. The linearity of the function is largely preserved from the cantilever's curvature, but trajectories deviate far less as p_{c} approaches the free end of the cantilever given the effective windowing of the spatial average that the inclusion of a realistic mode profile introduces. It is still the case that placement of magnetic material towards the fixed end of the cantilever yields larger values than those for the free end, and that g_0^{rec} offers slightly smaller values than the assumption of a flat magnetisation mode profile.

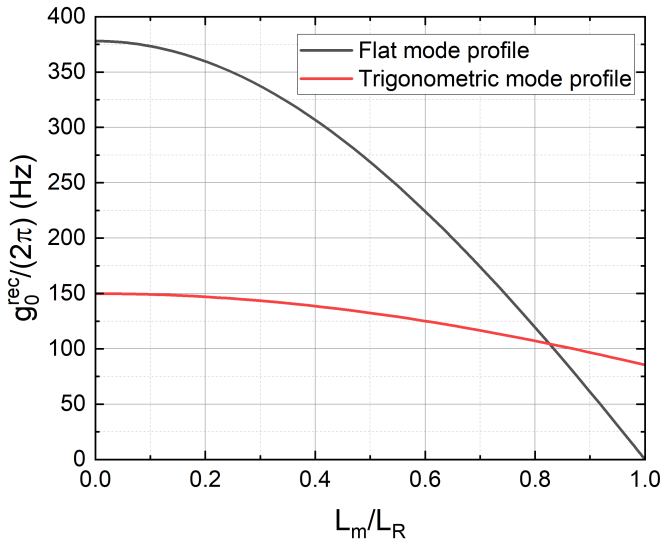

FIGURE 5.13: Trigonometric mode profile g_0^{rec} for a bridge resonator as a function of the ratio of magnetic structure length to resonator length, with the magnetic structure placed centrally at $x = L/2$.

5.3.4 Bridge

As was the case for the cantilever resonator, inclusion of the magnetisation mode profile windows the bridge's curvature which, in general, produces a reduction in the values of g_0^{rec}. However, there is a benefit to it's inclusion in that the length average of the curvature for a magnetic structure which covers the bridge resonator surface entirely no longer reduces to 0 as was seen in Figs. 5.8 and 5.9. Assumed again are comparable dimensions as were used for the previous figures ($L_{\text{R}} = 6\,\mu\text{m}$ and $w_{\text{R}} = 200\,\text{nm}$), and applied field of $H_{\text{e}} = 350\,\text{Oe}$, and the cross-section of the resonator is taken as isosceles in shape).

Shown again in Fig. 5.13 is analogous plot to Fig. 5.8. This is the behaviour of g_0^{rec} for the bridge resonator as a function of the ratio $L_{\text{m}}/L_{\text{R}}$, where the magnetic material begins at the bridge's centre point and approaches the bridge's fixed ends equally. In assuming a profiled magnetisation, larger values of g_0 are obtained for centrally placed lengths of magnetic structure of $0.84L$ or larger, with the largest increase in g_0 relative to the flat profile obtained for full coverage of the bridge which is now a viable geometry.

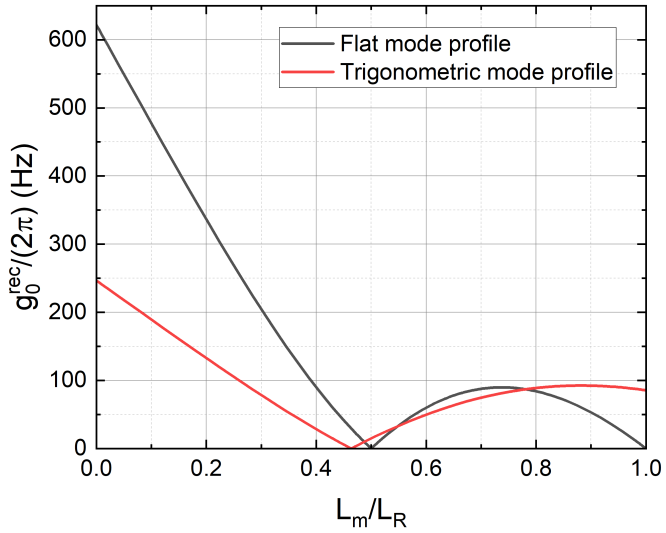

FIGURE 5.14: Trigonometric mode profile g_0^{rec} for a bridge resonator as a function of the ratio of magnetic length to resonator length, with the magnetic structure beginning from a fixed end of the bridge.

Fig. 5.14 is the analogous plot to Fig. 5.9. In this, g_0^{rec} is shown for the bridge resonator as a function of $L_{\text{m}}/L_{\text{R}}$, where the origin is taken at one of the bridge's fixed ends. Again, due to the symmetry of the curvature profile of the bridge, there is no distinguishing features between which end is fixed and which end is free. In adopting the spatial dependence of the magnetisation, there then exists a point at which preferential values for g_0^{rec} are seen. This corresponds to a magnetic structure length of $0.78L$ for this scheme. While not of huge significance, it is also seen that covering the first half of the cantilever no longer results in g_0^{rec} becoming 0 - this is instead seen for the slightly smaller ratio $L_{\text{m}}/L_{\text{R}} = 0.45$.

5.3.5 Higher order magnetisation profiles

While the trigonometric profile assumed in Sec. 5.3.1 offers a mathematically idealised description for the profile of the magnetisation in which the fluctuations vanish at the transverse boundaries of the magnetic structure, it is not necessarily the most physically accurate description to utilise. Maxwell's equations as applied to the boundary leave the amplitude of the dynamic magnetisation at the boundaries of a rectangular magnetic stripe undefined [149]. It is often assumed that the magnetisation at the lateral edges of a magnetic stripe act as magnetic walls and this can be treated as fictitious boundary conditions [14], which leads to a quantisation of the magnon wave-vector $\mathbf{k}$ along the finite size of the waveguide (which corresponds to the width, w_{m} for the geometry adopted in this thesis). Present here are two 'higher' order corrections to consider which arise from dipolar pinning of the magnetic moments at the lateral surfaces of the magnetic structure. One of these models is to still assume a simple trigonometric profile, but instead use an effective magnetic width description in the smaller of the two transverse dimensions, arising from the quantisation of the wave-vector in that dimension [156]. The other model is to fit a Fourier series directly to the simulated magnetisation profile of the magnetic structure as obtained from OOMMF simulations.

Dipolar pinning

In this section, the theory developed by Guslienko *et. al* [156] is followed. They consider an axially magnetised rectangular cross-section stripe. In the coordinate system presented in this thesis, their dimensions correspond to a thickness t_m and width w_m, with $t_m << w_m$, and a coordinate system taken to coincide with the centre of mass. This is depicted in Fig. 5.15.

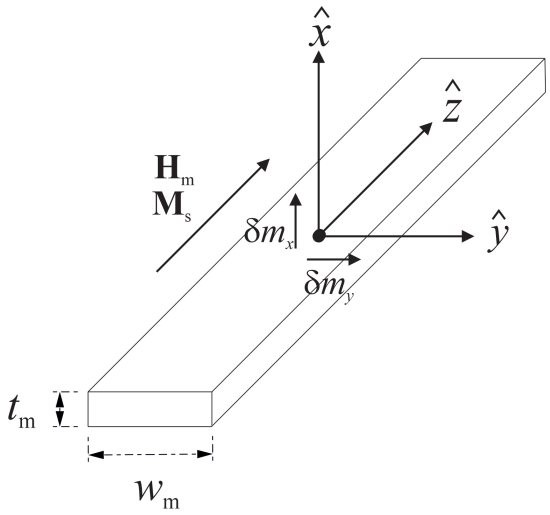

FIGURE 5.15: Geometry of the axially magnetised stripe.

The boundary condition assumptions produce a quantisation condition for the wave-vector directed along one of the lateral dimensions as

$$k = \frac{n\pi}{a}, \tag{5.70}$$

where $n = 0, 1, 2, ...$ is the mode number of the spin-wave, and a is the characteristic length of the dimension [14]. The profiles of the magnetisation are assumed to be trigonometric in nature but their behaviour at the edges is undetermined due to the boundary conditions. Analysis of the boundary conditions [156] leads to the introduction of the pinning parameter for the y-direction as

$$d(p) = \frac{2\pi}{p\left(1 + 2\ln\frac{1}{p}\right)} \tag{5.71}$$

where the aspect ratio of the cross-section is $p = t_m/w_m << 1$. With this condition, the wave-vector is augmented with

$$k_n = \frac{(n+1)\pi}{w_m}\left(1 - \frac{2}{d(p)}\right). \tag{5.72}$$

for $n = 0, 1, 2, ...$ It is then identifiable from this that there is an 'effective' magnetic width expressed as

$$w_{\text{eff}} = w_m\left(1 - \frac{2}{d(p)}\right)^{-1}. \tag{5.73}$$

As $p << 1$, then it must be the case that $d(p) < 0$ which further implies that $w_{\text{eff}} > w$ [157, 158, 159, 160].

This effective width description may then be used to proceed through the quantisation of the Kittel mode again. For this, the fluctuations of the Kittel mode are assumed to have spatial dependence as

$$(\delta m_x, \delta m_y) \rightarrow (\delta m_x, \delta m_y) \cos\left(\frac{\pi y}{w_{\text{eff}}}\right) \cos\left(\frac{\pi z}{L_{\text{m}}}\right), \tag{5.74}$$

where any limits in the integration over the width of the structure remain over $w_{\text{m}}/2$ to $-w_{\text{m}}/2$. As before, for convenience it is stated

$$\begin{aligned}\int_{V_{\text{m}}} \cos^2\left(\frac{\pi y}{w_{\text{eff}}}\right) \cos^2\left(\frac{\pi z}{L_{\text{m}}}\right) \mathrm{d}V \\ = V_{\text{m}} \int_{-\frac{1}{2}}^{\frac{1}{2}} \mathrm{d}x \int_{-\frac{1}{2}}^{\frac{1}{2}} \cos^2\left(\pi y \left(1 - \frac{2}{d}\right)\right) \mathrm{d}y \int_{-\frac{1}{2}}^{\frac{1}{2}} \cos^2(\pi z)\, \mathrm{d}z \\ = \frac{V_{\text{m}}}{4}\left(\frac{d \sin(2\pi/d)}{2\pi(d-2)} + \frac{1}{2}\right)\end{aligned} \tag{5.75}$$

where the argument of p from $d(p)$ is dropped for convenience only.

In following the quantisation procedure as in Sections 5.1.1 and 5.3.1, the Kittel mode Hamiltonian to the lowest order in the small parameter t_{m} is expressed as

$$H_{\text{SW}} = \frac{V_{\text{m}}}{4}\left(\frac{d \sin(2\pi/d)}{2\pi(d-2)} + \frac{1}{2}\right)\left(\frac{1}{2} M_{\text{s}} H_{\text{e}} \left(\delta m_x^2 + \delta m_y^2\right) + 2\pi M_{\text{s}}^2 \delta m_x^2\right) \tag{5.76}$$

which can be seen to again be equivalent to the simple trigonometric profile and flat mode profile Hamiltonian with the existance of a numerical prefactor. In proceeding through the coherent mode approach, it is found

$$\frac{g_{\text{e}}\mu_{\text{B}}}{2} V_{\text{m}} \left(\frac{d \sin(2\pi/d)}{2\pi(d-2)} + \frac{1}{2}\right) A_0^2 \left(2\pi M_{\text{s}} + \frac{H_{\text{e}}}{2}\right) = g_{\text{e}}\mu_{\text{B}} H_{\text{e}} \left(1 + \frac{4\pi M_{\text{s}}}{H_{\text{e}}}\right)^{\frac{1}{2}} \tag{5.77}$$

from which A_0 may be identified as

$$A_0 = 2\sqrt{\frac{1}{V_{\text{m}}}\left(\frac{d \sin(2\pi/d)}{2\pi(d-2)} + \frac{1}{2}\right)^{-1}} \left(1 + \frac{4\pi M_{\text{s}}}{H_{\text{e}}}\right)^{-\frac{1}{4}}. \tag{5.78}$$

The Kittel mode fluctuations are then

$$\begin{aligned}\delta m_{x,0}^{+} &= \sqrt{\frac{2\hbar\gamma_{\text{g}}}{M_{\text{s}} V_{\text{m}}}\left(\frac{d \sin(2\pi/d)}{2\pi(d-2)} + \frac{1}{2}\right)^{-1}} \left(1 + \frac{4\pi M_{\text{s}}}{H_{\text{e}}}\right)^{-\frac{1}{4}} c_0^{\dagger} \cos\left(\frac{\pi y}{w_{\text{eff}}}\right) \cos\left(\frac{\pi z}{L_{\text{m}}}\right) \\ \delta m_{y,0}^{+} &= i\sqrt{\frac{2\hbar\gamma_{\text{g}}}{M_{\text{s}} V_{\text{m}}}\left(\frac{d \sin(2\pi/d)}{2\pi(d-2)} + \frac{1}{2}\right)^{-1}} \left(1 + \frac{4\pi M_{\text{s}}}{H_{\text{e}}}\right)^{\frac{1}{4}} c_0 \cos\left(\frac{\pi y}{w_{\text{eff}}}\right) \cos\left(\frac{\pi z}{L_{\text{m}}}\right)\end{aligned} \tag{5.79}$$

where $\gamma_{\text{g}} = g_{\text{e}}\mu_{\text{B}}/\hbar$.

These expressions don't offer as large a boost to the quantisation pre-factor as in assuming a simple trigonometric profile. For an example, if an aspect ratio of $p = 10$ is assumed, then the first term in the bracket of Eq. 5.79 yields a value of 0.0127. Compared to the trigonometric profile, it is just slightly larger than the $1/2$ obtained. Nonetheless, they represent a more accurate interpretation of the mode profile.

While the pre-factors of the fluctuations are smaller than those of the trigonometric profiles, in the schemes considered for the device presented they make no difference. For our structures, a rectangular geometry is assumed. In determining the value of g_0, the magnetoelastic energy density is integrated over the magnetic structure yielding a spatial average as

$$\left\langle \sin^2\left(\frac{\pi y}{w_\mathrm{m}}\left(1-\frac{2}{d}\right)\right)\sin^2\left(\frac{\pi z}{L_\mathrm{m}}\right)\phi_n''(z)\right\rangle_{S_\mathrm{m}},$$

where the magnetic origin is changed to coincide with the elastic one. However, in assuming a rectangular geometry, the surface integral reduces to two separate integrals and it is found for the average along the width

$$\int_{-\frac{1}{2}}^{\frac{1}{2}}\cos^2\left(\pi y\left(1-\frac{2}{p}\right)\right)\,\mathrm{d}y=\frac{1}{2}\left(\frac{d\sin(2\pi/d)}{2\pi(d-2)}+\frac{1}{2}\right). \tag{5.80}$$

This factor cancels directly with the the fluctuation pre-factor obtained as a result of the quantisation. Gains/losses to g_0^rec are determined entirely by the magnetisation profile with respect to the length of the structure, which is unchanged with this dipolar pinning consideration.

OOMMF simulations

There are even higher order corrections that can be seen to the magnetisation profile. While the trigonometric interpretation is more representative of the physics at hand rather than assuming a flat profile, it still does not capture the actual physics of the system [161, 162, 163].

Present here is a simulation of a YIG thin-film structure using the Object Oriented MicroMagnetic Framework, otherwise known as OOMMF [164]. OOMMF is a micromagnetic simulator, in that magnetic properties are attributed as an average to a macroscopic cell, a number of which then make up a mesh representing the geometry being simulated; this is opposed to atomistic simulators that instead model the behaviour of individual magnetic moments that form the crystal structure and hence the sample geometry. Micromagnetic codes offer a significant reduction in the run-time of simulations in assuming bulk qualities [165, 166], and allow large-scale structures [167, 168, 169] to be simulated without the limiting factor of computational power as is often required with atomistic models [170, 171].

To match the required inputs for OOMMF, the parameters used for the YIG system are given in the MKS unit system. To describe the YIG material, assumed are a saturation magnetisation $M_s = 1.4\times10^5\,\mathrm{Am}^{-1}$ [172, 173], an exchange stiffness $A = 3.7\times10^{-12}\,\mathrm{Jm}^{-1}$ [174], and a Gilbert damping $\alpha = 0.0001$ [12]. As anistropy is known to be very weak in YIG [175], it is neglected from inclusion in the simulations to match the theory derived so far. A rectangular geometry of dimensions 30 nm by 400 nm by 10 μm, corresponding to the thickness, width, and length of the structure, is assumed as well as this geometry being sufficiently generic to apply to dimensions in which the relevant aspect ratios are approximately held. This geometry is then discretised using a rectangular mesh of cells of dimensions $(30\times15\times15)$ nm, resulting in a geometry that is 1 by 27 by 667 cells. The stopping time used in outputting stage data is $\delta t = 10^{-11}$s, which in Fourier space gives a maximum frequency of 50 GHz, and run the simulation for 2000 stages, giving a resolution of 0.025 GHz. The geometry of the mesh has imposed that the structure is one cell thick, which in essence is asserting that there is no variation of the magnetisation

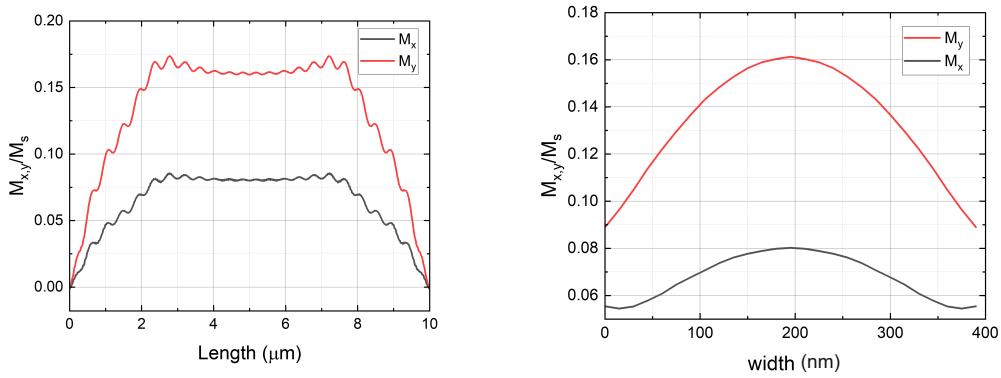

FIGURE 5.16: Fluctuations of the magnetisation profile along the length and width of a thin-film magnetic structure.

through the thickness of the structure. For thin-film simulations this grid may seem coarse, but in the lateral dimensions the cell-size is less than the exchange length of YIG (roughly around 17 nm) which in principle means that exchange effects are still captured. Further, assuming a one cell thick film also presents valid results provided that the cell-size is less than the wavelength of spin-wave being investigated [176, 177]. For the fundamental mode, this is easily satisfied. An external biasing field of 35 mT is applied along the length of the structure, and a sinusoidally varying driving magnetic field is induced, applied across the width of the structure, to excite the resonant dynamics. The amplitude of this field has been chosen to be 0.05 mT, and its frequency is equivalent to the fundamental resonant mode of the film ($f_m \approx 2.7$ GHz).

Shown in Fig. 5.16 are the components of the magnetisation profile along the length and width of the magnetic structure under simulation. Here, the x and y components are taken at their maximum, and then oscillate $\propto \exp(i\omega_m t)$ along with the driving field. Note that a number of these profiles were checked at timescales on the order of 10, 100, and 1000 oscillations and all profiles look (roughly) the same; this eliminates the effect of any other possible transients. Clearly, the profiles presented in these plots do not match the flat assumptions first assumed in deriving the theory contained withim. However, the x and y components are not too dissimilar from the trigonometric profiles that were assumed as a higher order correction. The magnetisation profile offered along the length of the structure more closely resembles the Mathieu functions as described by Gubbiotti [161] and seen experimentally [178]. Similarly, the magnetisation profile offered across the width of the structure shows the effective magnetic width as described by Guslienko [156]. The y-component of the magnetisation does not match this theory exactly, and even for being driven at the fundamental mode's frequency it appears that there are slight anti-nodes towards the extremes of the profile which isn't seen with the x-component. In principle, this would mean that the fundamental mode is not being exclusively excited, and some higher order mode is simultaneously existing. Finite size effects exist which act to break the symmetry of the structure and in turn allow higher order modes to be excited, such as edge modes, and the effect of demagnetisation cannot be simplified to that of an infinite film as has been assumed. Shown further in Fig. 5.17 are the Fourier transform of the oscillating magnetisation components such that the constituent frequencies may be identified. Additionally shown in Fig. 5.17 are the spatial character of the specific frequencies identified, which show where in the film these resonances are taking place. This data is presented as heatmaps, in

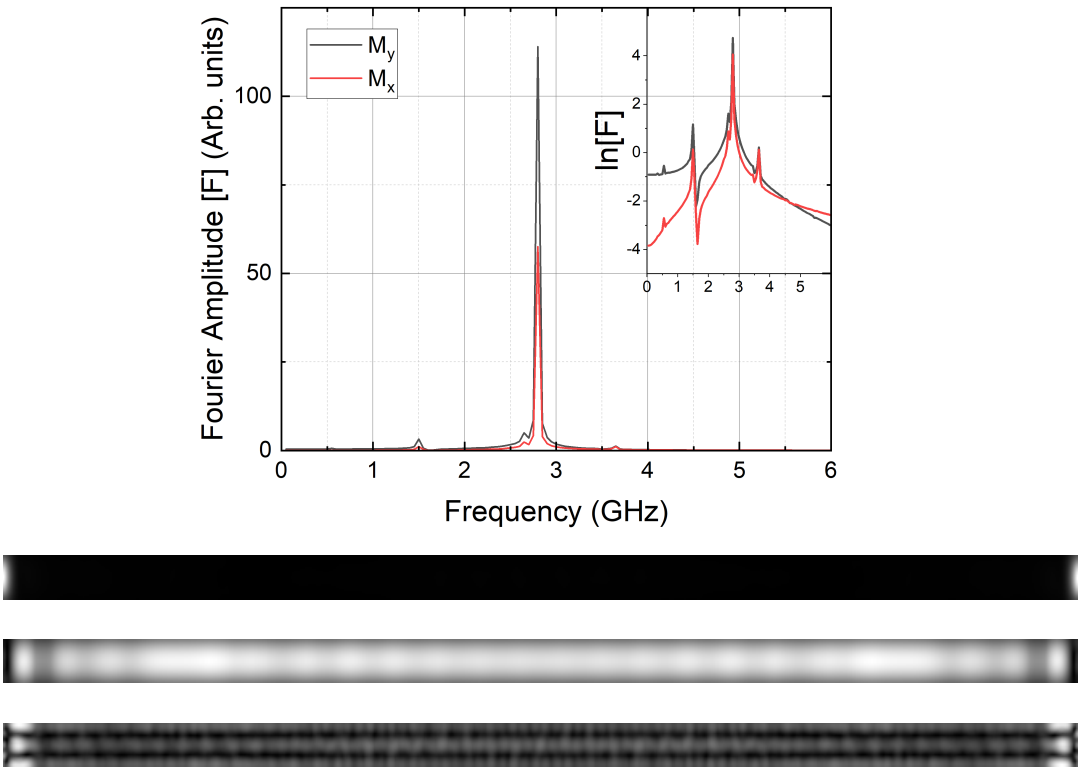

FIGURE 5.17: The graph shows the resonant frequencies of the oscillating components of the magnetisation for a drive field at the Kittel mode frequency, obtained via Fourier transform. Heat maps depict the spatial character of the peaks identified, namely 1.5 GHz, 2.7 GHz, and 3.75 GHz, in descending order.

which white corresponds to maximal relative intensity of the individual frequencies. Clearly, despite the structure being driven at resonance, other modes still exist which impact the magnetisation profile. The existence of these modes goes some way to explaining the additional anti-nodes seen in the magnetisation profile.

Lastly, a function is fitted to the simulated mode profile to obtain a semi-analytic function which describes the mode profile of the fluctuations of the magnetisation. For this, a progressive sinusoidal fitting is used whereby successive terms in the series represent sine waves of increasing numbers of anti-nodes, akin to a Fourier decomposition. This function has the form

$$f_n(x) = \sum_n A_n \sin\left(\frac{(2n-1)\pi x}{L}\right), \tag{5.81}$$

where A_n are the amplitudes of each sin term of number of anti-nodes n, and L is the length of the dimension. Assuming a rectangular magnetic structure which was seen to cancel the influence of the mode profile across the width, only the mode profile along the length of the structure is focused on. For this, the profile is normalised such that its maximum is 1, and for the simplicity of fitting it is further assumed $L = 1$. Shown in Table 5.2 are the pre-factors for this expression for the first 8 functions.

n	A_1	A_2	A_3	A_4	A_5	A_6	A_7	A_8
1	1.121	-	-	-	-	-	-	-
2	1.121	0.152	-	-	-	-	-	-
3	1.121	0.152	-0.011	-	-	-	-	-
4	1.121	0.152	-0.011	0.012	-	-	-	-
5	1.121	0.152	-0.011	0.012	0.027	-	-	-
6	1.121	0.152	-0.011	0.012	0.027	0.006	-	-
7	1.121	0.152	-0.011	0.012	0.027	0.006	-0.010	-
8	1.121	0.152	-0.011	0.012	0.027	0.006	-0.010	-0.008

TABLE 5.2: Prefactors for the sine wave fitting of Eq. 5.81 for successive values of n. Here, the first 8 terms are given.

Likewise, shown in Fig. 5.18 are the R-square values for these functions, along with the inset showing the conformity of the first 2 functions to the simulated mode profile. Fig. 5.18 shows that for terms above $n = 2$ the correction to the R-square value is less than 0.01, and so these corrections can be considered negligible. Likewise, even for a single term of the sine expansion, an R-square of 0.85 can be achieved which is a good agreement, and the addition of a second term increases that to 0.99 which is almost maximal.

Finally, the effect of these mode profiles on the spatial average in the calculation of g_0^{rec} is considered in Fig. 5.19. The magnetic structure is taken to be rectangular such that the spatial average reduces to the length average and the solid lines in these plots represent the length averages of the fitting functions collated in Table 5.2. The non-solid lines are used for comparison; the dotted lines represent the length average under the assumption of a flat mode profile, and the dashed line represents the

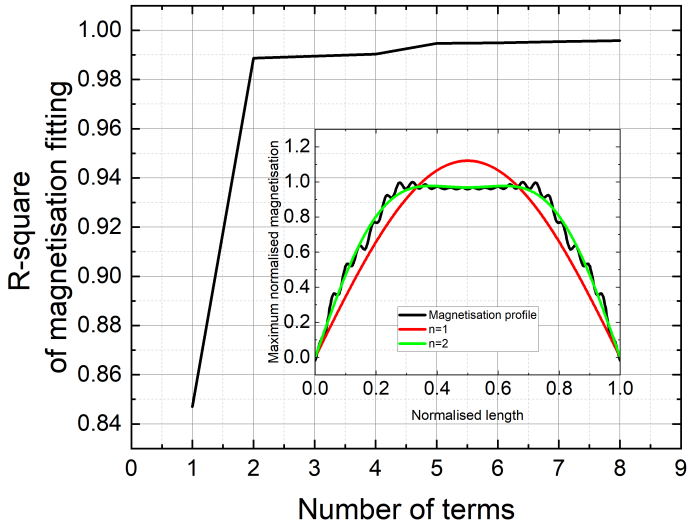

FIGURE 5.18: R-square fitting values for fitting the sine wave decomposition in Eq. 5.81 to the maximum normalised magnetisation profile. Inset shows form of the functions for $n = 1$ and $n = 2$ terms plotted alongside the magnetisation profile.

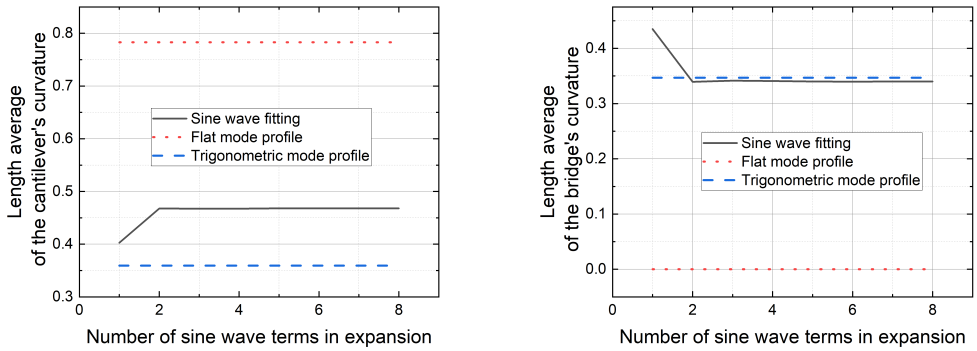

FIGURE 5.19: Plots showing the length average of the resonator's curvature as a function of the number of sine terms used in a fitting.

length average under the assumption of a simple trigonometric description. Interesting, for the bridge convergence is seen towards the simple trigonometric profile assumed, presumably because of the similarity in shape between the profile and the curvature. For the cantilever there is divergence away from description until the value plateaus. Clearly, in both cases, the length average using the flat mode profile massively deviates from the more realistic interpretation. As has been seen for the R-square value, relative correction to the length averages falls off after 2 terms in the sine fitting.

5.4 Photon decay into magnon modes

In the classical picture, the oscillating drive field of the transmission line applies a 'torque' to the magnetic moments which causes them to precess. In the quantum picture, photons excited by the transmission line can decay into the magnons modes of the magnetic material. Considered here is this decay of photons into the Kittel mode, a step necessary in the determination of the number of magnomechanically relevant magnons in Eq. 4.24. The magnetic structure is assumed to be placed a distance d_c centrally above a conducting wire, and is pictorially represented in Fig. 5.20.

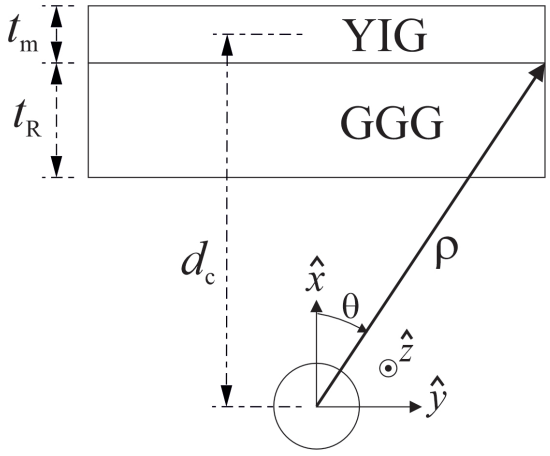

FIGURE 5.20: Representation of the magnetic material above a conducting wire. The plane of view is taken down the length of the structure

The magnetic field of this wire is known to be given by [179]

$$\mathbf{B}(\boldsymbol{\rho}) = \frac{2I}{c\rho}\hat{\theta} \tag{5.82}$$

where ρ is the magnitude of the radial distance from the wire, I is the current flowing through the wire, and $\hat{\theta}$ is a radial unit vector.

In considering the interaction between the magnetic moments and the magnetic field, one need only consider the fluctuating part as driving the dynamics, and only consider the magnetic field coupling to the fluctuations of the Kittel mode, expressed by the integral

$$H_{\mathrm{M}} = -M_{\mathrm{s}} \int_{V_{\mathrm{m}}} \delta\mathbf{m}(\mathbf{r}) \cdot \mathbf{B}(\mathbf{r})\, \mathrm{d}V. \tag{5.83}$$

It is assumed that the description of the mode profile reverts to that of the flat one discussed in Sec. 5.1.2 as a lowest order approximation. The effect and accuracy of this will be considered later. Under this assumption, one has

$$\delta\mathbf{m}(\mathbf{r}) \cdot \mathbf{B}(\mathbf{r}) = \delta\mathbf{m} \cdot \mathbf{B}(\mathbf{r}) = \frac{2I\delta m_y}{c\rho}\cos(\theta) \tag{5.84}$$

where θ is the angle measured from the plane perpendicular to both the planes of the magnetic structure and the conducting wire. Here, contributions of δm_x can be immediately neglected as these can be seen to average to 0 due to the reflection symmetry.

From elementary geometry, it is trivial to see that

$$\rho = \sqrt{x^2 + y^2}, \qquad \cos(\theta) = \frac{x}{\sqrt{x^2 + y^2}}, \tag{5.85}$$

such that the interaction between the magnetic field and magnetic moments may be expressed as

$$H_{\mathrm{M}} = -\frac{2IM_{\mathrm{s}}\delta m_y}{c} \int_{V_{\mathrm{m}}} \frac{x}{x^2 + y^2}\, \mathrm{d}V. \tag{5.86}$$

In the thin-film limit for which $t_{\mathrm{m}} << w_{\mathrm{m}}, L_{\mathrm{m}}$, the further approximation that variation in the $x-$direction is negligible as compared to the variation in the $y-$direction of the structure can be made; this then permits, as a rudimentary simplification, $x \to d_{\mathrm{c}}$ and the integral is further reduced to

$$H_{\mathrm{M}} = -\frac{2IM_{\mathrm{s}}\delta m_y}{c} \int_{V_{\mathrm{m}}} \frac{d_{\mathrm{c}}}{d_{\mathrm{c}}^2 + y^2}\, \mathrm{d}V. \tag{5.87}$$

Upon evaluation of this integral

$$\begin{aligned} H_{\mathrm{M}} = -\frac{2IM_{\mathrm{s}}\delta m_y}{c} \int_{-\frac{L_{\mathrm{m}}}{2}}^{\frac{L_{\mathrm{m}}}{2}} \mathrm{d}z \int_{d_{\mathrm{c}}-\frac{t_{\mathrm{m}}}{2}}^{d_{\mathrm{c}}+\frac{t_{\mathrm{m}}}{2}} \mathrm{d}x \int_{-\frac{w_{\mathrm{m}}}{2}}^{\frac{w_{\mathrm{m}}}{2}} \frac{d_{\mathrm{c}}}{d_{\mathrm{c}}^2 + y^2}\, \mathrm{d}y \\ = -\frac{4IM_{\mathrm{s}}\delta m_y L_{\mathrm{m}} t_{\mathrm{m}}}{2} \arctan\left(\frac{w_{\mathrm{m}}}{2d_{\mathrm{c}}}\right). \end{aligned} \tag{5.88}$$

The issue of quantising the modes of a transmission line is non-trivial but has been done in prior work [180] which is summised in Appendix A. For quantisation, it is found following from Eq. A.44 that the left- and right-propagating voltage modes

can be expressed as

$$\hat{V} = V^{\rightarrow} + V^{\leftarrow} = \sqrt{\frac{2\hbar\omega_q Z_{TL} v_p}{L_t}} \left(\hat{b}_q + \hat{b}_q^\dagger\right) \tag{5.89}$$

where ω_q is the photon frequency, Z_{TL} is the transmission line characteristic impedance, L_t is the length of the transmission line, and v_p is the group velocity. It is then easy to convert this expression to a current through Ohm's law. In substituting for Eq. 5.89 and Eq. 5.41, the interaction Hamiltonian becomes

$$H_M = -\frac{4M_s L_m t_m}{c} i \sqrt{\frac{\hbar\gamma_g}{2M_s V_m}} \left(1 + \frac{4\pi M_s}{H_e}\right)^{\frac{1}{4}} \arctan\left(\frac{w_m}{2d_c}\right) \times \sum_q \sqrt{\frac{2\hbar\omega_q v_p}{L_t Z_{TL}}} \left(\hat{b}_q + \hat{b}_q^\dagger\right) \left(c_0 - c_0^\dagger\right). \tag{5.90}$$

The decay rate between photon modes and the Kittel mode then follows from Fermi's Golden Rule [108, 181]

$$2\kappa_{ex} = \frac{2\pi}{\hbar} |\langle i|H|f\rangle|^2 \, \delta\left(\hbar\omega_q - \hbar\omega_m\right) \tag{5.91}$$

where $\langle i|$ and $|f\rangle$ are the initial and final states, respectively, and H is the interaction Hamiltonian. Note that here the factor of 2 accounts for both the left- and right-moving modes in the transmission line. The matrix elements can be evaluated and one finds for the decay rate

$$\kappa_{ex} = \frac{\pi}{\hbar} \frac{16 M_s^2 L_m^2 t_m^2}{c^2} \frac{\hbar\gamma_g}{2M_s V_m} \left(1 + \frac{4\pi M_s}{H_e}\right)^{\frac{1}{2}} \arctan^2\left(\frac{w_m}{2d_c}\right) \sum_q \frac{2\hbar\omega_q c}{L_t Z_{TL}} \delta\left(\hbar\omega_q - \hbar\omega_m\right), \tag{5.92}$$

which is then to be integrated over the density of states of the transmission line. For a transmission line producing a 1-dimensional density of states [179], it is known

$$|q| = \frac{\omega_q}{c}, \qquad q_n = \frac{2\pi n}{L_t}, \tag{5.93}$$

and the density of states follows as

$$g(\omega_q) = \frac{L_t}{\pi c}. \tag{5.94}$$

Exchanging summation for integration over this density, the decay rate is constructed as

$$\kappa_{ex} = \frac{\pi}{\hbar} \frac{16 M_s^2 L_m^2 t_m^2}{c^2} \frac{\hbar\gamma_g}{2M_s V_m} \left(1 + \frac{4\pi M_s}{H_e}\right)^{\frac{1}{2}} \arctan^2\left(\frac{w_m}{2d_c}\right) \frac{2\hbar c}{L_t Z_{TL}} \times \frac{L_t}{\pi c} \int_q \delta\left(\hbar\omega_q - \hbar\omega_m\right) \omega_q \, d\omega_q \tag{5.95}$$

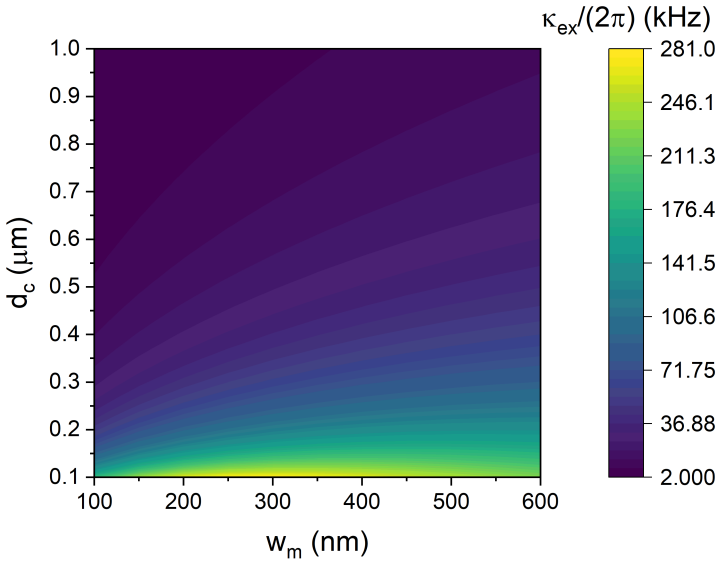

FIGURE 5.21: k_{ex} for a rectangular magnetic structure of width w_m placed centrally a distance d_c above a transmission line.

and, finally, an expression for the decay of photon modes into the Kittel mode is obtained as

$$\kappa_{ex} = \frac{16 M_s \gamma_g L_m t_m \omega_m}{c^2 w_m Z_{TL}} \left(1 + \frac{4\pi M_s}{H_e}\right)^{\frac{1}{2}} \arctan^2\left(\frac{w_m}{2d_c}\right) \tag{5.96}$$

which offers a rudimentary estimate.

The function is linear in L_m and t_m, and presents more complex scaling with w_m. Shown in Fig. 5.21 is the behaviour of this function for a YIG magnetic structure with regards to the parameters w_m and d_c in the ranges $[100 : 600]$ nm and $[0.1 : 1]$ μm. Considered are a magnetic structure length of $L_m = 6\,\mu$m, thickness $t_m = 25a_0$, an applied field of $H_e = 350\,$Oe and the transmission line is assumed to have an impedance of $Z_{TL} = 50\,\Omega$. As the cantilever and bridge structures are required to undergo flexure, central distances of the order of maximal displacement are not possible without interfering with the dynamics. To this end, $0.1\,\mu$m is assumed as the lower possible limit of the central distance. For reasonable dimensions (micron sized magnetic structure and central distance lengths with nanometer sized structure widths) then decay rates $\sim 10 - 100\,$KHz are attainable.

While the strength of interaction between the magnetic field and the magnetisation fluctuations simply increases with the magnetic volume (towards some plateauing value), for the decay rate (a quantum consideration) competition is introduced from the magnon quantisation for which the pre-factor is larger for a smaller magnetic volume. As such, the decay rate into the Kittel modes with this formulation has a maximal value for a specific width of magnetic structure relative to the central distance from the transmission line. From differentiation, the location of this maxima can be found as

$$\cot\left(\frac{2d_c}{w_m}\right)\left(\frac{1}{w_m}\cot\left(\frac{2d_c}{w_m}\right) - \frac{4d_c}{4d_{c^2} + w_m^2}\right) = 0 \tag{5.97}$$

for which there is no analytical solution. Shown in Fig. 5.22 is the decay rate as a

function of the width w_m, taken for a central distances of 0.10 μm, 0.15 μm, 0.20 μm, and 0.25 μm, with the same dimensions of YIG as prior. This produces a saturated decay rate of around $\kappa_{ex} = 300$ kHz at a magnetic structure width $w_m \approx 275$ nm and a central distance $d_c = 0.1\,\mu$m. For central distances $d_c \gtrsim 200$ nm, then saturating the decay rate doesn't appear feasible for our geometry of interest.

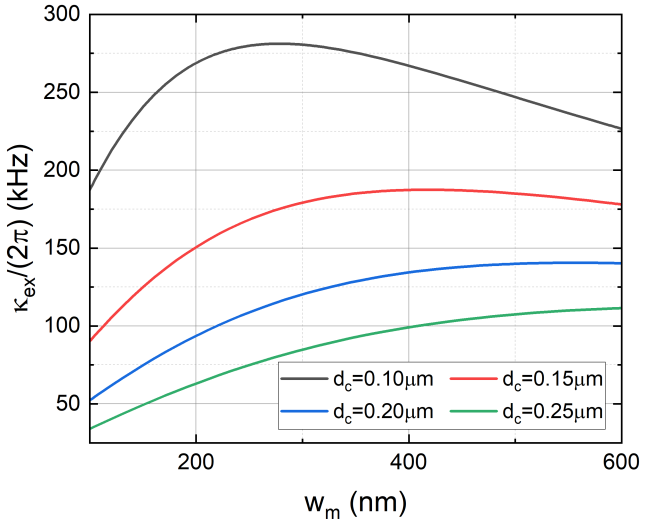

FIGURE 5.22: k_{ex} for a rectangular magnetic structure of width w_m, placed for varying central distance dc above a transmission line.

5.4.1 Higher order corrections to the decay rate

While prior it was stated that the flat mode profile is non-physical in representing the Kittel mode, there are significant complexities arising in repeating the procedure for the decay rate for a more physical description of the magnetisation. Specifically, complexities arise in evaluating the integral

$$\int_{-\frac{w_m}{2}}^{\frac{w_m}{2}} \cos\left(\frac{\pi y}{w_m}\right) \frac{d_c}{d_c^2 + y^2}\,\mathrm{d}y. \tag{5.98}$$

to a simple form which is non-trivial. In full, the integral can be shown to evaluate to

$$\frac{1}{2}\cosh\left(\frac{\pi d_c}{w_m}\right)\left(\pi - i\left(\mathcal{C}_i(F_-) + \mathcal{C}_i(F_+ - \pi) - 2\mathcal{C}_i(F_+)\right)\right) - \sinh\left(\frac{\pi d_c}{w_m}\right)\left(\mathcal{S}_i(F_-) + S_i(F_+)\right) \tag{5.99}$$

where the cos and sin integrals are defined as

$$\mathcal{C}_i(z) = -\int_z^\infty \frac{\cos(t)}{t}\,\mathrm{d}t \quad \text{and} \quad \mathcal{S}_i = \int_0^z \frac{\sin(t)}{t}\,\mathrm{d}t \tag{5.100}$$

with the argument

$$F_\pm = \pi\left(\frac{1}{2} \pm \frac{i d_c}{w_m}\right). \tag{5.101}$$

Given that this is not a simple function to evaluate, the behaviour is illustrated by considering the integral numerically, and it is solved for a few cases to compare against the analytic behaviour of the integral under the assumption of the flat mode profile. In Fig. 5.23 the difference between the two approaches of the integral is presented. In this, the black line represents the analytic solution to the integral under the assumption of a flat mode profile (which is to say $2\arctan(w_m/2d_c)$ is solved) and the red line represents the numerical solutions to Eq. 5.98. This is shown for the central distance $d_c = 1\,\mu$m, and then the width w_m is varied. The more realistic solution of a trigonometric mode profile lessens the decay rate, and as the width becomes larger this deviation from the analytic result for the flat mode profile becomes larger. In the theory presented, this under-prediction of the decay rate will most likely mean that fewer magnons are excited than what is representative, which would mean that the validity of the Kittel mode (i.e. much more spin sites than magnons) will be easier to meet than initially considered. As such, this does not present a concern for the theory contained within.

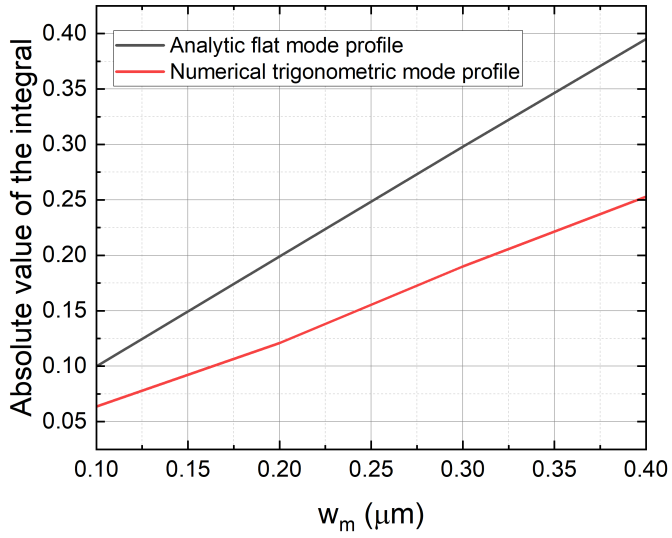

FIGURE 5.23: The behaviour of the integral over width in the decay rate for a rectangular magnetic structure of width w_m placed centrally a distance $d_c = 1\mu$m above a transmission line. Considered are the simple flat magnetisation mode profile and the trigonometric mode profile.

5.5 Justification of the single-mode model

Throughout this work, it has been assumed that the coupling of phonons only occurs to a single magnon mode (the single-mode model), but have yet to elaborate on this. Hybrid system theories may be derived under the assumption of a multi-mode model [182, 183, 184], and recent work has explored the coupling of the drive field used in magnomechanics to higher-order Walker modes in YIG spheres [185] finding variation within the coupling strengths. To this end, it would be preferential to ensure that there is coupling only to a single magnon mode.

To justify a single-mode model, one is required to show that the mode spacing of the magnons, denoted Δ_m, is much greater than that of the phonon frequency

($\Delta_m >> \omega_R$), such that the phonons do not couple to higher order magnetic excitations. This ratio

$$\frac{\omega_R}{\Delta_m} << 1 \tag{5.102}$$

is referred to as the single mode criterion (SMC), and ultimately is what is necessary to meet to consider a single mode model. With magnons in a thin-film magnetic structure, it is not as easy a task to consider the spacing between individual modes which is dependent on the dimensions of the magnetic structure, unlike with Walker modes of a sphere in which the higher order frequencies are close to that of the Kittel mode and largely independent of dimensions [186].

To determine how far in frequency space the Kittel mode of a thin film is from the next nearest magnon mode, one can again use OOMMF to investigate. The same YIG thin film structure as in Sec. 5.3.5 is considered, and the structure retains the same magnetic parameters as were listed. In order to investigate the higher order modes, an excitation which is non-uniform such that the symmetry of the structure is broken must be used. This could either be achieved by applying a uniform excitation to only a portion of the structure (for example, applying a Gaussian pulse to only a strip of the nanostructure), or applying an excitation that varies cell to cell for all cells (for example, applying a sinc pulse across the entire structure). Adopted here is the latter of the two approaches, where a sinc pulse [157] of the form

$$h(y,z,t) = \Gamma \frac{\sin(q_c y')}{q_c y'} \frac{\sin(q_c z')}{q_c z'} \frac{\sin(2\pi f_c t')}{2\pi f_c t'}, \tag{5.103}$$

where $y' = y - y_0$, $z' = z - z_0$, and $t' = t - t_0$ represent the 'offsets' in space and time, q_c are the bounds of the excitation wave-vector such that $-q_c < q < q_c$, f_c is the bounds of the excitation frequency such that $-f_c < f < f_c$, and Γ as the maximum amplitude of the sinc pulse. For the simulation, $(y_0, z_0) = (225\,\text{nm}, 5\,\mu\text{m})$ is chosen such that the pulse is applied centrally to the structure. Further, $q_c = 250 \times \frac{\pi}{L_m}$ which should excite the first 250 modes of the structure, and set $f_c = 50\,\text{GHz}$ (although, note that the magnetic moments are coupled and so modes with higher frequency can still be excited, in the same way that driving at the FMR frequency was seen to excite edge modes in Sec. 5.3.5). $\Gamma = 1\,\text{kA/m}$ is assumed to provide a sufficiently weak excitation to steer clear of non-linear dynamics.

For the meshing of our structure, a slight deviation from what was presented in Sec. 5.3.5 is needed. As $\omega(k)$ is the parameter of interest, it will be required to perform a 2-dimensional Fourier transform on the response of the structure in both the time-step, and also the relevant cell length. With this, the mesh size is not only relevant from the perspective of the accuracy of the simulation, but also relates to the accuracy of the Fourier transform. As aliasing is known to be an issue with the discrete Fourier transform [187], in which modes are folded back into the cut-off frequency regime, the large discrepancy between the sampling size of the frequency $\delta t = 10^{-11}$s, and the sampling size which is attainable with the mesh is a point to consider. Simulations are performed on a YIG thin-film structure for length $10\,\mu$m, width 450 nm and thickness 30 nm and the mesh is formed of cells of lengths 10 nm for the width and length of the resonator, and for thickness the thickness the cell length of 30 nm is retained. This corresponds to a mesh geometry of $1001 \times 4 \times 1$.

To obtain the dispersion branches, a 'slice' of the cells along the length of the structure down the centre of the width may be constructed, and a stack of these in time can be formed as the dynamics evolve from the application of the pulse. A two-dimensional Fourier transform is then applied to obtain the surface map of the

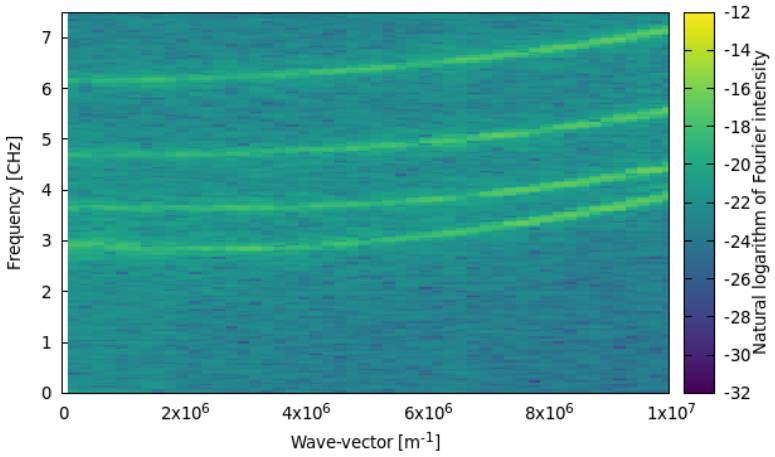

FIGURE 5.24: Dispersion branches obtained for a YIG thin film structure, with the wave-vector taken along the z-direction.

magnetisation intensities as a function of wave-vector and frequency, such that

$$m_z\left(q_z,\omega\right)=\mathscr{F}\left[m_z\left(x_0,y_0,z,t\right)-m_z\left(x_0,y_0,z,0\right)\right] \tag{5.104}$$

where $\mathscr{F}$ is used to denote the two dimensional Fourier transform and x_0 and z_0 are at the centre of the strip. The result of this procedure is shown in Fig. 5.24. From this, a branch separation of around 0.8 GHz can be extracted. The branch separation is not the next nearest mode, however. Each branch is composed of individual modes, but the simulations lack the spectral resolution to determine specifically what the separation between them is. For the frequency, a sampling of 0.025 GHz is attained from the time-step, but for the wave-vector a sampling of only 1.5×10^5 can be achieved. It's not immediately clear what the separation between the modes on a branch are, but it is clearly much less than these sampling frequencies.

Given that it is indeterminate what resolution OOMMF requires to resolve the modes along a branch, one can instead analyse the magnon dispersion relation in the case that the wave-vectors are small from a mathematical viewpoint, such that the modes considered approach the Kittel mode. The reader is referred to Appendix C for the derivation of the dispersion relation for a magnetostatic slab whose surface lays in the $y-z$ plane, and the magnetic field and saturation both being in-plane. In this procedure, it is found that the resonant frequencies may be expressed as

$$\omega^2=\gamma_\mathrm{g}H_\mathrm{e}\left(\gamma_\mathrm{g}H_\mathrm{e}+4\pi\gamma_\mathrm{g}M_\mathrm{s}\frac{q_x^2+q_y^2}{q^2}\right). \tag{5.105}$$

and that the permissible wave-vectors could be found via the relation

$$2q_x\cot\left(q_xt_\mathrm{m}\right)=\frac{1}{\sqrt{q_y^2+q_z^2}}\left(q_x^2-q_y^2-q_z^2-\frac{4\pi\gamma_\mathrm{g}M_\mathrm{s}}{\Omega}q^2\frac{q_y^2}{q_z^2}\right). \tag{5.106}$$

To analyse the behaviour of the resonant frequencies, a number of re-definitions are made to clarify nomenclature. Firstly, the dimensionless reduced saturation, defined as $\tilde{M}_\mathrm{s}=4\pi M_\mathrm{s}/H_\mathrm{e}$ is introduced. Also defined is the in-plane wave-vector as $q_\mathrm{p}^2=q_y^2+q_z^2$. As, in principle, the derivations performed in Appendix C are done

under the assumption that the thickness $t_m \to 0$, it makes little sense to discuss an $x-$component of the wave-vector. As such, this component is relabeled as $q_x \equiv q_<$ such that it appears distinct from the other components and avoids confusion. Also introduced is the reduced dimensionless wave-vector, $\tilde{q}$, which is express as the ratio of $\tilde{q} \equiv q_z^2/q_y^2$. Finally, the resonant frequency is defined, $\omega_* = \gamma_g H_e$, as well as the magnon resonance for a thin film, $\omega_0^2 = \omega_*^2(1+\tilde{M}_s)$, using the new notation for the reduced magnetisation.

With these re-definitions accounted for, one may re-express Eq. 5.105 in a slightly less cumbersome form

$$\omega^2 = \omega_*^2 + \omega_*^2 \tilde{M}_s \frac{q_x^2 + q_y^2}{q^2}. \tag{5.107}$$

These terms are then reorganised to find the expression

$$\omega^2 = \omega_*^2 + \omega_*^2 \tilde{M}_s - \omega_*^2 \tilde{M}_s \frac{q_z^2}{q^2}, \tag{5.108}$$

and hence the magnon frequency spectrum is re-expressed

$$\omega^2 = \omega_0^2 - \omega_*^2 \tilde{M}_s \frac{q_z^2}{q^2}. \tag{5.109}$$

Solving the partial fraction and dividing through by ω_*^2, the re-arranged expression

$$\frac{\omega}{\omega_*} = \sqrt{1 + \tilde{M}_s - \tilde{M}_s \frac{\tilde{q}}{1+\tilde{q}} \frac{q_p^2}{q_<^2 + q_p^2}}. \tag{5.110}$$

in terms of $\tilde{q}$ and q_p can be arrived at. With these expressions, the characteristic equation for the wave-vectors can be redefined as

$$2 q_p q_< \cot(q_< t_m) = q_<^2 - q_p^2 - \tilde{M}_s \left(q_<^2 + q_p^2\right) \frac{1}{\tilde{q}}. \tag{5.111}$$

Some elementary behaviour of these equations is first considered, in which two notable case are examined. These are the cases of $q_z = 0$, which results in surface waves, and of $q_y = 0$, which results in backwards volume waves.

Surface waves

For the case of surface waves (often called Damon-Eshbach modes), one assumes $q_z = 0$ such that waves have a wave-vector perpendicular to the saturation magnetisation and field. With some rearrangement, the characteristic equation in Eq. 5.111 can be reduced to

$$2\tilde{q} q_p q_< \cot(q_< t_m) = \tilde{q}(q_<^2 - q_p^2) - \tilde{M}_s(q_<^2 + q_p^2). \tag{5.112}$$

In the case that $q_z = 0$, the only way for this equation to hold is that

$$\tilde{M}_s(q_<^2 + q_p^2) = 0, \tag{5.113}$$

and since $\tilde{M}_s$ is non-zero, this further implies the unique property that

$$q_<^2 = -q_p^2 \Rightarrow q_< = i q_p. \tag{5.114}$$

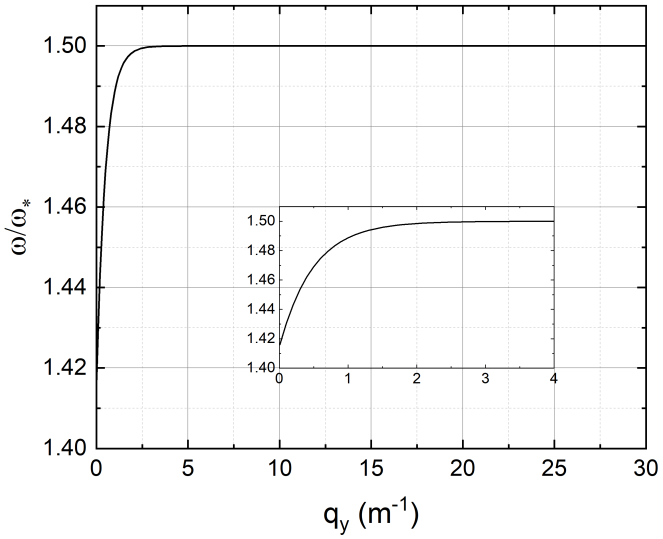

FIGURE 5.25: Magnon surface mode branch for a thin film as plotted from Eq. 5.118. Note that it is taken $\tilde{M}_s = 1$ as well as $t_m = 1$.

This relation is then used to solve for $q_<^2 + q_\mathrm{p}^2$, finding

$$\begin{aligned}
\tilde{M}_\mathrm{s}(q_<^2 + q_\mathrm{p}^2 &= \tilde{q}(q_<^2 - q_\mathrm{p}^2) - 2\tilde{q}q_\mathrm{p}q_< \cot\left(q_< t_\mathrm{m}\right) \\
\Rightarrow q_<^2 + q_\mathrm{p}^2 &= \frac{1}{\tilde{M}_\mathrm{s}}(-2\tilde{q}q_\mathrm{p}^2 - 2\tilde{q}q_\mathrm{p}^2 i\cot\left(iq_\mathrm{p}t_\mathrm{m}\right) \\
&= -\frac{2\tilde{q}q_\mathrm{p}^2}{\tilde{M}_\mathrm{s}}\left(1 + i\cot\left(iq_\mathrm{p}t_\mathrm{m}\right)\right) \\
&= -\frac{2\tilde{q}q_\mathrm{p}^2}{\tilde{M}_\mathrm{s}}\left(1 + \coth\left(q_\mathrm{p}t_\mathrm{m}\right)\right). \qquad (5.115)
\end{aligned}$$

With the relation

$$1 + \coth\left(x\right) = \frac{2\exp\left(2x\right)}{\exp\left(2x\right) - 1}. \qquad (5.116)$$

it follows from Eq. 5.115 that

$$q_<^2 + q_\mathrm{p}^2 = -\frac{4\tilde{q}q_\mathrm{p}^2}{\tilde{M}_\mathrm{s}}\left(\frac{\exp\left(2q_\mathrm{p}t_\mathrm{m}\right)}{\exp\left(2q_\mathrm{p}t_\mathrm{m}\right) - 1}\right). \qquad (5.117)$$

Lastly, substituting this into Eq. 5.110 and with some further rearranging the exact solution

$$\frac{\omega}{\omega_*} = \sqrt{\frac{\omega_0^2}{\omega_*^2} + \frac{\tilde{M}_\mathrm{s}{}^2}{4}\left(1 - \exp\left(-2q_\mathrm{p}t_\mathrm{m}\right)\right)} \qquad (5.118)$$

can be yielded, which is identical to the surface wave equation as derived prior by Stancil [24]. Note that there only exists a single branch branch with the surface wave character. Shown in Fig. 5.25 is the profile of this frequency spectrum under the assumption that $\tilde{M}_\mathrm{s} = 1$ such that $\omega_0^2 = 2\omega_*^2$, where $t_\mathrm{m} = 1$ is also taken for simplicity.

Backwards volume waves

For the case of backwards volume waves, it is assumed $q_y = 0$ such that the waves have a wave-vector parallel to the saturation magnetisation and field. With some rearrangement, the characteristic equation in Eq. 5.111 can be expressed as

$$2q_z q_< \cot\left(q_< t_\mathrm{m}\right) = q_<^2 - q_z^2 \tag{5.119}$$

Likewise, the frequency equation in Eq. 5.110 can be shown to reduce to

$$\frac{\omega}{\omega_*} = \sqrt{\frac{\omega_0^2}{\omega_*^2} - \tilde{M}_\mathrm{s}\frac{q_z^2}{q_<^2 + q_z^2}}. \tag{5.120}$$

Unlike was the case for the surface waves, the characteristic equation presents no analytic form and is transcendental. As such, there are two approaches to consider to yield solutions. The first of these is that, as $q_< t_m$ is small, an expansion of the cot term as a function of the small parameter $q_< t_\mathrm{m}$ can be used to achieve an approximate analytic form for the spin-wave frequencies close to the origin. The alternative is to numerically solve the characteristic equation to find the roots of the equation and then plot the frequency with these to find an exact, although not immediately conformable to an analytic form, solution.

Considered here is the first case in expanding the function. For small x, it can be shown that the cot function has a series expansion as given by

$$\cot(x) \approx \frac{1}{x} - \frac{x}{3} - \frac{x^3}{45} - \mathcal{O}(x^6), \tag{5.121}$$

where, as is standard, an infinite number of terms in the expansion are required to perfectly replicate the function at the specified point. As more higher order terms are included, the result becomes more accurate towards the function being replicated. For simplicity, the solution using the 1$^{\mathrm{st}}$-, 2$^{\mathrm{nd}}$-, and 3$^{\mathrm{rd}}$-order expansions of the cot function is used.

In using the 1$^{\mathrm{st}}$-order expansion, the characteristic equation in Eq. 5.119 reduces to find

$$q_<^2 = \frac{2}{t_\mathrm{m}} q_z + q_z^2. \tag{5.122}$$

With this, the frequency equation may be shown to reduce to

$$\frac{\omega}{\omega_*} = \sqrt{\frac{\omega_0^2}{\omega_*^2} - \frac{\tilde{M}_\mathrm{s}}{2}\frac{q_z t_\mathrm{m}}{q_z t_\mathrm{m} + 1}} \tag{5.123}$$

In using the 2$^{\mathrm{nd}}$-order expansion, the characteristic equation in Eq. 5.119 reduces to find

$$q_<^2 = \frac{\frac{2}{t_\mathrm{m}} q_z + q_z^2}{1 + \frac{2t_\mathrm{m}}{3} q_z} \tag{5.124}$$

With this, the frequency equation may be shown to reduce to

$$\frac{\omega}{\omega_*} = \sqrt{\frac{\omega_0^2}{\omega_*^2} - \tilde{M}_\mathrm{s}\frac{q_z t_\mathrm{m}\left(2q_z t_\mathrm{m} + 3\right)}{2q_z t_\mathrm{m}\left(q_z t_\mathrm{m} + 3\right) + 6}} \tag{5.125}$$

In using the 3rd-order expansion, the characteristic equation in Eq. 5.119 results in the polynomial

$$q_<^4\left(\frac{2}{45}q_z t\mathrm{m}^3\right)+q_<^2\left(1+\frac{2}{3}q_z t_\mathrm{m}\right)+\left(-q_z\left(\frac{2}{t_\mathrm{m}}+q_z\right)\right). \tag{5.126}$$

With the redefinition $x=q_<^2$, $x^2=q_<^4$ this may be solved this as a quadratic, under which it is find

$$x_{1,2}=\frac{-\left(1+\frac{2}{3}q_z t_\mathrm{m}\right)\pm\sqrt{\left(1+\frac{2}{3}q_z t_\mathrm{m}\right)^2+4\left(\frac{2}{45}q_z t_\mathrm{m}^3\right)\left(q_z\left(\frac{2}{t_\mathrm{m}}+q_z\right)\right)}}{\frac{4}{45}q_z t_\mathrm{m}^3} \tag{5.127}$$

and then reduced to the form

$$x_{1,2}=\frac{-1-\frac{2}{3}q_z t_\mathrm{m}\pm\sqrt{\frac{4}{45}q_z t_\mathrm{m}\left(q_z t_\mathrm{m}\left(2q_z t_\mathrm{m}+9\right)+15\right)+1}}{\frac{4}{45}q_z t_\mathrm{m}}. \tag{5.128}$$

With this, the frequency equation may be shown to reduce to

$$\frac{\omega}{\omega_*}=\sqrt{\frac{\omega_0^2}{\omega_*^2}-\tilde{M}_\mathrm{s}\frac{q_z^2}{\frac{-1-\frac{2}{3}q_z t_\mathrm{m}+\sqrt{\frac{4}{45}q_z t_\mathrm{m}\left(q_z t_\mathrm{m}\left(2q_z t_\mathrm{m}+9\right)+15\right)+1}}{\frac{4}{45}q_z t_\mathrm{m}}+q_z^2}}. \tag{5.129}$$

Clearly, successively higher terms give more unwieldy equations for use in a mathematical theory. An approximate form for the backwards volume mode has been derived by Kalinikos [188], giving

$$\frac{\omega}{\omega_*}=\sqrt{1+\tilde{M}_\mathrm{s}\left(\frac{1-\exp\left(-2q_z t_\mathrm{m}\right)}{q_z t_\mathrm{m}}\right)}. \tag{5.130}$$

As such, the functions derived from the series expansion are plotted against this to check their validity. For this, $\tilde{M}_\mathrm{s}=1$ such that $\omega_0=2\omega_0$, and again take $t_\mathrm{m}=1$ for simplicity. Shown in Fig. 5.26 is this comparison plot, along with an inset showing the behaviour of the functions for $q_z<0.03$. Clearly, the 1st-order approximation does not accurately capture the behaviour of the correct function beyond $q_z\gtrapprox 1$. However, the 2nd- and 3rd-order approximations offer much more accurate behaviour in the limit $q_z\gtrapprox 1$. If one assumes a length of magnetic structure of L_m 10, μm, a thickness of 30 nm, and assume that the wave-vectors are quantised as $q_z=n\pi/L_\mathrm{m}$, then one finds for the fundamental mode $q_z t_\mathrm{m}\approx 10^{-2}$ for which all orders of the approximation as well as the analytic form converge to the same line. As such, the 1st-order approximation would appear fine for the description of the magnon modes.

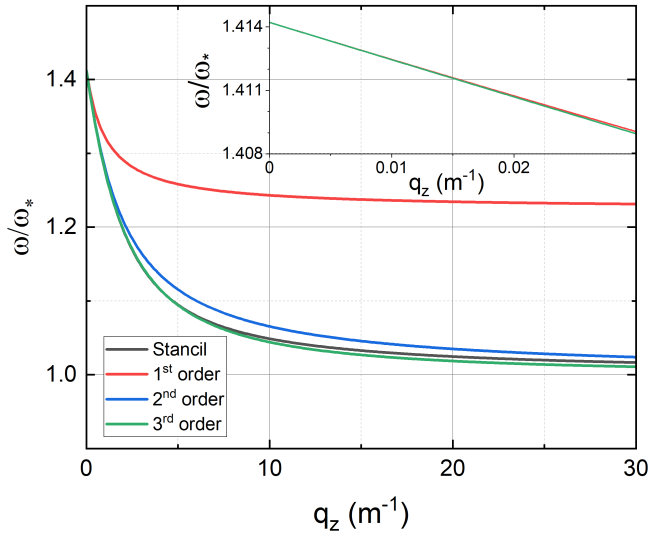

FIGURE 5.26: Comparison of the backwards volume mode description of a thin film as plotted from frequency equations using the series expansion in Eq. 5.121.

Lastly, the numerical behaviour of the characteristic equation for the backwards volume mode can be investigated, and plot the frequency obtained. Upon inspection of Eq. 5.119, it can be seen by means of a rudimentary plot (shown in Fig. 5.27) that, in taking $q_z = 1$, the fundamental root of the equation roughly corresponds to $\pi/2$, and that higher order roots converge to $n\pi$. This can be used as approximate lower bounds for each of the roots to start from with Mathematica's inbuilt Newton method. The simplified frequency equation

$$\frac{\omega}{\omega_*} = \sqrt{2 - \frac{q_z^2}{q_<^2 + q_z^2}} \tag{5.131}$$

can then be plotted where $\tilde{M}_s = 1$ and $t_m = 1$. The solutions to this are then also shown in Fig. 5.27 as a function of q_z, as well as the approximate expression obtained by Kalinikos. Clearly, for the limit of small q_z, it is seen again that the $n = 1$ and the approximate form both converge to the same line. Unlike for the surface waves, there exist an infinite number of branches with backwards volume behaviour - plotted only is the first 5.

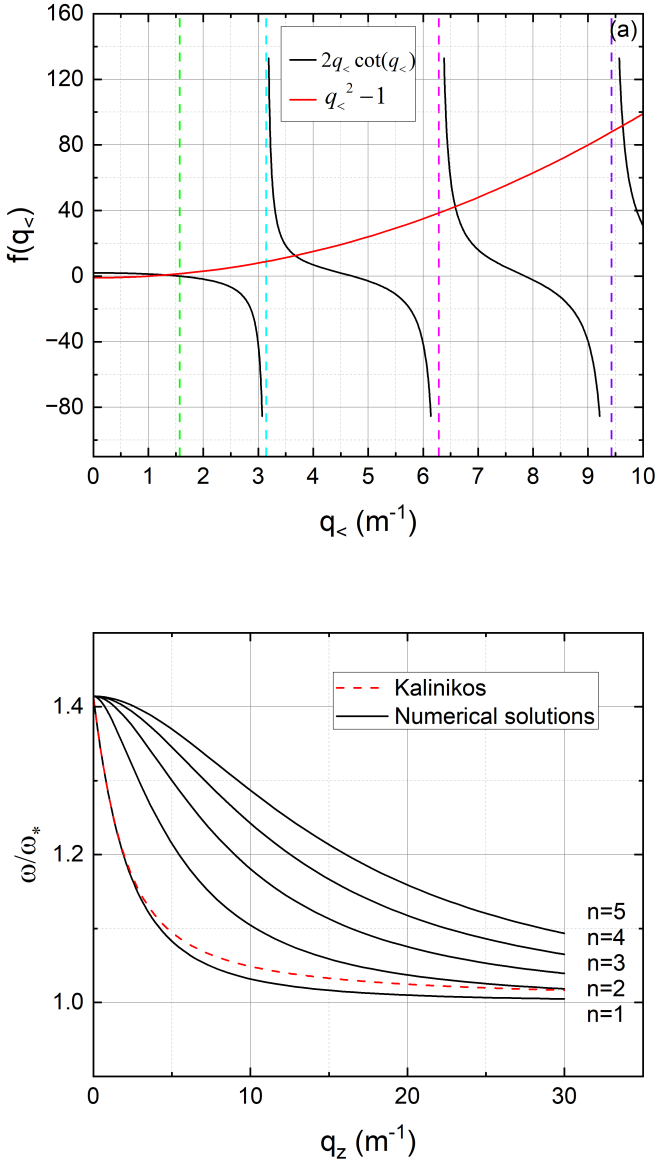

FIGURE 5.27: (a) The roots of the characteristic equation in Eq. 5.119, assuming that $q_z = 1$ and $t_m = 1$ for simplicity. Dashed vertical lines show the following: green represents $\pi/2$, cyan represents π, magenta represents 2π, and violet represents 3π. (b) The frequency that these characteristic roots yield as a function of q_z, compared to the expression obtained by Kalinikos.

Mixed modes

The characteristic equation is known to present a rich manifold of modes, and has been explored by Damon and Eshbach [189], pictorally presented in Fig. 5.28. This has the interesting feature that only the highest branch of the backwards volume mode shares the same plane with the surface wave branch, and that all other backwards volume branches converge to the Kittel mode. Also, the density of modes is infinite at the top of the bands, and decreases monotonically with frequency to the bottom of the band.

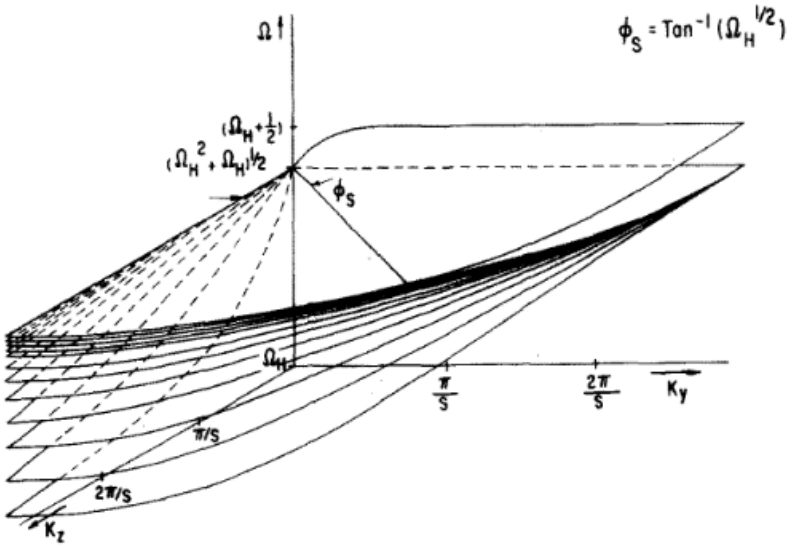

FIGURE 5.28: The spin-wave manifold of a magnetostatic slab [189]

Due to the quantisation of the wavevectors (in the most rudimentary consideration, the wavevectors would be found as $q_i = \frac{n\pi}{L_i}$, for $i = y, x$), the case of purely backwards volume mode or surface mode cannot be considered. As the geometries of the device proposed are of lengths an order of magnitude greater than widths, one should equally expect q_z to be about an order of magnitude larger than q_y, but not sufficiently so that it may be considered one or the other to be 0 with comparison to each. Rather, it is required to seek the expansion of the characteristic equation for the case of both pertinent wavevectors being small. In practice, this requires expanding for small $\tilde{q}$ which places no constraints on q_y, and then expanding for small q_y, which sets that q_y and q_z are both small. It is not possible to expand directly in q_y and q_z as this type of expansion is undefined given $1/q_z$.

Starting with the characteristic equation, this may be expanded to the lowest order in the small parameter $q_< t_\mathrm{m}$ to find an approximate analytical solution to use;

$$\frac{2q_p}{t_\mathrm{m}} \approx q_<^2 - q_\mathrm{p}^2 - \tilde{M}_\mathrm{s}\left(q_<^2 + q_\mathrm{p}^2\right)\frac{1}{\tilde{q}}. \tag{5.132}$$

In powers of q_p, this is rearranged to

$$q_<^2 = \frac{1}{t_\mathrm{m}}\frac{2\tilde{q}}{\tilde{q} - \tilde{M}_\mathrm{s}}q_\mathrm{p} + \frac{\tilde{q} + \tilde{M}_\mathrm{s}}{\tilde{q} - \tilde{M}_\mathrm{s}}q_\mathrm{p}^2, \tag{5.133}$$

which may then be expanded in powers of $\tilde{q}$ such that

$$q_<^2(q_\mathrm{p}, \tilde{q}) \approx q_<^2(q_\mathrm{p}, \tilde{q} = 0) + q_<^{2'}(q_\mathrm{p}, \tilde{q} = 0)\tilde{q} + \frac{1}{2}q_<^{2''}(q_\mathrm{p}, \tilde{q} = 0)\tilde{q}^2 + \ldots \tag{5.134}$$

To cubic order, this finds

$$q_<^2(q_\mathrm{p}, \tilde{q}) = -q_\mathrm{p}^2 - \frac{1}{t_\mathrm{m}}\frac{2}{\tilde{M}_\mathrm{s}}q_\mathrm{p}\tilde{q} - \frac{2}{M_\mathrm{s}}q_\mathrm{p}^2\tilde{q} - \frac{1}{t_\mathrm{m}}\frac{2}{\tilde{M}_\mathrm{s}^2}q_\mathrm{p}\tilde{q}^2 + \ldots \tag{5.135}$$

Substitution of this expression into Eq. 5.110, and expanding first as a function of $\tilde{q}$ to first order finds

$$\frac{\omega}{\omega_*} \approx \sqrt{1+\tilde{M}_\mathrm{s}+\frac{{\tilde{M}_\mathrm{s}}^2 q_y t_\mathrm{m}}{2(1+q_y t_\mathrm{m})}} - \frac{{\tilde{M}_\mathrm{s}}^2\left(3q_y t_\mathrm{m}+2\left(q_y t_\mathrm{m}\right)^2\right)\tilde{q}}{8\left(1+q_y t_\mathrm{m}\right)^2\sqrt{1+\tilde{M}_\mathrm{s}+\frac{M_\mathrm{s}^2 q_y t_\mathrm{m}}{2\left(1+q_y t_\mathrm{m}\right)}}} \tag{5.136}$$

which is then to be expanded again as a function of q_y, again to first order. Using that $q_y = l\pi/w_\mathrm{m}$ and $q_z = \frac{n\pi}{L_\mathrm{m}}$ for integers l and n, one finds

$$\frac{\omega}{\omega_*} \approx \sqrt{1+\tilde{M}_\mathrm{s}} + \frac{{\tilde{M}_\mathrm{s}}^2}{4\sqrt{1+\tilde{M}_\mathrm{s}}}\left(\frac{\pi t_\mathrm{m}}{w_\mathrm{m}}l - \frac{3}{2}\frac{t_\mathrm{m} w_\mathrm{m}}{\pi l}\left(\frac{n\pi}{L_\mathrm{m}}\right)^2\right). \tag{5.137}$$

To compare this against the branch spacing obtained from the OOMMF simulations, first consider the mode spacing for the case $l = 1$, $n = 1$ and $l = 2$, $n = 1$. This correlates to the branch spacing, denoted η_m, that was found from the 2-dimensional Fourier transform. Under this assumption, one finds

$$\frac{\eta_\mathrm{m}}{\omega_*} = \frac{{\tilde{M}_\mathrm{s}}^2}{4\sqrt{1+\tilde{M}_\mathrm{s}}}\left(\frac{\pi t_\mathrm{m}}{w_\mathrm{m}} - \frac{3}{2}\frac{t_\mathrm{m} w_\mathrm{m}}{\pi}\left(\frac{\pi}{L_\mathrm{m}}\right)^2\right) \tag{5.138}$$

which results in a branch spacing (taking the parameters used in the OOMMF simulation) of around $\eta_\mathrm{m} \approx 0.8\,\mathrm{GHz}$, roughly corresponding to what was observed.

Considering now the next nearest magnon which exists on the same branch, then the magnon mode spacing, denoted Δ_m, can be expressed as

$$\frac{\Delta_\mathrm{m}}{\omega_*} \approx \frac{3\gamma_\mathrm{g}\pi p t_\mathrm{m} w_\mathrm{m}(4\pi M_\mathrm{s})^2}{8H_\mathrm{e}L_\mathrm{m}^2\omega_0} \tag{5.139}$$

where $p = n_2^2 - n_1^2$ and has values of $p = 3$ for the cantilever ($l_1 = 1$, $l_2 = 1$ and $n_1 = 1$, $n_2 = 2$) and $p = 8$ for the bridge ($l_1 = 1$, $l_2 = 1$ and $n_1 = 1$, $n_2 = 3$) due to the absence and presence of symmetry, respectively.

Taking some choice parameters to illustrate an example ($t_m = 25a_0$, $w_\mathrm{m} = 400\,\mathrm{nm}$, $L_\mathrm{m} = 10\,\mu\mathrm{m}$, $H_e = 350\,\mathrm{Oe}$), and consider that the surface of the resonator is fully covered, the mode spacing to the next nearest Kittel-like magnon mode is

$$\Delta_\mathrm{m} \approx 3.4 \times 10^6 p. \tag{5.140}$$

With these dimensions, as a rough order of estimate for the cantilever and bridge geometries as having mechanical frequencies of the order of a MHz, then it appears that the geometries do not conform to the consideration of the single mode model being valid (it would appear that $\omega_\mathrm{R}/\Delta_\mathrm{m} \approx 0.5$ as a very rough estimate which does not present $\Delta_\mathrm{m} >> \omega_\mathrm{R}$). Further schemes in which this condition is met will be explored later. In order to resolve this frequency difference using OOMMF, it would be required to run the simulation for a total of ≈ 500000 stages to get a resolution of 0.1 MHz.

The ratio of the mechanical mode frequency to the mode spacing has some interesting features. Assuming first that the length of the resonator is fully covered with the magnetic material (although not necessarily the width), and considering only the fundamental elastic mode (which makes the criterion easier to meet given that higher order modes are of larger mechanical frequency), the ratio of the mechanical

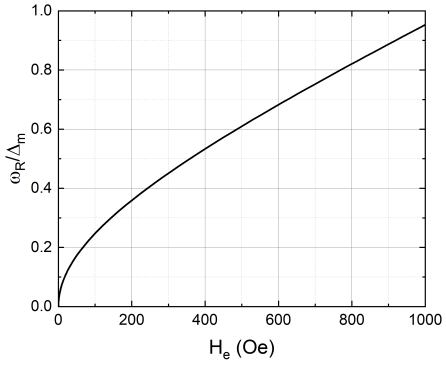

FIGURE 5.29: The character of Eq. 5.141 in varying the applied magnetic field for an isosceles cross-section cantilever.

mode frequency to the magnetic mode spacing may be expressed as

$$\frac{\omega_R}{\Delta_m} = \frac{8}{3}\sqrt{\frac{E}{\rho}}\frac{qo}{p}\frac{H_e(H_e+4\pi M_s)}{(4\pi M_s)^2}\frac{1}{\pi\omega_M}\frac{t_R}{t_m w_m} \tag{5.141}$$

where it is defined $q = \sqrt{3}/6$ for a rectangular resonator cross-section and $q = \sqrt{2}/6$ for an isosceles triangle cross-section, and $o = 1.8751^2$ for the cantilever and $o = 4.7300^2$ for the bridge. First, having an isosceles triangular cross-section provides the most benefit to meeting the criterion, as this provides an immediate prefactor that is smaller than that of the rectangular cross-section. It is also beneficial for meeting the single mode criterion to use a cantilever resonator due to the the ratio $o/p = 1.172$ being smaller than that of the bridge ($o/p = 2.797$). Regardless of the cross-sectional shape of choice, the mechanical mode frequency is independent of the width of the cross-section, but the ratio of the mechanical frequency to the magnetic mode spacing still depends on the width of the magnetic structure. This would imply that that it would be beneficial to have $w_m > w_R$ but this clearly isn't possible - w_m should be treated as the limiting case for the width of the resonator, at best, although it isn't necessary to have $w_m = w_R$ and $w_m < w_R$ is also perfectly valid under the mathematical considerations. To provide an optimal mode spacing such that the single mode criterion is met, it seems necessary to saturate the width of the resonator with the magnetic material. For full coverage in the length of the structure being sought, then the ratio of the mechanical mode frequency to the magnetic mode spacing is independent of the length of the magnetic structure. Finally, the ratio of the mechanical mode frequency to the magnetic mode spacing scales as t_R/t_m, which implies that the resonator should be made as thin as possible while also making the magnetic thin film as thick as possible - this is not an easy condition to optimise to given that it is required $t_R >> t_m$ in order to neglect the elastic influence of depositing a thin film on top of the resonator.

Shown in Fig. 5.29 is the variation of Eq. 5.141 with the applied field, H_e. For this, a cantilever of isosceles cross-section is assumed of $w_R = w_m = t_R = 400\,\text{nm}$, and a magnetic thickness of $t_m = 25a_0$, to give a 'best case scenario' type approach. It is then seen to be preferential to minimise the applied field as much as possible to meet the single mode criterion, although this is not necessarily feasible when trying to achieve saturation of the magnetic structure.

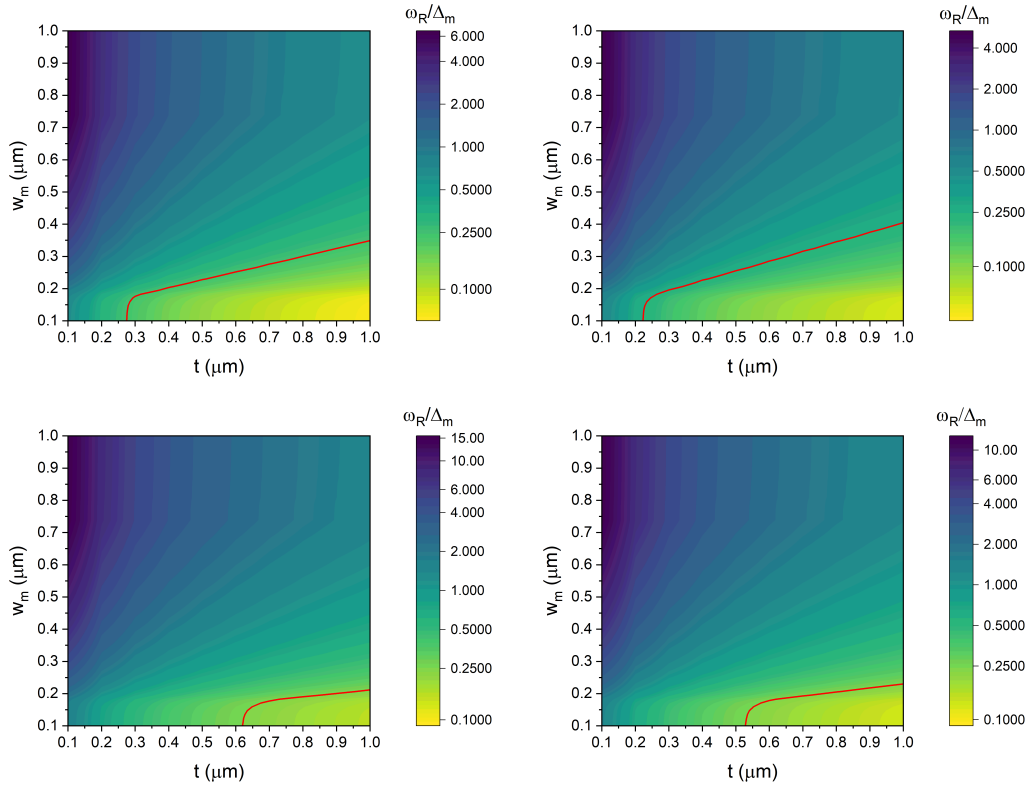

FIGURE 5.30: Eq. 5.141 for cantilever and bridge geometries as functions of resonator thickness and width, assuming full coverage with the magnetic material. The top plots are for rectangular and isosceles cantilever cross-section, respectively, and the bottom plots are for bridge geometry, respectively. The red line denotes $\omega_R/\Delta_m = 0.25$.

Likewise, Fig. 5.30 shows density plots of ω_R/Δ_m as a function of the width and thickness of the resonator, assuming full coverage with the magnetic material, for both the cantilever and bridge geometries and for square and isosceles cross-sections. These plots have been generated for an applied field of $H_e = 350\,\text{Oe}$, and for a thickness of the magnetic structure of $t_m = 25a_0$. Note that the red lines are used to denote the point $\omega_R/\Delta_m = 0.25$. For full coverage, it is required to make the resonator thickness exceptionally large and shrink the width as much as possible in order to satisfy the single mode criterion which is not preferential in maximising the magnomechanical parameters.

If one instead assumes that the magnetic structure does not fully cover the length of the resonator, then a more robust landscape which makes attaining the single mode criterion far more feasible opens up. Under the assumption that $L_m < L_R$, the ratio of the mechanical mode frequency to the magnetic mode spacing can be expressed as

$$\frac{\omega_R}{\Delta_m} = \frac{3}{8}\sqrt{\frac{E}{\rho}}\frac{qo}{p}\frac{H_e(H_e + 4\pi M_s)}{(4\pi M_s)^2}\frac{1}{\pi\omega_m}\frac{t_R}{t_m}\left(\frac{L_m}{L_R}\right)^2\frac{1}{w_m} \tag{5.142}$$

where q, o, and p retain their same definitions as before. With regards to the geometry of choice for the resonator, the same reasoning still applies as before, which is to say that choosing the cantilever is best for minimising single mode criterion, maximising the width such that $w_m = w_R$ is preferential, and using an isosceles

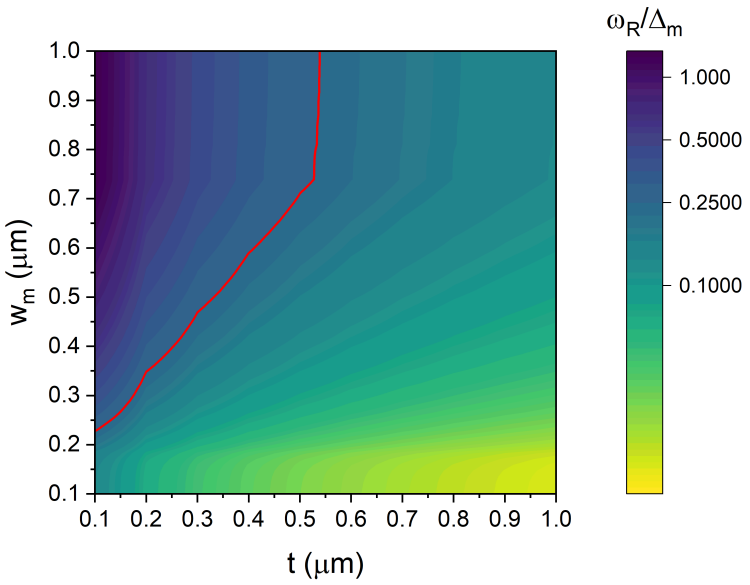

FIGURE 5.31: The character of Eq. 5.142 in varying the thickness and width of a cantilever of isosceles cross-section cantilever. The red line denotes $\omega_R/\Delta_m = 0.25$

cross-section is best. However, in considering the scheme in which $L_m < L_R$ then in order to minimise ω_R/Δ_m it is beneficial to minimise the length of magnetic material placed on the resonator. For example, covering only half of the length of the resonator provides a ratio $(L_m/L_R)^2$ of $1/4$, which acts to aid in meeting the single mode criterion. While this, in principle, deteriorates the magnomechanical parameters by having less magnetic material present on the beam, the ability to choose where exactly to place the magnetic material such that g_0^{rec}, and hence g^{rec} and C^{rec}, may be maximised through the curvature profile helps offset this while also offering a conformity to the single mode criterion.

Shown in Fig. 5.31 is a density plot of Eq. 5.142 a cantilever in assuming an isosceles cross-section and full coverage in the width, as a function of the width and thickness of the resonator. Taken as before is an applied field of $H_e = 350\,\text{Oe}$, and assumed is a ratio of lengths of $L_m/L_R = 0.5$. The red line is used again to denote $\omega_R/\Delta_m = 0.25$. Clearly, the scheme in which the magnetic material does not fully cover the length of the resonator offers a much more versatile regime of dimensions, and offers geometries in which meeting the single model criterion is viable while retain small dimensions that should maximise the magnomechanical parameters.

5.6 Characterisation of g and C

While g_0 is in itself a useful parameter, it only represents the interaction between a single magnon and a single phonon. Often, the figures of merit for these hybrid systems are the, in the case of the theory presented, multimagnon-phonon coupling (denoted g), and the cooperativity (denoted C). The multimagnon-phonon coupling is defined as

$$g = g_0\sqrt{n_{mag}}, \tag{5.143}$$

where n_{mag} is the number of magnons, and may be determined from Eq. 4.24. This parameter then encapsulates the total strength of all interactions taking place between magnons and phonons in the system. Likewise, the cooperativity, defined as

$$\mathcal{C} = \frac{4g^2}{\kappa\Gamma}, \tag{5.144}$$

is then a parameter used to to quantify the systems efficiency in exchanging magnons and phonons. In essence, it represents the product of ratios between coupling and losses of the system.

As was done for g_0^{rec}, presented now is the scaling of the multi-magnon coupling strength as well as the cooperativity assuming that the geometry of the surface of the magnetic structure forms a rectangle. Owing to their dependence on the decay rate into magnon modes, κ_{ex}, the mechanical damping, Γ_{R}, and the number of magnomechanically relevant magnons, n_{mag}, all of which are functions of the dimensions of the resonator and magnetic structure, the scalings of g^{rec} and $\mathcal{C}^{\mathrm{rec}}$, while depending on g_0^{rec}, are no longer equivalent as this. As such, the parameter space for the two is briefly reconsidered. In addition, with the various constraints placed on the system (the single mode criterion, the mode validity criterion, the resolved side-band condition, and the magnon non-linearity condition specifically), this parameter space is non-trivial in considering which regimes are permissible, and how to maximise these parameters subject to the constraints. Assumed in the following is only isosceles cross-sections, given that this produces lower mechanical mode frequencies and should gives the largest value of g_0^{rec}. Given that the mechanical damping is proportional to the frequency, it would seem apparent that the isosceles cross-section would in turn provide another boost for $\mathcal{C}^{\mathrm{rec}}$ for the same set of parameters as that of a rectangular cross-section with this lower mode frequency. Lastly, as the magnomechanical parameters are maximised for smaller applied fields, the applied field is again assumed to be $H_{\mathrm{e}} = 350\,\mathrm{Oe}$. There is little point is repeating these procedures for g_0^{rec} as derived under the assumption of a flat mode profile given that it does not represent a physical system. Hence, only considered are g_0^{rec} and $\mathcal{C}^{\mathrm{rec}}$ for the trigonometric mode profile as the physically representative case.

First, the scaling of g^{rec} with central distance from the transmission line, d_{c} introduced in Sec. 5.4, is considered. It was seen that the decay rate, κ_{ex} was a linear function in the length and thickness of the magnetic material, but had a saturation value with regards to the ratio $w_{\mathrm{m}}/2d_{\mathrm{c}}$. With this in mind, it would appear intuitive to characterise the scaling of g^{rec} for w_{m} as the parameter d_{c} is varied. As now the system is dependent on the resonator dimensions, and taken for this example is $w_{\mathrm{m}} = w_{\mathrm{R}}$, it makes little sense to consider $w_{\mathrm{R}} << t_{\mathrm{R}}$ despite scaling suggesting this would maximise parameters. The minimum limit of t_{R} is around $250a_0$ owing to the elasticity criteria, and so widths in the region $w_{\mathrm{m}} = [250 : 600]$ are used for illustrative purposes. Lengths are then taken of $L_{\mathrm{m}} = L_{\mathrm{R}} = 6\,\mu\mathrm{m}$, $t_{\mathrm{R}} = 350\,\mathrm{nm}$, a transmission line power of $P_{\mathrm{in}} = 250\,\mathrm{nW}$, a detuning $\Delta = \omega_{\mathrm{R}}$, and the variation of g^{rec} for the central distances $d_{\mathrm{c}} = \{0.1, 0.25, 0.5, 1\}\,\mu\mathrm{m}$ is presented for a cantilever geometry in Fig. 5.32. The magnetic and elastic parameters are retained from Table 5.1. The cooperativity is expected to scale largely the same since the dominating decay factor is the intrinsic decay of the magnon mode $\kappa_0 = \alpha\omega_{\mathrm{m}}$ which is independent of dimensions. Clearly, smaller central distances offer larger coupling for the same dimension of resonator. As the central distance becomes larger, the coupling becomes relatively insensitive to changes in the width of magnetic material.

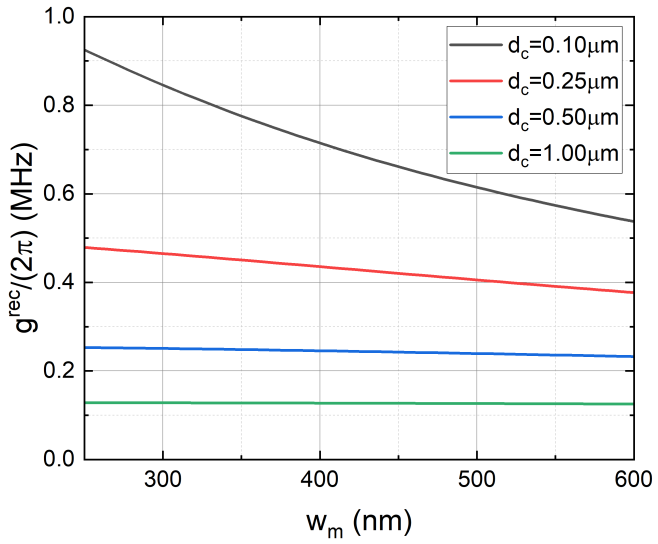

FIGURE 5.32: g^{rec} for the cantilever resonators as a function of the magnetic width, plotted for different central distances d_{rec} from the transmission line.

For exploring the dependence of g and $\mathcal{C}$, two relevent cases may be identified. These are

- that there is full coverage of the resonator surface with the magnetic material,
- that the magnetic material coincides with the cantilever's fixed end and is allowed to vary.

Given that the deflection of the cantilever was largely linear and that placing material on or towards the cantilever's free end provided lesser values of g_0^{rec}, these two cases present the most sensible geometry. Shown first is the scaling of g^{rec} and $\mathcal{C}^{\mathrm{rec}}$ in assuming full coverage of a cantilever resonator as a function of resonator surface dimensions in Fig. 5.33. Also shown in Fig. 5.34 is how g^{rec} and $\mathcal{C}^{\mathrm{rec}}$ varies expressed as the ratio $L_{\mathrm{m}}/L_{\mathrm{R}}$, where the origin is taken to start at the cantilever's fixed end. A detuning $\Delta = \omega_{\mathrm{R}}$ is used as well as an applied field $H_{\mathrm{e}} = 350\,\mathrm{Oe}$, and $d_{\mathrm{c}} = 0.1\,\mu\mathrm{m}$ is taken to form a benchmark. An isosceles cross-section is assumed, and g^{rec} and $\mathcal{C}^{\mathrm{rec}}$ is plotted with respect to w_{m} and t_{m}. The inset shows the dependence on L_{m}. Unless the dimension is varied, geometry is taken as $L_{\mathrm{m}} = L_{\mathrm{R}} = 6\,\mu\mathrm{m}$, $w_{\mathrm{m}} = w_{\mathrm{R}} = t_{\mathrm{R}} = 350\,\mathrm{nm}$. The parameter t_{R} has only been plotted to a minimum of $t_{\mathrm{R}} = 100\,\mathrm{nm}$ due to sharp scaling - the value of g^{rec} approaches 22 MHz. Regardless, the scaling in this region isn't accessible due to the thickness constraints. The parameters t_{R} and w_{R} retain roughly the same scaling with $\mathcal{C}^{\mathrm{rec}}$, whereas L_{R} shifts from linear scaling in the depicted region for g^{rec} into roughly quadratic scaling for $\mathcal{C}^{\mathrm{rec}}$.

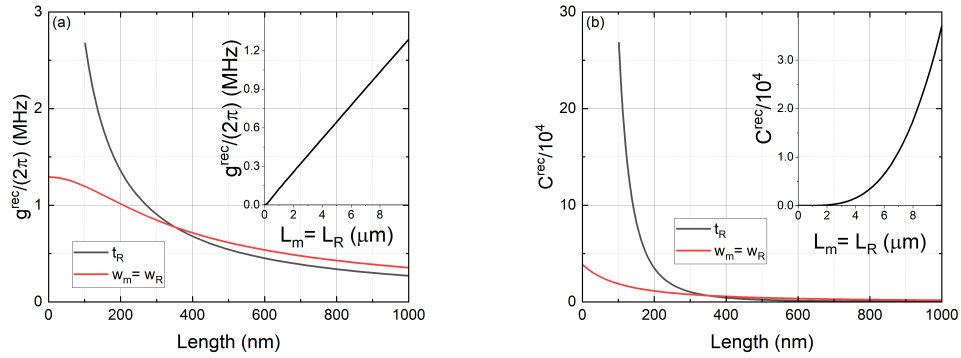

FIGURE 5.33: (a) g^{rec} and (b) $\mathcal{C}^{rec}$ for a cantilever resonator with isosceles cross-sections for full coverage with magnetic material as a function of dimensions.

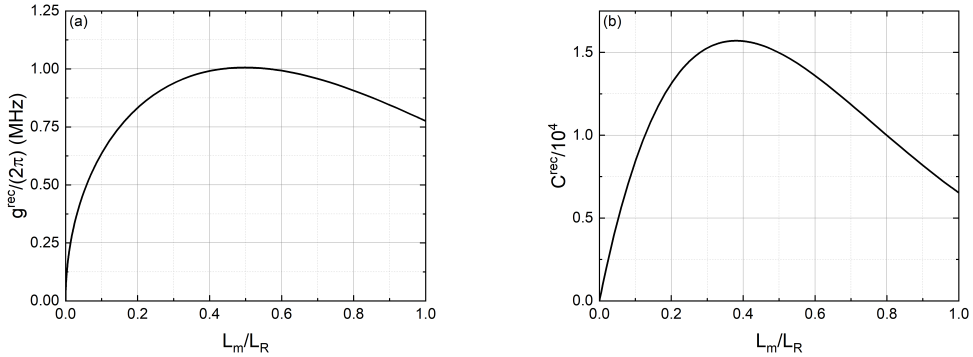

FIGURE 5.34: (a) g^{rec} and (b) $\mathcal{C}^{rec}$ for a cantilever resonator with isosceles cross-sections as a ratio of lengths. The origin is taken at the cantilever's fixed end.

Likewise, for the bridge the cases

- that there is full coverage of the resonator surface with the magnetic material,
- that the magnetic material is placed centrally and approaches the bridge's fixed ends equally,

are considered. Again, these represent the most logical schemes from the bridge as inferred from the characterisation of g_0^{rec}. Shown in Fig. 5.35 is the dependence of g^{Rec} and $\mathcal{C}^{rec}$ for the bridge in assuming full coverage with magnetic material. Identical dimensions to that of the cantilever have been assumed for comparison. The scaling for the two parameters is identical, but the attainable g^{rec} is around an order of magnitude less, with $\mathcal{C}^{rec}$ around two orders of magnitude lower, than that of the cantilever. Also shown in Fig. 5.36 is the variation of g^{rec} and $\mathcal{C}^{rec}$ as a function of bridge coverage. For this, the origin is taken to be at the bridge's midpoint, and the ends of the magnetic structure approach the bridge's fixed ends equally.

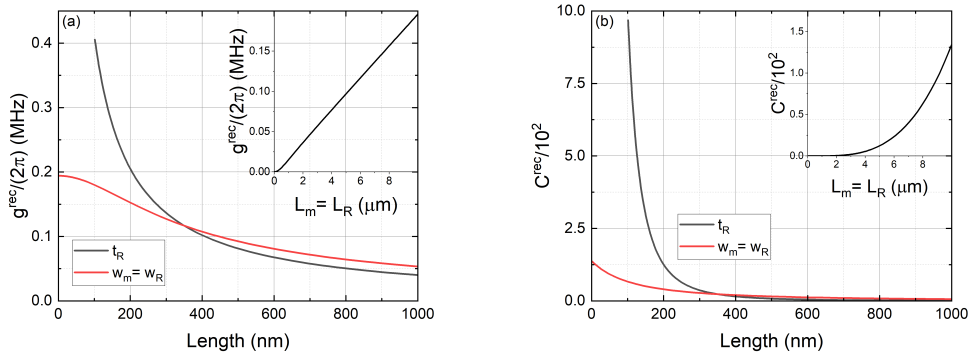

FIGURE 5.35: (a) g^{rec} and (b) $\mathcal{C}^{\text{rec}}$ for a bridge resonators with isosceles cross-sections for full coverage with magnetic material as a function of dimensions.

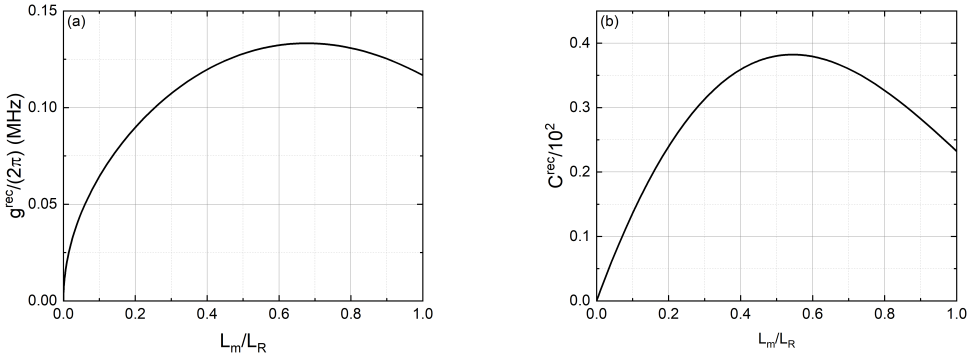

FIGURE 5.36: (a) g^{rec} and (b) $\mathcal{C}^{\text{rec}}$ for a bridge resonator with isosceles cross-sections as a ratio of lengths. The origin is taken at the bridge's midpoint.

5.6.1 Optimisation

Given not only the scaling of the parameters g^{rec} and $\mathcal{C}^{\text{rec}}$, but also the scaling of the constraints themselves on our system, optimising the device dimensions to provide maximal g^{rec} and $\mathcal{C}^{\text{rec}}$ is non-trivial and offers a diverse space to consider. There are, however, routines available to find maximal values (or minimal) of a function subject to constraints. To this end, `Mathematica` is made use of along with it's `NMaximize` function to find the largest values of g^{rec} and $\mathcal{C}^{\text{rec}}$ subject to the specific constraints. These constraints are as follows;

- the mode validity criterion which set limits on the aspect ratios of the resonator itself. This criterion stem from the validity of the Euler-Bernoulli beam theory, and realistically can be taken as

$$k_n w_{\text{R}} < 0.15, \quad \text{and} \quad k_n t_{\text{R}} < 0.15 \tag{5.145}$$

  given that, in principle, the theory holds for wave-vectors $ka = 0.6$.

- the resolved sideband condition

$$\frac{\kappa}{\omega_{\text{R}}} << 1 \tag{5.146}$$

which is a function of both the magnetic structure's dimensions and the resonator's dimensions. As κ is largely dominated by the intrinsic losses, $\alpha\omega_m$, and this is of the order of 10^6, at minimum one requires a mechanical frequency of 10 MHz which is largely attainable with any configuration of nanodimensions that also obey the mode validity criterion. As a guideline, a length $L_R = 10\,\mu$m and thicknesses and widths $t_R = w_R = 400\,$nm provide a mechanical mode frequency of $\omega_R \approx 10\,$MHz for the cantilever and $\omega_R \approx 100\,$MHz for the bridge, both of which would meet this criterion.

- the Kittel mode quantisation condition

$$\frac{n_{mag}}{n_S} << 1 \tag{5.147}$$

which requires that the number of magnomechanically relevant magnons is much less that the number of magnetic moment spin sites, such that the expansion used for deriving the Kittel mode operators can be assumed to hold. Somewhat awkwardly, this depends not only on the magnetic structure's dimensions, but also on the dimensions of the resonator which enter through the detuning, Δ. The number of spin sites scales linearly with the volume of magnetic material, but the number of magnons does not, which tends to mean that larger volumes would be preferable for meeting this criterion.

- the single mode criterion

$$\frac{\omega_R}{\Delta_m} << 1, \tag{5.148}$$

which has already been seen to offer a complicated parameter landscape in Sec. 5.5. Ultimately, the finding for this was that it would be necessary to only cover a portion of the resonator else the the restrictions on the device design would make it difficult to meet the other criterions.

- the elastic interface condition

$$\frac{t_R}{t_m} << 1 \tag{5.149}$$

which limits the thickness of the resonator. For the consideration of $t_m = 25a_0$, this essentially puts a cap on how thin the resonator can be at $t = 310\,$nm.

For the geometry of the device proposed within, parameter dimensions are considered in the ranges

$$\begin{gathered} 1\,\mu\text{m} \leq L_R \leq 40\,\mu\text{m}, \\ 200\,\text{nm} \leq w_m = w_R \leq 800\,\text{nm}, \\ 350\,\text{nm} \leq t \leq 800\,\text{nm}. \end{gathered} \tag{5.150}$$

In principle, the thickness can be taken down to $t_R = 310\,$nm, but this level of precision seems redundant given the resolution of manufacturing processes. With these conditions clarified, `Mathematica` is able to find the maximum of a function subject to these constraints. In the following cases, an input power $P_{in} = 250\,$nW is assumed as well as an applied field of $H_e = 350\,$Oe, and consideration is only given to the fundamental mechanical modes of the resonators. Note that optimisation for the structure is done to different values of the constraints (apart from the mode validity constraint, which is kept static at < 0.15). In principle, one should take these constraints to be as small as possible, and as the leniency of the constraints is made smaller, it will be seen the magnomechanical parameters deteriorate.

In optimising the structures for g^{rec} and $\mathcal{C}^{\text{rec}}$ under the assumption that the resonator surface is entirely covered with magnetic material and subjected to the constraints, there are are no geometries in which all of the conditions are able to be met. As such, full coverage for the cantilever is not a regime that can be physically considered while also meeting the required constraints to specified tolerances. For the optimisation, the central distances $d_{\text{c}} = \{0.1, 0.25, 0.5, 1\}$ μm are taken as exemplar dimensions, but the upper limit is not arbitrary; it presents the largest central distance for an approximation of a uniform driving field used within Chapter 6 but presents no constraints to what has been presented so far.

Cantilever

For the geometries of consideration, g^{rec} is always of the order of MHz. In tandem with the lower mechanical mode frequency optimisation of only the cooperativity to be as large as possible seems the most intuitive given that the strong coupling regime will, under most circumstances, be satisfied. No geometries were found for the rectangular cross-section for which the constraints had tolerances < 0.05, although two regimes did exist for the isosceles cross-section within the central distances considered. The isosceles cross-section is able to offer larger g^{rec} and $\mathcal{C}^{\text{rec}}$ than the rectangular one, and also allows the constraints to be kept to more stringently, but both geometries present feasible regimes.

In optimising the cantilever for $\mathcal{C}^{\text{rec}}$ for the fundamental mode under the assumption of partial coverage, the origin of the magnetic placement is taken to be at the cantilever's fixed end such that the large curvature of the mode profile may be exploited to boost the single magnon-phonon coupling as much as possible in line with Sec. 5.3.2. With this geometry, it is possible to meet the constraints imposed on the system while also giving large magnomechanical parameters. The results of the optimisation for a cantilevered beams having $25a_0$ layers of YIG deposited are presented in Table 5.3 for isosceles cross-section, and in Table 5.4 for rectangular cross-section. The lateral dimensions of the YIG film are then specified within these tables. Note that the cantilever can produce attractive cooperativies of order 10^3, three orders of magnitude larger than previously reported using the cavity implementation [27]

Bridge

In a similar vein to the cantilever, owing both to the higher mechanical mode frequency as well as the smaller g^{rec} of order of 100s of KHz, this again lends itself to performing optimisation for the cooperativity to be as large as possible solely given that it is unlikely to be optimised to the extent that it meets the strong coupling threshold significantly. Optimisation is again performed for the bridge for $\mathcal{C}^{\text{rec}}$ for the fundamental mode. Coverage of magnetic material is assumed as a ratio of the resonator length, and the origin of the magnetic placement is taken at the centre of the bridge. The results of the optimisation for $25a_0$ layers of YIG are shown in Table 5.5 assuming an isosceles cross-section, and in Table 5.6 assuming a rectangular cross-section, where again the lateral dimensions of the YIG film are contained within.

In general, the bridge produces cooperativities around an order of magnitude less than the cantilever but still exceeds those previously reported using the cavity implementation [27]. However, the bridge requires a much longer resonator length to attain comparable mechanical frequencies to that of the cantilever, and in turn

geometries which stringently meet the constraints are easier to access given the simple numerical pre-factor that enters into the mode spacing and excitation of fewer magnomechanically relevent magnons. Optimising the constaints to tolerances of $\lesssim 0.05$ finds regimes for both rectangular and isosceles cross-sections whereas these tolerances were only attainable for the isosceles cross-sectional cantilever. Values of d_c which do not appear in the Table represent regimes in which maximisation produced ratios $L_m/L_R = 0$ which are neglected as nonphysical, in which optimisation placed preference on minimising the amount of magnetic material placed on the beam rather than being physically unable to satisfy the constraints.

Constraints	d_c (μm)	L_R (μm)	$w_{R,m}$ (μm)	t_R (μm)	$\frac{L_m}{L_R}$	$\frac{g^{rec}}{2\pi}$ (MHz)	$\frac{g^{rec}}{\kappa}$	$\mathcal{C}^{rec}$
$\lesssim 0.20$	0.10	4.9	0.20	0.35	0.40	1.06	3.2	12.7×10^3
	0.25	7.0	0.20	0.35	0.40	0.73	2.7	15.0×10^3
	0.50	9.7	0.25	0.35	0.45	0.53	2.1	16.0×10^3
	1.00	13.7	0.25	0.35	0.50	0.38	1.5	17.0×10^3
$\lesssim 0.15$	0.10	4.5	0.20	0.35	0.35	0.95	3.1	9.1×10^3
	0.25	6.5	0.25	0.35	0.35	0.65	2.4	10.0×10^3
	0.50	9.0	0.30	0.35	0.40	0.48	1.9	11.4×10^3
	1.00	12.5	0.25	0.35	0.40	0.34	1.4	11.5×10^3
$\lesssim 0.10$	0.10	4.5	0.30	0.35	0.35	0.79	2.5	6.3×10^3
	0.25	6.1	0.35	0.35	0.40	0.59	2.1	7.1×10^3
	0.50	8.3	0.40	0.35	0.40	0.43	1.7	7.8×10^3
	1.00	10.2	0.35	0.35	0.40	0.28	1.1	5.0×10^3
$\lesssim 0.05$	0.50	7.1	0.50	0.35	0.35	0.35	1.4	3.8×10^3
	1.00	7.2	0.60	0.35	0.35	0.19	0.8	1.1×10^3

TABLE 5.3: Optimisation of the cantilever nanostructure of isosceles cross-section for maximal cooperativity including the fundamental constraints listed at the beginning of Sec. 5.6.1.

Constraints	d_c (μm)	L_R (μm)	$w_{R,m}$ (μm)	t_R (μm)	$\frac{L_m}{L_R}$	$\frac{g^{rec}}{2\pi}$ (MHz)	$\frac{g^{rec}}{\kappa}$	$\mathcal{C}^{rec}$
$\lesssim 0.20$	0.10	5.4	0.20	0.35	0.40	0.61	1.8	4.0×10^3
	0.25	7.7	0.20	0.35	0.40	0.42	1.5	4.8×10^3
	0.50	10.8	0.25	0.35	0.45	0.31	1.2	5.3×10^3
	1.00	15.2	0.30	0.35	0.45	0.22	0.9	5.6×10^3
$\lesssim 0.15$	0.10	6.5	0.50	0.35	0.40	0.44	1.3	3.0×10^3
	0.25	7.3	0.25	0.35	0.35	0.38	1.4	3.6×10^3
	0.50	10.0	0.35	0.35	0.40	0.28	1.1	3.7×10^3
	1.00	13.8	0.30	0.35	0.40	0.20	0.8	3.7×10^3
$\lesssim 0.10$	0.10	5.6	0.45	0.35	0.40	0.41	1.2	2.0×10^3
	0.25	6.9	0.40	0.35	0.40	0.33	1.2	2.3×10^3
	0.50	9.3	0.50	0.35	0.40	0.25	0.9	2.5×10^3
	1.00	11.3	0.40	0.35	0.40	0.16	0.7	1.6×10^3

TABLE 5.4: Optimisation of the cantilever nanostructure of rectangular cross-section for maximal cooperativity including the fundamental constraints listed at the beginning of Sec. 5.6.1.

Constraints	d_c (μm)	L_R (μm)	$w_{R,m}$ (μm)	t_R (μm)	$\frac{L_m}{L_R}$	$\frac{g^{rec}}{2\pi}$ (MHz)	$\frac{g^{rec}}{\kappa}$	$\mathcal{C}^{rec}$
$\lesssim 0.20$	0.10	15.7	0.50	0.35	0.40	0.25	0.50	7.5×10^2
	0.25	18.7	0.40	0.35	0.40	0.21	0.57	10.0×10^2
	0.50	25.4	0.55	0.35	0.45	0.16	0.51	10.2×10^2
	1.00	34.8	0.55	0.35	0.45	0.12	0.43	10.5×10^2
$\lesssim 0.15$	0.10	14.0	0.45	0.35	0.35	0.23	0.51	5.5×10^2
	0.25	18.6	0.60	0.35	0.40	0.18	0.48	7.3×10^2
	0.50	24.3	0.75	0.35	0.45	0.14	0.44	9.2×10^2
	1.00	30.8	0.50	0.35	0.35	0.01	0.37	8.2×10^2
$\lesssim 0.10$	0.10	12.1	0.40	0.35	0.25	0.19	0.50	3.2×10^2
	0.25	16.4	0.50	0.35	0.30	0.15	0.47	4.7×10^2
	1.00	25.2	0.60	0.35	0.35	0.08	0.30	3.6×10^2
$\lesssim 0.05$	0.25	13.3	0.40	0.35	0.20	0.11	0.40	1.9×10^2
	1.00	18.1	0.60	0.35	0.20	0.04	0.8	0.6×10^2

TABLE 5.5: Optimisation of the bridge nanostructure of isosceles cross-section for maximal cooperativity including the fundamental constraints listed at the beginning of Sec. 5.6.1.

Constraints	d_c (μm)	L_R (μm)	$w_{R,m}$ (μm)	t_R (μm)	$\frac{L_m}{L_R}$	$\frac{g^{rec}}{2\pi}$ (MHz)	$\frac{g^{rec}}{\kappa}$	$\mathcal{C}^{rec}$
$\lesssim 0.20$	0.10	18.4	0.60	0.35	0.40	0.13	0.26	2.3×10^2
	0.25	21.2	0.45	0.35	0.40	0.12	0.31	3.3×10^2
	0.50	28.3	0.60	0.35	0.40	0.09	0.28	3.9×10^2
	1.00	38.5	0.55	0.35	0.40	0.07	0.25	4.6×10^2
$\lesssim 0.15$	0.10	16.4	0.50	0.35	0.35	0.14	0.27	1.8×10^2
	0.25	21.2	0.65	0.35	0.40	0.10	0.26	2.4×10^2
	0.50	27.4	0.85	0.35	0.40	0.08	0.23	2.8×10^2
	1.00	33.9	0.50	0.35	0.35	0.06	0.20	2.6×10^2
$\lesssim 0.10$	0.10	14.0	0.45	0.35	0.25	0.10	0.27	1.0×10^2
	0.25	18.6	0.60	0.35	0.30	0.08	0.25	1.4×10^2
$\lesssim 0.05$	0.25	15.0	0.45	0.35	0.20	0.06	0.22	0.6×10^2
	0.50	19.5	0.45	0.35	0.20	0.05	0.18	0.6×10^2
	1.00	20.0	0.65	0.35	0.20	0.03	0.10	0.2×10^2

TABLE 5.6: Optimisation of the bridge nanostructure of rectangular cross-section for maximal cooperativity including the fundamental constraints listed at the beginning of Sec. 5.6.1.

Chapter 6

Applications

Ultimately, while photons and phonons have been introduced to magnons separately, the three are free to form a coupled hybrid photon-magnon-phonon system. Explored here is the application of this system in the context of magnomechanics [129]. For this, the description of the interaction of elasticity with magnetism will be brought into place with the prior mentioned description of photons interacting with magnetism, and the feasibility of ground state cooling, magnomechanically induced transparency, and the magnon spring effect will be explored as 'benchmarking' for the proposed device.

6.1 Magnon-photon coupling

In this section, incorporating the proposed device into the strong magnon-photon regime while retaining strong magnon-phonon coupling. Strong coupling is a prerequisite for coherent information transfer in which losses are exceeded by the coupling into the system, and so bringing magnons and photons into the strong coupling regime would permit coherent information transfer between the three particle types. The coupling between magnons and photons on a superconducting waveguide realisation is proportional to $\sqrt{V_m}$, and so geometries here which could permit this strong coupling consideration are considered here.

In the absence of a cavity, it has been derived that the coupling between photons of a transmission line and individual spins in the a magnetic material, g_s, can be found as [119]

$$g_s = \gamma_g \beta_{rf} \omega_p \sqrt{\frac{\hbar}{8 Z_{TL}}}, \tag{6.1}$$

where γ_g is the electron gyromagnetic ratio, β_{rf} is the magnetic field per unit current, and ω_p and Z_{TL} is the transmission line photon frequency and characteristic impedance, respectively. The multispin-photon coupling is then given by

$$g_{ma} = g_s \sqrt{N_s}, \tag{6.2}$$

where the subscript ma is used to distinguish between g, which has prior been used as the multimagnon-phonon coupling.In this expression, N_s is the number of spins, determined by $N_s = V_m \rho_s$ for the spin-density ρ_s. For YIG, this spin-density is taken as $\rho_{s,YIG} = 4.22 \times 10^{27}\,\mathrm{m}^{-3}$ [14].

For geometry which permits the length of the inductive wire sufficiently long relative to the length of the magnetic structure such that edge effects can be neglected, and that the spacing of the magnetic structure from the inductive wire, d_c, is much less than the width of the inductive wire, w_{CPW}, (i.e. $d_c << w_{CPW}$), then one may

use the approximation for the rf field [190]

$$b_{\mathrm{rf}} = \frac{\mu_0}{2w_{\mathrm{CPW}}}\sqrt{\frac{P_{\mathrm{in}}}{Z_{\mathrm{TL}}}} \tag{6.3}$$

from which $\beta_{\mathrm{rf}} = \mu_0/2w_{\mathrm{CPW}}$ is the prior expression. Associated with these resonators is a linewidth denoted κ_a which may be obtained by means of a microwave transmission spectrum.

There exists a wide range of quality factors for on-chip microwave resonators [191] made of a variety of materials. Of particular interest are superconducting resonators, which offer large quality factors and are versatile as single photon detectors [192]. To this end, it makes sense to adopt this consideration for the microwave resonator given the potential quantum applications of our device. The superconducing materials used in these transmission line require cooling (typically down to a few Kelvin) to exhibit their properties, which naturally lends itself to the ground-state cooling scheme. In addition to this, they also only operate below a critical magnetic field, H_{c} above which they no longer behave fully as a superconductor. For magnetic applications, a superconducting transmission would require a large critical field. A common material used as a superconductor in such a transmission lines is aluminium [193], having a critical field $H_{\mathrm{c}} = 100\,\mathrm{Oe}$ [194]. More popular for magnetic experiments is niobium [195], which has a much larger critical field $H_{\mathrm{c}} \approx 2000\,\mathrm{Oe}$ [196].

6.1.1 Coplanar waveguide

Considered here is a superconducting niobium transmission line as used by Hou *et. al* [119]. They fabricated a winding transmission line of length $l_{\mathrm{CPW}} = 12\,\mathrm{mm}$, leading to a fundamental resonant frequency of $\omega_{\mathrm{a}}/2\pi = 4.69\,\mathrm{GHz}$, which was close to their magnon frequency. Microwave transmission measurements then found a linewidth $\kappa_{\mathrm{a}}/2\pi = 1.5\,\mathrm{MHz}$ for a transmission line of width $w_{\mathrm{CPW}} = 20\,\mu\mathrm{m}$, and having characteristic impedance $Z_{\mathrm{TL}} \approx 50\Omega$. For our work, considered is an applied magnetic field $H_{\mathrm{e}} = 350\,\mathrm{Oe}$ leading to a Kittel mode frequency $\omega_{\mathrm{m}}/2\pi = 2.4\,\mathrm{GHz}$. In making the transmission line shorter to support a resonance close to this, it is extrapolated that the line-width of the microwave resonator is not significantly effected.

With the measurements prior, a single spin-photon coupling strength $g_{\mathrm{s}}/2\pi = 7.2\,\mathrm{Hz}$ could be achieved. To attain strong coupling, it is required that $g_{\mathrm{s}}\sqrt{N_{\mathrm{s}}}/\kappa_{\mathrm{p}} > 1/2$. For the YIG thin film device proposed, it is then possible to calculate dimensions that access the strong magnon-photon coupling regime. First, the minimum number of spins to satisfy the inequality strong coupling inequality is expressed as

$$N_{\mathrm{s}} \gtrsim \left(\frac{1}{2}\frac{\kappa_{\mathrm{a}}}{g_{\mathrm{s}}}\right)^2 = 10^{10} \tag{6.4}$$

by rearrangement. Using this and the spin density of YIG, one can calculate the volume of YIG that must be in excess of to support strong magnon-photon coupling. Assuming a rectangular film of thickness $t_{\mathrm{m}} = 25a_0$, one finds for the surface area required at mimumum a product

$$L_{\mathrm{m}}w_{\mathrm{m}} \gtrsim \frac{10^{10}}{\rho_{\mathrm{s,YIG}}t_{\mathrm{m}}} = 77\ (\mu\mathrm{m})^2\,. \tag{6.5}$$

For the nano-device proposed, this requires lengths in excess of some 100 μm, for which there is no geometry that satisfies the constraints placed by our magnomechanical theory.

6.1.2 Lumped element resonator

If instead one uses the parameters for the lumped element resonator as used by Hou *et. al* [119], one finds a much more attractive geometry landscape. Their fabricated lumped element resonator had a fundamental mode frequency $\omega_a/2\pi = 5.42\,\text{GHz}$, a line-width $\kappa_a/2\pi = 1.05\,\text{MHz}$, a width $w_{LE} = 4\,\mu\text{m}$ and a characteristic impedance $Z_{TL} \approx 15\Omega$. Again, it is assumed that in fabricating such a lumped element resonator to have a fundamental mode frequency similar to the Kittel mode frequency that the line-width and impedance can be extrapolated.

For these parameters, one finds for the single spin-photon coupling strength, $g_s/2\pi = 66\,\text{Hz}$, an order of magnitude larger than for the coplanar waveguide owing both to the smaller waveguide width and lower impedance. Following the same procedure as before, the minimum number of spins to reach the strong coupling threshold can be found as $N_s \gtrsim 6.33 \times 10^7$, which in turn corresponds to a surface area of the YIG film of $L_m w_m \gtrsim 0.5\ (\mu\text{m})^2$. This is a geometry that is far more accessible for the YIG film, and all of the dimensions listed in Tables 5.3, 5.4, 5.5, and 5.6 meet it.

Takes more stringent adherence to the strong coupling threshold ($g_s\sqrt{N_s}/\kappa_a > 1$) to account for any kind of deviations from the parameters used, then the minimum number of spins required is found as

$$N_s \gtrsim \left(\frac{\kappa_a}{g_s}\right)^2 = 2.5 \times 10^8. \tag{6.6}$$

With this, a minimum surface of YIG is found as $L_m w_m \gtrsim 2$. No values in the aforementioned Tables meet this, but it can be included as an additional constraint in the optimisation process at the detriment to the magnitude of some of the magnomechanical parameters

Shown in Table 6.1 is the optimisation of the magnomechanical parameters to constraints satisfying $k_n\{w_R t_R\}/L_R \lesssim 0.15$ and $\{\kappa_m/\omega_R, n_{mag}/n_s, \omega_R/\Delta_m\} \lesssim 0.1$ for the bridge and cantilever. The cross-section is taken to be isosceles as producing the largest magnomechanical parameters. Note that the criterion for the application of β_{rf} limits the value of the central distance that can be considered, and so d_c is not considered as the same regime like was performed before. Optimisation here has been performed for $L_m w_m \gtrsim 2\,(\mu\text{m})^2$ where possible, and otherwise to $L_m w_m \gtrsim 0.5\,(\mu\text{m})^2$ With the parameters listed in the Table, magnon-photon strong coupling is attainable to $g_s\sqrt{N_s}/\kappa_a > 0.5$ while also retaining magnon-phonon coupling strengths comparable to what was seen in the prior maximisation processes. Only the bridge resonator is able to attain the regime $g_s\sqrt{N_s}/\kappa_a > 1$, specifically for the central distances $d_c = \{0.25, 0.50\}\,\mu\text{m}$ given the larger lengths of magnetic material able to be considered. The cantilever is unable to be optimised to this level of stringency while also meeting the magnomechanical constraints. Specifically, the single mode criterion is the limiting constraint which approaches $\omega_R/\Delta_m \approx 1$ given the higher mode frequency than the bridge.

Geometry	d_c	L_R	$w_{R,m}$	t_R	$\frac{L_m}{L_R}$	$\frac{g^{rec}}{2\pi}$	$\frac{g^{rec}}{\kappa}$	C^{rec}
Cantilever	0.10	5.0	0.40	0.35	0.40	0.76	2.3	6.8×10^3
	0.25	6.1	0.35	0.35	0.40	0.59	2.1	7.1×10^3
	0.50	8.3	0.4	0.35	0.40	0.43	1.7	7.8×10^3
Bridge	0.10	12.1	0.40	0.35	0.25	0.19	0.50	3.3×10^2
	0.25	18.0	0.55	0.40	0.30	0.14	0.42	4.2×10^2
	0.50	21.8	0.70	0.35	0.35	0.12	0.40	5.7×10^2

TABLE 6.1: Optimisation of C^{rec} for the magnon-photon strong coupling criteria $L_m w_m \gtrsim 0.5\,(\mu m)^2$. Lengths are given in microns, and g^{rec} is given in MHz

6.1.3 Larger-Q microwave resonators

The niobium microwave resonators considered correspond to Q-factors of $Q_{CPW} = 3 \times 10^3$ and $Q_{LE} = 5 \times 10^3$ for the coplanar waveguide and lumped element resonators, respectively. With regards to superconducting niobium microwave resonators, quality factors of 10^4 have been achieved [197]. Should the quality factor of the resonator be improved, then the linewidth is decreased and the number of spins required to reach the strong coupling is reduced quadratically.

There are perhaps also more suitable materials for the fabrication of these superconducting waveguides. Niobium-titanium alloys have also been noted for the superconducting properties [198], and have critical fields on the order of 10 T [199, 200]. Microwave resonators utilising this material are able to attain $Q-$factors of 10^4 [201] to 10^5 [202, 203] although not necessarily to the same degree of miniaturisation. Other materials have been noted for their superconducting coplanar waveguide properties [204], so transitioning to a higher Q resonator would be beneficial for the device.

6.2 Hybridised modes

When the magnons and photons are brought into strong coupling, the modes become hybridised in which they behave as 'part' magnon and 'part' photon. Note that the standard naming convention that has been used so far for the operators is continued; that is, that photons are described by the operators $\hat{a}$, phonons by $\hat{b}$, and magnons by $\hat{c}$. To distinguish between the magnon-photon and the magnon-phonon coupling rates, the subscripts ma and mb are used, respectively. To denote the single couplings from the multi-couplings, a superscript 0 is used for the former and the latter is left as $g_{..}$.

The mathematical description of cavity magnomechanics has already been provided by Tang [27], in which the normal modes of a hybridised magnon-photon system, denoted $\hat{A}_{\pm}$, are described by the matrix

$$\begin{pmatrix} \hat{A}_+ \\ \hat{A}_- \end{pmatrix} = \begin{pmatrix} \cos(\theta) & \sin(\theta) \\ -\sin(\theta) & \cos(\theta) \end{pmatrix} \begin{pmatrix} \hat{a} \\ \hat{m} \end{pmatrix} \tag{6.7}$$

where the coupling angle can be found as

$$\tan(2\theta) = \frac{2g_{ma}}{|\omega_m - \omega_a|}, \tag{6.8}$$

with θ varying between $\theta = [0, \pi/2]$ and 'maximal' hybridisation occurring for the angle $\theta = \pi/4$. The frequency of these hybridised modes is described by the expression

$$\omega_\pm = \frac{\omega_a + \omega_m}{2} \pm \frac{1}{2}\sqrt{(4g_{ma})^2 + \Delta_{ma}^2}, \tag{6.9}$$

resulting in a splitting proportional to g_{ma}. The normal mode splitting, $\Delta\omega$, is $\omega_+ - \omega_- = \sqrt{4g_{ma}^2 + \Delta_{ma}^2}$. Each of these resulting hybridised modes then have a hybridised decay rate found as

$$\begin{aligned} \kappa_+ &= \cos^2(\theta)\,\kappa_a + \sin^2(\theta)\,\kappa_m, \\ \kappa_- &= \sin^2(\theta)\,\kappa_a + \cos^2(\theta)\,\kappa_m. \end{aligned} \tag{6.10}$$

Note that for $\kappa_a \approx \kappa_m$ then each of these modes has a decay rate that is equal, which is what will be assumed throughout.

The Hamiltonian for the system can be expressed as [129]

$$\begin{aligned} \mathcal{H} = &-\hbar\Delta_+\hat{A}_+^\dagger\hat{A}_+ - \hbar\delta_-\hat{A}_-^\dagger\hat{A}_- \\ &+ \hbar\omega_b\hat{b}^\dagger\hat{b} + \hbar g_+\left(\hat{A}_+^\dagger + \hat{A}_+\right)\left(\hat{b}^\dagger + \hat{b}\right) + \hbar g_-\left(\hat{A}_-^\dagger + \hat{A}_-\right)\left(\hat{b}^\dagger + \hat{b}\right) \end{aligned} \tag{6.11}$$

where the Hamiltonian has been linearised using the hybrid modes. Note that it is defined the parametrically-enhanced magnon-phonon coupling rates, $g_\pm$ as

$$g_\pm = g_{mb}^0 A_{\pm,ss}\frac{1 \mp \cos(2\theta)}{2}. \tag{6.12}$$

where $A_{\pm,ss}$ is the steady state excitation of the hybridised mode. In the simple single mode regime, this steady state excitation is given by

$$A_{\pm,ss} = \frac{i\sqrt{2\kappa_{\pm,ex}}}{-i(\omega_\pm - \omega_d) - \kappa_\pm}\sqrt{\frac{P_{in}}{\hbar\omega_d}}, \tag{6.13}$$

in analogy to the cavity population n_{cav}, for a hybridised external decay rate

$$\kappa_{\pm,ex} = \frac{1 \pm \cos(2\theta)}{2}\kappa_{ex}. \tag{6.14}$$

For modes which are maximally hybridised, $\theta = \pi/4$ and the expression reduces to $g_\pm = g_{mb}^0 A_{\pm,ss}/2$. The cooperativity of the system is then defined as

$$C = \frac{|g_\pm|^2}{\kappa_\pm\kappa_b}, \tag{6.15}$$

which, for a cavity resonant with the magnon modes at a field H_e, becomes the cooperativities and multimagnon-phonon coupling rates shown in Sec. 5.

6.2.1 Magnon-phonon cooling

Often, quantum control requires oscillators to be in their ground state for use in quantum applications. At minimum, it is often considered that the oscillator is at least near the ground state, for which $\bar{n}_{\mathrm{f}} << 1$. Following from Bose-Einstein statistics, the thermal population of phonons at a temperature T is found as

$$\bar{n}_{\mathrm{th}} = \frac{1}{\exp\left(\frac{\hbar\omega_{\mathrm{R}}}{k_{\mathrm{B}}T}\right) - 1}. \tag{6.16}$$

To consider the oscillator in its ground state, it is required that $T << \hbar\omega_{\mathrm{R}}/k_{\mathrm{B}}$. As a figure of merit, for a mechanical oscillator at MHz frequency, the notional temperature required for this ground-state assumption require $T << 10^{-5}\,\mathrm{K}$. Experimentally, this proves a (very) difficult temperature to achieve [205], and so often additional cooling methods of the mechanical oscillator is required.

Dynamical back-action offers a feasible implementation of this involving exploiting the hybrid damping rate. For a classical oscillator at an initial temperature, T_{i}, subjected to an additional source of damping providing a damping rate, Γ_{opt}, the final temperature of the oscillator in the classical picture can be thought of as [206]

$$T_{\mathrm{f}} = T_{\mathrm{i}}\frac{\Gamma_{\mathrm{m}}}{\Gamma_{\mathrm{m}} + \Gamma_{\mathrm{c}}}. \tag{6.17}$$

This expression, however, is not valid at sufficiently low temperatures due to the fluctuations of the radiation pressure from photon noise, which are not present in the classical theory.

In deriving a quantum picture of hybrid cooling, that presented in optomechanics in the scattering picture is the easiest to interpret. Photons that are red-detuned from the resonance of the cavity need to scatter upwards in order to enter. In doing so, they absorb a phonon from the oscillator via the optomechanical interaction, and carry away the mechanical energy from the resonator, being blue-shifted in the process. In ket notation, this transition describes $|0\rangle_{\mathrm{p}}|n\rangle \rightarrow |0\rangle_{\mathrm{p}}|n-1\rangle$. This occurs at a rate A^{-}, such that the associated transition rate can be expressed as

$$\Gamma_{n-1} = nA^{-}. \tag{6.18}$$

The alternative arrangement is then that the photons interact with the resonator and are red-shifted, where they then impart a phonon. In ket notation, this transition describes $|0\rangle_{\mathrm{p}}|n\rangle \rightarrow |0\rangle_{\mathrm{p}}|n+1\rangle$. This occurs at a rate A^{+}, such that the associated transition rate can be expressed as

$$\Gamma_{n+1} = (n+1)A^{+}. \tag{6.19}$$

The full damping rate then expressed as the sum of these two individual rates,

$$\Gamma_{\mathrm{opt}} = A^{-} + A^{+}. \tag{6.20}$$

There also exists additional transition rates due to the thermal environment, which has a mean thermal population as given by Eq. 6.16. These inherent processes are dictated by mechanical damping [172],

$$A^{+}_{\mathrm{th}} = \bar{n}_{\mathrm{th}}\Gamma_{\mathrm{m}} \qquad \text{and} \qquad A^{-}_{\mathrm{th}} = (\bar{n}_{\mathrm{th}}+1)\Gamma_{\mathrm{m}}. \tag{6.21}$$

The evolution of the average phonon number, $\bar{n}$, can then be determined from the transition rates, Γ_{n-1}, and Γ_{n+1}, augmented with the thermal contributions (i.e. $A^{\pm} \mapsto A^{\pm} + A^{\pm}_{\mathrm{th}}$). It is found

$$\frac{\mathrm{d}\bar{n}}{\mathrm{d}t} = (\bar{n}+1)\left(A^{+} + A^{+}_{\mathrm{th}}\right) - \bar{n}\left(A^{-} + A^{-}_{\mathrm{th}}\right), \tag{6.22}$$

such that the steady-state final average number of phonons is

$$\bar{n}_{\mathrm{f}} = \frac{A^{+} + \bar{n}_{\mathrm{th}}}{\Gamma_{\mathrm{opt}} + \Gamma_{\mathrm{m}}}. \tag{6.23}$$

In the absence of any thermal effects, the minimum average phonon number is

$$\bar{n}_{\mathrm{min}} = \frac{A^{+}}{\Gamma_{\mathrm{opt}}} = \frac{A^{+}}{A^{+} + A^{-}}. \tag{6.24}$$

It can be shown by analysis of the quantum noise spectra [88, 172] that the average minimum number of phonons is determined by

$$\bar{n}_{\mathrm{min}} = \left(\frac{(\Delta - \omega_{\mathrm{R}})^2 + (\kappa/2)^2}{(\Delta + \omega_{\mathrm{R}})^2 + (\kappa/2)^2} - 1\right)^{-1}, \tag{6.25}$$

and hence the average final number of phonons as re-expressed as

$$\bar{n}^{(0)}_{\mathrm{f}} = \frac{\Gamma_{\mathrm{opt}}\bar{n}_{\mathrm{min}} + \Gamma_{\mathrm{m}}\bar{n}_{\mathrm{th}}}{\Gamma_{\mathrm{opt}} + \Gamma_{\mathrm{m}}}. \tag{6.26}$$

In the case that there is strong coupling (c.f. Section 4.6), then ground state cooling becomes less effective as transition routes become subjected to the cavity decay rate [207], and so the modified average final number of phonons

$$\bar{n}_{\mathrm{f}} = \bar{n}^{(0)}_{\mathrm{f}} + \bar{n}_{\mathrm{th}}\frac{\Gamma_{\mathrm{m}}}{\kappa} + 2\bar{n}_{\mathrm{min}}\frac{\Gamma_{\mathrm{opt}}}{\kappa} \tag{6.27}$$

While, in principle, Γ_{opt} should be evaluated at $\omega = \omega_{\pm}$ for both the hybrid modes that arise as a consequence of the normal-mode splitting, the correction to the magnon-hybridised mode frequency is of the order of $\pm$ MHz. Compared to the assumed magnon mode frequency of 10s of GHz, it is assumed that this makes negligible differences to the coupling damping rate.

Dynamical back-action cooling has been seen in a number of systems [85, 208, 209], whereby reductions in temperature have been observed as a result of the coupling between resonator modes. Cooling to the ground state, for which phonon occupancy are (well) below 1 is non-trivial. To provide a head-start to attaining ground-state cooling, often cryostats and dilution fridges are used to pre-cool devices down to temperature on the order tens of milliKelvin. The pre-cooling temperature of $T_{\mathrm{i}} = 20\,\mathrm{mK}$ is attainable with dilution fridges [210, 211], but works have demonstrated ground ground state cooling from higher environmental temperatures [86], as well as room-temperature ground state cooling [212, 213]. Explored here is the regime of magnomechanical cooling under the assumption of exemplar cryogenic temperatures of $T_{\mathrm{i}} = 4\,\mathrm{K}$, $T_{\mathrm{i}} = 200\,\mathrm{mK}$, and $T_{\mathrm{i}} = 20\,\mathrm{mK}$, for which the input power assumption down the transmission line thus far for the transmission line is compatible with the cooling power of all these temperatures [205, 214, 215].

onsidered are the geometries listed in Tables 5.3 and 5.5, and take the values with the largest g^{rec} to give the largest cooling rates. While magnomechanical cooling has not been observed to the ground state [216], proposals based on the YIG sphere-magnetic cavity device have hypothesised that ground-state cooling should be feasible with realistic parameters [217] - note that, for this proposal a sphere diameter of 250 μm is used, which retains the bulky size non-compatible with on-chip designs. The device proposed within achieves comparable ground state final phonon occupancies in both the bridge and cantilever geometries, while having dimensions on the nano-scale. The system also presents coupling strengths $g^{\text{rec}}/\omega_{\text{R}} \approx 1/10$ on which their theory is derived. While pre-cooling of the system is required (they assume a thermal occupation $\bar{n}_{\text{th}} = 1000$), this should allow the ground state cooling proposal to translate directly to our device.

For the cantilever, the resonator is in the strong coupling regime, and evaluation of the modified final phonon number in Eq. 6.27 is required. Strong coupling deteriorates cooling, but ground state cooling should should be possible with sufficient pre-cooling. A resonator geometry $L_{\text{R}} = 4.5\,\mu$m, $L_{\text{m}} = 0.35L_{\text{R}}$, $w_{\text{m}} = w_{\text{R}} = 300\,$nm, and $t_{\text{R}} = 350\,$nm for an isosceles cross-section is assumed. For this, it was found there was an associated multimagnon-phonon coupling rate $g^{\text{rec}}/2\pi = 0.79\,$MHz and decay rate $\kappa/2\pi = 0.316\,$MHz. The mechanical mode frequency of the fundamental mode of the resonator is $\omega_{\text{R}}/2\pi = 12.7\,$MHz. From Eq. 6.25, the minimum number of phonons that these parameters give is $\bar{n}_{\text{min}} = 3.8 \times 10^{-5}$. The magnomechanical damping rate is then $\Gamma_{\text{opt}}/2\pi = 7.9\,$MHz, and the mechanical damping rate (assuming $Q_{\text{GGG}} = 10^4$) finds $\Gamma_{\text{m}}/2\pi = 1270\,$Hz.

Taking a pre-cooled temperature of $T_{\text{i}} = 20\,$mK, then the final phonon number in the strong coupling regime is found as

$$\bar{n}_{\text{f}}\,(20\,\text{mK}) = 5.2 \times 10^{-3} + 1.3 \times 10^{-1} + 1.9 \times 10^{-3} \approx 0.14. \tag{6.28}$$

For a pre-cooled temperature $T_{\text{i}} = 200\,$mK, the final number of phonons in the strong coupling regime is

$$\bar{n}_{\text{f}}\,(200\,\text{mK}) = 5.3 \times 10^{-2} + 1.3 + 1.9 \times 10^{-3} \approx 1.4. \tag{6.29}$$

For a pre-cooled temperature $T_{\text{i}} = 4\,$K, the final number of phonons in the strong coupling regime is

$$\bar{n}_{\text{f}}\,(4\,\text{K}) = 1.1 + 26.3 + 1.9 \times 10^{-3} \approx 27.4. \tag{6.30}$$

These correspond to 0.14 quantas, 1.4 quantas, and 27.4 quantas of mechanical energy in the oscillator. Only at a pre-cooling of $T_{\text{i}} = 20\,$mK can the cantilever be considered in it's ground state.

For the bridge, the resonator can be considered in the strong coupling and the weak coupling regime, depending on both the resonator dimensions and the resonator cross-section. The isosceles device presents geometries which attain strong coupling quite well, whereas the rectangular device is unable to replicate this. Presented here are cases for which the resonator has dimensions placing it in strong coupling (requiring Eq. 6.27), and also dimensions placing it in weak coupling (requiring Eq. 6.26).

For strong coupling, the resonator geometry $L_{\text{R}} = 12.1\,\mu$m, $L_{\text{m}} = 0.25L_{\text{R}}$, $w_{\text{m}} = w_{\text{R}} = 400\,$nm, and $t_{\text{R}} = 350\,$nm for an isosceles cross-section is assumed. For this, it was found there was an associated multimagnon-phonon coupling rate $g^{\text{rec}}/2\pi = 0.19\,$MHz and decay rate $\kappa/2\pi = 0.38\,$MHz. The mechanical mode frequency of the

fundamental mode of the resonator is $\omega_R/2\pi = 11.2\,\text{MHz}$. From Eq. 6.25, the minimum number of phonons that these parameters give is $\bar{n}_{\text{min}} = 1.8 \times 10^{-6}$. The magnomechanical damping rate is then $\Gamma_{\text{opt}}/2\pi = 2\,\text{MHz}$, and the mechanical damping rate (assuming $Q_{\text{GGG}} = 10^4$) finds $\Gamma_m/2\pi = 1120\,\text{Hz}$. For a pre-cooled temperature of $T_i = 20\,\text{mK}$, then the final phonon number in the strong coupling regime is found as

$$\bar{n}_f\,(20\,\text{mK}) = 7.4 \times 10^{-2} + 1.1 \times 10^{-1} + 1.9 \times 10^{-5} \approx 0.18. \tag{6.31}$$

Higher temperatures are neglected as these follow the same trend as for the cantilever. Again, in the strong coupling regime the only accessible temperature for ground state cooling is of the order of 20 mK.

For weak coupling, the resonator geometry $L_R = 14\,\mu\text{m}$, $L_m = 0.25L_R$, $w_m = w_R = 450\,\text{nm}$, and $t_R = 350\,\text{nm}$ for a rectangular cross-section is assumed. For this, it was found there was an associated multimagnon-phonon coupling rate $g^{\text{rec}}/2\pi = 0.10\,\text{MHz}$ and decay rate $\kappa/2\pi = 0.37\,\text{MHz}$. The mechanical mode frequency of the fundamental mode of the resonator is $\omega_R/2\pi = 10.2\,\text{MHz}$. From Eq. 6.25, the minimum number of phonons that these parameters give is $\bar{n}_{\text{min}} = 2.1 \times 10^{-6}$. The magnomechanical damping rate is then $\Gamma_{\text{opt}}/2\pi = 0.11\,\text{MHz}$, and the mechanical damping rate (assuming $Q_{\text{GGG}} = 10^4$) finds $\Gamma_m/2\pi = 1000\,\text{Hz}$. Taking a pre-cooled temperature of $T_i = 20\,\text{mK}$, then one finds for the final phonon number in the weak coupling regime

$$\bar{n}_f\,(20\,\text{mK}) = 7.4 \times 10^{-2} + 1.1 \times 10^{-1} + 1.9 \times 10^{-5} \approx 0.36. \tag{6.32}$$

Even in the weak coupling regime where cooling is more effective the final number of phonons achievable is still higher than in the strong coupling regime.

Lastly, some comments are made on the 'quantum' cooperativity at these temperatures, defined as

$$\mathcal{C}_q = \frac{\mathcal{C}}{\bar{n}_{\text{th}}}. \tag{6.33}$$

This parameter quantifies the efficiency of state transfer, and quantum cooperativities of order unity signify that state transfer between magnons and phonons is faster than the decoherence rate to the thermal environment, an important scheme for applications such as quantum computing. If one takes the same dimensions as noted for the cooling schemes, then it is found for the cantilever a cooperativity of $\mathcal{C} = 6.3 \times 10^3$ at a mechanical frequency $\omega_R/2\pi = 12.7\,\text{MHz}$. If one takes the scheme for which the structure was within the ground state (i.e. 20 mK), then it is found for the average phonon occupation $\bar{n}_{\text{th}} \approx 32$. In turn, this corresponds to a quantum cooperativity $\mathcal{C}_q(20\,\text{mK}) \approx 200$ while also being compatible with ground state cooling. Instead considering the other cryogenic temperatures, one finds for the quantum cooperativity $\mathcal{C}_q(200\,\text{mK}) \approx 20$ and $\mathcal{C}_q(4\,\text{K}) \approx 1$. Note that quantum cooperativies of order unity at moderate cryogenic temperatures (typical helium cryostats operating at 4 K) have not been seen typical cavity optomechanical setups until recent [218]. Instead assuming the bridge geometry mentioned, then one finds a cooperativity of $\mathcal{C} = 3.2 \times 10^2$ at a mechanical frequency $\omega_R/2\pi = 11.2\,\text{MHz}$. This then corresponds to quantum cooperativities at each temperature roughly an order of magnitude lower than that of the cantilever, which means that the bridge can only attain quantum cooperativities of order unity up to 200 mK.

6.2.2 Magnomechanically induced transparency

In analogy with optomechanically induced transparency [96], the theory of magnomechanics also predicts the emergence of an interference of a probe signal, an effect which is necessary for slow light conversion and quantum memories [219]. The effect of magnomechanically induced transparency can be investigated via consideration of the output field of the weak probe [219]. In full, the solution [129] to this field is found as

$$X_1 = g_{\mathrm{ma}}^2 \left((2G_{\mathrm{mb}}^2 \left(\chi_{\mathrm{b}-} - \chi_{\mathrm{b}+} \right) - \chi_{\mathrm{b}-}\chi_{\mathrm{b}+}\chi_{\mathrm{m}-} \right), \tag{6.34}$$

$$X_2 = \chi_{\mathrm{a}+} \left(G_{\mathrm{mb}}^2 \left(\chi_{\mathrm{b}-} - \chi_{\mathrm{b}+} \right) \left(\chi_{\mathrm{m}-} - \chi_{\mathrm{m}+} \right) + \chi_{\mathrm{b}-}\chi_{\mathrm{b}+}\chi_{\mathrm{m}-}\chi_{\mathrm{m}+} \right), \tag{6.35}$$

$$X_3 = g_{\mathrm{ma}}^2 \left(\chi_{\mathrm{b}-}\chi_{\mathrm{b}+} \left(\chi_{\mathrm{a}-}\chi_{\mathrm{m}-} + \chi_{\mathrm{a}+}\chi_{\mathrm{m}+} \right) - G_{\mathrm{mb}}^2 \left(\chi_{\mathrm{a}-} - \chi_{\mathrm{a}+} \right) \left(\chi_{\mathrm{b}-} - \chi_{\mathrm{b}+} \right) \right), \tag{6.36}$$

$$X_4 = \chi_{\mathrm{a}-}\chi_{\mathrm{a}+} \left(G_{\mathrm{mb}^2} \left(\chi_{\mathrm{b}-} - \chi_{\mathrm{b}+} \right) \left(\chi_{\mathrm{m}-} - \chi_{\mathrm{m}+} \right) + \chi_{\mathrm{b}-}\chi_{\mathrm{b}+}\chi_{\mathrm{m}-}\chi_{\mathrm{m}+} \right), \tag{6.37}$$

where it is defined

$$\chi_{\mathrm{a}\pm} = \pm i \left(\omega_{\mathrm{a}} - \omega_{\mathrm{d}} \pm \omega_{\mathrm{s}} \right) - \kappa_{\mathrm{a}}, \tag{6.38}$$

$$\chi_{\mathrm{b}\pm} = \pm i \left(\omega_{\mathrm{b}} \pm \omega_{\mathrm{s}} \right) - \kappa_{\mathrm{b}}, \tag{6.39}$$

$$\chi_{\mathrm{m}\pm} = \pm i \left(\omega_{\mathrm{m}} - \omega_{\mathrm{d}} \pm \omega_{\mathrm{s}} \right) - \kappa_{\mathrm{m}}, \tag{6.40}$$

with cavity-boosted magnon-phonon coupling $G_{\mathrm{mb}} = g_{\mathrm{mb}}^0 m_{\mathrm{ss}}$ and m_{ss} being the steady-state population of magnons. Note that this is distinct to the parametrically-enhanced coupling rate $g_{\pm}$ which is the parameter of consequence for applications. The reflection spectrum may be then calculated from

$$r = 1 + i\sqrt{2\kappa_{\mathrm{ex}}} \frac{X_1 - X_2}{X_3 + X_4 + \chi_{\mathrm{b}-}\chi_{\mathrm{b}+}g_{\mathrm{ma}^4}}. \tag{6.41}$$

The steady-state population of magnons is found via use of the Heisenberg equation for the magnon, photon, and phonon operators, and solving by setting time derivatives to 0. In doing so, one finds the expression [31]

$$m_{\mathrm{ss}} = \frac{i g_{\mathrm{ma}} \epsilon_{\mathrm{d}} \sqrt{2\kappa_{\mathrm{ex}}}}{\left(i \left(\omega_{\mathrm{d}} - \omega_{\mathrm{a}} \right) - \kappa_{\mathrm{a}} \right) \left(i \left(\omega_{\mathrm{d}} - \omega_{\mathrm{m}} \right) - \kappa_{\mathrm{m}} \right) + g_{\mathrm{ma}}^2}, \tag{6.42}$$

where $\epsilon_{\mathrm{d}} = \sqrt{P_{\mathrm{in}}/\hbar\omega_{\mathrm{d}}}$. It is then possible to plot the output spectrum to explore magnomechanically induced transparency.

Presented here are two speculative geometries that may be of interest relating to the bridge and cantilever nanostructures. For this, isosceles cross-sections are assumed such that g_{mb}^0 is maximised relative to the geometry, and again consider an applied field of $H_{\mathrm{e}} = 350\,\mathrm{Oe}$, resulting in a magnon frequency $\omega_{\mathrm{m}}/2\pi = 2.408\,\mathrm{GHz}$ assumed to be resonant with the cavity frequency ω_{a}. For simplicity, the device is only considered at a central distance $d_{\mathrm{c}} = 1\,\mu\mathrm{m}$ above a transmission line. With these assumptions, the single mode criterion in particular presents difficulties, but a strong coupling regime of interest is accessible. The geometries are described as follows;

- For the bridge, a resonator of length $L_{\mathrm{R}} = 22.5\,\mu\mathrm{m}$, thickness $t_{\mathrm{R}} = 0.35\,\mu\mathrm{m}$, and width $w_{\mathrm{R}} = 0.5\,\mu\mathrm{m}$ is taken, with associated flexural mode frequency $\omega_{\mathrm{R}}/2\pi = 3.23\,\mathrm{MHz}$ and mechanical damping $\Gamma_{\mathrm{R}}/2\pi = 323\,\mathrm{Hz}$. Placed centrally on this bridge resonator is a YIG magnetic structure of length $L_{\mathrm{m}} = 9\,\mu\mathrm{m}$, width $w_{\mathrm{m}} = w_{\mathrm{R}}$, thickness $t_{\mathrm{m}} = 25a_0$, resulting in a decay rate into magnon

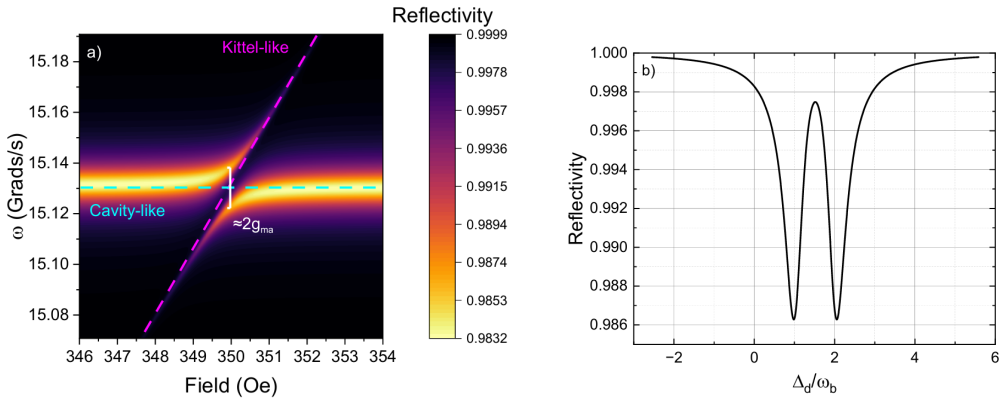

FIGURE 6.1: The reflection spectrum (a) of the cantilever-YIG resonator structure as a function of field and frequency, as well as the cross-section of the plot (b) taken at $H_e = 350\,\text{Oe}$, with $g_{mb^0} = 0$.

modes $\kappa_{ex}/2\pi = 15.7\,\text{KHz}$. With these dimensions, one finds for the constraints a mode validity $k_0\{w_R, t_R\}/L_R = \{0.1, 0.07\}$, a resolved sideband of $\kappa/\omega_R = 0.08$, a magnon nonlinearity $n_{mag}/N_S = 0.06$ and a slightly obtuse single mode criterion, $\omega_R/\Delta_m = 0.18$. One finds for the single magnon-phonon coupling $g^0_{mb}/2\pi = 12.0\,\text{Hz}$, a multimagnon-phonon coupling $g_{mb}/2\pi = 73.8\,\text{KHz}$, a multimagnon-photon coupling $g_{ma}/2\pi = 1.6\,\text{MHz}$, and a magnon-phonon cooperativity $\mathcal{C}_{mb} = 262$. Note that these parameters put the device on the triple resonance scheme for which $\omega_R/g_{ma} \approx 2$.

- For the cantilever, a resonator of length $L_R = 12.5\,\mu\text{m}$, thickness $t_R = 0.5\,\mu\text{m}$, and width $w_R = 0.65\,\mu\text{m}$ is taken, with associated flexural mode frequency $\omega_R/2\pi = 2.35\,\text{MHz}$ and mechanical damping $\Gamma_R/2\pi = 235\,\text{Hz}$. The first $1/3$ of the cantilever's surface from the fixed edge is covered with magnetic material, producing dimensions of $L_m \approx 4\,\mu\text{m}$ and $w_m = w_R$, and take the film to be $t_m = 25a_0$. This then results in a decay rate into magnon modes $\kappa_{ex}/2\pi = 8.83\,\text{KHz}$. With these dimensions, one finds for the constraints a mode validity $k_0\{w_R, t_R\}/L_R = \{0.12, 0.08\}$, a resolved sideband of $\kappa/\omega_R = 0.11$, a magnon nonlinearity $n_{mag}/N_S = 0.12$ and a single mode criterion $\omega_R/\Delta_m = 0.05$. One also finds for the single magnon-phonon coupling $g^0_{mb}/2\pi = 57\,\text{Hz}$, a multimagnon-phonon coupling $g_{mb}/2\pi = 0.223\,\text{MHz}$, a multimagnon-photon coupling $g_{ma}/2\pi = 1.22\,\text{MHz}$ and a magnon-phonon cooperativity $\mathcal{C}_{cb} = 3404$, over an order of magnitude larger than for the bridge. These parameters also put the device close to the triple resonance scheme with $\omega_R = 1.9 g_{ma}$.

When plotting Eq. 6.41 as a function of applied magnetic field and frequency, ω, for when the magnon-phonon coupling is 'switched' off (that is $g^0_{mb} = 0$, then one recovers the familiar simple strong coupling splitting [2] as illustrated in Fig. 6.1. For this figure, a red-detuning is assumed such that $\Delta_d = \omega_m(H_e = 350\,\text{Oe}) - \omega_b$ for the cantilever parameters listed prior. Shown also in this figure is the cross-section in frequency taken at $\omega_m(He = 350\,\text{Oe}) = \omega_a$, plotted as a function of the rationalised detuning Δ_d/ω_b, which shows that the splitting is equal to $2g_{ma} = \omega_b$.

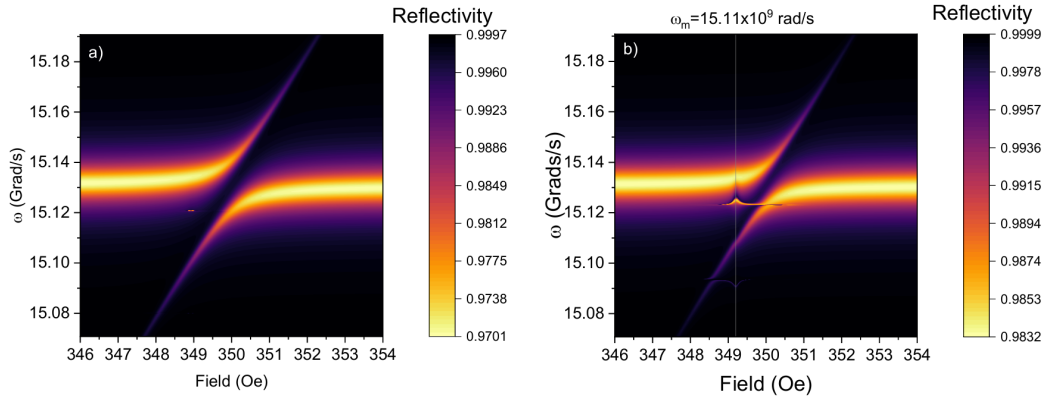

FIGURE 6.2: The reflection spectrum of the (a) cantilever-YIG and (b) bridge-YIG resonator structures as a function of field and frequency.

When the system is red-detuned and the magnon-phonon coupling is 'switched' on with the values listed in the prior sections, far more interesting behaviour emerges in the reflection spectrum. Depicted in Fig. 6.2 is the reflection spectrum for both the cantilever and bridge parameters. When the effect of the magnon-phonon coupling included, one sees the emergence of new mechanical side-bands in the reflection spectrum, a unit of ω_b either side of the drive tone. The frequency of the side-bands vary as a function of field, and the separation changes in frequency at the field which provides a magnon mode that is equal to the drive tone of the system; for the parameters used for the cantilever, this frequency is at $H_e \approx 349.2$ as is seen in the plot. The emergence of the mechanical side-bands, which in turn is a consequence of the magnon-phonon coupling, is not as well seen in the reflection spectrum of the bridge, owing to the smaller single magnon-phonon coupling rate of the system (some factor of 4 smaller than what is attained for the cantilever).

Taking a cross-section for where the magnon modes are resonant with the cavity mode, $H_e = 350\,\text{Oe}$, one can see the influence of the side-bands within the reflection spectrum and the emergence of the transparency window, a plot which is shown in Fig. 6.3 (a). As the bridge has a larger decay rate into the magnon modes, κ_{ex} than the cantilever, a larger dip in the reflection spectrum is attainable and provides a reflectivity in the trench of the reflection twice as deep as that of the cantilever. However, the cantilever is able to offer a much larger transparency window, essentially providing a resonance dip depth to transparency window depth of almost 1. From the graph, one can relate the linewidth of the transparency window to the mechanical damping to find an estimate of the cooperativity [220] of roughly $\mathcal{C}_{mb} \approx 3000$ as anticipated for the cantilever. Also shown in Fig. 6.3 (b) and (c) are cases which cross-sections which on the cantilever plot where the side-bands are more visible and taking cross-sections at a field where the separation of the emergent side-bands is greatest. In these, (b) shows the cross-section taken where the side-band separation is greatest ($H_e = 349.2\,\text{Oe}$), and (c) shows another cross-section to right of this where the increase in separation begins ($H_e = 349.5\,\text{Oe}$). Firstly, one can see that the separation of the side-bands increases. At points away from this feature, the separation of the peaks is given by $2\omega_b$ (i.e they are a factor of ω_b either side of the drive tone). Where this feature occurs at a field supplying a magnon mode equal to the drive tone, then the separation of the side-bands is (roughly) $\omega_b + 0.004\,\text{MHz}$. In addition to this change in separation, an increase in the line-width of the side-band occurs, roughly doubling it. Neither of these features have been previously seen in

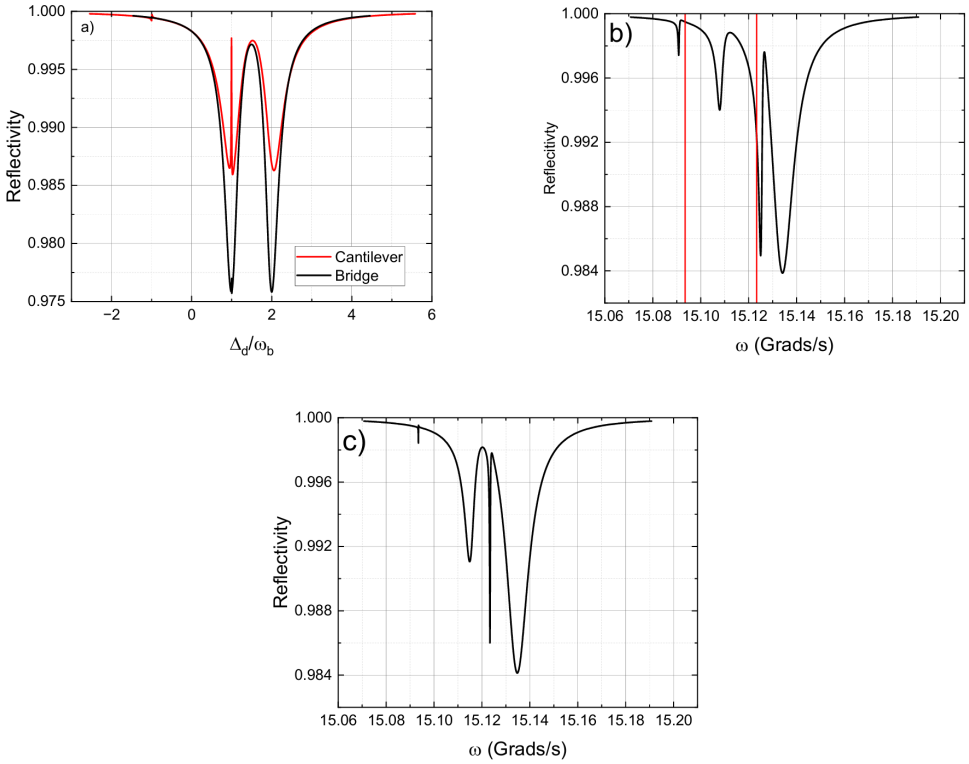

FIGURE 6.3: Cross-section of the reflection plot taken at the field (a) $H_e = 350\,\mathrm{Oe}$ showing the transparency window for the cantilever and bridge devices, and additional cross-sections taken at the fields (b) $H_e = 349.2\,\mathrm{Oe}$ and (c) $H_e = 349.5\,\mathrm{Oe}$. The red bars on (b) denote the shift in the side-band positions.

experimental data [129, 216], and remain as a hallmark of the significant boosts to g^0_{mb} and g_{mb} that the theory contained within presents (some 3 orders of magnitude and 2 orders of magnitude larger, respectively)

6.2.3 Magnon spring effect and magnomechanical damping

As a consequence of the magnon-phonon coupling, and in analogy with the dynamical backaction presented in Sec. 4.7, magnons impart a parametric force on the phonons. One can solve the equations of motion in the frequency domain to find an approximation for the phonon self-energy as a consequence of the dynamical backaction [216, 221] as

$$\Sigma(\omega) = i\left|g^0_{mb} m_{ss}\right|^2 \left(\Theta(\omega) - \Theta^*(-\omega)\right) \tag{6.43}$$

where

$$\Theta = \frac{1}{\chi_{m+} + g^2_{ma}\chi^{-1}_{a+}}, \tag{6.44}$$

and is an expression of the modification to the susceptibility of the phonons as a result of it's interactions with the magnons. Through the expression Σ it is then possible to consider the influence of the magnon spring effect, in analogy to the optical spring effect and the magnomechanical damping rate, where the two effects

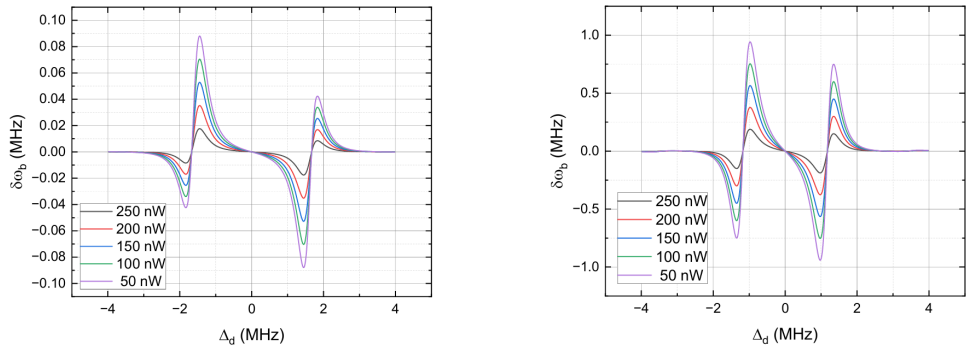

FIGURE 6.4: Magnon-spring effect as a function of drive detuning for (a) the bridge geometry and (b) the cantilever geometry for differing input powers.

enter as

$$\Omega_b = \omega_b + \delta\omega_b, \tag{6.45}$$

$$\Gamma_{tot} = \Gamma_b + \Gamma_c \tag{6.46}$$

where Γ_c represents the additional coupling as a result of the magnomechanical interaction.

Shown in Fig. 6.4 is the influence of the magnon spring effect, which finds that the phonon modes are (immensely) spring-hardened for the parameters suggested in the prior section. These plots are performed for a series of input powers, P_{in}, whereby the relationship appears linear. For the bridge, at the input power $P_{in} = 250\,\text{Oe}$, one would expect a maximum difference to the phonon mode frequency of $\delta\omega_b/\omega_b \approx 0.025$, whereas for the cantilever, one would expect a maximum difference of $\delta\omega_b/\omega_b \approx 0.43$. These represent significant deviations from reported values using the prior experimental approach to magnomechanics [216], where increases of the order of around 100 Hz were seen. This kind of modulation of the mechanical frequency with input power is necessary for the entangling of states [222], and the range of modulation to the phonon frequency could offer regimes to implement entanglement for magnons.

The regime of ground state cooling using the magnomechanical decay rate has already been explored in Sec. 6.2.1; regardless, the data is presented in Fig. 6.5 as a function of the drive detuning for completeness. As was already expected given the disparity in multimagnon-phonon coupling rates attainable, the cantilever far exceeds that of the bridge, offering rates almost a order of magnitude larger decay rates.

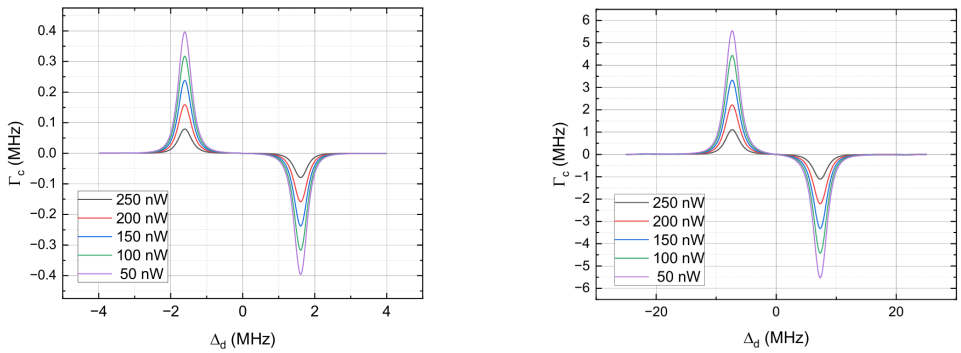

FIGURE 6.5: Magnomechanical decay rate as a function of drive detuning for (a) the bridge geometry and (b) the cantilever geometry for differing input powers.

Chapter 7

A Si_3N_4 device

Mechanical dissipation imposes fundamental constraints on the observation of quantum behaviour in optomechanical systems, which is clearly something that is needed to be minimised. Breakthroughs with regards to high quality low mechanical damping devices appeared in 2008, in which commercially available SiN membranes were used to form a membrane-in-the-middle type cavity with exceptional mechanical properties [36, 223].

Silicon nitride exhibits non-zero pre-stress, which exists as a consequence of it's manufacture. It is made using a process of low-pressure chemical vapour deposition (LPCVD), occuring at around 800 K and at $\sim$ 200 mTorr of pressure. In this, volatile constituent compounds are exposed to a silicon wafer, which react to form a thin layer of silicon nitride on the surface of the wafer. As the substrate cools, an intrinsic tensile stress is formed due to the thermal mismatch of silicon and silicon nitride. Due to the pre-stress originating from this thermal mismatch, it is not possible to manufacture resonators that are not doubly clamped (or equally pinned), else the silicon nitride film is allowed to relax through the free end.

Building on this, work now looks to incorporate high tensile stress silicon nitride films into hybrid quantum systems. High tensile pre-stress provides another way in which a mechanical resonator can store energy, without introducing a new energy loss mechanism in undergoing vibrations [224, 225, 226], and high stress silicon nitride, in particular, has been widely explored [227, 228, 229]. Initial optomechanical implementations used the fundamental mode of 1 mm^2 films, and obtained a Q-factor of 10^6 and $\omega_R \sim 0.1$ MHz, which can roughly be inferred as a pre-stress of $\sigma = 100$ MPa [230]. Stiochiometric silicon nitride, however, is able to achieve much higher pre-stresses [231], and with this came a demonstration of ground-state cooling from room temperature. Further, stoichiometric silicon nitride films with pre-stresses of up to 1 GPa are commercially available[1]. The Q-factor of high-tensile stress membranes has been studied, and an expression for such bridge structures is expressed as [226, 230]

$$Q^{\text{bridge}}(\sigma) = Q_{\text{intr}} \left(2L\sqrt{\frac{EI}{\sigma A}} + n^2\pi^2 L^2 \frac{EI}{\sigma A} \right)^{-1}, \tag{7.1}$$

where Q_{intr} is the intrinsic Q-factor of the material without the presence of pre-stress, n is the mode number of the bridge flexural mode, E is the material's Young's modulus, A is the cross-sectional area of the bridge and I is the bridge's second moment of area. The intrinsic Q-factor is not only a characteristic of the material, but phonon tunneling through the surface also contributes. Models of this behaviour introduce

[1] *Norcada*, for example, are one such manufacturer: *http://www.norcada.com*

the expression [230]

$$Q_{\text{intr}}^{-1} = Q_{\text{surf}}^{-1} + Q_{\text{vol}}^{-1} \equiv \beta t + Q_{\text{vol}}^{-1}, \tag{7.2}$$

where Q_{surf} and Q_{vol} are the surface and volume contributions to the intrinsic Q-factor, respectively, and t is the resonator thickness. Comprehensive fitting on Si_3N_4 has been performed by Villanueva and Schmidt [230], and found $Q_{\text{vol}} = 2.8 \times 10^4$ and $\beta = (60 \pm 40)\,\text{nm}^{-1}$. These values are used, along with Equations 7.1 and 7.2, to estimate the $Q-$factor of the resonator structure. Note that while the expressions are general, the parameter β has been fitted from a rectangular cross-section resonator, in which the width is linear as a function of thickness. It is unclear how well this fitting translates to isosceles cross-sections, whereby the width is dependent on the thickness. Regardless, it is assumed that any corrections are within the stated error. For some example dimensions, a 100 μm length resonator of width and thickness $w = t = 400\,\text{nm}$ finds a ratio of $Q(\sigma)/Q_{\text{vol}} \approx 10$. Q-factors are larger for longer and thinner resonators, and the Q-factor is independent of the resonator width.

The growth of high quality epitaxial YIG on Si_3N_4 has not been realised due to, in part, the large mismatch between the coefficients of thermal expansion (Si_3N_4 possesses one of $\sim 3.2 \times 10^{-6}\,\text{K}^{-1}$ [232] while YIG has one of $10.4 \times 10^{-6}\,\text{K}^{-1}$ [233]). This mismatch necessitates low growth temperatures to prevent the film from cracking [234, 235], and YIG films grown on such silicon substrates are polycrystalline [236]. These cracks present boundaries which act to raise the magnetic damping, and as such, a reconsideration of the Gilbert damping is required for the use of silicon nitride as a growth substrate. Crack-free thin films of YIG have been deposited onto SiO_2, and have achieved dampings of $\alpha \sim 10^{-3}$ [237, 238]. Thicker polycrystalline films of thickness 400 nm have achieved damping of $\alpha \sim 10^{-4}$, and with the aid of a thin platinum capping this damping was nearly halved [239]. In line with this literature, tentatively considered here is a Gilbert damping of $\alpha \sim 10^{-3}$ as a current limiting scenario. High quality YIG has also been grown on GGG substrates and then transferred to a silicon nitride membrane [240], although the dimensions of the structure were far larger than what this thesis aims to address - regardless, if the geometry and constraints permit, this could be a feasible implementation for the device.

7.1 Euler-Bernoulli theory and pre-stressed beams

Consider the case of an Euler-Bernoulli beam subjected to pre-stress alone, such that the general equation of motion becomes [67]

$$EI\frac{\partial^4 y}{\partial z^4} - \sigma A\frac{\partial^2 y}{\partial z^2} + \rho A\frac{\partial^2 y}{\partial t^2} = 0, \tag{7.3}$$

where σ is the intrinsic pre-stress, and other terms retain their definitions as in Eq. 3.68. In the so-called high-stress string limit [226, 230], which is to say

$$\sqrt{\frac{\sigma A}{EI}}L >> 1, \tag{7.4}$$

then the tension present in the beam can reduce the bending stiffness EI to zero. With this, the system can be treated simply as a string under tension [67]. Eq. 7.3 is then simplified to

$$\frac{\partial^2 y}{\partial z^2} = \frac{\rho}{\sigma}\frac{\partial^2 y}{\partial t^2}. \tag{7.5}$$

If one assumes propagating harmonic solutions of the form $\exp(kz - \omega t)$, then the familiar dispersion relation

$$\omega = k\sqrt{\frac{\sigma}{\rho}}, \tag{7.6}$$

of a tensile string is found. Assuming normal-modes of the form $y = \phi(z)\exp(-i\omega t)$, then substitution into Eq. 7.5 yields

$$\frac{\mathrm{d}^2\phi}{\mathrm{d}z^2} = -\omega^2\frac{\rho}{\sigma}\phi(z). \tag{7.7}$$

The equation has solutions offered by simple harmonic motion, for which one has the general solution

$$\phi(z) = A\sin(kz) + B\sin(kz). \tag{7.8}$$

While the system is now under pre-stress, the boundary conditions remain the same as outlined for the bridge in Sec. 3.6. Reiterating, these are

$$\phi(0) = \phi(L) = \phi'(0) = \phi'(L) = 0 \tag{7.9}$$

which can be used to solve the general solution to find

$$\phi(z) = \sin(kz) \tag{7.10}$$

with $k = n\pi/L$.

7.2 Magnon-phonon coupling in the pre-stressed regime

The reader is spared a drawn-out derivation for the single magnon-phonon coupling strength as it follows equivalently to Sec. 5.3.2, apart from having new mode profiles and mode frequencies. The normalisation constant of the mode profile can be expressed as

$$\mathcal{N} = \int_V |\mathbf{u}_n|^2\,\mathrm{d}V = \sqrt{\frac{2}{A_\mathrm{R}L_\mathrm{R}}}, \tag{7.11}$$

where the bridge, of length L_R, has been assumed to have constant cross-section A_R. Following the same procedure, one finds for the single magnon-phonon coupling strength

$$g_0^\mathrm{rec} = \frac{B_1(1+\nu)\gamma_\mathrm{g}}{M_\mathrm{s}(\rho\sigma)^{1/4}}\sqrt{\frac{\hbar k_n^3 t_\mathrm{R}^2}{A_\mathrm{R}L_\mathrm{R}}}\left(\left(1+\frac{4\pi M_\mathrm{s}}{H_\mathrm{e}}\right)^{\frac{1}{2}} + \left(1+\frac{4\pi M_\mathrm{s}}{H_\mathrm{e}}\right)^{-\frac{1}{2}}\right) \times \left\langle \sin\left(\frac{\pi z}{L_\mathrm{m}}\right)\phi_n''(z)\right\rangle. \tag{7.12}$$

Considering the fundamental mode of the bridge only, one further finds

$$g_0^\mathrm{rec}(n=1) = \frac{\pi^{3/2}B_1(1+\nu)\gamma_\mathrm{g}}{M_\mathrm{s}(\rho\sigma)^{1/4}}\frac{1}{L_\mathrm{R}^2}\sqrt{\frac{\hbar t_\mathrm{R}^2}{A_\mathrm{R}}}\left(\left(1+\frac{4\pi M_\mathrm{s}}{H_\mathrm{e}}\right)^{\frac{1}{2}} + \left(1+\frac{4\pi M_\mathrm{s}}{H_\mathrm{e}}\right)^{-\frac{1}{2}}\right) \times \left\langle \sin\left(\frac{\pi z}{L_\mathrm{m}}\right)\sin\left(\frac{\pi z}{L_\mathrm{R}}\right)\right\rangle \tag{7.13}$$

Parameter	Value	Reference
$4\pi M_s$	1750 Oe	[127]
B_1	3.48×10^6 dyne/cm^2	[140]
$\rho_{Si_3N_4}$	2.7 g/cm^3	[227]
$E_{Si_3N_4}$	2.2×10^{12} dyne/cm^2	[227, 241, 242].
$\nu_{Si_3N_4}$	0.23	[241]

TABLE 7.1: Choice parameters for use in $g^{\text{rec}}_{n=1}$ and their sources.

where the minus sign that enters through differentiation has been neglected as a further irrelevant phase factor.

Considering comparable dimensions to what was assumed for the bridge ($L_R = 6\,\mu$m and $w_R = t_R = 200$ nm), and taking full coverage of the resonator surface with magnetic material, then one finds for the single magnon-phonon coupling strength a value $g_0^{\text{rec}}(n = 1)/2\pi \approx 175$ Hz for a mechanical frequency $\omega_R/2\pi = 46.8$ MHz with a commercially available pre-stress of $\sigma = 1$ GPa. This coupling strength represents a factor of around 2 relative to the GGG substrate, primarily owing both to the reduction of the stress ratio

$$\left(\frac{E}{\sigma}\right)^{1/4} \approx 4 \tag{7.14}$$

and the increase in the mechanical mode frequency. If instead one wishes to compare against the mechanical mode frequency of the GGG bridge, then a length $L_R = 60\,\mu$m which yields a frequency $\omega_R/2\pi = 4.68$ MHz. With this, one finds a single magnon-phonon coupling strength $g_0^{\text{rec}}(n = 1)/2\pi \approx 1.8$ Hz. For comparable frequencies, then the silicon nitride resonator offers much smaller couplings relative to the GGG substrate, whereas for similar dimensions, an increase is seen.

7.3 g and $\mathcal{C}$

While the parameter landscape of the constraints for the Si_3N_4 device is far less robust than for the GGG substrate, it still seems possible to achieve $\mathcal{C} \approx 1$, which is generally considered the bare-minimum for quantum purposes. Feasible attainable values for g^{rec} and $\mathcal{C}^{\text{rec}}$ are presented here, and the parameters used for the system are given in Table 7.1. The Gilbert damping is assumed $\alpha = 10^{-3}$ in like with the discussion in the introduction to this Chapter.

Owing both to the higher mechanical mode frequency of the Si_3N_4 bridge and the larger line-width of the magnon mode due to higher magnetic damping, the limiting constraint for this regime is the resolved side-band condition (ω_R/κ). For the same reason, it is also highly unlikely that the device will be able to reach the strong magnon-phonon coupling regime. Because of the higher mechanical mode frequency, bridges made of isosceles cross-section are only considered - while in the high-stress string regime the mode frequency is independent of cross-sectional shape, it does provide an increase to g_0^{rec} which should permit longer resonators to be considered than for the square cross-section. In turn, this allows one to reduce the mechanical mode frequency which should make meeting the resolved side-band condition easier. An applied saturating field of $H_e = 350$ Oe has been taken.

With the complexity and limiting values of the constraints, performing a maximisation search to the same extent as for the GGG substrate is not something strictly

d_c	L_R	$w_{R,m}$	t_R	L_m	$\frac{g^{rec}}{2\pi}$	$\frac{g^{rec}}{\kappa}$	$\mathcal{C}^{rec}$	$\frac{N_S}{n_m}$	$\frac{\omega_R}{\Delta_m}$	$\sqrt{\frac{EI}{\sigma A}}\frac{1}{L}$	$\frac{\kappa}{\omega_R}$
0.10	13.7	0.50	0.35	2.0	69.8	0	16	0	0.06	0.09	0.11
0.25	13.8	0.30	0.35	2.0	52.4	0	9	0	0.10	0.09	0.11
0.50	15.0	0.50	0.35	3.0	30.3	0	4	0	0.12	0.08	0.12

TABLE 7.2: Some exemplar values dimensions to attain $\mathcal{C}^{rec}$ of order, at least, unity. Lengths are given in microns, and g^{rec} is given in kHz

feasible. To this end, presented are some benchmark values which give desirable magnomechanical parameters, but these may not be the 'best' which are attainable for the device. First, the limiting case for the thickness of the Si_3N_4 resonator is taken as $t_R = 350\,nm$ and is not something that is varied given that prior optimisation produces greater values for thinner resonators and that thinner structures also present higher Q-values, so this thickness seems nominal. With the reduction in the Gilbert damping, the line-width of the magnon mode is now some $\kappa_0 \approx 15\,MHz$. To then meet the resolved side-band condition, a mechanical mode frequency at least an order of magnitude larger than this is required, meaning short Si_3N_4 resonators must be employed; a value of $L_R = 20\,\mu m$ provides a mechanical mode frequency of some 100 MHz. Shorter structure lengths provide higher mechanical mode frequencies, and so this is taken as a limiting value. With these considerations, one may look for values which provide optomechanical parameters of interest which are presented in Table 7.2. As the optimisation hasn't taken place to the constraints, the values each of the constraints yield is also tabulated. The higher mechanical mode frequency excites fewer magnons, which in turn makes meeting the requirement of quantisation easier. This reduction in the number of magnons makes the multimagnon-phonon cooperativity far poorer, and a reduction of 2 orders of magnitude in g^{rec} is seen. Regardless, cooperativities of orders 10^0 and 10^1 can be obtained, with the best-case representing only an order of magnitude reduction relative to the GGG substrate bridge device.

Were smaller Gilbert dampings able to be considered, then larger cooperativities are achievable. Some benchmarking is presented in Table 7.3. A reduction in the damping of $1/4$ it's original value presents a doubling of the cooperativity for the smallest central distance, although it is quadratic at the largest - this owes itself to the increase in the excitation of magnons. Thicker substrates present larger cooperativities and also are able to meet the conditions imposed; substrates thicker than 500 nm are not considered in line with Si_3N_4 films commercially available, and that magnomechanical parameters are larger for smaller widths - this combination of large thickness and small width seems improbable from a manufacturing perspective.

Lastly, considered briefly is the scheme in which high-quality YIG is grown on GGG substrates and then transferred to the Si_3N_4 bridge via the omniprobe method. For this scheme, equivalent dimensions to the YIG film grown in [240] are considered. These are a YIG film of dimensions $13 \times 5 \times 0.185\,\mu m$, and taken for the Gilbert damping is a value of $\alpha = 10^{-4}$. Note that, in this paper, a thickness of GGG of some 150 nm remained on the film. In practice, to neglect the elastic effect on the Si_3N_4 substrate this requires that it's thickness be at least $3.5\,\mu m$, which is compatible with an isosceles cross-section for the width of the YIG film. As the resolved side-band condition requires shorter structures whereas the high-stress string limit requires

longer ones, this competition presents no feasible regime which stringently meets the constraints if one assumes that the width of the resonator is the same as the width of the thin film.

7.4 Potentials of application

To compare against the prospect of employing a silicon nitride substrate over a GGG one, briefly considered here is the benchmarking phenomena of ground state cooling. The benchmarking temperature of 20 mK is considered to yield the lowest theoretically attainable phonon number. As the Si_3N_4 device operates in the weak coupling regime, one can use the simplified final phonon number, $\bar{n}_{\mathrm{f}}^{(0)}$. Table 7.2 is used to provide the dimensions $L_{\mathrm{R}} = 13.7$, $L_{\mathrm{m}} = 2\,\mu$m, $w_{\mathrm{R,m}} = 500\,$nm and $t_{\mathrm{R}} = 350\,$nm, and a Gilbert damping $\alpha = 10^{-3}$ is assumed. These dimensions correspond to a $Q-$factor $Q = 45,000$ and mechanical mode frequency $\omega_{\mathrm{R}}/2\pi = 22.2\,$MHz, in turn finding a mechanical damping rate $\Gamma_{\mathrm{R}}/2\pi = 490\,$Hz. Also with these dimensions, one finds for the multimagnon-phonon coupling rate $g/2\pi = 69.8\,$kHz, a magnon decay rate $\kappa/2\pi = 2.5\,$MHz, leading to a cooling rate $\Gamma_{\mathrm{opt}}/2\pi = 7.8\,$kHz. From Eq. 6.25, the minimum number of phonons achievable is $\bar{n}_{\mathrm{min}} = 7.9 \times 10^{-4}$. At the temperature 20 mK, the average number of phonons is found as $\bar{n}_{\mathrm{th}}(20\,\mathrm{mK}) \approx 18$, and in turn one finds for the final number of phonons in the ground state cooling regime

$$\bar{n}_{\mathrm{f}}^{(0)}(20\,\mathrm{mK}) \approx 1.1 \tag{7.15}$$

which is insufficient to consider the device in the ground state even at the lowest of the benchmarking temperatures. Even if dimensions that maximise the multimagnon-phonon coupling rather than the cooperativity were adopted, it is still not possible to achieve final phonon occupations much lower than the above as the intrinsic damping of the magnon mode is far too high. As an exemplar consideration, multimagnon-phonon couplings higher than the order of MHz do not appear feasible in light of the constraints, and the resolved sideband condition presents inflexibilities with regards to larger phonon frequencies that the high-stress resonator supports. At best, while roughly meeting the constraints, it would appear that $\bar{n}_{\mathrm{f}}(20\,\mathrm{mK}) \approx 0.5$ would be possible for this scheme in assuming $L_{\mathrm{R}} = 12.25$, $L_{\mathrm{m}} = 2\,\mu$m, $w_{\mathrm{R,m}} = 250\,$nm and $t_{\mathrm{R}} = 350\,$nm. Additionally, quantum cooperativies of order unity are barely feasible even at the cryogenic temperature 20 mK.

α	d_c (μm)	L_R (μm)	$w_{R,m}$ (μm)	t_R (μm)	L_m (μm)	$\frac{g^{rec}}{2\pi}$ (kHz)	$\frac{g^{rec}}{\kappa}$	$\mathcal{C}^{rec}$	$\frac{N_S}{n_m}$	$\frac{\omega_R}{\Delta_m}$	$\sqrt{\frac{EI}{\sigma A}}\frac{1}{L}$	$\frac{\kappa}{\omega_R}$
0.75×10^{-3}	0.1	16	0.25	0.35	2.0	90.1	0.05	50	0.05	0.10	0.08	0.10
	0.25	16.5	0.35	0.35	2.5	47.5	0.03	15	0.01	0.11	0.08	0.10
	0.50	16.5	0.50	0.35	2.8	26.7	0.01	5	0.00	0.10	0.08	0.10
0.50×10^{-3}	0.1	21.6	0.25	0.35	2.5	74.7	0.06	97	0.10	0.12	0.06	0.09
	0.25	24.5	0.35	0.35	2.8	34.0	0.03	28	0.03	0.09	0.05	0.10
	0.50	25.0	0.50	0.35	3.5	19.8	0.02	10	0.01	0.10	0.05	0.10
0.25×10^{-3}	0.1	22	0.25	0.5	2.3	84.1	0.12	183	0.10	0.10	0.08	0.05
	0.25	45.5	0.4	0.5	4.1	25.6	0.04	90	0.10	0.10	0.04	0.10
	0.50	47.5	0.60	0.5	5.4	15.0	0.02	36	0.03	0.11	0.04	0.10
0.10×10^{-3}	0.1	21.5	0.25	0.5	2.3	86.1	0.25	370	0.10	0.10	0.08	0.02
	0.25	43.5	0.35	0.5	3.7	26.3	0.09	195	0.10	0.09	0.04	0.04
	0.50	86.5	0.60	0.5	7.2	9.54	0.03	110	0.11	0.10	0.02	0.08

TABLE 7.3: Dimensions and attainable $\mathcal{C}^{rec}$ for different values of the Gilbert damping for a silicon nitride based resonator.

Chapter 8

Conclusions and further work

Bolstered by the number of ways in which spin-waves are able to interact with subsystems, magnons have offered a promising new avenue to further develop the theory and applications of mechanical resonators in the quantum regime. Inspired by recent developments towards engineering cavity-free installations of strong magnon-photon coupling [118, 119], a new theory is identified to establish strong coupling between magnons and phonons, exploiting the Kittel mode of a thin film and the flexural modes of bridges and cantilevers. Current works are underpinned by the standard 'cavity' method [129], which may be considered bulky and offers little scope to adapt the mechanical properties, being dependent on a YIG sphere. To this end, this thesis proposes a nano-scale implementation of thin film YIG deposited on a thick substrate, in which the substrate consideration can be replaced to modify the elastic characteristic.

This thesis can be considered in two sections. The first section introduces the relevant background information. Chapter 2 begins with a description of magnetism from exchange and introduces the Landau-Lifshitz equation and the Kittel mode's origin from within it. Chapter 3 introduces the theory of elasticity beginning from considerations of stress and strain, their applications to crystal structures, and the Euler-Bernoulli equation governing beams under geometries comprising beams and rods. Chapter 4 then introduces the basic theory underpinning hybrid quantum systems as presented through optomechanics, in the form of the single photon-phonon and multiphoton-phonon coupling rates, strong coupling and the emergence of normal modes, and the effect of dynamical backaction on a mechanical resonator.

The second section is then comprised of the derivations relevant to the new theory and it's applications. This begins in Chapter 5, with the quantisation of magnons and subsequent derivation of the single magnon-phonon coupling rates to cantilever and bridge geometries. As the demagnetisation field within a sphere is known to be uniform [54], a feature which is present only within the bulk of a thin film, the dependence of the magnon-phonon coupling rates on the form of the profile of the magnetisation is investigated, assuming a simple trigonometric function as well as fitting to computational data. From this, it is established that only the magnetisation profile along the length of the structure, which can safely be assumed to be trigonometric in form as the larger of the transverse aspect ratios, is of relevance to the scheme considered in which the magnetic film forms rectangular geometry. The coupling of the waveguide modes to the Kittel mode is then investigated, and a formula is established to provide a rudimentary estimate under a flat profile assumption. This formula is then checked numerically against a trigonometric profile, and finds that the flat profile sets a higher bound such that values are free to be extrapolated without significant consequences. The validity of the single mode assumption made for a thin film is then established, and optimisation for the multimagnon-phonon coupling rate and the magnomechanical copoerativity is given for the cantilever

and bridge geometries as a function of several geometric parameters. Chapter 6 presents a tentative exploration of the applications of the device, including the possibility of exploiting the magnomechanical interaction to cool to the ground state and the emergence of magnomechanically induced transparency windows. Chapter 7 presents a possible avenue of using a high-Q silicon nitride substrate to realise a device compatible with the quantum regime for which low-loss mechanical resonators are preferable.

Experimental realisations have for magnomechanics have so far been realised only using cavities, from which extensive theoretical proposals have come. These all use a somewhat static configuration, in which the cavity provides a large device footprint and elastic parameters are dictated by a YIG sphere. In proposing this new device, it is anticipated a new emergence of work in magnomechanics in which compatibility with superconducting transmission lines, as well as significant boosts to the magnomechanical cooperativity, can be attained. In addition, the versatility of this theory provides scope to include other low-loss magnetic materials on alternative substrates of differing elastic character, such as spinel ferrite thin films [243] grown on $MgAl_2O_4$ [244], or [245] grown on MgO [246]. Also noted is the comparatively unexplored 'continuum' regime [247], in which the magnetic structure is continued beyond the support of the beam such that a continuum of magnon modes may be coupled to.

Appendix A

Quantisation of the transmission line

Transmission lines are media that confine electromagnetic fields, effectively reducing the number of relevant dimensions to one. In order to present a comprehensive magnomechanical theory of a thin-film resonator, the consideration of the coupling between transmission line modes and magnetic excitations are required. In turn, this requires a theory of quantisation for photons of the transmission line, for which this appendix follows the work of Clerk [180].

A.1 The Coaxial Cable

Consider a rudimentary transmission line formed by a coaxial wire as a perfect conductor. The wire has an inductance per unit length, given by ℓ, and a capacitance per unit length, given by c. The characteristic impedance of the transmission line is then found from

$$Z_{\mathrm{TL}} = \sqrt{\frac{\ell}{c}} \tag{A.1}$$

In general, the impedance is a complex number formed by the addition of both the resistance, R, of the element, and the reactance, X, where $Z_{\mathrm{TL}} = R + iX$. A generic impedance may be related to the current flowing through the element through Ohm's law

$$V = IZ_{\mathrm{TL}}. \tag{A.2}$$

The coaxial cable of consideration is such that it's length coincides with the $x-$axis of a coordinate system, and it's cross-section is parallel to the $y-z$ plane. If the wire supports a voltage, $V(x,t)$, at position x at a time t, then the charge density is given as

$$q(x,t) = cV(x,t) \tag{A.3}$$

As the coaxial cable forms a closed system, the current flowing, $I(x,t)$, obeys charge conservation. The current and charge densities may be related by the continuity equation

$$\partial_t q(x,t) + \partial_x I(x,t) = 0. \tag{A.4}$$

where $\partial_x = \partial/\partial x$ and $\partial_t = \partial/\partial t$. Similarly, in assuming a lossless transmission line, the acceleration of the charges is related to the gradient of the voltage as

$$\partial_x V(x,t) = -\ell \partial_t I(x,t). \tag{A.5}$$

Equations A.4 and A.5 are known as the *telegrapher's equations* [248], and form a set of coupled differential equations. These equations can be decoupled in assuming

that the system can be expressed as a sum of left- and right-propagating modes of the voltage. In doing so, one expresses the voltage and the current as

$$V(x,t) = [V^{\rightarrow} + V^{\leftarrow}], \tag{A.6}$$

$$I(x,t) = \frac{1}{Z_{\mathrm{TL}}}[V^{\rightarrow} - V^{\leftarrow}]. \tag{A.7}$$

Expressing Eqs. A.4 and A.5 in terms of these left- and right-propagators, it can be shown

$$v_p \partial_x V^{\rightarrow} + \partial_t V^{\rightarrow} = 0, \tag{A.8}$$

$$v_p \partial_x V^{\leftarrow} - \partial_t V^{\leftarrow} = 0. \tag{A.9}$$

where the wave phase velocity is defined as

$$v_p = \frac{1}{\sqrt{lc}} \tag{A.10}$$

These equations represent conservation laws, and have solutions which propagate by uniform translations [53]. As such, consider two arbitrary functions, V_{in} and V_{out}, of the arguments $t \pm x/v_p$, as

$$V^{\rightarrow}(x,t) = V_{\mathrm{out}}(t - \frac{x}{v_p}), \tag{A.11}$$

$$V^{\leftarrow}(x,t) = V_{\mathrm{in}}(t + \frac{x}{v_p}). \tag{A.12}$$

Were the transmission line infinite, then these functions would be completely independent of each other and the two solutions don't meet. However, for the realistic case of a semi-infinite transmission line these functions cannot be deemed to be independent as the transmission line is terminated at some point. The relation between the solutions is then determined by the boundary conditions being imposed by the termination. Assuming that the transmission line is terminated at the coordinate $x = 0$, then the boundary conditions may be expressed using the new functions V_{in} and V_{out} as

$$V(0,t) = [V_{\mathrm{out}}(t) + V_{\mathrm{in}}(t)] \tag{A.13}$$

$$I(0,t) = \frac{1}{Z_{\mathrm{TL}}}[V_{\mathrm{out}}(t) - V_{\mathrm{in}}(t)] \tag{A.14}$$

from which it follows that

$$V_{\mathrm{out}}(t) = V_{\mathrm{in}}(t) + Z_{\mathrm{TL}} I(0,t) \tag{A.15}$$

For an open circuit ($I(0,t) = 0$), then trivially $V_{\mathrm{in}} = V_{\mathrm{out}}$, and the output wave is the result of the input wave reflecting at the termination of the open circuit. In general, the current radiates an additional outgoing wave, injected into the transmission line by the system's dynamics. Without an incoming wave, the line simply acts as a resistor, carrying energy away with propagating waves rather than Ohmic heating.

A.2 Lagrangian Formulation of the Transmission Line

To quantise the modes of the transmission line, it is necessary to formulate the Lagrangian of the system and from this determine the canonical momentum and the Hamiltonian. The system conveniently acts as a collection of a large number of harmonic oscillators in the form of the normal modes. In the quantisation of the transmission line it is often deemed useful to define a flux [249, 250] as

$$\phi(x,t) \equiv \int_{-\infty}^{t} V(x,\tau)\,\mathrm{d}\tau \tag{A.16}$$

where τ is introduced as an integration variable to avoid ambiguity. The local voltage is expressed as $V(x,t) = \partial\phi/\partial t$. For an infinitesimal length of the transmission line, $\mathrm{d}x$, having inductance $\ell\mathrm{d}x$, the voltage drop along it given by $-\partial_x\partial_t\phi(x,t)\mathrm{d}x$. The flux through the infinitesimal length is then $-\partial_x\phi(x,t)\mathrm{d}x$ and the local current then follows from Eq. A.5 as

$$I(x,t) = -\frac{1}{\ell}\partial_x\phi(x,t). \tag{A.17}$$

It is known that the energy density of inductive and capacitive elements are determined by the expressions

$$u_\ell = \frac{1}{2}\ell I^2 = u_{\text{kin}} \tag{A.18}$$

$$u_c = \frac{1}{2c}V^2 = u_{\text{pot}} \tag{A.19}$$

where in determining their analogy with the kinetic and potential energy densities a more rigorous treatment is required [251, 252], but the result stands regardless. The Lagrangian density can then be expressed in terms of the flux

$$\mathscr{L} = u_{\text{kin}} - u_{\text{pot}} = \frac{c}{2}\left(\partial_t\phi\right)^2 - \frac{1}{2\ell}\left(\partial_x\phi\right)^2. \tag{A.20}$$

For a 1-dimensional transmission line, the Lagrangian of the system is then the integral over all x of the Lagrangian density, found as

$$L = \int_0^\infty \mathscr{L}dx = \int_0^\infty \left(\frac{c}{2}\left(\partial_t\phi\right)^2 - \frac{1}{2\ell}\left(\partial_x\phi\right)^2\right)\mathrm{d}x. \tag{A.21}$$

From this Lagrangian, one then invokes the action principle to find the Euler-Lagrange equation of the system as

$$\frac{\partial}{\partial x}\left(\frac{\partial\mathscr{L}}{\partial\left(\partial_x\phi\right)}\right) + \frac{\partial}{\partial t}\left(\frac{\partial\mathscr{L}}{\partial\left(\partial_t\phi\right)}\right) + \frac{\partial\mathscr{L}}{\partial\phi} = 0 \tag{A.22}$$

and in applying it find a massless Klein-Gordon type equation of the form

$$v_p^2\frac{\partial^2\phi}{\partial x^2} - \frac{\partial^2\phi}{\partial t^2} = 0. \tag{A.23}$$

The momentum that is canonically conjugate to the flux variable, $\phi(x,t)$, is simply found as

$$\frac{\partial\mathscr{L}}{\partial\left(\partial_t\phi\right)} = c\partial_t\phi = cV(x,t) \equiv q(x,t) \tag{A.24}$$

which is exactly the charge density at the point x and time t. The Hamiltonian density is then found from the Legendre transformation of the Lagrangian density, where

$$\mathscr{H} = \frac{\partial \mathscr{L}}{\partial (\partial_t \phi)} \partial_t \phi - \mathscr{L} = \int \left(\frac{1}{2c} q^2 - \frac{1}{2\ell} (\partial_x \phi)^2 \right) \mathrm{d}x. \tag{A.25}$$

Already seen in Sec. A.1 is that the charge density can be expressed as sums of left and right moving solutions given as arbitrary functions. As q is a real valued object, then it must necessarily contain both e^{ikx} and e^{-ikx} terms, even if it is only right or left moving. However, for $k > 0$ and a right mover, then the e^{ikx} is associated with the positive frequency term $e^{-i\omega_k t}$, and the e^{-ikx} is associated with the negative frequency term $e^{i\omega_k t}$, where $\omega_k = v_p |k|$. Clearly, the opposite holds for left movers, and so the issue is rectified. The mode amplitudes are defined such that

$$A_k = \frac{1}{\sqrt{L}} \int e^{-ikx} \left(\frac{1}{\sqrt{2c}} q(x,t) - i \sqrt{\frac{k^2}{2\ell}} \phi(x,t) \right) dx \tag{A.26}$$

where the fields are taken to obey periodic boundary conditions on a length L. Hence, the Hamiltonian is in the form

$$H = \frac{1}{2} \sum_k \left(A_k^* A_k + A_k A_k^* \right). \tag{A.27}$$

The equation of motion for the Lagrangian, Eq. (A.23), then becomes

$$\partial_t A_k = -i\omega_k A_k \tag{A.28}$$

such that

$$\begin{aligned} q(x,t) =& \sqrt{\frac{c}{2L}} \sum_k e^{ikx} \left[A_k(0) e^{-i\omega_k t} + A_k^*(0) e^{i\omega_k t} \right] \\ =& \sqrt{\frac{c}{2L}} \sum_k \left[A_k(0) e^{i(kx - \omega_k t)} + A_k^*(0) e^{-i(kx - \omega_k t)} \right] \end{aligned} \tag{A.29}$$

For $k > 0$, the wave is moving to the right and the e^{ikx} term is associated with positive frequency and e^{-ikx} with negative frequency (and vice versa for left movers). Note that to attain the voltages, one finds

$$V^{\rightarrow} = \sqrt{\frac{1}{2Lc}} \sum_{k>0} \left[A_k(0) e^{i(kx - \omega_k t)} + A_k^*(0) e^{-i(kx - \omega_k t)} \right] \tag{A.30}$$

$$V^{\leftarrow} = \sqrt{\frac{1}{2Lc}} \sum_{k<0} \left[A_k(0) e^{i(kx - \omega_k t)} + A_k^*(0) e^{-i(kx - \omega_k t)} \right] \tag{A.31}$$

A.3 Transmission Line Mode Quantisation

Eq. (A.24) shows that the momentum conjugate to the flux variable $\phi(x,t)$ is the charge density $q(x,t)$. Hence, to quantise the transmission line modes one needs to promote these two quantities to quantum operators by enforcing the canonical commutation relation

$$\left[\hat{q}(x), \hat{\phi}(x') \right] = -i\hbar \delta(x - x'). \tag{A.32}$$

From this, it follows that the mode amplitudes become quantum operators that obey

$$\left[\hat{A}_{k'}, \hat{A}_k^\dagger\right] = \hbar\omega_k \delta_{kk'}. \tag{A.33}$$

The ladder operators are identified as

$$\hat{A}_k = \sqrt{\hbar\omega_k}\hat{b}_k \tag{A.34}$$

where $\hat{b}_k$ destroys a photon in mode k. The quantum form of the Hamiltonian follows from Eq. A.27 as

$$H = \sum_k \hbar\omega_k \left[\hat{b}_k^\dagger \hat{b}_k + \frac{1}{2}\right]. \tag{A.35}$$

In Eqs. A.11 and A.12 is was seen that the voltage may be resolved into right and left moving components, such that

$$V(x,t) = V^{\rightarrow}(t - \frac{x}{v_p}) + V^{\leftarrow}(t + \frac{x}{v_p}) \tag{A.36}$$

As such, should $V^{\rightarrow}$ be specified for all points in space at $t = 0$ then the voltage is determined for all times. Conversely, specifying it for all times at $x = 0$ determines it's voltage at all spatial points. Extending Eqs. A.30 and A.31 to the quantum case and taking $x = 0$, it follows

$$\hat{V}^{\rightarrow} = \sqrt{\frac{1}{2Lc}} \sum_{k>0} \sqrt{\hbar\omega_k} \left[\hat{b}_k e^{-i\omega_k t} + H.c\right] \tag{A.37}$$

$$= \int_0^\infty \frac{1}{2\pi} \sqrt{\frac{\hbar\omega Z_{\mathrm{TL}}}{2}} \left[\hat{b}^{\rightarrow}[\omega] e^{-i\omega t} + H.c\right] \mathrm{d}\omega \tag{A.38}$$

where it is defined

$$\hat{b}^{\rightarrow} \equiv 2\pi \sqrt{\frac{v_p}{L}} \sum_{k>0} \hat{b}_k \delta(\omega - \omega_k). \tag{A.39}$$

Similarly

$$\hat{V}^{\leftarrow} = \int_0^\infty \frac{1}{2\pi} \sqrt{\frac{\hbar\omega Z_{\mathrm{TL}}}{2}} \left[\hat{b}^{\leftarrow}[\omega] e^{-i(kx-\omega t)} + H.c\right] d\omega, \tag{A.40}$$

with

$$\hat{b}^{\leftarrow} \equiv 2\pi \sqrt{\frac{v_p}{L}} \sum_{k<0} \hat{b}_k \delta(\omega - \omega_k). \tag{A.41}$$

Transmission lines support a relatively narrow band of frequencies, centered on some characteristic drive frequency, ω_q. In this case, one can Fourier transform the expressions $\hat{b}^{\rightarrow}$ and $\hat{b}^{\leftarrow}$ which finds

$$\hat{b}^{\rightarrow}(t) = \sqrt{\frac{v_p}{L}} \sum^{k>0} e^{-i(\omega_k - \omega_q)t} \hat{b}_q(0), \tag{A.42}$$

$$\hat{b}^{\leftarrow}(t) = \sqrt{\frac{v_p}{L}} \sum^{k<0} e^{-i(\omega_k - \omega_q)t} \hat{b}_q(0). \tag{A.43}$$

such that

$$\hat{V}^{\rightarrow}(0) \approx \sqrt{\frac{\hbar\omega_q Z_{\mathrm{TL}}}{2L}} \left[\hat{b}_q(0) + \hat{b}_q^\dagger(0)\right] \tag{A.44}$$

and a similar expression for $\hat{V}^{\leftarrow}$. These are then the quantum operators required to dedude the coupling rate between the transmission line and the magnon modes.

Appendix B

Magnetic susceptibility tensor of ferromagnets

Consider the oscillations in the magnetisation $\mathbf{M}(\mathbf{r},t)$ of a ferromagnet about the equilibrium magnetisation, $\mathbf{M}_0$. In addition to the magnetisation oscillations, there will also be some oscillation of the internal magnetic field $\mathbf{H}^{(\mathbf{i})}(\mathbf{r},t)$ around the equilibrium value $\mathbf{H}_\mathbf{0}^{(\mathbf{i})}$. These oscillations are denoted as $\mathbf{m}(\mathbf{r},t)$ and $\mathbf{h}(\mathbf{r},t)$ for the magnetisation and internal field, respectively. In turn these oscillations are related by the linearised equation of motion [54, 253]

$$\frac{\partial \mathbf{m}}{\partial t} = \gamma_g \Bigg[\mathbf{M_0} \times \Bigg(\mathbf{h} + \alpha_{ik} \frac{\partial^2 \mathbf{m}}{\partial x_i \partial x_k} + \beta \hat{\mathbf{n}} \left(\mathbf{m}.\hat{\mathbf{n}} \right) - \frac{1}{M_0^2} \left(\left(\mathbf{M_0}.\mathbf{H_0^{(i)}} \right) + \beta \left(\mathbf{M_0}.\hat{\mathbf{n}} \right)^2 \right) \mathbf{m} \Bigg) \Bigg] \tag{B.1}$$

where arguments are dropped for brevity. β is defined as the unixial anistropy constant, α_{ik} as the exchange tensor seen in Eq. 2.23, and $\hat{\mathbf{n}}$ as the anisotropy unit vector. Note that in setting β to 0 one recovers Eq. 2.52. Assuming that the oscillations are harmonic functions of time, one can express the fluctuations as

$$\begin{aligned} \mathbf{m}(\mathrm{r},t) &= \mathbf{m}(\mathbf{r}) \exp(i(\mathbf{k}.\mathbf{r} - \omega t)) \\ \mathbf{h}(\mathrm{r},t) &= \mathbf{h}(\mathrm{r}) \exp(i(\mathbf{k}.\mathbf{r} - \omega t)) \end{aligned} \tag{B.2}$$

The susceptibility tensor relates the oscillations of the internal magnetic field to the magnetisation. Consider an infinite plate, oriented such that the surface normal is parallel to the x axis and it's infinite extent lays in the $y-z$ plane. Considered here is the case that there is an anisotropy axis laying parallel to the plane of the plate, and that the equilibrium magnetisation and equilibrium magnetic field are oriented along this. Assumed further is that the magnetic field saturates the plate such that $\mathbf{M_0} = M_s \hat{\mathbf{z}}$ and that fluctuations of the magnetisation along this axis are negligible. With these assumptions in mind, one can substitute Eq. B.2 into Eq. B.1 and solve the cross product to find

$$-i\omega \begin{pmatrix} m_x \\ m_y \\ 0 \end{pmatrix} = g \left[\begin{pmatrix} -M_0 h_y \\ M_0 h_x \\ 0 \end{pmatrix} - \left(\alpha_{ij} k_i k_j + \frac{\mathbf{M_0}.\mathbf{H_0}}{M_0^2} + \beta \right) \begin{pmatrix} -M_0 m_y \\ M_0 m_x \\ 0 \end{pmatrix} \right] \tag{B.3}$$

Letting

$$\Omega = \gamma_g M_s \left(\alpha_{ij} k_i k_j + \frac{\mathbf{M_0} \cdot \mathbf{H_0^{(i)}}}{M_0^2} + \beta \right) \tag{B.4}$$

one can write the matrix relating the the field oscillations to the magnetisation oscillations as

$$\begin{pmatrix} m_x \\ m_y \end{pmatrix} = \frac{gM_0\Omega}{\Omega^2 - \omega^2} \begin{pmatrix} 1 & \frac{i\omega}{\Omega} \\ -\frac{i\omega}{\Omega} & 1 \end{pmatrix} \begin{pmatrix} h_x \\ h_y \end{pmatrix} \tag{B.5}$$

Hence, the full susceptibility of this specific geometry is then

$$\hat{\chi}(\hat{n} = \hat{z}) = \frac{gM_0\Omega}{\Omega^2 - \omega^2} \begin{pmatrix} 1 & \frac{i\omega}{\Omega} & 0 \\ -\frac{i\omega}{\Omega} & 1 & 0 \\ 0 & 0 & 0 \end{pmatrix} \tag{B.6}$$

Appendix C

Non-uniform ferromagnetic resonance of an infinite plate

The derivation of the dispersion relation for magnons is non-trivial, and was first presented by Walker for the case of spheroids of arbitrary axial ratios and presenting symmetry along the applied field direction, which led to the derivation of the so-called Walker equation [186]. In the years after this, Damon and Eshbach put forth their theory for the case of a uniformly magnetised slab [189, 254]. For this work, the same principles as was applied in their work is followed but with a formalism more appropriate for the work contained in this thesis. As such, the resulting dispersion relation is more tractable for a mathematical use.

Consider here the case of resonance where the field and the magnetisation are functions of the coordinates, but the oscillations of each remain essentially magnetostatic. The equations of magnetostatics apply, given by

$$\nabla \times \mathbf{h}^{(\mathbf{e})} = 0, \qquad \nabla . \mathbf{h}^{(\mathbf{e})} = 0 \tag{C.1}$$

$$\nabla \times \mathbf{h}^{(\mathbf{i})} = 0, \qquad \nabla . \left(\mathbf{h}^{(\mathbf{i})} + 4\pi\mathbf{m}\right) = 0 \tag{C.2}$$

for the components of the oscillations of the magnetic field inside (denoted with i) and outside (denoted with e) of a specimen. These oscillations are assumed to be harmonic functions of time, such that

$$\begin{aligned} \mathbf{h}^{(\mathbf{i})}(\mathbf{r}, t) &= \mathbf{h}^{(\mathbf{i})}(\mathbf{r}) \exp(-i\omega t), \\ \mathbf{h}^{(\mathbf{e})}(\mathbf{r}, t) &= \mathbf{h}^{(\mathbf{e})}(\mathbf{r}) \exp(-i\omega t) \end{aligned} \tag{C.3}$$

It is necessary to introduce the scalar potentials $\phi^{(i)}$ and $\phi^{(e)}$ to satisfy the curl magnetostatic equations, related to the fields such that

$$\begin{aligned} \mathbf{h}^{(\mathbf{i})}(\mathbf{r}) &= -\nabla\phi^{(i)}(\mathbf{r}) \\ \mathbf{h}^{(\mathbf{e})}(\mathbf{r}) &= -\nabla\phi^{(e)}(\mathbf{r}) \end{aligned} \tag{C.4}$$

Eq. C.4 may then be substituted into the remaining magnetostatic equations to find

$$\begin{aligned} \Delta\phi^{(e)} &= 0 \\ \Delta\phi^{(i)} + 4\pi\chi_{ik}\frac{\partial^2\phi^{(i)}}{\partial x_i \partial x_k} &= 0. \end{aligned} \tag{C.5}$$

Note that this uses the susceptibility relation $\mathbf{m} = \hat{\chi}\mathbf{h}^{(\mathbf{i})}$ for the magnetic susceptibility tensor, χ. In addition to these governing equations, there are also boundary conditions which must be imposed on the specimen. These require that both

the tangential components of the magnetic field and the normal components of the magnetic field must be continuous across the surface of the specimen, providing

$$\begin{aligned} \mathbf{h}_{\boldsymbol{\tau}}^{(\mathbf{i})} &= \mathbf{h}_{\boldsymbol{\tau}}^{(\mathbf{e})} \\ h_{\nu}^{(i)} + 4\pi m_{\nu} &= h_{\nu}^{(e)} \end{aligned} \tag{C.6}$$

where τ and ν represent the tangential and normal components, respectively. In addition, it is also required that as $r \to \infty$, the field $\mathbf{h}^{(\mathbf{e})}(\mathbf{r})$, and hence $\phi^{(e)}$, must vanish, giving

$$\lim_{r\to\infty} \phi^{(e)} = 0. \tag{C.7}$$

With Eq. C.4, the boundary conditions in Eq. C.6 may be rewritten

$$\begin{aligned} \phi^{(i)} &= \phi^{(e)} \\ v_k \frac{\partial \phi^i}{\partial x_k} + 4\pi v_k \chi_{kj} \frac{\partial \phi^{(i)}}{\partial x_j} &= v_k \frac{\partial \phi^{(e)}}{\partial x_k} \end{aligned} \tag{C.8}$$

where v_k is defined as the projection of the unit vector along the normal onto the k axis.

The oscillations of the magnetisation in an infinite extent plane-parallel plate can now be considered. The plate is assumed to have thickness t_m, it's y and z axes lie in the plane of the plate and the x axis is perpendicular to the surface (with $x = 0$ passing through the middle of the thickness). For these, one finds for the boundary conditions in Eq. C.8

$$\phi^{(e)}\Big|_{x=\pm\frac{t_m}{2}} = \phi^{(i)}\Big|_{x=\pm\frac{t_m}{2}}, \qquad \phi^{(e)}\Big|_{x=\pm\infty} = 0 \tag{C.9}$$

As v_k is 1 for the x axis and 0 for the y and z axes, one finds for the remaining boundary condition

$$\frac{\partial \phi^{(e)}}{\partial x}\Big|_{x=\pm\frac{t_m}{2}} = \left(\frac{\partial \phi^{(i)}}{\partial x} + 4\pi\chi_{xj}\frac{\partial \phi^{(i)}}{\partial x_j}\right)\Big|_{x=\pm\frac{t_m}{2}}, \tag{C.10}$$

and hence

$$\frac{\partial \phi^{(e)}}{\partial x}\Big|_{x=\pm\frac{t_m}{2}} = \left(\mu_{xx}\frac{\partial \phi^{(i)}}{\partial x} + \mu_{xy}\frac{\partial \phi^{(i)}}{\partial x} + \mu_{xz}\frac{\partial \phi^{(i)}}{\partial z}\right)\Big|_{x=\pm\frac{t_m}{2}} \tag{C.11}$$

where it is defined $\mu_{ik} = \delta_{ik} + 4\pi\chi_{ik}$.

Outside of the specimen, solutions of the form

$$\phi^{(e)} = \phi(x)\exp(i(q_y y + q_z z)) \tag{C.12}$$

are assumed. These may be substituted into Laplace's equation in Eq. C.4 to find

$$\phi'' - (q_x^2 + q_z^2)\phi = 0. \tag{C.13}$$

Hence, the solutions must be of the form

$$\phi^{(e)} = \exp(i(q_y y + q_z z)) \begin{cases} C\exp(-fx), & \text{if } x > \frac{t_m}{2} \\ D\exp(fx), & \text{if } x < -\frac{t_m}{2} \end{cases} \tag{C.14}$$

where it is defined

$$f = \sqrt{q_y^2 + q_z^2}$$

Inside the specimen, solutions of the form

$$\phi^{(i)} = \exp(i(q_y y + q_z z)) \left[A\cos(q_x x) + B\sin(q_x x)\right] \tag{C.15}$$

are sought. These may be substituted into the second of Eq. C.5 to find

$$(-q_x^2 - q_y^2 - q_z^2)\phi^{(i)} + 4\pi\left(-\chi_{xx}q_x^2 - \chi_{yy}q_y^2 - \chi_{zz}q_z^2\right) = 0 \tag{C.16}$$

and hence

$$q^2 + 4\pi\left(\chi_{xx}q_x^2 + \chi_{yy}q_y^2 + \chi_{zz}q_z^2\right) = 0 \tag{C.17}$$

where it is defined $q^2 = q_x^2 + q_y^2 + q_z^2$.

The boundary conditions may then be used to determine constants. Employing first Eq. C.9 for the surface at $x = t_m/2$, one finds

$$\begin{aligned} A\cos\left(\frac{q_x t_m}{2}\right) + B\sin\left(\frac{q_x t_m}{2}\right) &= C\exp\left(-\frac{f t_m}{2}\right) \\ \Rightarrow C &= \frac{A\cos\left(\frac{q_x t_m}{2}\right) + B\sin\left(\frac{q_x t_m}{2}\right)}{\exp\left(-\frac{f t_m}{2}\right)}. \end{aligned} \tag{C.18}$$

Similarly for the surface at $x = -t_m/2$, one finds

$$\begin{aligned} A\cos\left(\frac{q_x t_m}{2}\right) - B\sin\left(\frac{q_x t_m}{2}\right) &= D\exp\left(-\frac{f t_m}{2}\right) \\ \Rightarrow D &= \frac{A\cos\left(\frac{q_x t_m}{2}\right) - B\sin\left(\frac{q_x t_m}{2}\right)}{\exp\left(-\frac{f t_m}{2}\right)}. \end{aligned} \tag{C.19}$$

Using Eq. C.11 for the surface at $x = t_m/2$

$$\begin{aligned} -fC\exp\left(-\frac{f t_m}{2}\right) &= \mu_{xx}q_x\left(-A\sin\left(\frac{q_x t_m}{2}\right) + B\cos\left(\frac{q_x t_m}{2}\right)\right) \\ &+ i\mu_{xy}q_y\left(A\cos\left(\frac{q_x t_m}{2}\right) + B\sin\left(\frac{q_x t_m}{2}\right)\right) \\ &+ i\mu_{xz}q_z\left(A\cos\left(\frac{q_x t_m}{2}\right) + B\sin\left(\frac{q_x t_m}{2}\right)\right). \end{aligned} \tag{C.20}$$

Substituting for C from Eq. C.18, this may be re-expressed as

$$
\begin{aligned}
-f\left(A\cos\left(\frac{q_x t_m}{2}\right)+B\sin\left(\frac{q_x t_m}{2}\right)\right) = \\
\mu_{xx}q_x\left(-A\sin\left(\frac{q_x t_m}{2}\right)+B\cos\left(\frac{q_x t_m}{2}\right)\right) \\
+i\mu_{xy}q_y\left(A\cos\left(\frac{q_x t_m}{2}\right)+B\sin\left(\frac{q_x t_m}{2}\right)\right) \\
+i\mu_{xz}q_z\left(A\cos\left(\frac{q_x t_m}{2}\right)+B\sin\left(\frac{q_x t_m}{2}\right)\right).
\end{aligned}
\tag{C.21}
$$

Rearranging for A, one finds

$$
A = B\left[\frac{\left(f+i\mu_{xy}q_y+i\mu_{xz}q_z\right)\sin\left(\frac{q_x t_m}{2}\right)+\mu_{xx}q_x\cos\left(\frac{q_x t_m}{2}\right)}{\mu_{xx}q_x\sin\left(\frac{q_x t_m}{2}\right)-\left(f+i\mu_{xy}q_y+i\mu_{xz}q_z\right)\cos\left(\frac{q_x t_m}{2}\right)}\right]
$$

For simplicity of reading, a redefinition of variables

$$
\eta = f+i\mu_{xy}q_y+i\mu_{xz}q_z, \qquad \zeta = \mu_{xx}q_x
$$

is made. With this, one can express

$$
A = B\left[\frac{\eta+\zeta\cot\left(\frac{q_x t_m}{2}\right)}{\zeta-\eta\cot\left(\frac{q_x t_m}{2}\right)}\right] \tag{C.22}
$$

For the surface at $x=-\frac{t_m}{2}$, Eq. C.11 gives

$$
\begin{aligned}
fD\exp\left(-\frac{ft_m}{2}\right) = \mu_{xx}q_x\left(A\sin\left(\frac{q_x t_m}{2}\right)+B\cos\left(\frac{q_x t_m}{2}\right)\right) \\
+i\mu_{xy}q_y\left(A\cos\left(\frac{q_x t_m}{2}\right)-B\sin\left(\frac{q_x t_m}{2}\right)\right) \\
+i\mu_{xz}q_z\left(A\cos\left(\frac{q_x t_m}{2}\right)-B\sin\left(\frac{q_x t_m}{2}\right)\right)
\end{aligned}
\tag{C.23}
$$

Substituting for D from Eq. C.19, one finds

$$
\begin{aligned}
f\left(A\cos\left(\frac{q_x t_m}{2}\right)-B\sin\left(\frac{q_x t_m}{2}\right)\right) = \\
\mu_{xx}q_x\left(A\sin\left(\frac{q_x t_m}{2}\right)+B\cos\left(\frac{q_x t_m}{2}\right)\right) \\
+i\mu_{xy}q_y\left(A\cos\left(\frac{q_x t_m}{2}\right)-B\sin\left(\frac{q_x t_m}{2}\right)\right) \\
+i\mu_{xz}q_z\left(A\cos\left(\frac{q_x t_m}{2}\right)-B\sin\left(\frac{q_x t_m}{2}\right)\right)
\end{aligned}
\tag{C.24}
$$

which may be rearranged to

$$f = \mu_{xx} q_x \left[\frac{A \sin\left(\frac{q_x t_m}{2}\right) + B \cos\left(\frac{q_x t_m}{2}\right)}{A \cos\left(\frac{q_x t_m}{2}\right) - B \sin\left(\frac{q_x t_m}{2}\right)} \right] + i\mu_{xy} q_y + i\mu_{xz} q_z \tag{C.25}$$

Focussing on the prefactor in square brackets, substituting for Eq. C.22 yields

$$\frac{\left(\frac{\eta + \zeta \cot\left(\frac{q_y t_m}{2}\right)}{\zeta - \eta \cot\left(\frac{q_x t_m}{2}\right)}\right) \sin\left(\frac{q_x t_m}{2}\right) + \cos\left(\frac{q_x t_m}{2}\right)}{\left(\frac{\eta + \zeta \cot\left(\frac{q_x t_m}{2}\right)}{\zeta - \eta \cot\left(\frac{q_x t_m}{2}\right)}\right) \cos\left(\frac{q_x t_m}{2}\right) + \sin\left(\frac{q_x t_m}{2}\right)} \tag{C.26}$$

which can finally be reduced to

$$\frac{\zeta - \eta \cot\left(q_y t_m\right)}{\eta + \zeta \cot\left(q_y t_m\right)}. \tag{C.27}$$

Eq. C.25 then reads

$$f = \mu_{xx} q_x \left[\frac{\zeta - \eta \cot\left(q_x t_m\right)}{\eta + \zeta \cot\left(q_x t_m\right)} \right] + i\mu_{xy} q_y + i\mu_{xz} q_z \tag{C.28}$$

which can be expanded as

$$\cot\left(q_x t_m\right)\left(f\zeta + \mu_{xx} q_x \eta - i\mu_{xy} q_y \zeta - i\mu_{xz} q_z \zeta\right) = \mu_{xx} q_x \zeta + i\mu_{xy} q_y \eta + i\mu_{xz} q_z \eta - f\eta$$

$$\Rightarrow \cot\left(q_x t_m\right) = \frac{\mu_{xx} q_x \zeta + i\mu_{xy} q_y \eta + i\mu_{xz} q_z \eta - f\eta}{f\zeta + \mu_{xx} q_x \eta - i\mu_{xy} q_y \zeta - i\mu_{xz} q_z \zeta} \tag{C.29}$$

Inspecting terms, one notes

$$\begin{aligned}
i\mu_{xy} q_y \eta &= i\mu_{xy} q_y f - \mu_{xy}^2 q_y^2 - \mu_{xy}\mu_{xz} q_y q_z \\
i\mu_{xz} q_z \eta &= i\mu_{xz} q_z f - \mu_{xz}\mu_{xy} q_z q_y - \mu_{xz}^2 q_z^2 \\
\mu_{xx} q_x \eta &= \mu_{xx} q_x f + i\mu_{xx}\mu_{xy} q_y q_x + i\mu_{xx}\mu_{xz} q_x q_z \\
f\eta &= f^2 + i\mu_{xy} q_y f + i\mu_{xz} q_z f
\end{aligned} \tag{C.30}$$

such that for the numerator in Eq. C.29 one finds

$$\mu_{xx}^2 q_x^2 + i\mu_{xy} q_y \eta + i\mu_{xz} q_z \eta - f\eta = \left(\mu_{xx} q_x\right)^2 - \left(\mu_{xy} q_y + \mu_{xz} q_z\right)^2 - f^2 \tag{C.31}$$

and for the denominator

$$f\zeta + \mu_{xx} q_x \eta - i\mu_{xy} q_y \zeta - i\mu_{xz} q_z \zeta = 2\mu_{xx} q_x f. \tag{C.32}$$

Hence, one finally arrives at the expression

$$\cot\left(q_x t_m\right) = \frac{\left(\mu_{xx} q_x\right)^2 - \left(\mu_{xy} q_y + \mu_{xz} q_z\right)^2 - q_y^2 - q_z^2}{2\mu_{xx} q_x f}.$$

Summarising definitions, one has

$$f = \sqrt{q_y^2 + q_z^2}, \tag{C.33}$$

$$q^2 + 4\pi\left(\chi_{xx}q_x^2 + \chi_{yy}q_y^2 + \chi_{zz}q_z^2\right) = 0, \tag{C.34}$$

$$\cot\left(q_x t_m\right) = \frac{\left(\mu_{xx}q_x\right)^2 - \left(\mu_{xy}q_y + \mu_{xz}q_z\right)^2 - q_y^2 - q_z^2}{2\mu_{xx}q_x f} \tag{C.35}$$

The expressions can then be applied for the case of an infinite plate where the anisotropy axis is parallel to the surface of the plate, along with a saturating applied magnetic field. Such a susceptibility tensor was found in Appendix B as

$$\hat{\chi}(\hat{n} = \hat{z}) = \frac{\gamma_g M_0 \Omega}{\Omega^2 - \omega^2}\begin{pmatrix} 1 & \frac{i\omega}{\Omega} & 0 \\ -\frac{i\omega}{\Omega} & 1 & 0 \\ 0 & 0 & 0 \end{pmatrix}$$

and that under these conditions

$$\Omega = \gamma_g M_0\left(\frac{H_0^e}{M_0} + \beta\right)$$

where $\mathbf{H_0^i} = \mathbf{H_0^e} - 4\pi\hat{N}\mathbf{M_0}$ with $N_1 = N_3 = 0, N_2 = 1$, and ignored the spatial dispersion term for the lowest ordered mode in k. If one substitutes this into Eq. C.34

$$\begin{aligned} q^2 + \frac{4\pi\gamma_g M_0\Omega}{\Omega^2 - \omega^2}\left(q_x^2 + q_y^2\right) &= 0 \\ \Rightarrow \omega &= \sqrt{\Omega\left(\Omega + 4\pi\gamma_g M_0 \sin^2(\Theta)\right)} \end{aligned} \tag{C.36}$$

where it is defined

$$\sin^2(\Theta) = \frac{q_x^2 + q_y^2}{q^2}. \tag{C.37}$$

From Eq. C.35, one has

$$2q_x \cot\left(q_x t_m\right) = \frac{1}{\sqrt{q_y^2 + q_z^2}} \frac{\left(1 + \frac{4\pi\gamma_g M_0\Omega}{\Omega^2-\omega^2}\right)^2 q_x^2 - \left(\frac{-4\pi i\gamma_g M_0\omega}{\Omega^2-\omega^2}\right)^2 q_y^2 - q_y^2 - q_z^2}{\left(1 + \frac{4\pi\gamma_g M_0\Omega}{\Omega^2-\omega^2}\right)}. \tag{C.38}$$

Noted is

$$1 + \frac{4\pi\gamma_g M_0\Omega}{\Omega^2 - \omega^2} = 1 - \frac{1}{\sin^2(\Theta)} = \frac{-q_z^2}{q_x^2 + q_y^2} \tag{C.39}$$

as well as

$$\begin{aligned} \left(\frac{-4\pi i\gamma_g M_0\omega}{\Omega^2 - \omega^2}\right)^2 = -\left(\frac{4\pi\gamma_g M_0\omega}{\Omega^2 - \omega^2}\right)^2 &= -\left(\frac{\omega}{\Omega\sin^2(\Theta)}\right) \\ &= \frac{-q^4}{\left(q_x^2 + q_y^2\right)^2} - \frac{4\pi\gamma_g M_0}{\Omega}\frac{q^2}{q_x^2 + q_y^2}. \end{aligned} \tag{C.40}$$

Hence, the above fraction in q may be rearranged to

$$-\frac{q_x^2 q_z^2}{q_x^2+q_y^2}+\left(\frac{q_x^2+q_y^2}{q_z^2}\right)\left[\frac{-q^4 q_y^2}{\left(q_x^2+q_y^2\right)^2}-\frac{4\pi\gamma_g M_0}{\Omega}\frac{q^2 q_y^2}{q_x^2+q_y^2}+q_y^2+q_z^2\right] \tag{C.41}$$

which can be expanded to

$$-\frac{q_x^2 q_z^2}{q_x^2+q_y^2}-\frac{q^4 q_y^2}{q_z^2\left(q_x^2+q_y^2\right)}-\frac{4\pi\gamma_g M_0}{\Omega}q^2\frac{q_y^2}{q_z^2}+\frac{q_y^2\left(q_x^2+q_y^2\right)}{q_z^2}+q_x^2+q_y^2. \tag{C.42}$$

It can then be shown that

$$-\frac{q_x^2 q_z^2}{q_x^2+q_y^2}-\frac{q^4 q_y^2}{q_z^2\left(q_x^2+q_y^2\right)}+\frac{q_y^2\left(q_x^2+q_y^2\right)}{q_z^2}+q_x^2+q_y^2=q_x^2-q_y^2-q_z^2 \tag{C.43}$$

such that one finds for Eq. C.38

$$2q_x\cot\left(q_x t_m\right)=\frac{1}{\sqrt{q_y^2+q_z^2}}\left(q_x^2-q_y^2-q_z^2-\frac{4\pi\gamma_g M_0}{\Omega}q^2\frac{q_y^2}{q_z^2}\right) \tag{C.44}$$

Appendix D

Orthogonality of Euluer-Bernoulli eigenmodes

It is instructive to know that the Euler-Bernoulli eigenmodes form an orthogonal set, which can be proven from the integration of the functions. To do this, one may follow a standard proof as presented by Graff [67]. For brevity, one writes ϕ_n rather than $\phi_n(z)$, and hence in considering the integral one finds

$$k_n^4 \int_0^L \phi_n \phi_m \, \mathrm{d}z = \int_0^L \phi_n'''' \phi_m \, \mathrm{d}z \tag{D.1}$$

$$= \left[\phi_n''' \phi_m\right]_0^L - \left[\phi_n'' \phi_m'\right]_0^L + \left[\phi_n' \phi_m''\right]_0^L - \left[\phi_n \phi_m'''\right]_0^L + \int_0^L \phi_n \phi_m'''' \, \mathrm{d}z \tag{D.2}$$

$$= k_m^4 \int_0^L \phi_n \phi_m \, \mathrm{d}z \tag{D.3}$$

For the boundary conditions of interest, the terms integrated that are to be evaluated at 0 and L must be 0, and so for $n \neq m$ it must be the case that $\int_0^L \phi_n \phi_m \, \mathrm{d}z = 0$. For the case of $m = n$, the basis functions

$$\begin{aligned} R_0(z) &= \frac{1}{2}\left(\cosh(z) + \cos(z)\right) = R_1'(z), & R_2(z) &= \frac{1}{2}\left(\cosh(z) - \cos(z)\right) = R_3'(z), \\ R_1(z) &= \frac{1}{2}\left(\sinh(z) + \sin(z)\right) = R_2'(z), & R_3(z) &= \frac{1}{2}\left(\sinh(z) - \sin(z)\right) = R_0'(z). \end{aligned} \tag{D.4}$$

may be used. The trigonometric identities then $\cos^2(z) + \sin^2(z) = 1$ and $\cosh^2(z) - \sinh^2(z) = 1$ become

$$\begin{aligned} R_0^2 - 2R_1R_3 + R_2^2 &= 1 \\ R_1^2 - 2R_0R_2 + R_3^2 &= 0. \end{aligned} \tag{D.5}$$

Some integrals of use will be noted. These are

$$\begin{aligned} \int_0^2 R_2^2(\zeta) \, \mathrm{d}\zeta &= \frac{1}{4}\left(3R_2(z)R_3(z) - R_0(z)R_1(z) + z\right) \\ \int_0^L R_2(\zeta)R_3(\zeta) \, \mathrm{d}\zeta &= \frac{1}{2}R_3^2(z) \\ \int_0^L R_3^2(\zeta) \, \mathrm{d}\zeta &= \frac{1}{4}\left(3R_3(z)R_0(z) - R_1(z)R_2(z)\right) \end{aligned} \tag{D.6}$$

from which it can be expressed

$$\phi_x = 2D_2\left(R_2(k_n z) - BR_3(k_n z)\right), \qquad B = \frac{R_0(k_n L)}{R_1(k_n L)} = \frac{R_3(k_n L)}{R_0(k_n L)}. \tag{D.7}$$

Performing the integration, one then finds

$$\begin{aligned}\frac{1}{D_n^2}\int_0^L \phi_n^2 \,\mathrm{d}z &= 4\int_0^L \left(R_2(k_n z) - BR_3(k_n z)\right)^2 \,\mathrm{d}z \\ &= 4\int_0^L R_2^2(k_n z)\,\mathrm{d}z - 8B\int_0^L R_2(k_n L)R_3(k_n L)\,\mathrm{d}z + 4B^2\int_0^L R_3^2(k_n L)\,\mathrm{d}z \\ &= \frac{1}{k_n}\left(3R_2(k_n L)R_3(k_n L) - R_0(k_n L)R_1(k_n L) + k_n L\right) - \frac{4B}{k_n}R_3^2(k_n L) \\ &+ \frac{B^2}{k_n}\left(3R_3(k_n L)R_0(k_n L) - R_1(k_n L)R_2(k_n L)\right). \end{aligned} \tag{D.8}$$

In substituting for B or $1/B$, this becomes

$$\begin{aligned}\frac{1}{D_n^2}\int_0^2 \phi_n^2 \,\mathrm{d}z &= L + \frac{B}{k_n}\left(3R_0(k_n L)R_2(k_n L) - R_1^2(k_n L)\right) \\ &- \frac{4B}{k_n}R_3^2(k_n L) + \frac{B}{k_n}\left(3R_3^2(knL) - R_0(k_n L)R_2(k_n L)\right) \\ &= L + \frac{B}{k_n}\left(2R_0(k_n L)R_2(k_n L) - R_1^2(k_n L) - R_3^2(k_n L)\right) \end{aligned} \tag{D.9}$$

where the last term is seen to disappear from the trigonometric identity. Hence, in full

$$\int_0^L \phi_n(z)\phi_m(z)\,\mathrm{d}z = D_n D_m L\delta_{nm} \tag{D.10}$$

Proceeding in a similar fashion for the bridge will also yield this same orthogonality. In fact, this is true for any configuration in which the boundary conditions are not functions of time. From this, it can be interpreted $D = 1$ for like eigenmodes of the cantilever and bridge geometries.

References

[1] A. V. Chumak et al. “Advances in Magnetics Roadmap on Spin-Wave Computing”. In: *IEEE Transactions on Magnetics* 58.6 (June 2022), pp. 1–72. DOI: 10.1109/tmag.2022.3149664. URL: https://doi.org/10.1109/tmag.2022.3149664.

[2] Markus Aspelmeyer, Tobias J. Kippenberg, and Florian Marquardt. “Cavity optomechanics”. In: *Reviews of Modern Physics* 86.4 (Dec. 2014), pp. 1391–1452. DOI: 10.1103/revmodphys.86.1391. URL: https://doi.org/10.1103/revmodphys.86.1391.

[3] Tobias J. Kippenberg and Kerry J. Vahala. “Cavity Opto-Mechanics”. In: *Optics Express* 15.25 (2007), p. 17172. DOI: 10.1364/oe.15.017172. URL: https://doi.org/10.1364/oe.15.017172.

[4] Tal Carmon et al. “Temporal Behavior of Radiation-Pressure-Induced Vibrations of an Optical Microcavity Phonon Mode”. In: *Physical Review Letters* 94.22 (June 2005). DOI: 10.1103/physrevlett.94.223902. URL: https://doi.org/10.1103/physrevlett.94.223902.

[5] O. Arcizet et al. “Radiation-pressure cooling and optomechanical instability of a micromirror”. In: *Nature* 444.7115 (Nov. 2006), pp. 71–74. DOI: 10.1038/nature05244. URL: https://doi.org/10.1038/nature05244.

[6] J. D. Teufel et al. “Circuit cavity electromechanics in the strong-coupling regime”. In: *Nature* 471.7337 (Mar. 2011), pp. 204–208. DOI: 10.1038/nature09898. URL: https://doi.org/10.1038/nature09898.

[7] C. A. Regal, J. D. Teufel, and K. W. Lehnert. “Measuring nanomechanical motion with a microwave cavity interferometer”. In: *Nature Physics* 4.7 (May 2008), pp. 555–560. DOI: 10.1038/nphys974. URL: https://doi.org/10.1038/nphys974.

[8] Joerg Bochmann et al. “Nanomechanical coupling between microwave and optical photons”. In: *Nature Physics* 9.11 (Sept. 2013), pp. 712–716. DOI: 10.1038/nphys2748. URL: https://doi.org/10.1038/nphys2748.

[9] Wentao Jiang et al. “Efficient bidirectional piezo-optomechanical transduction between microwave and optical frequency”. In: *Nature Communications* 11.1 (Mar. 2020). DOI: 10.1038/s41467-020-14863-3. URL: https://doi.org/10.1038/s41467-020-14863-3.

[10] Vladimir Cherepanov, Igor Kolokolov, and Victor L’vov. “The saga of YIG: Spectra, thermodynamics, interaction and relaxation of magnons in a complex magnet”. In: *Physics Reports* 229.3 (July 1993), pp. 81–144. DOI: 10.1016/0370-1573(93)90107-o. URL: https://doi.org/10.1016/0370-1573(93)90107-o.

[11] A A Serga, A V Chumak, and B Hillebrands. "YIG magnonics". In: *Journal of Physics D: Applied Physics* 43.26 (June 2010), p. 264002. DOI: 10.1088/0022-3727/43/26/264002. URL: https://doi.org/10.1088/0022-3727/43/26/264002.

[12] Christoph Hauser et al. "Yttrium Iron Garnet Thin Films with Very Low Damping Obtained by Recrystallization of Amorphous Material". In: *Scientific Reports* 6.1 (Feb. 2016). DOI: 10.1038/srep20827. URL: https://doi.org/10.1038/srep20827.

[13] R.C. Linares. "Epitaxial growth of narrow linewidth yttrium iron garnet films". In: *Journal of Crystal Growth* 3-4 (Jan. 1968), pp. 443–446. DOI: 10.1016/0022-0248(68)90196-6. URL: https://doi.org/10.1016/0022-0248(68)90196-6.

[14] A. G. Gurevich and G. A. Melkov. *Magnetization Oscillations and Waves*. CRC Press, Sept. 1996.

[15] G. Bertotti, I. D. Mayergoyz, and C. Serpico. *Nonlinear Magnetization Dynamics in Nanosystems*. Elsevier, 2009.

[16] Hans Huebl et al. "High Cooperativity in Coupled Microwave Resonator Ferrimagnetic Insulator Hybrids". In: *Physical Review Letters* 111.12 (Sept. 2013). DOI: 10.1103/physrevlett.111.127003. URL: https://doi.org/10.1103/physrevlett.111.127003.

[17] Silvia Viola Kusminskiy, Hong X. Tang, and Florian Marquardt. "Coupled spin-light dynamics in cavity optomagnonics". In: *Physical Review A* 94.3 (Sept. 2016). DOI: 10.1103/physreva.94.033821. URL: https://doi.org/10.1103/physreva.94.033821.

[18] S. V. Kusminskiy. *Quantum Magnetism, Spin Waves, and Optical Cavities*. 1st ed. SpringerBriefs in physics. Springer Nature, Mar. 2019.

[19] Xufeng Zhang et al. "Strongly Coupled Magnons and Cavity Microwave Photons". In: *Physical Review Letters* 113.15 (Oct. 2014). DOI: 10.1103/physrevlett.113.156401. URL: https://doi.org/10.1103/physrevlett.113.156401.

[20] Yutaka Tabuchi et al. "Hybridizing Ferromagnetic Magnons and Microwave Photons in the Quantum Limit". In: *Physical Review Letters* 113.8 (Aug. 2014). DOI: 10.1103/physrevlett.113.083603. URL: https://doi.org/10.1103/physrevlett.113.083603.

[21] Yutaka Tabuchi et al. "Coherent coupling between a ferromagnetic magnon and a superconducting qubit". In: *Science* 349.6246 (July 2015), pp. 405–408. DOI: 10.1126/science.aaa3693. URL: https://doi.org/10.1126/science.aaa3693.

[22] Yutaka Tabuchi et al. "Quantum magnonics: The magnon meets the superconducting qubit". In: *Comptes Rendus Physique* 17.7 (Aug. 2016), pp. 729–739. DOI: 10.1016/j.crhy.2016.07.009. URL: https://doi.org/10.1016/j.crhy.2016.07.009.

[23] Yi Li et al. "Advances in coherent coupling between magnons and acoustic phonons". In: *APL Materials* 9.6 (June 2021). DOI: 10.1063/5.0047054. URL: https://doi.org/10.1063/5.0047054.

[24] D. Stancil and A. Prabhakar. *Spin waves*. Springer, Oct. 2010.

[25] Charles Kittel. "Physical Theory of Ferromagnetic Domains". In: *Reviews of Modern Physics* 21.4 (Oct. 1949), pp. 541–583. DOI: 10.1103/revmodphys.21.541. URL: https://doi.org/10.1103/revmodphys.21.541.

[26] C. Kittel. "Interaction of Spin Waves and Ultrasonic Waves in Ferromagnetic Crystals". In: *Physical Review* 110.4 (May 1958), pp. 836–841. DOI: 10.1103/physrev.110.836. URL: https://doi.org/10.1103/physrev.110.836.

[27] Xufeng Zhang et al. "Cavity magnomechanics". In: *Science Advances* 2.3 (Mar. 2016). DOI: 10.1126/sciadv.1501286. URL: https://doi.org/10.1126/sciadv.1501286.

[28] Bijita Sarma, Thomas Busch, and Jason Twamley. "Cavity magnomechanical storage and retrieval of quantum states". In: *New Journal of Physics* 23.4 (Apr. 2021), p. 043041. DOI: 10.1088/1367-2630/abf535. URL: https://doi.org/10.1088/1367-2630/abf535.

[29] Wenyue Qiu et al. "Controlling quantum coherence and entanglement in cavity magnomechanical systems". In: *Physical Review A* 105.6 (June 2022). DOI: 10.1103/physreva.105.063718. URL: https://doi.org/10.1103/physreva.105.063718.

[30] Jie Li, Shi-Yao Zhu, and G. S. Agarwal. "Magnon-Photon-Phonon Entanglement in Cavity Magnomechanics". In: *Physical Review Letters* 121.20 (Nov. 2018). DOI: 10.1103/physrevlett.121.203601. URL: https://doi.org/10.1103/physrevlett.121.203601.

[31] Jie Li and Simon Gröblacher. "Entangling the vibrational modes of two massive ferromagnetic spheres using cavity magnomechanics". In: *Quantum Science and Technology* 6.2 (Feb. 2021), p. 024005. DOI: 10.1088/2058-9565/abd982. URL: https://doi.org/10.1088/2058-9565/abd982.

[32] Jie Li, Shi-Yao Zhu, and G. S. Agarwal. "Squeezed states of magnons and phonons in cavity magnomechanics". In: *Physical Review A* 99.2 (Feb. 2019). DOI: 10.1103/physreva.99.021801. URL: https://doi.org/10.1103/physreva.99.021801.

[33] R. C. LeCraw, E. G. Spencer, and E. I. Gordon. "Extremely Low Loss Acoustic Resonance in Single-Crystal Garnet Spheres". In: *Physical Review Letters* 6.11 (June 1961), pp. 620–622. DOI: 10.1103/physrevlett.6.620. URL: https://doi.org/10.1103/physrevlett.6.620.

[34] Matthew W. Puckett et al. "422 Million intrinsic quality factor planar integrated all-waveguide resonator with sub-MHz linewidth". In: *Nature Communications* 12.1 (Feb. 2021). DOI: 10.1038/s41467-021-21205-4. URL: https://doi.org/10.1038/s41467-021-21205-4.

[35] R. A. Norte, J. P. Moura, and S. Gröblacher. "Mechanical Resonators for Quantum Optomechanics Experiments at Room Temperature". In: *Physical Review Letters* 116.14 (Apr. 2016). DOI: 10.1103/physrevlett.116.147202. URL: https://doi.org/10.1103/physrevlett.116.147202.

[36] B. M. Zwickl et al. "High quality mechanical and optical properties of commercial silicon nitride membranes". In: *Applied Physics Letters* 92.10 (Mar. 2008). DOI: 10.1063/1.2884191. URL: https://doi.org/10.1063/1.2884191.

[37] E.P. Wohlfarth. "Chapter 1 Iron, cobalt and nickel". In: *Handbook of Ferromagnetic Materials*. Elsevier, 1980, pp. 1–70. DOI: 10.1016/s1574-9304(05)80116-6. URL: https://doi.org/10.1016/s1574-9304(05)80116-6.

[38] J. C. Slater. "The Ferromagnetism of Nickel". In: *Physical Review* 49.7 (Apr. 1936), pp. 537–545. DOI: 10.1103/physrev.49.537. URL: https://doi.org/10.1103/physrev.49.537.

[39] Edmund C. Stoner. "Collective Electron Ferromagnetism". In: *Proceedings of the Royal Society of London. Series A, Mathematical and Physical Sciences* 165.922 (1938), pp. 372–414. ISSN: 00804630. URL: http://www.jstor.org/stable/97057 (visited on 08/01/2023).

[40] M. Shimizu. "Ferromagnetism in iron, cobalt, nickel and their alloys". In: *Physica BC* 91 (July 1977), pp. 14–23. DOI: 10.1016/0378-4363(77)90162-0. URL: https://doi.org/10.1016/0378-4363(77)90162-0.

[41] G E Bacon, R Street, and R H Tredgold. "The antiferromagnetic properties of mixed cobalt and manganese oxides". In: *Proceedings of the Royal Society of London. Series A. Mathematical and Physical Sciences* 217.1129 (Apr. 1953), pp. 252–261. DOI: 10.1098/rspa.1953.0060. URL: https://doi.org/10.1098/rspa.1953.0060.

[42] A B Lidiard. "Antiferromagnetism". In: *Reports on Progress in Physics* 17.1 (Jan. 1954), pp. 201–244. DOI: 10.1088/0034-4885/17/1/307. URL: https://doi.org/10.1088/0034-4885/17/1/307.

[43] R. K. Nesbet. "Antiferromagnetic Superexchange Effect". In: *Physical Review* 119.2 (July 1960), pp. 658–662. DOI: 10.1103/physrev.119.658. URL: https://doi.org/10.1103/physrev.119.658.

[44] Edmund C Stoner. "Ferromagnetism". In: *Reports on Progress in Physics* 11.1 (Jan. 1947), pp. 43–112. DOI: 10.1088/0034-4885/11/1/304. URL: https://doi.org/10.1088/0034-4885/11/1/304.

[45] G. A. Sawatzky, F. Van Der Woude, and A. H. Morrish. "Mössbauer Study of Several Ferrimagnetic Spinels". In: *Physical Review* 187.2 (Nov. 1969), pp. 747–757. DOI: 10.1103/physrev.187.747. URL: https://doi.org/10.1103/physrev.187.747.

[46] S. Geller and M.A. Gilleo. "The crystal structure and ferrimagnetism of yttrium-iron garnet, Y3Fe2(FeO4)3". In: *Journal of Physics and Chemistry of Solids* 3.1-2 (Jan. 1957), pp. 30–36. DOI: 10.1016/0022-3697(57)90044-6. URL: https://doi.org/10.1016/0022-3697(57)90044-6.

[47] Lucile Savary and Leon Balents. "Quantum spin liquids: a review". In: *Reports on Progress in Physics* 80.1 (Nov. 2016), p. 016502. ISSN: 1361-6633. DOI: 10.1088/0034-4885/80/1/016502. URL: http://dx.doi.org/10.1088/0034-4885/80/1/016502.

[48] E. Stryjewski and N. Giordano. "Metamagnetism". In: *Advances in Physics* 26.5 (Sept. 1977), pp. 487–650. ISSN: 1460-6976. DOI: 10.1080/00018737700101433. URL: http://dx.doi.org/10.1080/00018737700101433.

[49] Subhankar Bedanta and Wolfgang Kleemann. "Supermagnetism". In: *Journal of Physics D: Applied Physics* 42.1 (Dec. 2008), p. 013001. ISSN: 1361-6463. DOI: 10.1088/0022-3727/42/1/013001. URL: http://dx.doi.org/10.1088/0022-3727/42/1/013001.

[50] X. Z. Yu et al. "Near room-temperature formation of a skyrmion crystal in thin-films of the helimagnet FeGe". In: *Nature Materials* 10.2 (Dec. 2010), pp. 106–109. ISSN: 1476-4660. DOI: 10.1038/nmat2916. URL: http://dx.doi.org/10.1038/nmat2916.

[51] Pierre Weiss. "L'hypothèse du champ moléculaire et la propriété ferromagnétique". In: *Journal de Physique Théorique et Appliquée* 6.1 (1907), pp. 661–690. DOI: 10.1051/jphystap:019070060066100. URL: https://doi.org/10.1051/jphystap:019070060066100.

[52] J Coey. *Magnetism and magnetic materials*. Cambridge University Press, 2010.

[53] K. F. Riley, M. P. Hobson, and S. J. Bence. *Mathematical Methods for Physics and Engineering*. 3rd ed. Cambridge University Press, Mar. 2006.

[54] A. I. Akhiezer, Bar'yakhtar V. G., and S. V. Peletminskii. *Spin Waves*. Ed. by C. J. Gorter, R. De Bruyn Ouboter, and D. De Klerk. North-Holland Series in Low Temperature Physics. North-Holland Publishing Company, 1968.

[55] J. A. Osborn. "Demagnetizing Factors of the General Ellipsoid". In: *Physical Review* 67.11-12 (June 1945), pp. 351–357. DOI: 10.1103/physrev.67.351. URL: https://doi.org/10.1103/physrev.67.351.

[56] M. Sato and Y. Ishii. "Simple and approximate expressions of demagnetizing factors of uniformly magnetized rectangular rod and cylinder". In: *Journal of Applied Physics* 66.2 (July 1989), pp. 983–985. DOI: 10.1063/1.343481. URL: https://doi.org/10.1063/1.343481.

[57] Mahmut Obol and Carmine Vittoria. "Microwave permeability of Y-type hexaferrites in zero field". In: *Journal of Applied Physics* 94.6 (Aug. 2003), pp. 4013–4017. DOI: 10.1063/1.1601291. URL: https://doi.org/10.1063/1.1601291.

[58] M. Darby and E. Isaac. "Magnetocrystalline anisotropy of ferro- and ferrimagnetics". In: *IEEE Transactions on Magnetics* 10.2 (June 1974), pp. 259–304. DOI: 10.1109/tmag.1974.1058331. URL: https://doi.org/10.1109/tmag.1974.1058331.

[59] S. Blundell. *Magnetism in Condensed Matter*. Oxford Master Series in Condensed Matter Physics. Oxford University Press, Aug. 2001.

[60] L. D. Landau and E. M. Lifshitz. "On the Theory of the Dispersion of Magnetic Permeability in Ferromagnetic Bodies". In: *Phys. Zeitsch. der Sow.* 10 (1935), pp. 153–164.

[61] T.L. Gilbert. "Classics in Magnetics A Phenomenological Theory of Damping in Ferromagnetic Materials". In: *IEEE Transactions on Magnetics* 40.6 (Nov. 2004), pp. 3443–3449. DOI: 10.1109/tmag.2004.836740. URL: https://doi.org/10.1109/tmag.2004.836740.

[62] Charles Kittel. "Interpretation of Anomalous Larmor Frequencies in Ferromagnetic Resonance Experiment". In: *Physical Review* 71.4 (Feb. 1947), pp. 270–271. DOI: 10.1103/physrev.71.270.2. URL: https://doi.org/10.1103/physrev.71.270.2.

[63] Charles Kittel. "On the Theory of Ferromagnetic Resonance Absorption". In: *Physical Review* 73.2 (Jan. 1948), pp. 155–161. DOI: 10.1103/physrev.73.155. URL: https://doi.org/10.1103/physrev.73.155.

[64] J. H. E. GRIFFITHS. "Anomalous High-frequency Resistance of Ferromagnetic Metals". In: *Nature* 158.4019 (Nov. 1946), pp. 670–671. DOI: 10.1038/158670a0. URL: https://doi.org/10.1038/158670a0.

[65] O Yalçın. *Ferromagnetic Resonance - Theory and Applications*. InTech, 2013.

[66] L. D. Landau and E. M. Lifshitz. *Mechanics*. 3rd ed. Course of Theoretical Physics. Butterworth-Heinemann, 1976.

[67] Karl F Graff. *Wave motion in elastic solids*. Dover Books on Physics. Dover Publications, June 1991.

[68] Lord Rayleigh. "On waves propagated along the plane surface of an elastic body". In: *Proc. Math. Soc. London* (1885).

[69] S.P. Timoshenko. "LXVI. iOn the correction for shear of the differential equation for transverse vibrations of prismatic bars/i". In: *The London, Edinburgh, and Dublin Philosophical Magazine and Journal of Science* 41.245 (May 1921), pp. 744–746. DOI: 10.1080/14786442108636264. URL: https://doi.org/10.1080/14786442108636264.

[70] S.P. Timoshenko. "X. iOn the transverse vibrations of bars of uniform cross-section/i". In: *The London, Edinburgh, and Dublin Philosophical Magazine and Journal of Science* 43.253 (Jan. 1922), pp. 125–131. DOI: 10.1080/14786442208633855. URL: https://doi.org/10.1080/14786442208633855.

[71] J. R. Hutchinson. "Transverse Vibrations of Beams, Exact Versus Approximate Solutions". In: *Journal of Applied Mechanics* 48.4 (Dec. 1981), pp. 923–928. DOI: 10.1115/1.3157757. URL: https://doi.org/10.1115/1.3157757.

[72] N.G. Stephen and S. Puchegger. "On the valid frequency range of Timoshenko beam theory". In: *Journal of Sound and Vibration* 297.3-5 (Nov. 2006), pp. 1082–1087. DOI: 10.1016/j.jsv.2006.04.020. URL: https://doi.org/10.1016/j.jsv.2006.04.020.

[73] SEON M. HAN, HAYM BENAROYA, and TIMOTHY WEI. "DYNAMICS OF TRANSVERSELY VIBRATING BEAMS USING FOUR ENGINEERING THEORIES". In: *Journal of Sound and Vibration* 225.5 (Sept. 1999), pp. 935–988. DOI: 10.1006/jsvi.1999.2257. URL: https://doi.org/10.1006/jsvi.1999.2257.

[74] Dennison Bancroft. "The Velocity of Longitudinal Waves in Cylindrical Bars". In: *Physical Review* 59.7 (Apr. 1941), pp. 588–593. DOI: 10.1103/physrev.59.588. URL: https://doi.org/10.1103/physrev.59.588.

[75] G. E. Hudson. "Dispersion of Elastic Waves in Solid Circular Cylinders". In: *Physical Review* 63.1-2 (Jan. 1943), pp. 46–51. DOI: 10.1103/physrev.63.46. URL: https://doi.org/10.1103/physrev.63.46.

[76] L. D. Landau et al. *Theory of elasticity*. 3rd ed. Course of Theoretical Physics. Butterworth-Heinemann, Jan. 1986.

[77] Peter Lebedew. "Untersuchungen über die Druckkräfte des Lichtes". In: *Annalen der Physik* 311.11 (1901), pp. 433–458. DOI: 10.1002/andp.19013111102. URL: https://doi.org/10.1002/andp.19013111102.

[78] E. F. Nichols and G. F. Hull. "A Preliminary Communication on the Pressure of Heat and Light Radiation". In: *Physical Review (Series I)* 13.5 (Nov. 1901), pp. 307–320. DOI: 10.1103/physrevseriesi.13.307. URL: https://doi.org/10.1103/physrevseriesi.13.307.

[79] Thomas Corbitt and Nergis Mavalvala. "Review: Quantum noise in gravitational-wave interferometers". In: *Journal of Optics B: Quantum and Semiclassical Optics* 6.8 (July 2004), S675–S683. DOI: 10.1088/1464-4266/6/8/008. URL: https://doi.org/10.1088/1464-4266/6/8/008.

[80] Xinmiao Liu et al. "Progress of optomechanical micro/nano sensors: a review". In: *International Journal of Optomechatronics* 15.1 (Jan. 2021), pp. 120–159. DOI: 10.1080/15599612.2021.1986612. URL: https://doi.org/10.1080/15599612.2021.1986612.

[81] Thomas Corbitt et al. "An All-Optical Trap for a Gram-Scale Mirror". In: *Physical Review Letters* 98.15 (Apr. 2007). DOI: 10.1103/physrevlett.98.150802. URL: https://doi.org/10.1103/physrevlett.98.150802.

[82] Benjamin S. Sheard et al. "Observation and characterization of an optical spring". In: *Physical Review A* 69.5 (May 2004). DOI: 10.1103/physreva.69.051801. URL: https://doi.org/10.1103/physreva.69.051801.

[83] A. Dorsel et al. "Optical Bistability and Mirror Confinement Induced by Radiation Pressure". In: *Physical Review Letters* 51.17 (Oct. 1983), pp. 1550–1553. DOI: 10.1103/physrevlett.51.1550. URL: https://doi.org/10.1103/physrevlett.51.1550.

[84] A. Gozzini et al. "Light-pressure bistability at microwave frequencies". In: *Journal of the Optical Society of America B* 2.11 (Nov. 1985), p. 1841. DOI: 10.1364/josab.2.001841. URL: https://doi.org/10.1364/josab.2.001841.

[85] Constanze Höhberger Metzger and Khaled Karrai. "Cavity cooling of a microlever". In: *Nature* 432.7020 (Dec. 2004), pp. 1002–1005. DOI: 10.1038/nature03118. URL: https://doi.org/10.1038/nature03118.

[86] Jasper Chan et al. "Laser cooling of a nanomechanical oscillator into its quantum ground state". In: *Nature* 478.7367 (Oct. 2011), pp. 89–92. DOI: 10.1038/nature10461. URL: https://doi.org/10.1038/nature10461.

[87] I. Wilson-Rae et al. "Theory of Ground State Cooling of a Mechanical Oscillator Using Dynamical Backaction". In: *Physical Review Letters* 99.9 (Aug. 2007). DOI: 10.1103/physrevlett.99.093901. URL: https://doi.org/10.1103/physrevlett.99.093901.

[88] Florian Marquardt et al. "Quantum Theory of Cavity-Assisted Sideband Cooling of Mechanical Motion". In: *Physical Review Letters* 99.9 (Aug. 2007). DOI: 10.1103/physrevlett.99.093902. URL: https://doi.org/10.1103/physrevlett.99.093902.

[89] K. Stannigel et al. "Optomechanical Transducers for Long-Distance Quantum Communication". In: *Physical Review Letters* 105.22 (Nov. 2010). DOI: 10.1103/physrevlett.105.220501. URL: https://doi.org/10.1103/physrevlett.105.220501.

[90] G. D. de Moraes Neto et al. "Quantum state transfer in optomechanical arrays". In: *Physical Review A* 93.6 (June 2016). DOI: 10.1103/physreva.93.062339. URL: https://doi.org/10.1103/physreva.93.062339.

[91] T. P. Purdy et al. "Strong Optomechanical Squeezing of Light". In: *Physical Review X* 3.3 (Sept. 2013). DOI: 10.1103/physrevx.3.031012. URL: https://doi.org/10.1103/physrevx.3.031012.

[92] Nancy Aggarwal et al. "Room-temperature optomechanical squeezing". In: *Nature Physics* 16.7 (July 2020), pp. 784–788. DOI: 10.1038/s41567-020-0877-x. URL: https://doi.org/10.1038/s41567-020-0877-x.

[93] Xin-You Lü et al. "Steady-state mechanical squeezing in an optomechanical system via Duffing nonlinearity". In: *Physical Review A* 91.1 (Jan. 2015). DOI: 10.1103/physreva.91.013834. URL: https://doi.org/10.1103/physreva.91.013834.

[94] I. Mahboob et al. "Phonon Lasing in an Electromechanical Resonator". In: *Physical Review Letters* 110.12 (Mar. 2013). DOI: 10.1103/physrevlett.110.127202. URL: https://doi.org/10.1103/physrevlett.110.127202.

[95] Ivan S. Grudinin et al. "Phonon Laser Action in a Tunable Two-Level System". In: *Physical Review Letters* 104.8 (Feb. 2010). DOI: 10.1103/physrevlett.104.083901. URL: https://doi.org/10.1103/physrevlett.104.083901.

[96] Stefan Weis et al. "Optomechanically Induced Transparency". In: *Science* 330.6010 (Dec. 2010), pp. 1520–1523. DOI: 10.1126/science.1195596. URL: https://doi.org/10.1126/science.1195596.

[97] Peng-Cheng Ma et al. "Tunable double optomechanically induced transparency in an optomechanical system". In: *Physical Review A* 90.4 (Oct. 2014). DOI: 10.1103/physreva.90.043825. URL: https://doi.org/10.1103/physreva.90.043825.

[98] M. Karuza et al. "Optomechanically induced transparency in a membrane-in-the-middle setup at room temperature". In: *Physical Review A* 88.1 (July 2013). DOI: 10.1103/physreva.88.013804. URL: https://doi.org/10.1103/physreva.88.013804.

[99] J. P. Marangos. "Electromagnetically induced transparency". In: *Journal of Modern Optics* 45.3 (Mar. 1998), pp. 471–503. DOI: 10.1080/09500349808231909. URL: https://doi.org/10.1080/09500349808231909.

[100] Hao Xiong and Ying Wu. "Fundamentals and applications of optomechanically induced transparency". In: *Applied Physics Reviews* 5.3 (Sept. 2018), p. 031305. DOI: 10.1063/1.5027122. URL: https://doi.org/10.1063/1.5027122.

[101] V. B. Braginsky, F. Y. Khalili, and K. S. Thorne. *Quantum Measurement*. Ed. by Kip S Thorne. Cambridge University Press, Dec. 2009.

[102] F. Armata et al. "Quantum limits to gravity estimation with optomechanics". In: *Physical Review A* 96.4 (Oct. 2017). DOI: 10.1103/physreva.96.043824. URL: https://doi.org/10.1103/physreva.96.043824.

[103] Heiko Groß et al. "Near-field strong coupling of single quantum dots". In: *Science Advances* 4.3 (Mar. 2018). DOI: 10.1126/sciadv.aar4906. URL: https://doi.org/10.1126/sciadv.aar4906.

[104] Hiroki Takahashi et al. "Strong Coupling of a Single Ion to an Optical Cavity". In: *Physical Review Letters* 124.1 (Jan. 2020). DOI: 10.1103/physrevlett.124.013602. URL: https://doi.org/10.1103/physrevlett.124.013602.

[105] Fumiki Yoshihara et al. "Superconducting qubit–oscillator circuit beyond the ultrastrong-coupling regime". In: *Nature Physics* 13.1 (Oct. 2016), pp. 44–47. DOI: 10.1038/nphys3906. URL: https://doi.org/10.1038/nphys3906.

[106] C. K. Law. "Interaction between a moving mirror and radiation pressure: A Hamiltonian formulation". In: *Physical Review A* 51.3 (Mar. 1995), pp. 2537–2541. DOI: 10.1103/physreva.51.2537. URL: https://doi.org/10.1103/physreva.51.2537.

[107] S. Mancini, V. I. Man'ko, and P. Tombesi. "Ponderomotive control of quantum macroscopic coherence". In: *Physical Review A* 55.4 (Apr. 1997), pp. 3042–3050. DOI: 10.1103/physreva.55.3042. URL: https://doi.org/10.1103/physreva.55.3042.

[108] J. J. Sakurai and J. Napolitano. *Modern Quantum Mechanics*. 2nd ed. Cambridge University Press, Sept. 2017.

[109] Thomas M. Barlow, Robert Bennett, and Almut Beige. "A master equation for a two-sided optical cavity". In: *Journal of Modern Optics* 62.sup2 (Jan. 2015), S11–S20. DOI: 10.1080/09500340.2014.992992. URL: https://doi.org/10.1080/09500340.2014.992992.

[110] C. W. Gardiner and P. Zoller. *Quantum Noise*. Springer Series in Synergetics. Springer, Dec. 2010.

[111] C. W. Gardiner and M. J. Collett. "Input and output in damped quantum systems: Quantum stochastic differential equations and the master equation". In: *Physical Review A* 31.6 (June 1985), pp. 3761–3774. DOI: 10.1103/physreva.31.3761. URL: https://doi.org/10.1103/physreva.31.3761.

[112] P. Meystre et al. "Theory of radiation-pressure-driven interferometers". In: *Journal of the Optical Society of America B* 2.11 (Nov. 1985), p. 1830. DOI: 10.1364/josab.2.001830. URL: https://doi.org/10.1364/josab.2.001830.

[113] Yong-Chun Liu et al. "Review of cavity optomechanical cooling". In: *Chinese Physics B* 22.11 (Nov. 2013), p. 114213. DOI: 10.1088/1674-1056/22/11/114213. URL: https://doi.org/10.1088/1674-1056/22/11/114213.

[114] Mani Hossein-Zadeh et al. "Characterization of a radiation-pressure-driven micromechanical oscillator". In: *Physical Review A* 74.2 (Aug. 2006). DOI: 10.1103/physreva.74.023813. URL: https://doi.org/10.1103/physreva.74.023813.

[115] Mani Hossein-Zadeh and Kerry J. Vahala. "Observation of optical spring effect in a microtoroidal optomechanical resonator". In: *Optics Letters* 32.12 (June 2007), p. 1611. DOI: 10.1364/ol.32.001611. URL: https://doi.org/10.1364/ol.32.001611.

[116] Ö. O. Soykal and M. E. Flatté. "Size dependence of strong coupling between nanomagnets and photonic cavities". In: *Physical Review B* 82.10 (Sept. 2010). DOI: 10.1103/physrevb.82.104413. URL: https://doi.org/10.1103/physrevb.82.104413.

[117] Ö. O. Soykal and M. E. Flatté. "Strong Field Interactions between a Nanomagnet and a Photonic Cavity". In: *Physical Review Letters* 104.7 (Feb. 2010). DOI: 10.1103/physrevlett.104.077202. URL: https://doi.org/10.1103/physrevlett.104.077202.

[118] Yi Li et al. “Strong Coupling between Magnons and Microwave Photons in On-Chip Ferromagnet-Superconductor Thin-Film Devices”. In: *Physical Review Letters* 123.10 (Sept. 2019). DOI: 10.1103/physrevlett.123.107701. URL: https://doi.org/10.1103/physrevlett.123.107701.

[119] Justin T. Hou and Luqiao Liu. “Strong Coupling between Microwave Photons and Nanomagnet Magnons”. In: *Physical Review Letters* 123.10 (Sept. 2019). DOI: 10.1103/physrevlett.123.107702. URL: https://doi.org/10.1103/physrevlett.123.107702.

[120] Side Guo et al. “Strong on-Chip Microwave Photon–Magnon Coupling Using Ultralow-Damping Epitaxial Y3Fe5O12 Films at 2 K”. In: *Nano Letters* 23.11 (May 2023), pp. 5055–5060. ISSN: 1530-6992. DOI: 10.1021/acs.nanolett.3c00959. URL: http://dx.doi.org/10.1021/acs.nanolett.3c00959.

[121] Björn Heinz et al. “Long-range spin-wave propagation in transversely magnetized nano-scaled conduits”. In: *Applied Physics Letters* 118.13 (Mar. 2021). DOI: 10.1063/5.0045570. URL: https://doi.org/10.1063/5.0045570.

[122] Huajun Qin et al. “Nanoscale magnonic Fabry-Pérot resonator for low-loss spin-wave manipulation”. In: *Nature Communications* 12.1 (Apr. 2021). DOI: 10.1038/s41467-021-22520-6. URL: https://doi.org/10.1038/s41467-021-22520-6.

[123] Yong-Jun Seo et al. “Fabrication and magnetic control of Y3Fe5O12 cantilevers”. In: *Applied Physics Letters* 110.13 (Mar. 2017). DOI: 10.1063/1.4979553. URL: https://doi.org/10.1063/1.4979553.

[124] Kazuya Harii et al. “Spin Seebeck mechanical force”. In: *Nature Communications* 10.1 (June 2019). DOI: 10.1038/s41467-019-10625-y. URL: https://doi.org/10.1038/s41467-019-10625-y.

[125] F. Heyroth et al. “Monocrystalline Freestanding Three-Dimensional Yttrium-Iron-Garnet Magnon Nanoresonators”. In: *Physical Review Applied* 12.5 (Nov. 2019). ISSN: 2331-7019. DOI: 10.1103/physrevapplied.12.054031. URL: http://dx.doi.org/10.1103/PhysRevApplied.12.054031.

[126] D. Cheshire. “Magnetic X-Ray Spectroscopy and FMR Spin-Pumping Studies of PLD Amorphous YIG”. Available at https://etheses.whiterose.ac.uk/32380/. PhD thesis. University of York, 2023.

[127] Naresh Kumar et al. “Magnetic properties of pulsed laser ablated YIG thin films on different substrates”. In: *Journal of Magnetism and Magnetic Materials* 272-276 (May 2004), E899–E900. DOI: 10.1016/j.jmmm.2003.12.223. URL: https://doi.org/10.1016/j.jmmm.2003.12.223.

[128] M. C. Onbasli et al. “Pulsed laser deposition of epitaxial yttrium iron garnet films with low Gilbert damping and bulk-like magnetization”. In: *APL Materials* 2.10 (Oct. 2014). DOI: 10.1063/1.4896936. URL: https://doi.org/10.1063/1.4896936.

[129] Chi Tang et al. “Exquisite growth control and magnetic properties of yttrium iron garnet thin films”. In: *Applied Physics Letters* 108.10 (Mar. 2016). DOI: 10.1063/1.4943210. URL: https://doi.org/10.1063/1.4943210.

[130] Yiyan Sun et al. "Growth and ferromagnetic resonance properties of nanometer-thick yttrium iron garnet films". In: *Applied Physics Letters* 101.15 (Oct. 2012). DOI: 10.1063/1.4759039. URL: https://doi.org/10.1063/1.4759039.

[131] Georg Schmidt et al. "Ultra Thin Films of Yttrium Iron Garnet with Very Low Damping: A Review". In: *physica status solidi (b)* 257.7 (Apr. 2020), p. 1900644. DOI: 10.1002/pssb.201900644. URL: https://doi.org/10.1002/pssb.201900644.

[132] Haiming Yu, Jiang Xiao, and Philipp Pirro. ""Magnon Spintronics"". In: *Journal of Magnetism and Magnetic Materials* 450 (Mar. 2018), pp. 1–2. DOI: 10.1016/j.jmmm.2017.12.033. URL: https://doi.org/10.1016/j.jmmm.2017.12.033.

[133] X.-Y. Wei et al. "Giant magnon spin conductivity in ultrathin yttrium iron garnet films". In: *Nature Materials* 21.12 (Sept. 2022), pp. 1352–1356. ISSN: 1476-4660. DOI: 10.1038/s41563-022-01369-0. URL: http://dx.doi.org/10.1038/s41563-022-01369-0.

[134] L. J. Graham and Roger Chang. "Elastic Moduli of Single-Crystal Gadolinium Gallium Garnet". In: *Journal of Applied Physics* 41.5 (Apr. 1970), pp. 2247–2248. DOI: 10.1063/1.1659197. URL: https://doi.org/10.1063/1.1659197.

[135] A. E. Clark and R. E. Strakna. "Elastic Constants of Single-Crystal YIG". In: *Journal of Applied Physics* 32.6 (June 1961), pp. 1172–1173. DOI: 10.1063/1.1736184. URL: https://doi.org/10.1063/1.1736184.

[136] V. Monteseguro et al. "Electronic and elastic properties of yttrium gallium garnet under pressure from iab initio/i studies". In: *Journal of Applied Physics* 113.18 (May 2013). DOI: 10.1063/1.4804133. URL: https://doi.org/10.1063/1.4804133.

[137] K. Andres and B. Lüthi. "Magnetostriction of yttrium iron garnet". In: *Journal of Physics and Chemistry of Solids* 24.4 (Apr. 1963), pp. 584–586. DOI: 10.1016/0022-3697(63)90158-6. URL: https://doi.org/10.1016/0022-3697(63)90158-6.

[138] Noboru Tsuya et al. "Magnetostriction Measurement by Three Terminal Capacitance Method". In: *Japanese Journal of Applied Physics* 13.11 (Nov. 1974), pp. 1808–1810. DOI: 10.1143/jjap.13.1808. URL: https://doi.org/10.1143/jjap.13.1808.

[139] A. B. Smith and R. V. Jones. "Magnetostriction Constants from Ferromagnetic Resonance". In: *Journal of Applied Physics* 34.4 (Apr. 1963), pp. 1283–1284. DOI: 10.1063/1.1729473. URL: https://doi.org/10.1063/1.1729473.

[140] E. R. Callen et al. "Magnetostriction in Cubic Néel Ferrimagnets, with Application to YIG". In: *Physical Review* 130.5 (June 1963), pp. 1735–1740. DOI: 10.1103/physrev.130.1735. URL: https://doi.org/10.1103/physrev.130.1735.

[141] R.L. Comstock. "Magnetoelastic coupling constants of the ferrites and garnets". In: *Proceedings of the IEEE* 53.10 (1965), pp. 1508–1517. DOI: 10.1109/proc.1965.4263. URL: https://doi.org/10.1109/proc.1965.4263.

[142] Z. Kleszczewski and J. Bodzenta. "Phonon–Phonon Interaction in Gadolinium–Gallium Garnet Crystals". In: *physica status solidi (b)* 146.2 (Apr. 1988), pp. 467–474. DOI: 10.1002/pssb.2221460207. URL: https://doi.org/10.1002/pssb.2221460207.

[143] M. Dutoit. "Microwave phonon attenuation in yttrium aluminum garnet and gadolinium gallium garnet". In: *Journal of Applied Physics* 45.7 (July 1974), pp. 2836–2840. DOI: 10.1063/1.1663688. URL: https://doi.org/10.1063/1.1663688.

[144] M. KRZESISKA and T. SZUTA-BUCHAC. "Hypersonic wave attenuation in yttrium aluminium garnet and gadolinium gallium garnet". In: *Physica Status Solidi. A* 15 (22 1984), pp. 421–424.

[145] M. Dragoman and D. Dragoman. "Microelectromechanical Systems". In: *Encyclopedia of Condensed Matter Physics*. Elsevier, 2005, pp. 415–423. DOI: 10.1016/b0-12-369401-9/01163-3. URL: https://doi.org/10.1016/b0-12-369401-9/01163-3.

[146] R Sandberg et al. "Effect of gold coating on theiQ/i-factor of a resonant cantilever". In: *Journal of Micromechanics and Microengineering* 15.12 (Oct. 2005), pp. 2249–2253. DOI: 10.1088/0960-1317/15/12/006. URL: https://doi.org/10.1088/0960-1317/15/12/006.

[147] G. N. Greaves et al. "Poisson's ratio and modern materials". In: *Nature Materials* 10.11 (Oct. 2011), pp. 823–837. DOI: 10.1038/nmat3134. URL: https://doi.org/10.1038/nmat3134.

[148] D. Faurie et al. "Measurement of thin film elastic constants by X-ray diffraction". In: *Thin Solid Films* 469-470 (Dec. 2004), pp. 201–205. DOI: 10.1016/j.tsf.2004.08.097. URL: https://doi.org/10.1016/j.tsf.2004.08.097.

[149] K. Yu. Guslienko and A. N. Slavin. "Boundary conditions for magnetization in magnetic nanoelements". In: *Physical Review B* 72.1 (July 2005). DOI: 10.1103/physrevb.72.014463. URL: https://doi.org/10.1103/physrevb.72.014463.

[150] Charles Kittel. *Quantum theory of solids*. en. 2nd ed. Nashville, TN: John Wiley & Sons, Mar. 1987.

[151] T. Holstein and H. Primakoff. "Field Dependence of the Intrinsic Domain Magnetization of a Ferromagnet". In: *Physical Review* 58.12 (Dec. 1940), pp. 1098–1113. DOI: 10.1103/physrev.58.1098. URL: https://doi.org/10.1103/physrev.58.1098.

[152] S. V. Tyablikov. *Methods in the Quantum theory of Magnetism*. Springer, Jan. 1967.

[153] C. Gonzalez-Ballestero et al. "Theory of quantum acoustomagnonics and acoustomechanics with a micromagnet". In: *Physical Review B* 101.12 (Mar. 2020). DOI: 10.1103/physrevb.101.125404. URL: https://doi.org/10.1103/physrevb.101.125404.

[154] I. Wilson-Rae. "Intrinsic dissipation in nanomechanical resonators due to phonon tunneling". In: *Physical Review B* 77.24 (June 2008). DOI: 10.1103/physrevb.77.245418. URL: https://doi.org/10.1103/physrevb.77.245418.

[155] M. Mruczkiewicz et al. "Standing spin waves in magnonic crystals". In: *Journal of Applied Physics* 113.9 (Mar. 2013). DOI: 10.1063/1.4793085. URL: https://doi.org/10.1063/1.4793085.

[156] K. Yu. Guslienko et al. "Effective dipolar boundary conditions for dynamic magnetization in thin magnetic stripes". In: *Physical Review B* 66.13 (Oct. 2002). DOI: 10.1103/physrevb.66.132402. URL: https://doi.org/10.1103/physrevb.66.132402.

[157] G. Venkat et al. "Proposal for a Standard Micromagnetic Problem: Spin Wave Dispersion in a Magnonic Waveguide". In: *IEEE Transactions on Magnetics* 49.1 (Jan. 2013), pp. 524–529. DOI: 10.1109/tmag.2012.2206820. URL: https://doi.org/10.1109/tmag.2012.2206820.

[158] Paul Bryant and Harry Suhl. "Thin-film magnetic patterns in an external field". In: *Applied Physics Letters* 54.22 (May 1989), pp. 2224–2226. DOI: 10.1063/1.101131. URL: https://doi.org/10.1063/1.101131.

[159] M. P. Kostylev et al. "Dipole-exchange propagating spin-wave modes in metallic ferromagnetic stripes". In: *Physical Review B* 76.5 (Aug. 2007). DOI: 10.1103/physrevb.76.054422. URL: https://doi.org/10.1103/physrevb.76.054422.

[160] R. E. De Wames and T. Wolfram. "Dipole-Exchange Spin Waves in Ferromagnetic Films". In: *Journal of Applied Physics* 41.3 (Mar. 1970), pp. 987–993. DOI: 10.1063/1.1659049. URL: https://doi.org/10.1063/1.1659049.

[161] G Gubbiotti et al. "Magnetic field dependence of quantized and localized spin wave modes in thin rectangular magnetic dots". In: *Journal of Physics: Condensed Matter* 16.43 (Oct. 2004), pp. 7709–7721. DOI: 10.1088/0953-8984/16/43/011. URL: https://doi.org/10.1088/0953-8984/16/43/011.

[162] P. Pirro et al. "Spin-wave excitation and propagation in microstructured waveguides of yttrium iron garnet/Pt bilayers". In: *Applied Physics Letters* 104.1 (Jan. 2014). DOI: 10.1063/1.4861343. URL: https://doi.org/10.1063/1.4861343.

[163] P. S. Keatley et al. "Time-resolved investigation of magnetization dynamics of arrays of nonellipsoidal nanomagnets with nonuniform ground states". In: *Physical Review B* 78.21 (Dec. 2008). DOI: 10.1103/physrevb.78.214412. URL: https://doi.org/10.1103/physrevb.78.214412.

[164] M. J. Donahue and D. G. Porter. *OOMMF User's Guide, Version 1.0*. Tech. rep. 1999. DOI: 10.6028/nist.ir.6376. URL: https://doi.org/10.6028/nist.ir.6376.

[165] Sidi Fu et al. "Finite-Difference Micromagnetic Solvers With the Object-Oriented Micromagnetic Framework on Graphics Processing Units". In: *IEEE Transactions on Magnetics* 52.4 (Apr. 2016), pp. 1–9. DOI: 10.1109/tmag.2015.2503262. URL: https://doi.org/10.1109/tmag.2015.2503262.

[166] R F L Evans et al. "Atomistic spin model simulations of magnetic nanomaterials". In: *Journal of Physics: Condensed Matter* 26.10 (Feb. 2014), p. 103202. DOI: 10.1088/0953-8984/26/10/103202. URL: https://doi.org/10.1088/0953-8984/26/10/103202.

[167] C. Schoeppner et al. “Angular dependent ferromagnetic resonance analysis in a single micron sized cobalt stripe”. In: *Journal of Applied Physics* 116.3 (July 2014), p. 033913. DOI: 10.1063/1.4890515. URL: https://doi.org/10.1063/1.4890515.

[168] K. S. Buchanan et al. “Magnetic-field tunability of the vortex translational mode in micron-sized permalloy ellipses: Experiment and micromagnetic modeling”. In: *Physical Review B* 74.6 (Aug. 2006). DOI: 10.1103/physrevb.74.064404. URL: https://doi.org/10.1103/physrevb.74.064404.

[169] Qi Wang et al. “Design of nanostrip magnonic crystal waveguides with a single magnonic band gap”. In: *Journal of Magnetism and Magnetic Materials* 340 (Aug. 2013), pp. 23–26. DOI: 10.1016/j.jmmm.2013.03.017. URL: https://doi.org/10.1016/j.jmmm.2013.03.017.

[170] Zlatko Nedelkoski et al. “Origin of reduced magnetization and domain formation in small magnetite nanoparticles”. In: *Scientific Reports* 7.1 (Apr. 2017). DOI: 10.1038/srep45997. URL: https://doi.org/10.1038/srep45997.

[171] Fabian R. Lux et al. “Chiral Hall Effect in Noncollinear Magnets from a Cyclic Cohomology Approach”. In: *Physical Review Letters* 124.9 (Mar. 2020). DOI: 10.1103/physrevlett.124.096602. URL: https://doi.org/10.1103/physrevlett.124.096602.

[172] Tao Liu et al. “Ferromagnetic resonance of sputtered yttrium iron garnet nanometer films”. In: *Journal of Applied Physics* 115.17 (Jan. 2014). DOI: 10.1063/1.4852135. URL: https://doi.org/10.1063/1.4852135.

[173] Biswanath Bhoi et al. “Stress-induced magnetic properties of PLD-grown high-quality ultrathin YIG films”. In: *Journal of Applied Physics* 123.20 (May 2018). DOI: 10.1063/1.5031198. URL: https://doi.org/10.1063/1.5031198.

[174] S Klingler et al. “Measurements of the exchange stiffness of YIG films using broadband ferromagnetic resonance techniques”. In: *Journal of Physics D: Applied Physics* 48.1 (Dec. 2014), p. 015001. DOI: 10.1088/0022-3727/48/1/015001. URL: https://doi.org/10.1088/0022-3727/48/1/015001.

[175] Mingzhong Wu. “Nonlinear Spin Waves in Magnetic Film Feedback Rings”. In: *Solid State Physics*. Elsevier, 2010, pp. 163–224. DOI: 10.1016/b978-0-12-374293-3.00003-1. URL: https://doi.org/10.1016/b978-0-12-374293-3.00003-1.

[176] Ádám Papp et al. “Nanoscale spectrum analyzer based on spin-wave interference”. In: *Scientific Reports* 7.1 (Aug. 2017). DOI: 10.1038/s41598-017-09485-7. URL: https://doi.org/10.1038/s41598-017-09485-7.

[177] Jae Hyun Kwon et al. “Characterization of magnetostatic surface spin waves in magnetic thin films: evaluation for microelectronic applications”. In: *Applied Physics A* 111.2 (Jan. 2013), pp. 369–378. DOI: 10.1007/s00339-012-7542-x. URL: https://doi.org/10.1007/s00339-012-7542-x.

[178] A. Talalaevskij et al. “Magnetic properties of spin waves in thin yttrium iron garnet films”. In: *Physical Review B* 95.6 (Feb. 2017). DOI: 10.1103/physrevb.95.064409. URL: https://doi.org/10.1103/physrevb.95.064409.

[179] John David Jackson. *Classical Electrodynamics*. 3rd ed. John Wiley & Sons, July 1998.

[180] A. A. Clerk et al. "Introduction to quantum noise, measurement, and amplification". In: *Reviews of Modern Physics* 82.2 (Apr. 2010), pp. 1155–1208. DOI: 10.1103/revmodphys.82.1155. URL: https://doi.org/10.1103/revmodphys.82.1155.

[181] A. I. M. Rae and J. Napolitano. *Quantum Mechanics*. 6th ed. Cambridge Academic Press, Dec. 2015.

[182] William Hvidtfelt Padkær Nielsen et al. "Multimode optomechanical system in the quantum regime". In: *Proceedings of the National Academy of Sciences* 114.1 (Dec. 2016), pp. 62–66. DOI: 10.1073/pnas.1608412114. URL: https://doi.org/10.1073/pnas.1608412114.

[183] Francesco Massel et al. "Multimode circuit optomechanics near the quantum limit". In: *Nature Communications* 3.1 (Aug. 2012). DOI: 10.1038/ncomms1993. URL: https://doi.org/10.1038/ncomms1993.

[184] D. Lee et al. "Multimode optomechanical dynamics in a cavity with avoided crossings". In: *Nature Communications* 6.1 (Feb. 2015). DOI: 10.1038/ncomms7232. URL: https://doi.org/10.1038/ncomms7232.

[185] V. A. S. V. Bittencourt et al. "Magnomechanical backaction corrections due to coupling to higher-order Walker modes and Kerr nonlinearities". In: *Physical Review B* 107.14 (Apr. 2023). ISSN: 2469-9969. DOI: 10.1103/physrevb.107.144411. URL: http://dx.doi.org/10.1103/PhysRevB.107.144411.

[186] L. R. Walker. "Magnetostatic Modes in Ferromagnetic Resonance". In: *Physical Review* 105.2 (Jan. 1957), pp. 390–399. DOI: 10.1103/physrev.105.390. URL: https://doi.org/10.1103/physrev.105.390.

[187] W. H. Press et al. *Numerical recipes in FORTRAN 77: Volume 1*. 2nd ed. Cambridge University Press, Sept. 1992.

[188] B.A. Kalinikos. "Excitation of propagating spin waves in ferromagnetic films". In: *IEE Proceedings H Microwaves, Optics and Antennas* 127.1 (1980), p. 4. DOI: 10.1049/ip-h-1.1980.0002. URL: https://doi.org/10.1049/ip-h-1.1980.0002.

[189] R.W. Damon and J.R. Eshbach. "Magnetostatic modes of a ferromagnet slab". In: *Journal of Physics and Chemistry of Solids* 19.3-4 (May 1961), pp. 308–320. DOI: 10.1016/0022-3697(61)90041-5. URL: https://doi.org/10.1016/0022-3697(61)90041-5.

[190] D. A. Arena et al. "A compact apparatus for studies of element and phase-resolved ferromagnetic resonance". In: *Review of Scientific Instruments* 80.8 (Aug. 2009). DOI: 10.1063/1.3190402. URL: https://doi.org/10.1063/1.3190402.

[191] M. Göppl et al. "Coplanar waveguide resonators for circuit quantum electrodynamics". In: *Journal of Applied Physics* 104.11 (Dec. 2008). DOI: 10.1063/1.3010859. URL: https://doi.org/10.1063/1.3010859.

[192] Jonas Zmuidzinas. "Superconducting Microresonators: Physics and Applications". In: *Annual Review of Condensed Matter Physics* 3.1 (Mar. 2012), pp. 169–214. DOI: 10.1146/annurev-conmatphys-020911-125022. URL: https://doi.org/10.1146/annurev-conmatphys-020911-125022.

[193] Zijun Chen et al. “Fabrication and characterization of aluminum airbridges for superconducting microwave circuits”. In: *Applied Physics Letters* 104.5 (Feb. 2014). DOI: 10.1063/1.4863745. URL: https://doi.org/10.1063/1.4863745.

[194] Sandor Caplan and Gerald Chanin. “Critical-Field Study of Superconducting Aluminum”. In: *Physical Review* 138.5A (May 1965), A1428–A1433. DOI: 10.1103/physrev.138.a1428. URL: https://doi.org/10.1103/physrev.138.a1428.

[195] Igor A. Golovchanskiy et al. “Ferromagnet/Superconductor Hybrid Magnonic Metamaterials”. In: *Advanced Science* 6.16 (July 2019), p. 1900435. DOI: 10.1002/advs.201900435. URL: https://doi.org/10.1002/advs.201900435.

[196] K. Saito and Oho Tsukuba-shi. “Critical field limitation of the niobium superconducting RF cavity”. In: 2001. URL: https://api.semanticscholar.org/CorpusID:59499828.

[197] Simin Zou et al. “High-Quality Factor Superconducting Flexible Resonators Embedded in Thin-Film Polyimide HD-4110”. In: *IEEE Transactions on Applied Superconductivity* 27.7 (Oct. 2017), pp. 1–5. DOI: 10.1109/tasc.2017.2732281. URL: https://doi.org/10.1109/tasc.2017.2732281.

[198] Pingxiang Zhang et al. “NbTi superconducting wires and applications”. In: *Titanium for Consumer Applications*. Elsevier, 2019, pp. 279–296. DOI: 10.1016/b978-0-12-815820-3.00010-1. URL: https://doi.org/10.1016/b978-0-12-815820-3.00010-1.

[199] A. Godeke et al. “Limits of NbTi and Nb_3Sn, and Development of W&R Bi–2212 High Field Accelerator Magnets”. In: *IEEE Transactions on Applied Superconductivity* 17.2 (June 2007), pp. 1149–1152. DOI: 10.1109/tasc.2007.898447. URL: https://doi.org/10.1109/tasc.2007.898447.

[200] T. Boutboul et al. “Critical Current Density in Superconducting Nb-Ti Strands in the 100 mT to 11 T Applied Field Range”. In: *IEEE Transactions on Applied Superconductivity* 16.2 (June 2006), pp. 1184–1187. DOI: 10.1109/tasc.2006.870777. URL: https://doi.org/10.1109/tasc.2006.870777.

[201] S. Ulmer et al. “The quality factor of a superconducting rf resonator in a magnetic field”. In: *Review of Scientific Instruments* 80.12 (Dec. 2009). DOI: 10.1063/1.3271537. URL: https://doi.org/10.1063/1.3271537.

[202] M. R. Vissers et al. “Frequency-tunable superconducting resonators via nonlinear kinetic inductance”. In: *Applied Physics Letters* 107.6 (Aug. 2015). DOI: 10.1063/1.4927444. URL: https://doi.org/10.1063/1.4927444.

[203] Philipp Kurpiers et al. “Characterizing the attenuation of coaxial and rectangular microwave-frequency waveguides at cryogenic temperatures”. In: *EPJ Quantum Technology* 4.1 (May 2017). DOI: 10.1140/epjqt/s40507-017-0059-7. URL: https://doi.org/10.1140/epjqt/s40507-017-0059-7.

[204] Jeremy M. Sage et al. “Study of loss in superconducting coplanar waveguide resonators”. In: *Journal of Applied Physics* 109.6 (Mar. 2011). DOI: 10.1063/1.3552890. URL: https://doi.org/10.1063/1.3552890.

[205] H. Zu, W. Dai, and A.T.A.M. de Waele. "Development of dilution refrigerators—A review". In: *Cryogenics* 121 (Jan. 2022), p. 103390. DOI: 10.1016/j.cryogenics.2021.103390. URL: https://doi.org/10.1016/j.cryogenics.2021.103390.

[206] Florian Marquardt, A.A. Clerk, and S.M. Girvin. "Quantum theory of optomechanical cooling". In: *Journal of Modern Optics* 55.19-20 (Nov. 2008), pp. 3329–3338. DOI: 10.1080/09500340802454971. URL: https://doi.org/10.1080/09500340802454971.

[207] J. M. Dobrindt, I. Wilson-Rae, and T. J. Kippenberg. "Parametric Normal-Mode Splitting in Cavity Optomechanics". In: *Physical Review Letters* 101.26 (Dec. 2008). DOI: 10.1103/physrevlett.101.263602. URL: https://doi.org/10.1103/physrevlett.101.263602.

[208] Dustin Kleckner and Dirk Bouwmeester. "Sub-kelvin optical cooling of a micromechanical resonator". In: *Nature* 444.7115 (Nov. 2006), pp. 75–78. DOI: 10.1038/nature05231. URL: https://doi.org/10.1038/nature05231.

[209] Nils T. Otterstrom et al. "Optomechanical Cooling in a Continuous System". In: *Physical Review X* 8.4 (Nov. 2018). DOI: 10.1103/physrevx.8.041034. URL: https://doi.org/10.1103/physrevx.8.041034.

[210] A. D. O'Connell et al. "Quantum ground state and single-phonon control of a mechanical resonator". In: *Nature* 464.7289 (Mar. 2010), pp. 697–703. DOI: 10.1038/nature08967. URL: https://doi.org/10.1038/nature08967.

[211] J. D. Teufel et al. "Sideband cooling of micromechanical motion to the quantum ground state". In: *Nature* 475.7356 (July 2011), pp. 359–363. DOI: 10.1038/nature10261. URL: https://doi.org/10.1038/nature10261.

[212] Lorenzo Magrini et al. "Real-time optimal quantum control of mechanical motion at room temperature". In: *Nature* 595.7867 (July 2021), pp. 373–377. DOI: 10.1038/s41586-021-03602-3. URL: https://doi.org/10.1038/s41586-021-03602-3.

[213] Uroš Delić et al. "Cooling of a levitated nanoparticle to the motional quantum ground state". In: *Science* 367.6480 (Feb. 2020), pp. 892–895. DOI: 10.1126/science.aba3993. URL: https://doi.org/10.1126/science.aba3993.

[214] L. Duband, J.M. Duval, and N. Luchier. "SAFARI engineering model 50 mK cooler". In: *Cryogenics* 64 (Nov. 2014), pp. 213–219. ISSN: 0011-2275. DOI: 10.1016/j.cryogenics.2014.02.008. URL: http://dx.doi.org/10.1016/j.cryogenics.2014.02.008.

[215] N. Luchier et al. "50mK cooling solution with an ADR precooled by a sorption cooler". In: *Cryogenics* 50.9 (Sept. 2010), pp. 591–596. ISSN: 0011-2275. DOI: 10.1016/j.cryogenics.2010.02.022. URL: http://dx.doi.org/10.1016/j.cryogenics.2010.02.022.

[216] C. A. Potts et al. "Dynamical Backaction Magnomechanics". In: *Physical Review X* 11.3 (Sept. 2021). ISSN: 2160-3308. DOI: 10.1103/physrevx.11.031053. URL: http://dx.doi.org/10.1103/PhysRevX.11.031053.

[217] Ming-Song Ding, Li Zheng, and Chong Li. "Ground-state cooling of a magnomechanical resonator induced by magnetic damping". In: *Journal of the Optical Society of America B* 37.3 (Feb. 2020), p. 627. DOI: 10.1364/josab.380755. URL: https://doi.org/10.1364/josab.380755.

[218] Jamie M. Fitzgerald et al. “Cavity optomechanics with photonic bound states in the continuum”. In: *Physical Review Research* 3.1 (Feb. 2021). DOI: 10.1103/physrevresearch.3.013131. URL: https://doi.org/10.1103/physrevresearch.3.013131.

[219] Kamran Ullah, M. Tahir Naseem, and Özgür E. Müstecaplıoğlu. “Tunable multiwindow magnomechanically induced transparency, Fano resonances, and slow-to-fast light conversion”. In: *Physical Review A* 102.3 (Sept. 2020). ISSN: 2469-9934. DOI: 10.1103/physreva.102.033721. URL: http://dx.doi.org/10.1103/PhysRevA.102.033721.

[220] Mingyun Yuan et al. “Large cooperativity and microkelvin cooling with a three-dimensional optomechanical cavity”. In: *Nature Communications* 6.1 (Oct. 2015). ISSN: 2041-1723. DOI: 10.1038/ncomms9491. URL: http://dx.doi.org/10.1038/ncomms9491.

[221] C.A. Potts et al. “Magnon-Phonon Quantum Correlation Thermometry”. In: *Physical Review Applied* 13.6 (June 2020). ISSN: 2331-7019. DOI: 10.1103/physrevapplied.13.064001. URL: http://dx.doi.org/10.1103/PhysRevApplied.13.064001.

[222] Amit Rai and G. S. Agarwal. “Quantum optical spring”. In: *Physical Review A* 78.1 (July 2008). ISSN: 1094-1622. DOI: 10.1103/physreva.78.013831. URL: http://dx.doi.org/10.1103/PhysRevA.78.013831.

[223] A M Jayich et al. “Dispersive optomechanics: a membrane inside a cavity”. In: *New Journal of Physics* 10.9 (Sept. 2008), p. 095008. DOI: 10.1088/1367-2630/10/9/095008. URL: https://doi.org/10.1088/1367-2630/10/9/095008.

[224] S. Schmid et al. “Damping mechanisms in high-Q micro and nanomechanical string resonators”. In: *Physical Review B* 84.16 (Oct. 2011). DOI: 10.1103/physrevb.84.165307. URL: https://doi.org/10.1103/physrevb.84.165307.

[225] Quirin P. Unterreithmeier, Thomas Faust, and Jörg P. Kotthaus. “Damping of Nanomechanical Resonators”. In: *Physical Review Letters* 105.2 (July 2010). DOI: 10.1103/physrevlett.105.027205. URL: https://doi.org/10.1103/physrevlett.105.027205.

[226] P.-L. Yu, T. P. Purdy, and C. A. Regal. “Control of Material Damping in High-Q Membrane Microresonators”. In: *Physical Review Letters* 108.8 (Feb. 2012). DOI: 10.1103/physrevlett.108.083603. URL: https://doi.org/10.1103/physrevlett.108.083603.

[227] Scott S. Verbridge et al. “High quality factor resonance at room temperature with nanostrings under high tensile stress”. In: *Journal of Applied Physics* 99.12 (June 2006), p. 124304. DOI: 10.1063/1.2204829. URL: https://doi.org/10.1063/1.2204829.

[228] Scott S. Verbridge, Harold G. Craighead, and Jeevak M. Parpia. “A megahertz nanomechanical resonator with room temperature quality factor over a million”. In: *Applied Physics Letters* 92.1 (2008), p. 013112. DOI: 10.1063/1.2822406. URL: https://doi.org/10.1063/1.2822406.

[229] D. R. Southworth et al. “Stress and Silicon Nitride: A Crack in the Universal Dissipation of Glasses”. In: *Physical Review Letters* 102.22 (June 2009). DOI: 10.1103/physrevlett.102.225503. URL: https://doi.org/10.1103/physrevlett.102.225503.

[230] L. G. Villanueva and S. Schmid. "Evidence of Surface Loss as Ubiquitous Limiting Damping Mechanism in SiN Micro- and Nanomechanical Resonators". In: *Physical Review Letters* 113.22 (Nov. 2014). DOI: 10.1103/physrevlett.113.227201. URL: https://doi.org/10.1103/physrevlett.113.227201.

[231] D. J. Wilson et al. "Cavity Optomechanics with Stoichiometric SiN Films". In: *Physical Review Letters* 103.20 (Nov. 2009). DOI: 10.1103/physrevlett.103.207204. URL: https://doi.org/10.1103/physrevlett.103.207204.

[232] Chuen-Lin Tien and Tsai-Wei Lin. "Thermal expansion coefficient and thermomechanical properties of SiNsubx/sub thin films prepared by plasma-enhanced chemical vapor deposition". In: *Applied Optics* 51.30 (Oct. 2012), p. 7229. DOI: 10.1364/ao.51.007229. URL: https://doi.org/10.1364/ao.51.007229.

[233] Xue Yin Sun et al. "Single-Step Deposition of Cerium-Substituted Yttrium Iron Garnet for Monolithic On-Chip Optical Isolation". In: *ACS Photonics* 2.7 (June 2015), pp. 856–863. DOI: 10.1021/acsphotonics.5b00026. URL: https://doi.org/10.1021/acsphotonics.5b00026.

[234] A Delgado et al. "Combining the sol gel method and spin coating to obtain YIG films with low FMR linewidth on silicon (100) substrate". In: *Materials Research Express* 5.2 (Feb. 2018), p. 026419. DOI: 10.1088/2053-1591/aaaff8. URL: https://doi.org/10.1088/2053-1591/aaaff8.

[235] Kangfu Li et al. "Crack-free Y3Fe5O12 films deposited on Si substrate obtained by two-step annealing process". In: *Materials Letters* 228 (Oct. 2018), pp. 21–24. DOI: 10.1016/j.matlet.2018.05.113. URL: https://doi.org/10.1016/j.matlet.2018.05.113.

[236] Taichi Goto, Mehmet C. Onbaşlò, and C. A. Ross. "Magneto-optical properties of cerium substituted yttrium iron garnet films with reduced thermal budget for monolithic photonic integrated circuits". In: *Optics Express* 20.27 (Dec. 2012), p. 28507. DOI: 10.1364/oe.20.028507. URL: https://doi.org/10.1364/oe.20.028507.

[237] Jianyun Lian et al. "Annealing effects on the microstructure and magnetic properties of Y3Fe5O12 films deposited on Si/SiO2 substrates by RF magnetron sputtering". In: *Ceramics International* 43.10 (July 2017), pp. 7477–7481. DOI: 10.1016/j.ceramint.2017.03.023. URL: https://doi.org/10.1016/j.ceramint.2017.03.023.

[238] Rongxin Xiang et al. "Electrical generation and detection of spin waves in polycrystalline YIG/Pt grown on silicon wafers". In: *Materials Research Express* 7.4 (Apr. 2020), p. 046105. DOI: 10.1088/2053-1591/ab87d7. URL: https://doi.org/10.1088/2053-1591/ab87d7.

[239] Satya Prakash Pati. "Study on the Gilbert damping of polycrystalline YIG films with different capping layers". In: *Current Applied Physics* 20.1 (Jan. 2020), pp. 167–171. DOI: 10.1016/j.cap.2019.10.022. URL: https://doi.org/10.1016/j.cap.2019.10.022.

[240] J. Förster et al. "Nanoscale X-ray imaging of spin dynamics in yttrium iron garnet". In: *Journal of Applied Physics* 126.17 (Nov. 2019). DOI: 10.1063/1.5121013. URL: https://doi.org/10.1063/1.5121013.

[241] R. L. Edwards, G. Coles, and W. N. Sharpe. "Comparison of tensile and bulge tests for thin-film silicon nitride". In: *Experimental Mechanics* 44.1 (Feb. 2004), pp. 49–54. DOI: 10.1007/bf02427976. URL: https://doi.org/10.1007/bf02427976.

[242] A. Khan, J. Philip, and P. Hess. "Young's modulus of silicon nitride used in scanning force microscope cantilevers". In: *Journal of Applied Physics* 95.4 (Jan. 2004), pp. 1667–1672. DOI: 10.1063/1.1638886. URL: https://doi.org/10.1063/1.1638886.

[243] Satoru Emori et al. "Coexistence of Low Damping and Strong Magnetoelastic Coupling in Epitaxial Spinel Ferrite Thin Films". In: *Advanced Materials* 29.34 (July 2017). ISSN: 1521-4095. DOI: 10.1002/adma.201701130. URL: http://dx.doi.org/10.1002/adma.201701130.

[244] M. F. Lewis. "Elastic Constants of Magnesium Aluminate Spinel". In: *The Journal of the Acoustical Society of America* 40.3 (Sept. 1966), pp. 728–729. ISSN: 1520-8524. DOI: 10.1121/1.1910143. URL: http://dx.doi.org/10.1121/1.1910143.

[245] O. M. Chumak et al. "Magnetoelastic interactions and magnetic damping in Co2Fe0.4Mn0.6Si and Co2FeGa0.5Ge0.5 Heusler alloys thin films for spintronic applications". In: *Scientific Reports* 11.1 (Apr. 2021). ISSN: 2045-2322. DOI: 10.1038/s41598-021-87205-y. URL: http://dx.doi.org/10.1038/s41598-021-87205-y.

[246] K Marklund and S A Mahmoud. "Elastic Constants of Magnesium Oxide". In: *Physica Scripta* 3.2 (Feb. 1971), pp. 75–76. ISSN: 1402-4896. DOI: 10.1088/0031-8949/3/2/005. URL: http://dx.doi.org/10.1088/0031-8949/3/2/005.

[247] Peter Rakich and Florian Marquardt. "Quantum theory of continuum optomechanics". In: *New Journal of Physics* 20.4 (Apr. 2018), p. 045005. ISSN: 1367-2630. DOI: 10.1088/1367-2630/aaac4f. URL: http://dx.doi.org/10.1088/1367-2630/aaac4f.

[248] D. M. Pozar. *Microwave Engineering*. 4th ed. John Wiley & Sons, Nov. 2011.

[249] Uri Vool and Michel Devoret. "Introduction to quantum electromagnetic circuits". In: *International Journal of Circuit Theory and Applications* 45.7 (June 2017), pp. 897–934. DOI: 10.1002/cta.2359. URL: https://doi.org/10.1002/cta.2359.

[250] M. H. Devoret. *Quantum Fluctuations: Volume 63*. Ed. by S. Reynaud, E. Giacobino, and F. David. Les Houches. North-Holland, June 1997.

[251] Michael J. Morgan. "Lagrangian formulation of a transmission line". In: *American Journal of Physics* 56.7 (July 1988), pp. 639–643. DOI: 10.1119/1.15530. URL: https://doi.org/10.1119/1.15530.

[252] Dimitri Jeltsema and Arjan J. Van Der Schaft. "Lagrangian and Hamiltonian formulation of transmission line systems with boundary energy flow". In: *Reports on Mathematical Physics* 63.1 (Feb. 2009), pp. 55–74. DOI: 10.1016/s0034-4877(09)00009-3. URL: https://doi.org/10.1016/s0034-4877(09)00009-3.

[253] A I Akhiezer, V G Bar'yakhtar, and Moisei I Kaganov. "SPIN WAVES IN FERROMAGNETS AND ANTIFERROMAGNETS. I". In: *Soviet Physics Uspekhi* 3.4 (Apr. 1961), pp. 567–592. DOI: 10.1070/pu1961v003n04abeh003309. URL: https://doi.org/10.1070/pu1961v003n04abeh003309.

[254] R. W. Damon and J. R. Eshbach. "Magnetostatic Modes of a Ferromagnetic Slab". In: *Journal of Applied Physics* 31.5 (May 1960), S104–S105. DOI: 10.1063/1.1984622. URL: https://doi.org/10.1063/1.1984622.